

AD-A265 346

MENTATION PAGE



1. AGENCY USE ONLY (leave blank)		2. REPORT DATE	3. REPORT TYPE AND DATES COVERED THESIS /DISSERTATION
4. TITLE AND SUBTITLE On the Vertical Structure of Seasonal, Interannual and Intraseasonal Flows			5. FUNDING NUMBERS
6. AUTHOR(S) Steven Reino Gilbert, Major			
7. PERFORMING ORGANIZATION NAME(S) AND ADDRESS(ES) AFIT Student Attending: University of Utah			8. PERFORMING ORGANIZATION REPORT NUMBER AFIT/CI/CIA- 92-30D
9. SPONSORING/MONITORING AGENCY NAME(S) AND ADDRESS(ES) AFIT/CI Wright-Patterson AFB OH 45433-6583			10. SPONSORING/MONITORING AGENCY REPORT NUMBER
11. SUPPLEMENTARY NOTES			
12a. DISTRIBUTION/AVAILABILITY STATEMENT Approved for Public Release IAW 190-1 Distribution Unlimited MICHAEL M. BRICKER, SMSgt, USAF Chief Administration			12b. DISTRIBUTION CODE
13. ABSTRACT (Maximum 200 words)			
<div style="text-align: center;">DTIC ELECTE JUN 07 1993 S A D</div> <div style="text-align: right; margin-top: 20px;">93-12598 </div> <div style="text-align: center; margin-top: 20px;">024</div>			
14. SUBJECT TERMS			15. NUMBER OF PAGES 198
			16. PRICE CODE
17. SECURITY CLASSIFICATION OF REPORT	18. SECURITY CLASSIFICATION OF THIS PAGE	19. SECURITY CLASSIFICATION OF ABSTRACT	20. LIMITATION OF ABSTRACT

300

ON THE VERTICAL STRUCTURE OF SEASONAL, INTERANNUAL AND INTRASEASONAL FLOWS

by

Steven Reino Gilbert

A dissertation submitted to the faculty of
The University of Utah
in partial fulfillment of the requirements for the degree of

Doctor of Philosophy

Department of Meteorology

The University of Utah

December 1992

Acquisition for	
NTIS - Original	A
DTIC - The	
Department of	
Information	
By	
Date	
Approved by	
Doc	Approved
	Special
A-1	

Copyright © Steven Reino Gilbert 1992

All Rights Reserved

THE UNIVERSITY OF UTAH GRADUATE SCHOOL

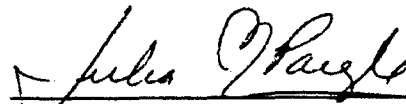
SUPERVISORY COMMITTEE APPROVAL

of a dissertation submitted by

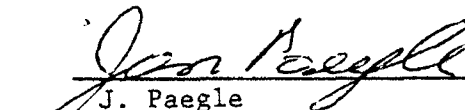
Steven R. Gilbert

This dissertation has been read by each member of the following supervisory committee and by majority vote has been found to be satisfactory.

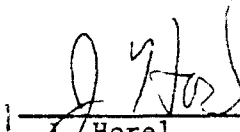
August 3, 1992


Chairman: J.N. Paegle


August 3, 1992


J. Paegle

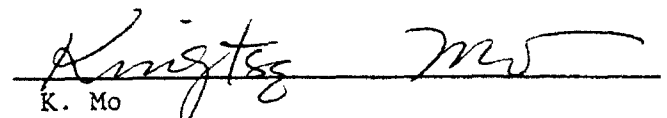
August 3, 1992


J. Horel

August 3, 1992


J.E. Geisler

August 3, 1992


K. Mo

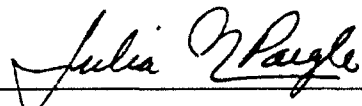
THE UNIVERSITY OF UTAH GRADUATE SCHOOL

FINAL READING APPROVAL

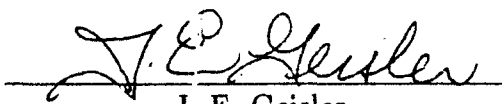
To the Graduate Council of The University of Utah:

I have read the dissertation of Steven R. Gilbert in its final form and have found that (1) its format, citations, and bibliographic style are consistent and acceptable; (2) its illustrative materials including figures, tables, and charts are in place; and (3) the final manuscript is satisfactory to the Supervisory Committee and is ready for submission to the Graduate School.

September 9, 1992
Date


Julia Nogués-Paegle
Chair, Supervisory Committee

Approved for the Major Department


J. E. Geisler
Chair/Dean

Approved for the Graduate Council

B. Cale Dick
Dean of The Graduate School

ABSTRACT

The vertical structure of the height and wind fields associated with the seasonal, interannual, and intraseasonal cycles is documented by making use of global ECMWF operational analyses for seven pressure levels (1000-100 mb) and spanning a 10 year period (1980-89). The role of tropical convection is examined for each of these time scales.

The seasonal cycle is described through the structure of the geopotential height field standing waves, the vertical structure of the first seven wavenumbers of the rotational and divergent winds, and latitude/time cross-sections for the vertical structure of the planetary waves. The change in the vertical structure from the internal mode combinations found in the tropics to a dominant external mode of the extratropics occurs rapidly and within 10° of the convective source regions. Extensive use is made of a primitive equation (PE) model, as a diagnostic tool, to explore the extent to which tropical heating might influence the extratropical vertical structure. The PE response indicates the possibility that 25-40% of the Northern Hemisphere and 30-55% of the Southern Hemisphere kinematic vertical structure could be the result of tropical heating.

Two significant El Niño Southern Oscillation (ENSO) events occur during this 10 year period and their vertical structures are examined. The cold phase is found to be dominated by higher internal modes than the warm phase. This may be linked to different air-sea interactive processes during cold and warm ENSO phases. The tie to tropical convection is also seen in the PE model response which shows wave trains and zonal wind maxima moving westward from the warm to cold phase of the ENSO events, consistent with observations.

The intraseasonal oscillation, as found in the near-equatorial 200 mb velocity potential, is composited for three seasons. A link between this oscillation and tropical convection is only clearly established during the convective phase, when convective activity is present across the Western Pacific and Indian Oceans. Composite cases for each season are selected to be in phase with one another and during times when the convective phase of the intraseasonal oscillation is strong. It is found that when convective regions in the composites are collocated with those present in the seasonal average, the kinematic vertical structure is dominated by the two deepest vertical modes. This is different for other locations, where the convection in the composites does not coincide with regions of convection in the seasonal average. In this case the kinematic vertical structure favors higher internal modes.

CONTENTS

ABSTRACT	iv
LIST OF TABLES	viii
LIST OF FIGURES	ix
ACKNOWLEDGMENTS	xvii

CHAPTERS

1. INTRODUCTION	1
2. DATA AND METHODOLOGY	8
2.1 Data	8
2.2 Methodology	9
2.2.1 Fourier Transforms	10
2.2.2 Normal Mode Vertical Structure Decomposition	11
2.2.3 Vertical Mode Projection of Fourier Coefficients	15
2.2.4 Shallow Water Equation Model	16
2.2.5 The Primitive Equation Model	17
3. THE SEASONAL CYCLE	23
3.1 Zonally Averaged Seasonal Cycle	26
3.2 Seasonal Wave Cycle	33
3.2.1 Stationary Waves	33
3.2.2 Fourier Analysis	48
3.3 Wavenumber Vertical Structure	52
3.3.1 The Zonal Rotational Wind	52
3.3.2 The Meridional Rotational Wind	61
3.3.3 The Zonal Divergent Wind	65
3.3.4 The Meridional Divergent Wind	65
3.3.5 Seasonal March of Selected Waves and Modes	67
3.4 Model Response to Tropical Heating	88
4. LOW-FREQUENCY OSCILLATIONS	110
4.1 El Niño - Southern Oscillation Phenomenon	111
4.1.1 1983 - 1985 ENSO	113
4.1.2 1987 - 1989 ENSO	136
4.2 Intraseasonal Oscillations	156
4.2.1 Equatorial Wave One Statistics	157
4.2.2 Global Departures from the Annual Mean	166

4.2.3 Vertical Structure of Divergent Winds	17
5. DISCUSSION AND CONCLUSIONS	18
REFERENCES	19

LIST OF TABLES

2.1	Changes in the analyses at ECMWF after 1980 which might affect tropical divergent motions (extracted from Trenberth and Olson, 1988).	
3.1	Maxima (m s^{-1}) for zonal rotational wind summed for the first seven wavenumbers over the latitudinal belts for January, April, July and October 1980-1989.	5
3.2	Maxima (m s^{-1}) for meridional rotational wind summed for the first seven wavenumbers over the latitudinal belts for January and July 1980-1989.	5
3.3	Maxima (m s^{-1}) for zonal divergent wind summed for the first seven wavenumbers over the latitudinal belts for January and July 1980-1989.	5
3.4	Maxima (m s^{-1}) for meridional divergent wind summed for the first seven wavenumbers over the latitudinal belts for January and July 1980-1989.	5
4.1	Pentad (PTD) for which annual seasonal maxima (in units of $10^6 \text{ m}^2 \text{ s}^{-1}$), amplitude (AMP), and phase occurred for wave one component of the 200 mb velocity potential field. Velocity potential is averaged between 5° N - 5° S	15

LIST OF FIGURES

- 2.1 Vertical structure function for seven levels of the ECMWF data set. Equivalent depths are 9262, 930, 152, 37, 11, 4, and 0.7 m for modes one through seven, respectively.
- 2.2 Equivalent barotropic vertical structure. Represented on this graph are the external mode (solid line), third mode (dashed line), and combination of mode one plus 50% of mode three at each level (heavy solid line).
- 2.3 Tropical deep convection vertical structure. Represented on this graph are the second mode (solid line), third mode (dashed line), and combination of mode two plus mode three at each level (heavy solid line).
- 2.4 Profile of the annual mean zonal wind for January 1980-1989 at (a) 200, (b) 300, (c) 500, and (d) 850 mb.
- 3.1 Mean seasonal zonal wind. Maximum values at 200 mb for NH and SH are, respectively 41.9 and 29.9 m s^{-1} for DJF, 31.3 and 27.7 m s^{-1} for MAM, 21.1 and 39.1 m s^{-1} for JJA, and 26.5 and 31.6 m s^{-1} for SON. Contour interval is 3 m s^{-1} with light and medium dots shading winds between 15-30 m s^{-1} and 30-45 m s^{-1} , respectively.
- 3.2 Mean seasonal meridional wind. Maximum values at 200 mb centered over the equator for the NH and SH are, respectively 2.15 and -0.242 m s^{-1} for DJF, 1.77 and -0.674 m s^{-1} for MAM, 0.494 and -1.81 m s^{-1} for JJA, and 1.06 and -0.97 m s^{-1} for SON. Contour interval is 0.3 m s^{-1} with light and medium dots shading winds between ± 1.5 -3.0 m s^{-1} and ± 3.0 -4.5 m s^{-1} , respectively.
- 3.3 January and July 1980-1989. Zonal wind shown in (a,c). Contour interval is 5 m s^{-1} with light, medium and dark shading for speeds of 15-30 m s^{-1} , 30-45 m s^{-1} , and 45-60 m s^{-1} . OLR, velocity potential and divergent winds are shown in (b,d). OLR shading discussed in text. Maximum winds are 5.4 m s^{-1} near 23° N, 124° E in (b) and 4.6 m s^{-1} near 18° N, 90° E in (d). Wind less than 2 m s^{-1} are not plotted in (b,d).

- 3.4 Time-longitude sections of (a) 200 mb zonal wind, (b) OLR, and (c) 850 mb zonal wind at 15° N. Contour interval for (a) and (c) are 5 m s^{-1} and 2 m s^{-1} . OLR shading follows the same convention described in text. 3
- 3.5 Height-longitude cross-section of the stationary wave geopotential height for December–February 1980–1989 at (a) 60° N, (b) 45° N, and (c) 25° N and for June–August 1980–1989 at (d) 60° N, (e) 45° N, and (f) 25° N. Contour interval is 30 m. 3
- 3.6 Height-longitude cross-section of the stationary wave geopotential height for June–August 1980–1989 at (a) 25° S, (b) 45° S, and (c) 60° S and for December–February 1980–1989 at (d) 25° S, (e) 45° S, and (f) 60° S. Contour interval is 30 m. 4
- 3.7 Height-longitude cross-section of the stationary wave geopotential height for March–May 1980–1989 at (a) 60° N, (b) 45° N, and (c) 25° N and for September–November 1980–1989 at (d) 60° N, (e) 45° N, and (f) 25° N. Contour interval is 30 m. 4
- 3.8 Height-longitude cross-section of the stationary wave geopotential height for September–November 1980–1989 at (a) 25° S, (b) 45° S, and (c) 60° S and for March–May 1980–1989 at (d) 25° S, (e) 45° S, and (f) 60° S. Contour interval is 30 m. 4
- 3.9 Zonally averaged seasonal momentum and heat transport for DJF (a,b), MAM (c,d), JJA (e,f) and SON (g,h). Contour interval is $2 \text{ m}^2 \text{ s}^{-2}$ in (a) and $2^\circ \text{ K m s}^{-1}$ in (b). Shading is for values of ± 10 units. . . 4
- 3.10 Latitude/time cross-section of amplitude for the 200 and 850 mb heights for wavenumbers one, two, and three. Contour interval is 10 m. and heights from 50–100 m are shaded with light dots, 100–150 m are shaded with medium dots, and 150+ m are shaded with heavy dots. The 10 m contour is highlighted. 4
- 3.11 Contribution of the first seven wavenumbers to the total wind variability during each season for the (a) zonal rotational, (b) meridional rotational, (c) zonal divergent, and (d) meridional divergent wind components. 4
- 3.12 Contribution by the first five vertical modes for the zonal rotational wind during (a) January and (b) April 1980–1989 for waves one through seven. Mode representation by arrows described in text. Maximum normalized vector shown in bottom right of each panel. 4

3.13	Contribution by the first five vertical modes for the zonal rotational wind during (a) July and (b) October 1980-1989 for waves one through seven. Mode representation by arrows described in text. Maximum normalized vector shown in bottom right of each panel.	62
3.14	Contribution by the first five vertical modes for the meridional rotational wind during (a) January and (b) July 1980-1989 for waves one through seven. Mode representation by arrows described in text. Maximum normalized vector shown in bottom right of each panel. .	64
3.15	Contribution by the first five vertical modes for the zonal divergent wind during (a) January and (b) July 1980-1989 for waves one through seven. Mode representation by arrows described in text. Maximum normalized vector shown in bottom right of each panel.	66
3.16	Contribution by the first five vertical modes for the meridional divergent wind during (a) January and (b) July 1980-1989 for waves one through seven. Mode representation by arrows described in text. Maximum normalized vector shown in bottom right of each panel. .	68
3.17	Latitude/time cross-section of the vertical modes for long wave contributions to the zonal rotational wind. The first three modes for wave number one are shown in (a), (b), and (c), for wavenumber two in (d), (e), and (f), and lastly for wavenumber three in (g), (h), and (i). Contour interval is 0.5 m s^{-1} . Dark shading represents speed from $2-4 \text{ m s}^{-1}$, medium dots are for speeds between $4-8 \text{ m s}^{-1}$, and light dots are for speeds ranging from $8-12 \text{ m s}^{-1}$. Regions with speeds greater than 12 m s^{-1} are clear.	70
3.18	Latitude/time cross-section of the vertical modes for long wave contributions to the meridional divergent wind. The internal modes two, three, and five for wavenumber one are shown in (a), (b), and (c), for wavenumber two in (d), (e), and (f), and lastly for wavenumber three in (g), (h), and (i). Contour interval is 0.05 m s^{-1} . Dark shading represents speed from $0.1-0.2 \text{ m s}^{-1}$, medium dots are for speeds between $0.2-0.4 \text{ m s}^{-1}$, heavy dots delineate speed of $0.3-0.4 \text{ m s}^{-1}$, and light dots are for speeds ranging from $0.4-0.5 \text{ m s}^{-1}$. Regions with speeds greater than 0.5 m s^{-1} are clear.	79

3.19	Latitude/time cross-section of the vertical modes for long wave contributions to the zonal divergent wind. The internal modes two, three, and four for wavenumber one are shown in (a), (b), and (c), for wavenumber two in (d), (e), and (f), and lastly for wavenumber three in (g), (g), and (i). Contour interval is 0.05 m s^{-1} . Dark shading represents speed from $0.1\text{--}0.2 \text{ m s}^{-1}$, medium dots are for speeds between $0.2\text{--}0.4 \text{ m s}^{-1}$, heavy dots delineate speed of $0.3\text{--}0.4 \text{ m s}^{-1}$, and light dots are for speeds ranging from $0.4\text{--}0.5 \text{ m s}^{-1}$. Regions with speeds greater than 0.5 m s^{-1} are clear.	89
3.20	Satellite derived (GPCP) mean monthly rainfall rates for the period 1986–1990 in mm/day for January and July. Graphs provided courtesy of K. Mo.	99
3.21	Heating rates in $^{\circ}\text{K day}^{-1}$ multiplied by 100 and contoured every $100^{\circ}\text{K day}^{-1}$ for January (a) and July (d); observed velocity potential contoured every $10^6 \text{ m}^2 \text{ s}^{-1}$ and divergent wind truncated to include only the first and second internal modes (b,e), velocity potential and divergent wind obtained as the average of the last 15 days of a 90 day PE integration (c,f). The level for (c)–(f) is $\sigma = 0.2$ and the maximum wind vectors are set at 2.5 m s^{-1}	100
3.22	Height wave response to tropical heating obtained from the linear shallow water equation model, contoured every 20 m (a, d). Height waves at $\sigma = 0.2$ averaged for the last 15 days of the second (b, d) and third (d, f) month integrations of the PE model. Contour interval is 40 m in panels b, c, e, and f.	103
3.23	Zonal wind wave component from analysis (a, contoured every 5 m s^{-1}) and from the PE simulation (b, contoured every 2 m s^{-1}) and meridional wind component from analysis (c) and PE simulation (d) contoured every 2 m s^{-1} for January.	106
3.24	Zonal wind wave component from analysis (a, contoured every 5 m s^{-1}) and from the PE simulation (b, contoured every 2 m s^{-1}) and meridional wind component from analysis (c) and PE simulation (d) contoured every 2 m s^{-1} for July.	107
4.1	Composite assessment of the correlations of annual mean sea level pressures with Darwin, Australia (taken from Trenberth and Shea, 1987). 112	

- 4.2 Monthly mean OLR (a), 200 mb streamfunction (b) and velocity potential (c) with OLR anomaly superimposed for February 1983, as well as PE simulations averaged for days 60-74 for the streamfunction (d) and velocity potential (e). Shading for OLR described in text. Contours intervals are $0.5 \times 10^7 \text{ m}^2 \text{ s}^{-1}$ in (b,d), and $1 \times 10^6 \text{ m}^2 \text{ s}^{-1}$ in (c,e). Maximum wind value in (e) of 3.35 m s^{-1} near 75° S , 157° W . 114
- 4.3 Monthly mean OLR (a), 200 mb streamfunction (b) and velocity potential (c) with OLR anomaly superimposed for February 1985, as well as PE simulations averaged for days 60-74 for the streamfunction (d) and velocity potential (e). Shading for OLR described in text. Contours intervals are $0.5 \times 10^7 \text{ m}^2 \text{ s}^{-1}$ in (b,d) and, $1 \times 10^6 \text{ m}^2 \text{ s}^{-1}$ in (c,e). Maximum wind value in (e) of 3.18 m s^{-1} near 75° S , 113° W . 119
- 4.4 Total root mean square value (a) and normalized modes one (b), two (c), and three (d) for February 1983 zonal rotational wind. Mode contributions in (b-d) are normalized using the total root mean square value in (a). Contour interval in (a) 5 m s^{-1} with light shading in area of $10\text{--}20 \text{ m s}^{-1}$, medium shading for $20\text{--}40 \text{ m s}^{-1}$, and heavy shading for $40\text{--}60 \text{ m s}^{-1}$. Contour interval in (b)-(d) is 0.25 with heavy shading for areas > 0.50 and light shading for regions < -0.50 . 122
- 4.5 Total root mean square value (a) and normalized modes one (b), two (c), and three (d) for February 1983 meridional rotational wind. Mode contributions in (b-d) are normalized using the total root mean square value in (a). Contour interval in (a) 2.5 m s^{-1} with light shading in area of $5\text{--}10 \text{ m s}^{-1}$, medium shading for $10\text{--}15 \text{ m s}^{-1}$, and heavy shading for $15\text{--}20 \text{ m s}^{-1}$. Contour interval in (b)-(d) is 0.25 with heavy shading for areas > 0.50 and light shading for regions < -0.50 125
- 4.6 Total root mean square value (a) and normalized modes one (b), two (c), and three (d) for February 1985 zonal rotational wind. Mode contributions in (b-d) are normalized using the total root mean square value in (a). Contour interval in (a) 5 m s^{-1} with light shading in area of $10\text{--}20 \text{ m s}^{-1}$, medium shading for $20\text{--}40 \text{ m s}^{-1}$, and heavy shading for $40\text{--}60 \text{ m s}^{-1}$. Contour interval in (b)-(d) is 0.25 with heavy shading for areas > 0.50 and light shading for regions < -0.50 . 128

- 4.7 Total root mean square value (a) and normalized modes one (b), two (c), and three (d) for February 1985 meridional rotational wind. Mode contributions in (b-d) are normalized using the total root mean square value in (a). Contour interval in (a) 2.5 ms^{-1} with light shading in area of $5\text{--}10 \text{ ms}^{-1}$, medium shading for $10\text{--}15 \text{ ms}^{-1}$, and heavy shading for $15\text{--}20 \text{ ms}^{-1}$. Contour interval in (b)-(d) is 0.25 with heavy shading for areas > 0.50 and light shading for regions < -0.50 131
- 4.8 Five-month running mean of the sea level pressure anomalies at Darwin (dashed) and Tahiti (solid). Taken from *Climate Diagnostics Bulletin*, January 1989, No. 89-1, US Department of Commerce. . 137
- 4.9 Monthly mean OLR (a), 200 mb streamfunction (b) and velocity potential (c) with OLR anomaly superimposed for February 1987. Shading for OLR described in text. Contours intervals are $0.5 \times 10^7 \text{ m}^2 \text{ s}^{-1}$ in (b) and $1 \times 10^6 \text{ m}^2 \text{ s}^{-1}$ in (c). 138
- 4.10 Monthly mean OLR (a), 200 mb streamfunction (b) and velocity potential (c) with OLR anomaly superimposed for February 1989. Shading for OLR described in text. Contours intervals are $0.5 \times 10^7 \text{ m}^2 \text{ s}^{-1}$ in (b) and $1 \times 10^6 \text{ m}^2 \text{ s}^{-1}$ in (c). 140
- 4.11 Total root mean square value (a) and normalized modes one (b), two (c), and three (d) for February 1987 zonal rotational wind. Mode contributions in (b-d) are normalized using the total root mean square value in (a). Contour interval in (a) 5 ms^{-1} with light shading in area of $10\text{--}20 \text{ ms}^{-1}$, medium shading for $20\text{--}40 \text{ ms}^{-1}$, and heavy shading for $40\text{--}60 \text{ ms}^{-1}$. Contour interval in (b)-(d) is 0.25 with heavy shading for areas > 0.50 and light shading for regions < -0.50 . 143
- 4.12 Total root mean square value (a) and normalized modes one (b), two (c), and three (d) for February 1987 meridional rotational wind. Mode contributions in (b-d) are normalized using the total root mean square value in (a). Contour interval in (a) 2.5 ms^{-1} with light shading in area of $5\text{--}10 \text{ ms}^{-1}$, medium shading for $10\text{--}15 \text{ ms}^{-1}$, and heavy shading for $15\text{--}20 \text{ ms}^{-1}$. Contour interval in (b)-(d) is 0.25 with heavy shading for areas > 0.50 and light shading for regions < -0.50 146

- 4.13 Total root mean square value (a) and normalized modes one (b), two (c), and three (d) for February 1989 zonal rotational wind. Mode contributions in (b-d) are normalized using the total root mean square value in (a). Contour interval in (a) 5 m s^{-1} with light shading in area of $10\text{--}20 \text{ m s}^{-1}$, medium shading for $20\text{--}40 \text{ m s}^{-1}$, and heavy shading for $40\text{--}60 \text{ m s}^{-1}$. Contour interval in (b)-(d) is 0.25 with heavy shading for areas > 0.50 and light shading for regions < -0.50 . 149
- 4.14 Total root mean square value (a) and normalized modes one (b), two (c), and three (d) for February 1989 meridional rotational wind. Mode contributions in (b-d) are normalized using the total root mean square value in (a). Contour interval in (a) 2.5 m s^{-1} with light shading in area of $5\text{--}10 \text{ m s}^{-1}$, medium shading for $10\text{--}15 \text{ m s}^{-1}$, and heavy shading for $15\text{--}20 \text{ m s}^{-1}$. Contour interval in (b)-(d) is 0.25 with heavy shading for areas > 0.50 and light shading for regions < -0.50 152
- 4.15 200 mb zonal wind representing the warm phase of February 1983 (solid), the cold phase of February 85 (short dashed), and their difference $[83 - 85]$ (medium dash). 156
- 4.16 Wave one contribution of mean equatorial 200 mb velocity potential (averaged from 5° N to 5° S) during pentads 11-33 for (a) 1985, (b) 1986, and (c) 1988. Contour interval $1 \times 10^7 \text{ m}^2 \text{ s}^{-1}$ and shading for areas less than $-2 \times 10^7 \text{ m}^2 \text{ s}^{-1}$ 160
- 4.17 Wave one contribution of mean equatorial 200 mb velocity potential (averaged from 5° N to 5° S) during pentads 29-51 for (a) 1983, (b) 1985, and (c) 1988. Contour interval $1 \times 10^7 \text{ m}^2 \text{ s}^{-1}$ and shading for areas less than $-2 \times 10^7 \text{ m}^2 \text{ s}^{-1}$ 162
- 4.18 Wave one contribution of mean equatorial 200 mb velocity potential (averaged from 5° N to 5° S) during pentads 51-73 for (a) 1982, (b) 1983, and (c) 1987. Contour interval $1 \times 10^7 \text{ m}^2 \text{ s}^{-1}$ and shading for areas less than $-2 \times 10^7 \text{ m}^2 \text{ s}^{-1}$ 164
- 4.19 Streamfunction (a) and velocity potential (b) anomalies with OLR anomalies superimposed for composite pentad 22. OLR anomaly shading describe in text. Contours in (a) every $0.5 \times 10^7 \text{ m}^2 \text{ s}^{-1}$ and in (b) every $1 \times 10^6 \text{ m}^2 \text{ s}^{-1}$. Maximum value of divergent wind in (b) of 4.5 m s^{-1} near 3° N , 48° E 167

- 4.20 Streamfunction (a) and velocity potential (b) anomalies with OLR anomalies superimposed for composite pentad 40. OLR anomaly shading describe in text. Contours in (a) every $0.5 \times 10^7 \text{ m}^2 \text{ s}^{-1}$ and in (b) every $1 \times 10^6 \text{ m}^2 \text{ s}^{-1}$. Maximum value of divergent wind in (b) of 4.7 m s^{-1} near 3° N , 34° E 169
- 4.21 Streamfunction (a) and velocity potential (b) anomalies with OLR anomalies superimposed for composite pentad 67. OLR anomaly shading describe in text. Contours in (a) every $0.5 \times 10^7 \text{ m}^2 \text{ s}^{-1}$ and in (b) every $1 \times 10^6 \text{ m}^2 \text{ s}^{-1}$. Maximum value of divergent wind in (b) of 3.4 m s^{-1} near 13° N , 87° E 171
- 4.22 OLR anomaly and vertical mode contribution to divergent wind anomaly at $\sigma = 0.2$ for composite of pentad 22 for (a) mode 2 (first internal mode), (b) mode 3, (c) mode 4, and (d) mode 5. OLR dark shading for areas $< -20 \text{ W m}^{-2}$, and light shading for areas $> 20 \text{ W m}^{-2}$. Divergent winds only shown when in excess of 0.5 m s^{-1} . Maximum wind values are 0.6 m s^{-1} near 3° S , 138° E in (a), 1.7 m s^{-1} near 5° N , 105° W in (b), 1.6 m s^{-1} near 8° N , 8° E , and 1.2 m s^{-1} near 3° N , 48° E 175
- 4.23 OLR anomaly and vertical mode contribution to divergent wind anomaly at $\sigma = 0.2$ for composite of pentad 40 for (a) mode 2 (first internal mode), (b) mode 3, (c) mode 4, and (d) mode 5. OLR dark shading for areas $< -20 \text{ W m}^{-2}$, and light shading for areas $> 20 \text{ W m}^{-2}$. Divergent winds only shown when in excess of 0.5 m s^{-1} . Maximum wind values are 1.3 m s^{-1} near 8° N , 53° E in (a), 2.2 m s^{-1} near 30° S , 15° W in (b), 1.2 m s^{-1} near 18° N , 70° E , and 1.1 m s^{-1} near 10° N , 70° E 178
- 4.24 OLR anomaly and vertical mode contribution to divergent wind anomaly at $\sigma = 0.2$ for composite of pentad 67 for (a) mode 2 (first internal mode), (b) mode 3, (c) mode 4, and (d) mode 5. OLR dark shading for areas $< -20 \text{ W m}^{-2}$, and light shading for areas $> 20 \text{ W m}^{-2}$. Divergent winds only shown when in excess of 0.5 m s^{-1} . Maximum wind values are 0.7 m s^{-1} near 10° S , 104° E in (a), 1.7 m s^{-1} near 28° N , 160° E in (b), 1.2 m s^{-1} near 25° N , 127° E , and 1.2 m s^{-1} near 15° N , 81° E 182

ACKNOWLEDGMENTS

First and foremost, I am deeply in debt to Prof. Julia Nogués-Paegle. Without her advice, encouragement, and down-right hard work, this dissertation would still be in the planning stages. I am also grateful to the U. S. Air Force for sending me back to school through the Air Force Institute of Technology (AFIT) program. In addition, many thanks to the members of my committee for their many helpful suggestions. This dissertation was supported, in part, by NSF grant ATM-9114073. The data sets were obtained from the Scientific Computing Division of the National Center for Atmospheric Research, which is supported by the National Science Foundation.

Special thanks to my fellow student and friend, Kim Rigling, without whose help I would have never made it through classes. Also, a special thanks to those two wonderful women in the front office, Leslie and Melea, who put up with my antics on a day-to-day basis and hardly ever beat me real bad.

Finally, to the family — Brenda, Amanda, and Chris — as always, you guys are the greatest!

CHAPTER 1

INTRODUCTION

A long-term global description of the atmosphere has become feasible only in the past decade, following the Global Weather Experiment (GWE), and the concurrent emergence of global analysis and forecast models. Much of this experience was a learning process that led to increasingly realistic data assimilation schemes and produced an awareness of the potential utility and major limitations of the current observation-analysis system. Diagnostic studies of atmospheric motions have contributed significantly to these rapid developments.

The description of atmospheric motions in terms of longitudinally asymmetric states has proved fruitful in the past to interpret observed atmospheric structures in terms of linear wave theory. The common practice has been to project data into zonal Fourier modes, and differentiate their stationary and transient components through Fourier analysis in time (such as in the studies of Deland 1964; Horn and Bryson 1963; Julian 1966; Wiin-Nielsen 1967; Kao and Wendell 1970; Hayashi 1971). Others have studied the horizontal two-dimensional spectra as represented by spherical harmonics (e.g., Eliassen and MACHENHAUER 1965, 1969; Paegle and Baker 1982; Nogués-Paegle et al. 1986).

Decomposition of the observed vertical variance has received relatively less attention. Holmström (1963) determined the empirical orthogonal functions of atmospheric data and found that much of the vertical variance can be explained by the first few vertical modes, while Wiin-Nielsen (1971a and b) studied the time

behaviour of long waves for various vertical structures. More recent investigations have projected atmospheric data into Hough functions and determined their vertical structures (Kasahara and Puri 1981; Tanaka 1985; Nogués-Paegle et al. 1989; Tanaka and Kung 1988, 1989). The main conclusion of these studies is that the Rossby modes exhibit dominant barotropic structure in the kinetic energy, while the available potential energy of the Rossby modes and both energy forms for the gravity modes exhibit vertically reversing circulations about a mid-atmospheric level.

Observational findings have also been reported regarding prevailing barotropic and baroclinic structures for different regions (e.g., Blackmon et al. 1979, for the Northern Hemisphere (NH), van Loon and Jenne 1972, for the Southern Hemisphere (SH), and Silva Dias and Bonatti 1985, for the tropics). Blackmon et al. (1979) describe the tendency for atmospheric motions in the NH to display barotropic structures in the eastern oceans and more baroclinic structures in the interior of continents. In the SH, van Loon and Jenne (1972) find nearly barotropic structures for long waves, while Silva Dias and Bonatti (1985) point out the vertically reversing structure over tropical South America. Projections on low-order spherical harmonics by Paegle and Baker (1982) and Nogués-Paegle et al. (1986) showed the baroclinic contributions of the tropics to be dominant throughout the globe when long meridional and zonal length scales are considered. Results from these and other studies can be summarized as follows: the tropics in general exhibit vertically reversing (baroclinic) structures, whereas mid-latitudes display equivalent barotropic variations. This general description focuses on two vertical modes, and much of the work cited above has been conducted for special or reduced data sets. The 10 years of post-GWE data, currently available from the European Centre for Medium-range Weather Forecasts (ECMWF), is well suited to explore the horizontal variations of other vertical modes and to differentiate the vertica

structure of rotational and divergent motions. These data are used in the research to determine the latitudinal range for which different vertical modes dominate the vertical variance for three low-frequency time scales — the seasonal, interannual, and intraseasonal.

The characteristics of the seasonal cycle are obtained by computing monthly averages for 10 years of data for all variables and levels. These averages filter out freely propagating modes and, therefore, the seasonal changes represent the atmospheric response to the seasonal shift of atmospheric energy sources. Such response depends on the zonal wavenumber and varies based on whether the forcing is located at the lower levels, as for sensible heating, or at mid-atmospheric levels, as for diabatic heating (e.g., Dickinson 1980; Geisler and Stevens 1982; Silva Dias et al. 1983).

The seasonal changes do not follow a simple meridional translation with the sun due partly to the distribution of oceans and continents on the earth surface and the seasonal changes of sea surface temperatures (SSTs). Horel (1982) documented the changes in SST in the eastern equatorial Pacific, and showed that, within the tongue of cool surface waters which extends westward from the South American coast, the maximum temperature occurs during March. This maximum decreases in amplitude as it moves westward. The westward progression of the SST is accompanied by high/low pressure to the west/east of the SST maximum, weakening the surface easterlies and producing wind-stress convergence over the SST maximum (Meehl 1990). Even small changes in SST anomalies near the equator may lead to the release of large amounts of diabatic heat and if SSTs are warm enough convection can be generated. This has been observationally confirmed by Gutzler and Wood (1990) who found significant correlations between monthly averaged SSTs and outgoing longwave radiation (OLR) in a broad horse-shoe pattern centered around the equator, east of the dateline, in the eastern Pacific. These studies indicate

that a better understanding of the seasonal cycle may be gained by decomposing the wind in its divergent and rotational components and relating these variables to OLR data.

The seasonal changes away from the equator can be more readily linked to changes in the insolation at the earth's surface. Warm continents during summer are characterized by monsoonal circulations with low pressure at the surface and high pressure at upper levels, and a reversed structure during winter. It is then apparent that a complete picture of the seasonal change requires documentation of the vertical structure of the atmosphere that is capable of capturing differences over continents and oceans. Such descriptions should also discriminate the different structures of the deep tropics of the western and eastern Pacific.

The analysis of the 12 months of data permits contrasting the transition from northern winter to spring with that from fall to winter. Fleming et al. (1987) have quantified differences in these two transition stages for the NH and shown that the spring position of the subtropical jet is located 5-10° equatorward of the fall position and that this jet is twice as intense in spring. The tropical rain belt is also about 5-10° further south in spring than in fall, which may partly explain the higher values of the zonal wind. Horel et al. (1989) have also studied the different seasonal transition from summer-to-winter and winter-to-summer over South America. Furthermore Meehl (1987) points out that the convective maximum that moves southeastwardly from the Asian continent from northern summer to winter is stronger than it is in its return northwestwardly path from winter to summer. This diagonal movement of the convection is attributed to the geography of the Indian-Australian region, and the differences in the convective patterns in the transition regions may be due to the Australian monsoon during northern winter. The expansion of the convection further east into the Pacific during spring results in less convection over Southeast Asia (Meehl 1987) than during fall.

Though these investigations have described important characteristics of the climatology of the seasonal cycle, questions still remain on causes of observed interannual variations of the seasonal cycle and on reasons for the differences between the intermediate seasons. The studies of Nogués-Paegle et al. (1986) and Nogués-Paegle and Mo (1987) during the two Special Observing Periods (SOP) of the GWE show that, for the seasonal and intraseasonal cycle, planetary scales that are vertically reversing dominate the adjustment of the flow to the changing heating sources. Nogués-Paegle and Mo (1987) concluded that the seasonal transition from spring to summer occurred abruptly, with pronounced excitation of planetary scale flows both in the velocity potential and the streamfunction. They also linked the transition to the 30-60 day oscillation, showing that the passage of the eastward propagating velocity potential disturbance over South America appears to trigger the displacement of negative OLR anomalies from their South America location in austral fall.

The relationship between organized tropical convection, divergent motions and subtropical zonal winds was also studied by Nogués-Paegle and Zhen (1987) who linked the strength of the Australian subtropical jet with divergent flows emanating from the Asian monsoon region.

Important elements of this linkage include regional and temporal variations of Hadley cells and possible teleconnection between high and low latitudes (e.g. Simmons 1982; Kasahara and Silva Dias 1986; Lim and Chang 1986; Garcia and Salby 1987). Some of these studies link an external mode response of mid-latitude with the baroclinic tropical structures excited by diabatic heating through the vertical shear of the basic state. A few recent observational studies have investigated the applicability of these linearized models for limited data sets (Mechoso and Hartmann 1982; Randel et al. 1987; Nogués-Paegle and Zhen 1987; Ziemke and Stanford 1990).

6

The global character of these tropical-extratropical connections could not be diagnosed in detail before the GWE due to the nondivergent assumptions introduced in gridded global analyses. The current investigation will study the global characteristics of low frequency oscillations for the 1980-1989 ECMWF gridded analyses that have been strongly promoted by ECMWF to represent the most advanced, stable assimilation system.

In general, the three main goals of this study are: 1) to describe the vertical structure of divergent motions for seasonal and low-frequency motions associated with tropical convection, 2) to quantify the turning latitude where the vertical structure of observed rotational motions changes from the internal structures, typical of tropically forced motions, into the equivalent barotropic patterns of mid-latitudes and 3) to assess how much of the seasonal and low-frequency extratropical structure is due to atmospheric response to tropical heating.

The remainder of this paper is organized in the following manner. Chapter 2 will discuss the data and diagnostic methods. Chapter 3 will examine the seasonal cycle, first in terms of reviewing the zonally- and meridionally-averaged wind and how they relate to convection. The seasonal wave cycle will be described in the geopotential height field through its zonally asymmetric component, averaged for each season, and through use of Fourier analysis. Following this the divergent and rotational wind components will be used to describe the vertical structure. The seasonal march of selected waves and their vertical mode amplitude will be displayed in Hovmöller diagrams. Lastly in this chapter, two numerical models, one a linear shallow water wave equation model, and the second, a nonlinear three-level PE model, are used to determine the influence of tropical heating on extratropical wave response.

In Chapter 4, the interannual changes associated with the ENSO and the intraseasonal variations containing the 30-60 day oscillation will be discussed. The

differences and similarities of the warm and cold phases of the 1983 and 1987 ENSO events will be discussed, as well as their vertical structure and relation to convection. As with the seasonal cycle, model simulations will be used to determine how much of the atmospheric response at midlatitudes, as suggested by this particular mode, can be attributed to tropical influences. Finally, the intraseasonal oscillations will be examined by determining the details of the divergent winds of pentad composites. The composites are made for times when the intraseasonal signal, as shown in the 200 mb velocity potential, was easily seen and the atmosphere was convectively active. These pentads are made for the transition season, summer monsoon, and NH winter. In conclusion, Chapter 5 will discuss the major findings and results of this paper.

CHAPTER 2

DATA AND METHODOLOGY

2.1 Data

The data used in this research are from the archives of the National Center for Atmospheric Research (NCAR), Scientific Computing Division. The data originate from the European Centre for Medium-range Weather Forecasts (ECMWF) and are stored at NCAR for use by the atmospheric research community. The data consist of twice daily (0000 and 1200 GMT) fields of six variables at seven isobaric levels on a global $2.5^\circ \times 2.5^\circ$ grid. The six meteorological variables include the height (z), temperature (T), zonal wind component (u), meridional wind component (v), relative humidity (RH), and vertical motion (ω), while the levels are, from bottom to top, 1000, 850, 700, 500, 300, 200, and 100 mb. The grid used to store the information results in an array, for each variable at each level, which contains 144×73 grid points.

The ECMWF assimilation system used to acquire these data has undergone many changes and improvements during the last decade. These changes and their effects have been reported in many conferences and journals. Uppala (1986) and Shaw et al. (1987) have documented the effect of changes from 1980 through 1985, while Trenberth and Olson (1988) have summarized some of the major changes at ECMWF since 1979. Of the 36 model changes reported by the latter, only a few may significantly affect the tropical divergent motions currently being examined (see Table 2.1). As an example, on May 1, 1985 the T106 spectral model replaced the T63, along with substantial changes to the Kuo convection scheme, the addition of

Table 2.1. Changes in the analyses at ECMWF after 1980 which might affect tropical divergent motions (extracted from Trenberth and Olson, 1988).

Date	Summary of change
May 1, 1985	T106 spectral model introduced with substantial changes to physical parameterization (clouds, convection, condensation).
March 4, 1986	Initialization modified to preserve tidal waves.
July 15, 1986	Gravity wave drag introduced into model.
January 26, 1988	Divergent structure functions introduced to mass and wind field analyses.

shallow convection, and changes in cloud representation. As a result, more realistic Hadley cells resulted, with strengths 50% larger than those of 1984 analyses for the same season.

2.2 Methodology

This study used the available ECMWF data set for the 10 year period from January 1, 1980 through December 31, 1989. The 30+ magnetic tapes were reduced by computing 5-day means using the daily mean for the 0000 and 1200 GMT time periods. This averaging process removes the diurnal cycle and filters out much of the high-frequency, synoptic-scale variability. Also, monthly means (12 monthly averages for each year of the 10 year period) and decade monthly means (12 monthly averages for the entire 10 year period) were obtained to quantify the seasonal cycle. Results were obtained from Fourier analyses and by projecting the rotational and divergent wind components onto vertical structure functions as described below. A linear shallow water equation model and a nonlinear primitive equation model were used to interpret results. These are also discussed in the following sections.

2.2.1 Fourier Transforms

As described in the introduction, the purpose of this research is to determine the latitudinal range for which different vertical modes dominate the vertical variance, both as a function of longitude and zonal wavenumber. The contributions by different zonal wavenumbers were obtained using fast Fourier transform algorithms (FFT).

Application of Fourier analyses requires expansion of the variable S_l at longitudinal grid points l in a Fourier series as follows:

$$S_l = \sum_{k=-n}^{n-1} \hat{S}_k e^{\frac{i2\pi kl}{N}}, \quad (2.1)$$

where \hat{S}_k are the complex Fourier coefficients, such that $\hat{S}_{-k} = \hat{S}_k^*$, where the asterisk denotes the complex conjugate, and

$$\hat{S}_k = \frac{1}{N} \sum_{l=-n}^{n-1} S_l e^{\frac{-i2\pi kl}{N}}, \quad (2.2)$$

where $N = 2n$ is the total number of grid points in the longitudinal direction. Also, the mean square value is given by

$$\frac{1}{N} \sum_{l=-n}^{n-1} S_l^2 = 2 \sum_{m=l}^{n-1} (\hat{S}_{mr}^2 + \hat{S}_{mi}^2) + \hat{S}_n^2 + \hat{S}_0^2, \quad (2.3)$$

where \hat{S}_n^2 is the component for the last wavenumber, n , and \hat{S}_0^2 is the square of the zonal mean. For the variance,

$$\sigma^2 = \frac{1}{N} \sum_{l=-n}^{n-1} (S_l - \hat{S}_0)^2 = 2 \sum_{m=l}^{n-1} (\hat{S}_{mr}^2 + \hat{S}_{mi}^2). \quad (2.4)$$

To use the FFT algorithms to describe the seasonal cycle, it is required that the original $2.5^\circ \times 2.5^\circ$ decade monthly mean data be interpolated from the 144×73 grid to a 128×73 grid. This yields 2^n grid points in the longitudinal direction which is a requirement for the FFT. Each latitude band is passed through the FFT and the resulting contribution by wavenumber, in terms of the amplitude and phase

of the given variable, can then be determined. With 128 grid points on input, the FFT yields information on the contribution of wavenumbers up to and including wavenumber 64, though most of the zonal variance is contained in the first 7-10 waves.

2.2.2 Normal Mode Vertical Structure Decomposition

The vertical structure of the flow is determined by projecting wind components onto vertical structure functions obtained from the solution of a linear primitive equation model. This technique offers at least two distinct advantages over single level analyses. First, the contribution from each vertical mode is distinguishable from all others (Kasahara 1976). This is helpful for applications which use linear models with a single vertical mode. Second, as a diagnostic tool, normal mode decomposition allows for discrimination between atmospheric structures which are and are not altered by the assimilation model (Nogués-Paegle et al. 1989), because initialization systems used in operational environments usually only adjust certain vertical modes.

Initially, the Poisson equations for vorticity and divergence are solved for the streamfunction and velocity potential by the method of Paegle and Tomlinson (1975), and from these the zonal and meridional components of the rotational and divergent wind are obtained. These data are then transformed from pressure to sigma coordinates so they may be projected onto the vertical modes in a terrain-following coordinate system.

At each grid point, these parameters are then projected onto the vertical structure functions referred to in the previous paragraph. This method is the same as that of Nogués-Paegle et al. (1989). In this study, the normal mode computer codes developed by Errico (1987a, 1987b) are used. Grid point values are projected onto the vertical structure functions as:

$$\begin{Bmatrix} u_n \\ v_n \end{Bmatrix} = \sum_{k=1}^7 \psi_{n,k} \begin{Bmatrix} u(k) \\ v(k) \end{Bmatrix} \sqrt{gh_n}, \quad (2.5)$$

where ψ is the vertical structure function, k indicates the vertical grid point value, and h_n is the equivalent depth for vertical mode n .

Since there are seven levels it is possible to decompose the data into seven vertical modes. Figure 2.1 depicts the vertical structure function for each mode in this data set. As can be seen in the figure, motions that project into the first mode are almost constant throughout the troposphere, hence this mode is known as the barotropic or external mode. Those modes that project mostly into the second or third modes possess reversal points at approximately 300 and 500 mb, respectively. The second and higher modes are referred to collectively as the internal modes. When compared to models with a greater number of levels, there is some consistency in the first three modes, but thereafter, there is usually little to no similarity. The fifth mode of this seven level model will be quite different from the fifth mode of a 19 level model.

As expected, there can be contributions to the vertical variance at a grid point by more than one mode. Two combinations which will be seen repeatedly in subsequent chapters are shown in Figs. 2.2 and 2.3. These are the equivalent barotropic and vertical structure resulting in regions with mid-atmospheric heating. The equivalent barotropic structure is a combination of a dominant first mode and a weaker third mode. This results in a projection that maintains a positive value throughout the troposphere, maximizing near 300 mb and then decreasing again through the lower levels of the stratosphere. This type of structure would be expected of the zonal wind components in or near a mid-latitude maximum wind band.

The structure shown in Fig. 2.3 is more indicative of deep tropical convection. This results from a near equal contribution by the second and third modes, which as stated previously, shows sign reversals near 300 and 500 mb. Note how this combination results in a baroclinic structure which almost equally divides the

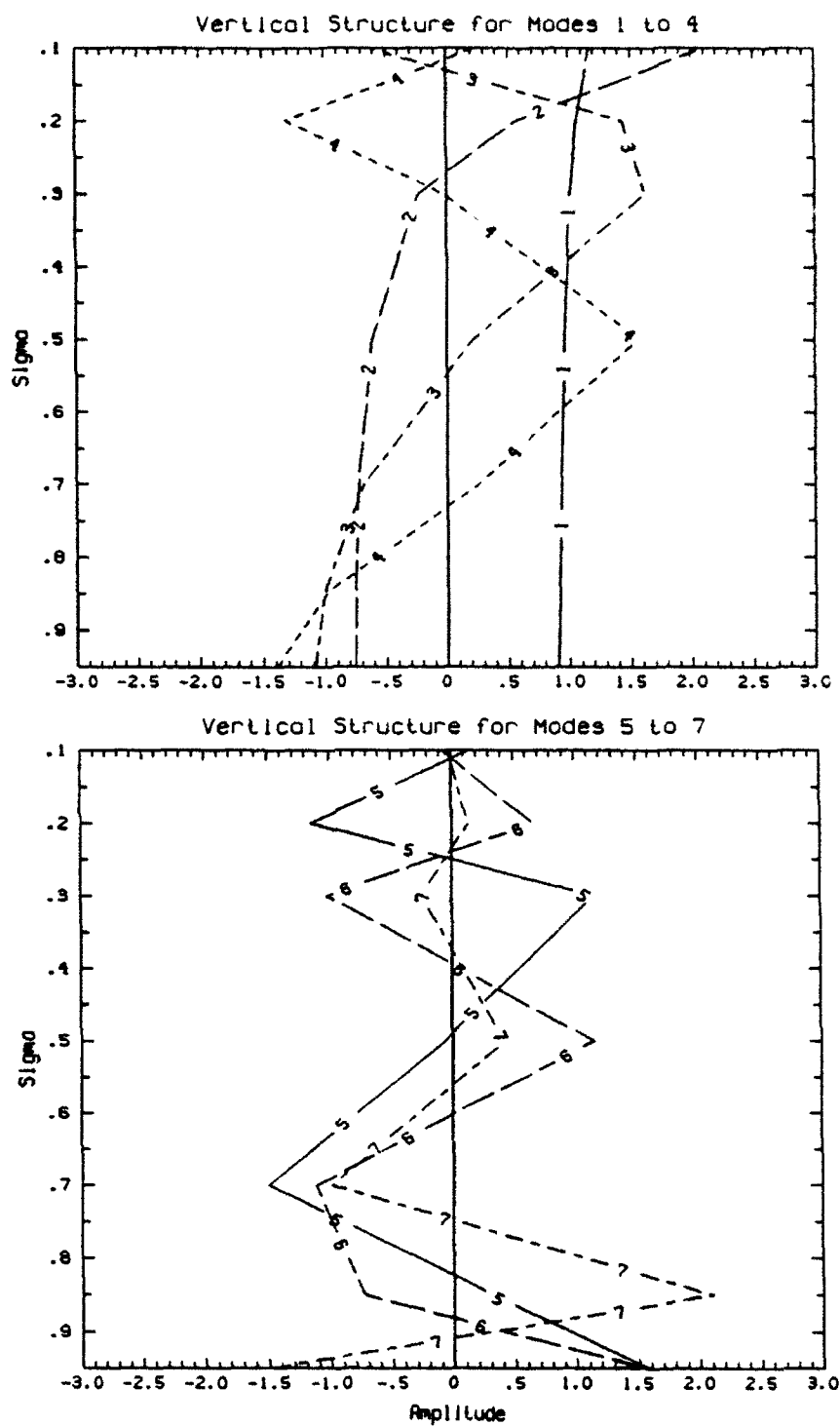


Figure 2.1. Vertical structure function for seven levels of the ECMWF data set. Equivalent depths are 9262, 930, 152, 37, 11, 4, and 0.7 m for modes one through seven, respectively.

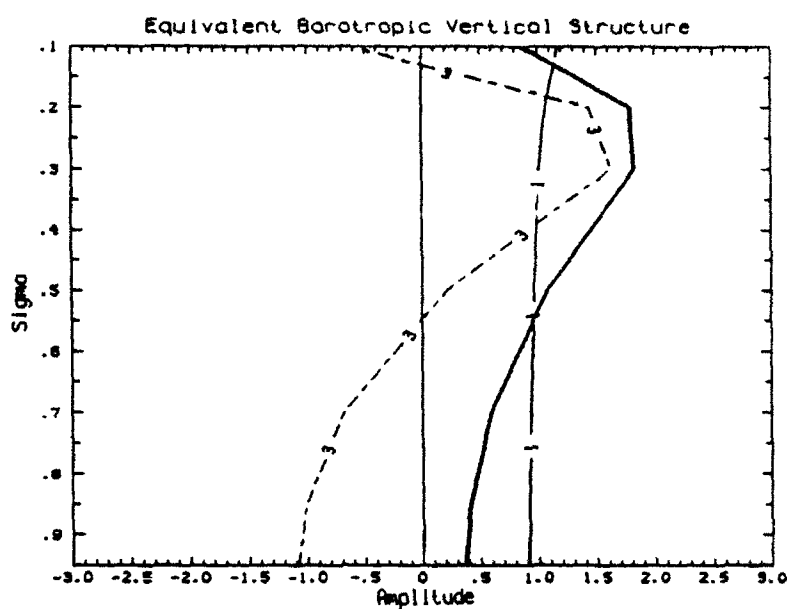


Figure 2.2. Equivalent barotropic vertical structure. Represented on this graph are the external mode (solid line), third mode (dashed line), and combination of mode one plus 50% of mode three at each level (heavy solid line).

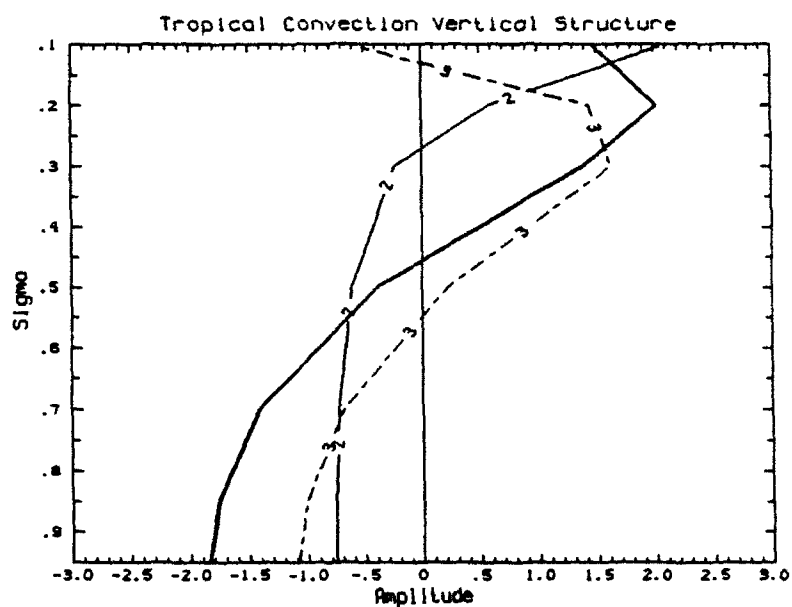


Figure 2.3. Tropical deep convection vertical structure. Represented on this graph are the second mode (solid line), third mode (dashed line), and combination of mode two plus mode three at each level (heavy solid line).

atmosphere into positive and negative areas with a sign change near 500 mb. This reasonably represents the vertical wind profile one would expect in a tropical convectively active area with the level of nondivergence at mid-tropospheric levels.

Graphically, these modes are plotted in a rosette fashion at each grid point with arrows to display the magnitude of each vertical mode in terms of the percentage of the grid point vertical variability. The arrow convention used for each mode is as follows: external or first mode (\rightarrow), second mode (\nearrow), third mode (\uparrow), fourth mode (\nwarrow), and fifth mode (\leftarrow). Only the first five modes are depicted at a grid point because these modes contribute most to the vertically integrated kinetic energy, as will be shown later. It is recognized, however, that contributions from the higher modes are necessary to define shallow layers at low levels, such as the structure within the boundary layer. The following chapters will show how these procedures are used to present details on the seasonal, interannual, and intraseasonal cycles.

2.2.3 Vertical Mode Projection of Fourier Coefficients

We assume a vertical dependence for the Fourier coefficients $\hat{S}_k(\phi, \sigma) = \bar{S}_k(\phi) \psi(\sigma)$ where $\psi(\sigma)$ satisfies the differential equation,

$$\frac{d}{d\sigma} \left(\frac{\sigma g}{R\Gamma_0} \frac{d\psi}{d\sigma} \right) + \frac{1}{D} \psi = 0, \quad (2.6)$$

with the boundary conditions (see Kasahara and Puri, 1981) defined as

$$\frac{d\psi}{d\sigma} = \text{finite} \quad \text{at } \sigma = 0, \quad (2.7)$$

$$\frac{d\psi}{d\sigma} + \frac{\Gamma_0}{T_0} \psi = 0 \quad \text{at } \sigma = 1, \quad (2.8)$$

where D is the eigenvalue of the differential equation 2.6. For the given boundary conditions, the eigen functions $\psi_i(\sigma)$ are obtained from Errico's programs for eigen

values D_i , ($1 < i < 7$). The eigen functions, ψ_i , are orthogonal and normalized so that

$$\int_0^1 \psi_i(\sigma) \psi_j(\sigma) d\sigma = \delta_{i,j} . \quad (2.9)$$

Therefore, the input Fourier coefficients, \hat{S}_k can be written as

$$\hat{S}_k(\phi, \sigma) = \sum_{n=1}^7 \tilde{S}_k^n(\phi) \psi_n(\sigma) . \quad (2.10)$$

Total vertical square value for wavenumber k , using the orthogonality condition in equation 2.9 is given by:

$$\begin{aligned} A_k^2 &= \int_0^1 \hat{S}_k(\phi, \sigma) \hat{S}_k^*(\phi, \sigma) d\sigma \\ &= \sum_{n=1}^7 \tilde{S}_k^n(\phi) \tilde{S}_k^{*n}(\phi) . \end{aligned} \quad (2.11)$$

So, projection onto $\psi_n(\sigma)$ permits quantification of how much of the squared amplitude of each zonal wavenumber k may be explained by each vertical mode n .

Furthermore, since the total squared value of the function $S(u_R, v_R, u_D, v_D)$ may be expressed by equation 2.3, its vertical integral (giving the total squared value both in the x and σ coordinates) is:

$$\int_0^1 \frac{1}{N} \sum_{l=-n}^{n-1} S_l^2 d\sigma = \sum_{n=1}^7 \left\{ |\tilde{S}_0^n(\phi)|^2 + |\tilde{S}_{\frac{N}{2}}^n(\phi)|^2 + 2 \sum_{m=1}^{n-1} |\tilde{S}_m^n(\phi)|^2 \right\} . \quad (2.12)$$

2.2.4 Shallow Water Equation Model

The linear shallow water model described in Paegle et al. (1983) is used to quantify how much of the global atmospheric response may be explained by a single mode linear model. The equations are:

$$\left(\frac{\partial}{\partial t} + \frac{\bar{u}}{r \cos \phi} \frac{\partial}{\partial \lambda} \right) u^* - f v^* = -\frac{g}{r \cos \phi} \frac{\partial n^*}{\partial \lambda} + \frac{\bar{u} v^* \tan \phi}{r} - \nu u^* , \quad (2.13)$$

$$\left(\frac{\partial}{\partial t} + \frac{\bar{u}}{r \cos \phi} \frac{\partial}{\partial \lambda} \right) v^* + f u^* = -\frac{gh}{r} \frac{\partial(n^*/h)}{\partial \phi} - \frac{2\bar{u}u^* \tan \phi}{r} - \nu v^*, \quad (2.14)$$

$$\begin{aligned} \left(\frac{\partial}{\partial t} + \frac{\bar{u}}{r \cos \phi} \frac{\partial}{\partial \lambda} \right) n^* &= -\frac{h}{r \cos \phi} \left[\frac{\partial u^*}{\partial \lambda} + \frac{\partial(v^* \cos \phi)}{\partial \phi} \right] \\ &+ hQ - \nu n^*. \end{aligned} \quad (2.15)$$

Here $u^* = uh$, $v^* = vh$, and $n^* = nh$, and u , v , n are the deviations of the zonal flow, meridional flow and free surface height from the longitudinally invariant basic state, respectively. The flow of this state (\bar{u}) is in geostrophic equilibrium with the basic state free surface displacement, i.e.,

$$\bar{u} = -\frac{g}{fr} \frac{\partial h}{\partial \phi}. \quad (2.16)$$

The variables λ, ϕ, t are longitude, latitude and time, respectively; r is the radius of the earth; f and g are the Coriolis parameter and gravitational acceleration; and Q represents the tropical forcing. Stationary solutions are obtained for the tropical heating as specified in Chapter 3. The mean zonal wind is taken as that of the decade annual average at 300 mb (see Fig. 2.4).

2.2.5 The Primitive Equation Model

Paegle's (1989) primitive equation model is used to generalize results obtained with the linear shallow water equations with a model that includes some nonlinear effects. The model is based on a finite element representation in the meridional direction while longitudinal structure is depicted with Fourier series. This latter feature permits the maintenance of selected wave coefficients at prescribed values. This option is implemented in this study to nudge the zonally invariant zonal wind back to the initial zonal wind profile. The initial profile is taken from the annual average of the 10 year data set at 200, 500, and 850 mb (see Fig. 2.4). Also, the

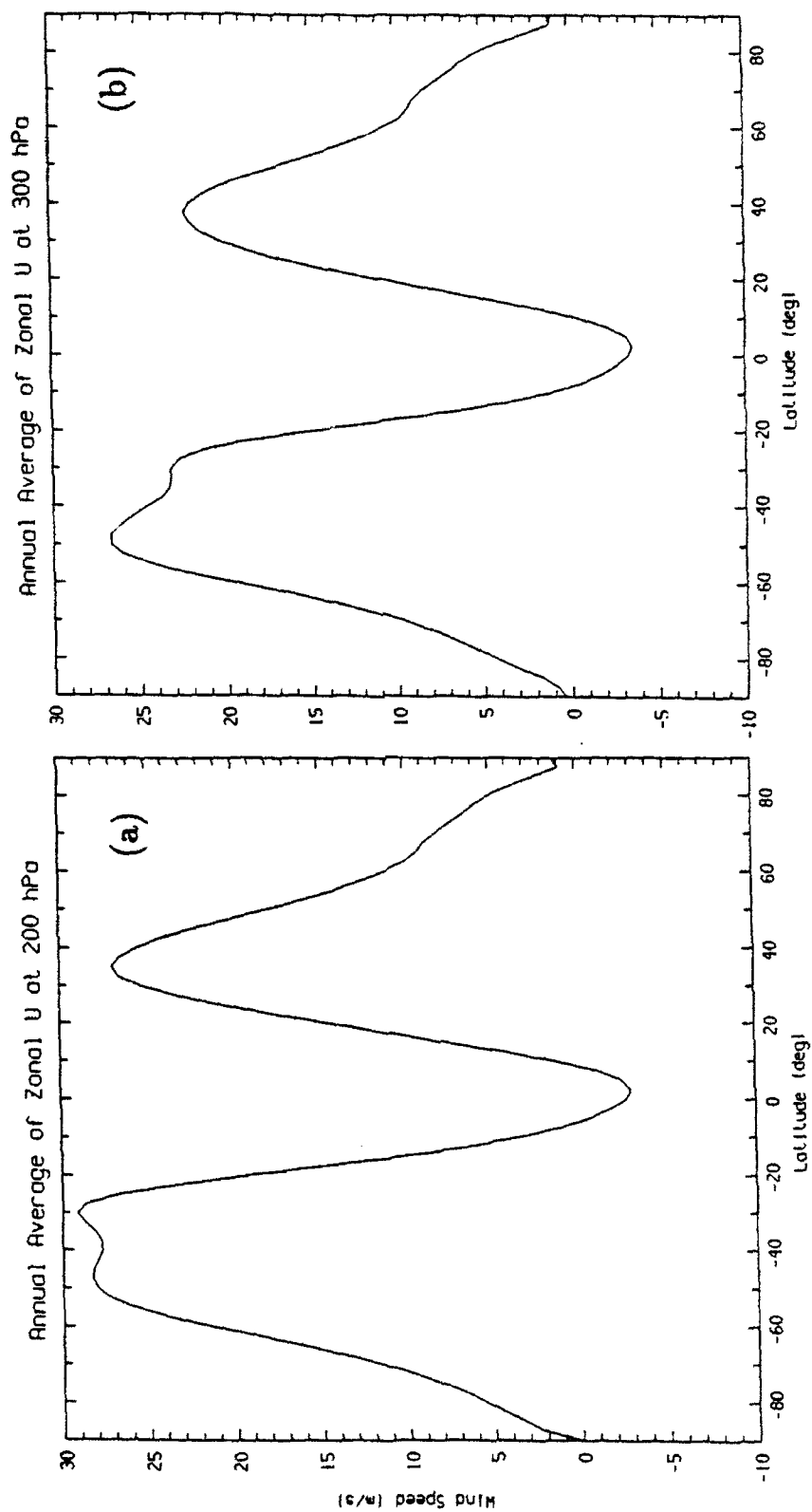
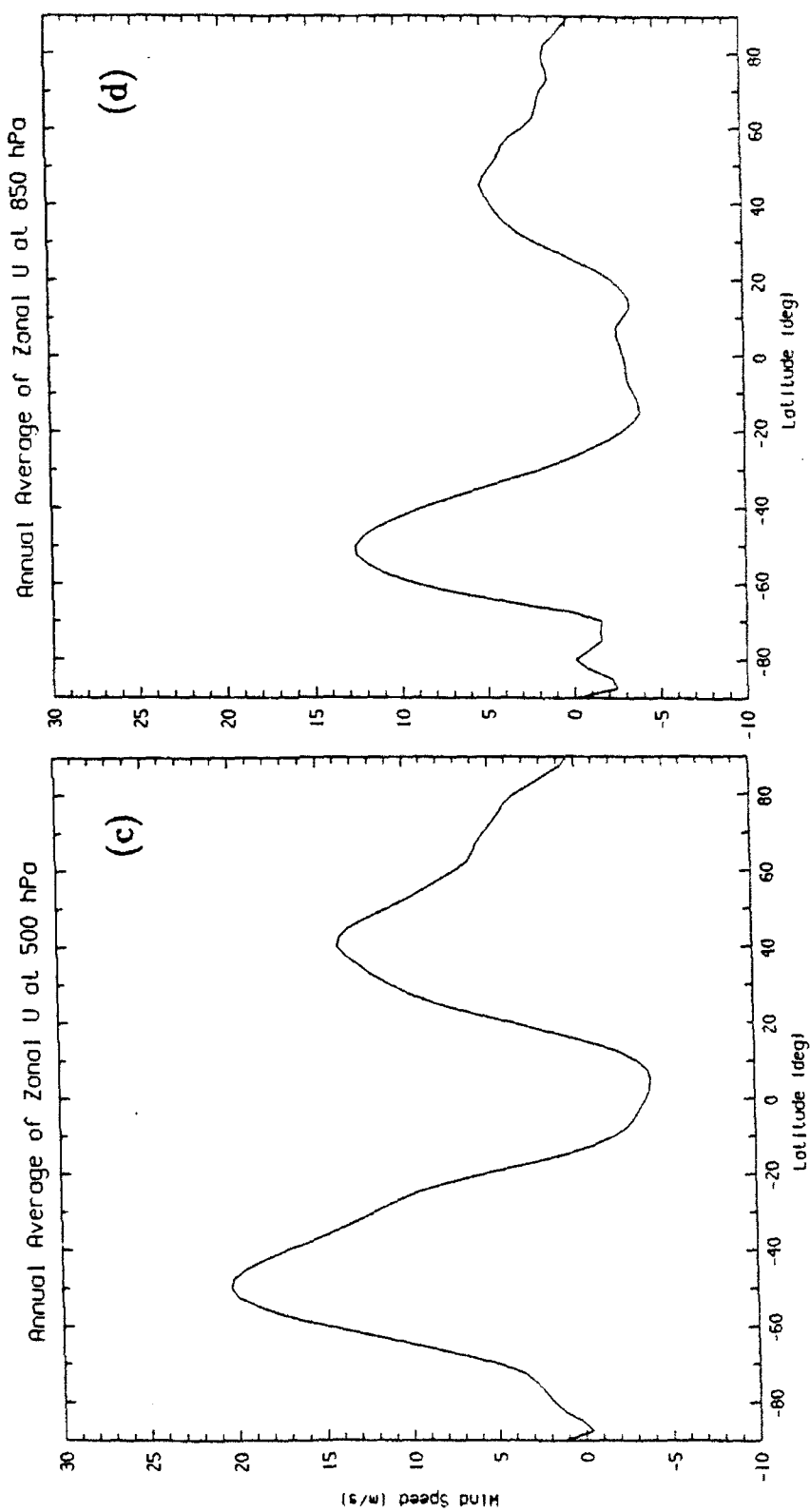


Figure 2.4. Profile of the annual mean zonal wind for January 1980-1989 at (a) 200, (b) 300, (c) 500, and (d) 850 mb.



model is truncated to 16 waves in the horizontal and as a result, small scale features and small scale features that evolve into large scale features are not well represented. Because only three levels are used in the model, the vertical truncation prohibits any representation from modes four or higher. These lost modes may be especially important in the shallower convective regions of South America.

There are no topographical or wave-mean flow feedbacks in the simulations. Wave patterns are allowed to develop in response to the tropical forcing which is maintained constant throughout the integration. This model permits a more complete assessment, that is, more so than does the linear shallow water model, of how much of the extratropical response may be attributed to the tropical forcing. The latter only allows for meridional propagation of a single vertical mode through a zonally symmetric basic state, whereas the primitive equation model resolves three vertical modes, allows conversion of baroclinic to barotropic flows by vertical shear, permits wave advection by the Hadley cell and includes the influence of longitudinally asymmetric states. The present application is simpler than other relatively complete simulations of tropical-extratropical flows because it has no directly forced wave sources outside the tropics. The primitive equation model is based on the vorticity and divergence equations as follows:

$$\begin{aligned} \frac{\partial \zeta}{\partial t} = & -\frac{1}{r \cos \phi} \frac{\partial}{\partial \phi} \{ \cos \phi [N_u + F_{u1}] \} \\ & + \frac{1}{r \cos \phi} \frac{\partial}{\partial \lambda} [N_v + F_{v1}] + \nabla \cdot (K_H \nabla \zeta) + \mu(\zeta - \bar{\zeta}) , \end{aligned} \quad (2.17)$$

$$\begin{aligned} \frac{\partial \delta}{\partial t} = & \frac{1}{r \cos \phi} \frac{\partial}{\partial \phi} \{ \cos \phi [N_v + F_{v1}] \} \\ & + \frac{1}{r \cos \phi} \frac{\partial}{\partial \lambda} [N_u + \cos \phi F_{u1}] \\ & - \nabla^2 \left[gZ + \frac{1}{2} - \mathbf{V} \cdot \mathbf{V} + RT_0 \ln P_s \right] + \nabla \cdot [K_H \nabla \delta] . \end{aligned} \quad (2.18)$$

where Z is the σ surface geopotential height, T_0 is the basic state virtual temperature, and P_s is the surface pressure.

The terms N_u and N_v are defined by

$$N_u = (\zeta + f)v - \left[\frac{RT'}{r \cos \phi} \right] \frac{\partial}{\partial \lambda} (\ln P_s) - \dot{\sigma} \frac{\partial u}{\partial \sigma}, \quad (2.19)$$

$$N_v = -(\zeta + f)u - \left[\frac{RT'}{r} \right] \frac{\partial}{\partial \phi} (\ln P_s) - \dot{\sigma} \frac{\partial v}{\partial \sigma}. \quad (2.20)$$

The thermodynamic equation has the form

$$\begin{aligned} \frac{\partial T'}{\partial t} = & -\frac{1}{r \cos \phi} \frac{\partial}{\partial \lambda} (uT') - \frac{1}{r \cos \phi} \frac{\partial}{\partial \phi} (vT' \cos \phi) \\ & + T' \delta - \sigma \frac{\partial T}{\partial \sigma} + \frac{RT}{C_p} \frac{\omega}{p} + Q + F_{TV} + \nabla \cdot [K \nabla T'], \end{aligned} \quad (2.21)$$

where ω is the vertical motion in pressure coordinates and Q is the diabatic heating specified as described in Chapters 3 and 4.

F_{uV} and F_{vV} parameterize vertical momentum mixing while F_{TV} parameterizes horizontal and vertical mixing of heat. The vertical diffusivity (K) equals $4 \text{ m}^2 \text{ s}^{-1}$ and the horizontal diffusivity (K_H) equals $5 \times 10^4 \text{ m}^2 \text{ s}^{-1}$, the relaxation coefficient (μ) is set to $\frac{1}{4\Delta t}$, where Δt is the time step (set equal to six minutes). Lastly, $\bar{\zeta}$, found in the last term of equation 2.17, is the initial relative vorticity of the zonal wind profile of Fig. 2.4. This term is the part of the experiment design which precludes changes from the zonal basic state by eddy-mean flow interactions. Again, this quick relaxation to the initial conditions, assures that the zonally-averaged basic state remains constant, and thus, any changes that occur in the model can be attributed as a response to the forcing. Otherwise, there is no certainty as to whether the response is due to the forcing, or a result of changes in the basic state.

The boundary conditions specify that $\dot{\sigma} = 0$ at $\sigma = 0, 1$. The vertically integrated continuity equation gives

$$\frac{\partial}{\partial t} \ln P_s = - \int_0^1 (\delta + \mathbf{V} \cdot \nabla \ln P_s) d\sigma, \quad (2.22)$$

$$\begin{aligned} \dot{\sigma} = & \sigma \int_0^1 (\delta + \mathbf{V} \cdot \nabla \ln P_s) d\sigma \\ & - \int_0^\sigma (\delta + \mathbf{V} \cdot \nabla \ln P_s) d\delta , \end{aligned} \quad (2.23)$$

$$\frac{\omega}{p} = \frac{\dot{\sigma}}{\sigma} + \frac{d \ln P_s}{dt} . \quad (2.24)$$

The vertical integral of the hydrostatic equation produces:

$$Z = Z_s - \frac{1}{g} \int_{\sigma=1}^\sigma RT d \ln \sigma , \quad (2.25)$$

where Z_s is surface geopotential height above sea level.

Further model details are given by Paegle (1989). All runs are integrated for 75 or 90 days and averaged for the last 15 days of integration to quantify the model response to tropical heating.

CHAPTER 3

THE SEASONAL CYCLE

Seasonal atmospheric changes are perhaps the best documented of the observed regular atmospheric cycles. Hsu and Wallace (1976a,b) present a summary of earlier investigations which focus on the seasonal changes of surface patterns. Three-dimensional data sets have been regularly archived only since the Global Weather Experiment of 1979. Therefore, it only recently has become possible to obtain a three-dimensional description of the seasonal cycle based on at least 10 years of data.

Certain features of this cycle are well known. Upper level winds are stronger in midlatitudes than in the tropics and are stronger in winter than in summer. Stationary waves exhibit larger amplitudes in the NH than in the SH, as expected from longitudinal gradients of surface forcing. These features can be explained in terms of the maintenance of the general circulation by transient eddies (e.g., Lorenz 1967) in the presence of dissipation and boundary forcing. This forcing includes both surface effects due to land-sea contrasts and orography, the thermal forcing resulting from the radiative balance of the atmosphere and the release of latent heat, as well as the remote forcing due to horizontal wave propagation.

Recently, there has been a renewed interest in the simulation of the seasonal cycle by general circulation models (GCMs) due to studies which have shown the interaction of the seasonal cycle with intraseasonal variations (e.g., Knutson and Weickmann 1987) and of the seasonal dependence of certain ENSO episodes (Rasmusson and Carpenter 1982). Verification of seasonal GCM integrations requires

climatologies that describe the average state of the atmosphere for different months, as well as second order statistics such as variances and covariances of different quantities such as the kinetic and available potential energy, heat and momentum transports, etc.

Current GCMs may perform well in describing the averaged state of the atmosphere (see e.g., Kanamitsu et al. 1990 or Kinter et al. 1988 for a description of the seasonal march of the National Meteorological Center GCM) but they do not do as well with second order quantities. Part of the difficulty resides in inadequate representation of forcing processes, and of these, the accurate representation of tropical heating is one of the most difficult. Statistics that differentiate the structures in tropical latitudes from those in extratropical latitudes are helpful to diagnose GCM integrations and to determine the latitudes where these integrations diverge from the observed seasonal evolution of the atmosphere. This chapter presents one possible set of statistics, with emphasis on vertical flow structures and decomposition of the wind into its rotational and divergent wind components. The discussion is presented as follows:

- First, the zonally averaged seasonal cycle is discussed and it is linked with the seasonal migration of tropical heating.
- Then, seasonally averaged waves in the height fields of isobaric surfaces are described. This description includes quantification of the momentum and heat transport by these stationary waves which are indicative of their horizontal and vertical tilt. The seasonal march of the height waves is presented in terms of the amplitude of Fourier components for different wavenumbers. Results presented in this and the previous section have been reported previously to a limited extent. Compilations, in the form of atlases, are given by Randel (1987) and Schubert et al. (1990a,b). Some aspects of the mean field characteristics discussed here have been reported in studies such as those of Oort and Rasmusson (1971), Blackmon

et al. (1977), Lau and Wallace (1979), Wallace (1983), etc. These studies have emphasized the structure of the height fields. A more unique aspect of the current study is its emphasis on the wind field, which does not have the latitudinal bias of the height field. This is considered next.

- The wind is separated in its rotational and divergent parts and projected into vertical structures as described in Chapter 2. The expected vertically reversing circulations of the tropics are shown to abruptly transition into the equivalent barotropic structure of the extratropics within 10° latitudinal bands. This abrupt transition suggests the limited applicability of linear models with a single vertical mode to describe the global response of the atmosphere to tropical heating. Though such linear models have been successfully used in the past to explain the tropical response, it has been shown that the transition from dominant internal tropical structures to the equivalent barotropic structure of mid-latitudes require the vertical shear of the mean wind (Simmons 1982; Kasahara and Silva Dias 1986). In this chapter, the observed stationary extratropical wave pattern is compared with numerical solutions of models forced in the tropics with a heating function derived from the OLR field.

- The linearized shallow water equation model permits an estimate of the extent to which the observed summer waves result from the linear response to tropical heating in the presence of a meridionally changing zonal wind. This linear solution does not allow much propagation into the winter hemisphere due to the presence of tropical easterlies. Also, this model allows excitation of only a single vertical mode. These limitations are removed by using a global primitive equation model nudged to maintain a basic state with vertical shear.

3.1 Zonally Averaged Seasonal Cycle

Interpretation of the observed response of the atmosphere to wave propagation in a latitudinally and vertically varying basic state requires determination of the meridional and vertical structure of the zonal wind. Figure 3.1 depicts seasonal latitude–height cross-sections of the zonally-averaged zonal wind, computed from the decade monthly means. Positive/negative values represent westerly/easterly winds, respectively.

In the NH, winds are strongest during the winter (DJF) with average winds exceeding 40 m s^{-1} at 200 mb. Speeds decrease in the jet core during spring (MAM), and reach their minimum value of 21 m s^{-1} during summer (JJA). At this time, a poleward shift of approximately 15° can be seen in the jet core, with a secondary maximum value near 70° N and lower in the troposphere, closer to 300 mb. This secondary arctic jet disappears during boreal fall (SON) and wind speeds within the jet core increase slightly.

As expected, similar results are found for the SH for similar seasons. During austral summer (DJF) maximum winds are only 29 m s^{-1} at 200 mb and located near 50° S . During SH fall (MAM), the jet migrates toward the equator. By winter (JJA), winds have reached their peak value with velocities in excess of 39 m s^{-1} at 200 mb. Also apparent at this time is a tongue of the stratospheric jet over 60° S . This structure persists through SON even though the speed of the zonal winds has decreased.

Comparison of the zonal wind profile for the intermediate seasons reveals higher NH values in boreal spring than in fall, with maximum values found about $10\text{--}15^\circ$ further south in spring.

All easterly winds are confined to the tropics and for the most part are weak and located near the surface. The exception is during JJA when easterlies in excess of 9 m s^{-1} push up into the tropical troposphere. The annual average of the

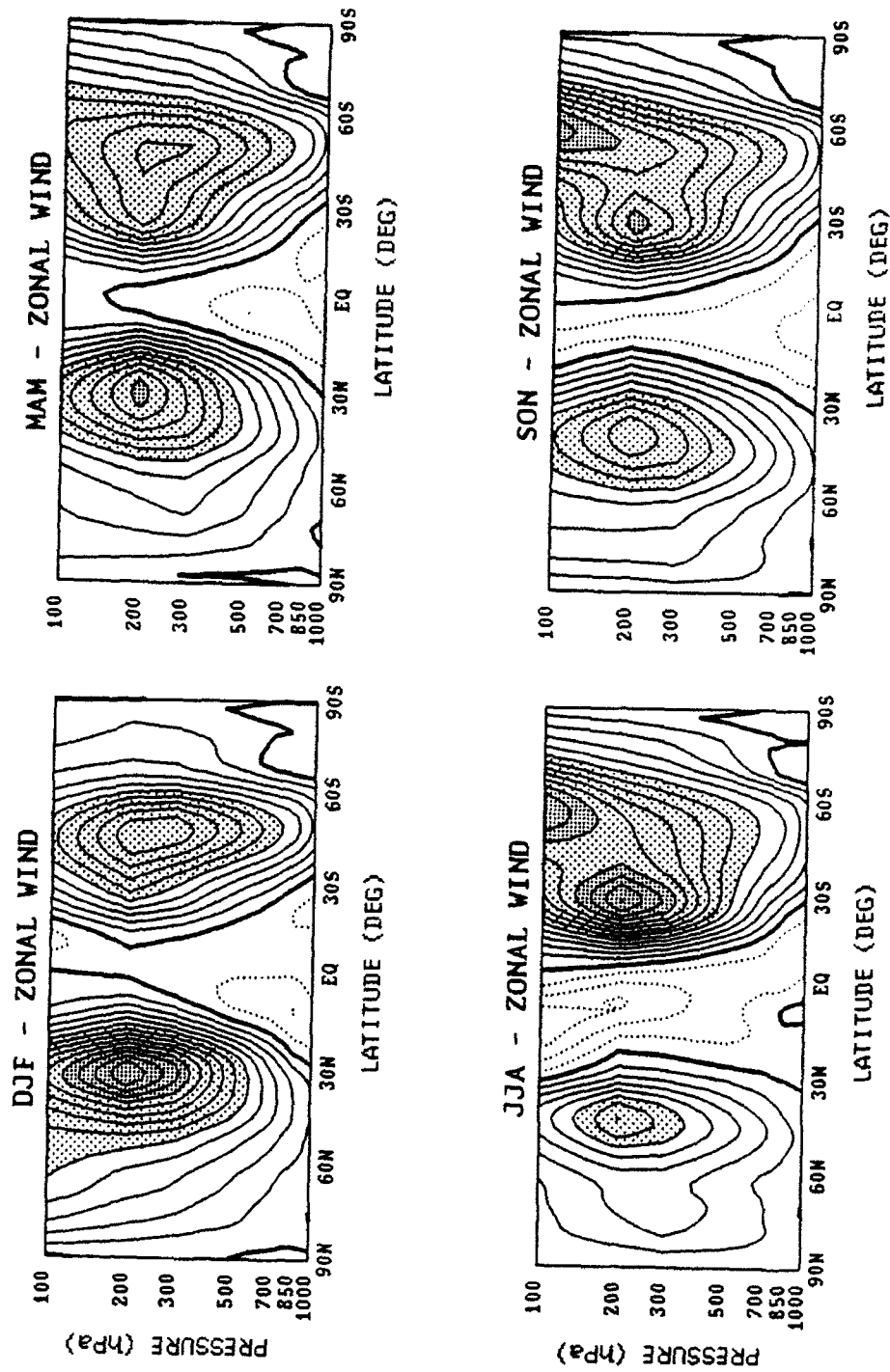


Figure 3.1. Mean seasonal zonal wind. Maximum values at 200 mb for NH and SH are, respectively 41.9 and 29.9 m s^{-1} for DJF, 31.3 and 27.7 m s^{-1} for MAM, 21.1 and 39.1 m s^{-1} for JJA, and 26.5 and 31.6 m s^{-1} for SON. Contour interval is 3 m s^{-1} with light and medium dots shading winds between 15-30 m s^{-1} and 30-45 m s^{-1} , respectively.

zonal wind exhibits equatorial easterlies at all levels. These easterlies prevent the interhemispheric propagation of linear waves in the annually-averaged basic state. It will be shown in Section 3.4 that the linear response of the shallow water equation model to the tropical heating is mostly confined to the summer hemisphere.

The seasonal averages for zonally-averaged meridional winds are shown in Fig. 3.2. In this figure, positive values are northerly winds and negative values are southerly winds. The zonally averaged meridional wind represents the Hadley cell and it is more than one order of magnitude less than the zonal wind. During boreal winter (DJF), strong southerly surface winds are present from 30° N to the Equator, where they converge with weaker, SH northerly winds. Aloft, maximum values occur at 200 mb with relatively strong northerly winds in the NH and weak southerly winds in the SH. A similar, but reversed pattern appears during austral winter (JJA) with the strongest winds in the Hadley Cell occurring again in the winter hemisphere. The intermediate spring/fall seasons are similar to each other, with winds both aloft and near the surface almost equal in magnitude. The zero line is found near the equator during MAM, whereas it is about 15° N in SON. This is consistent with the averaged position of the ITCZ, which is found in the NH during NH fall. Northerlies are stronger during MAM than during SON. By conservation of angular momentum, it would be expected that a stronger Hadley cell would result in higher zonal winds in the NH during boreal spring than fall. This is shown to be the case in Fig. 3.1. Similar results were found by Fleming et al. (1987).

When the values for the zonal and meridional wind are compared with NMC data (provided by Kingtse Mo), the zonal components are all in excellent agreement. There are significant variations in the meridional wind with the magnitudes of the ECMWF data at least twice as strong as the NMC data. However, although the magnitudes differ, the relative seasonal strengths are in agreement, that is, the

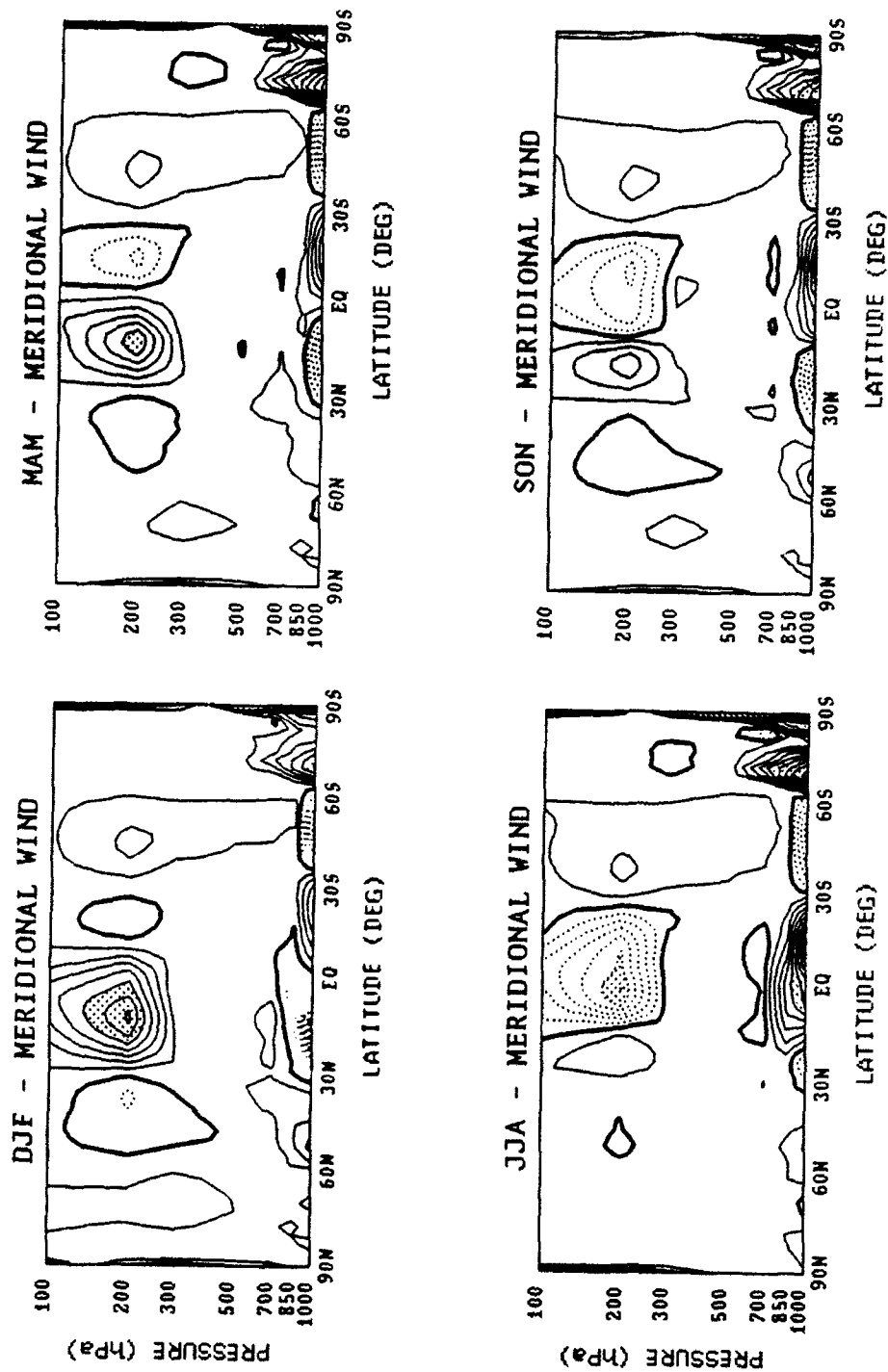


Figure 3.2. Mean seasonal meridional wind. Maximum values at 200 mb centered over the equator for the NH and SH are, respectively 2.15 and -0.242 m s^{-1} for DJF, 1.77 and -0.674 m s^{-1} for MAM, 0.494 and -1.81 m s^{-1} for JJA, and 1.06 and -0.97 m s^{-1} for SON. Contour interval is 0.3 m s^{-1} with light and medium dots shading winds between ± 1.5 – 3.0 m s^{-1} and ± 3.0 – 4.5 m s^{-1} , respectively.

southerlies are stronger in spring than in fall for both data sets.

This structure of convergence at the surface and divergence aloft is associated with rising motions, which take place in a convectively unstable environment and therefore result in tropical convection. The OLR is used here to delineate areas with tropical convection since high, cold cloud tops give small values of OLR. This relationship holds true in the tropics between 30° N and 30° S. Global maps of zonal winds, velocity potential and OLR fields are shown in Fig. 3.3. OLR values less than 200 Wm^{-2} are solid black, values between $200\text{--}220 \text{ Wm}^{-2}$ are shaded with heavy dots, and between $220\text{--}240 \text{ Wm}^{-2}$ with light dots.

During January, three centers of convection can be found south of the equator (Fig. 3.3b). They are located over southern Africa, the maritime continent, and central South America. The divergent wind flows out of the area of strong convective forcing and into the region of strong zonal wind, directly across the gradient of the velocity potential and into the region of maximum zonal wind at 200 mb. Enhancement of the subtropical jets have been long recognized to be common in regions of deep tropical convection (e.g., Bjerknes 1966, 1969) and explanation for their position has been sought as resulting from the excitation of Rossby waves due to tropical heating. Nevertheless, the observed longitudinal position of the wind maxima (see Fig. 3.3a,c) differs from that predicted by single level models such as that of Gill (1980). In the latter case, maximum westerlies are found to the west of the tropical heating instead of at similar longitudes.

Three convection centers are also present during July (Fig. 3.3d), but they have migrated north of the Equator, following the sun. The center over the Bay of Bengal, previously over the maritime continent, is the only center to increase in areal coverage. The divergent winds can again be seen exiting the areas of strong convective forcing and moving toward areas of strong zonal wind (e.g., Krishnamurti 1971). The most pronounced outflow is found over southern Asia associated with

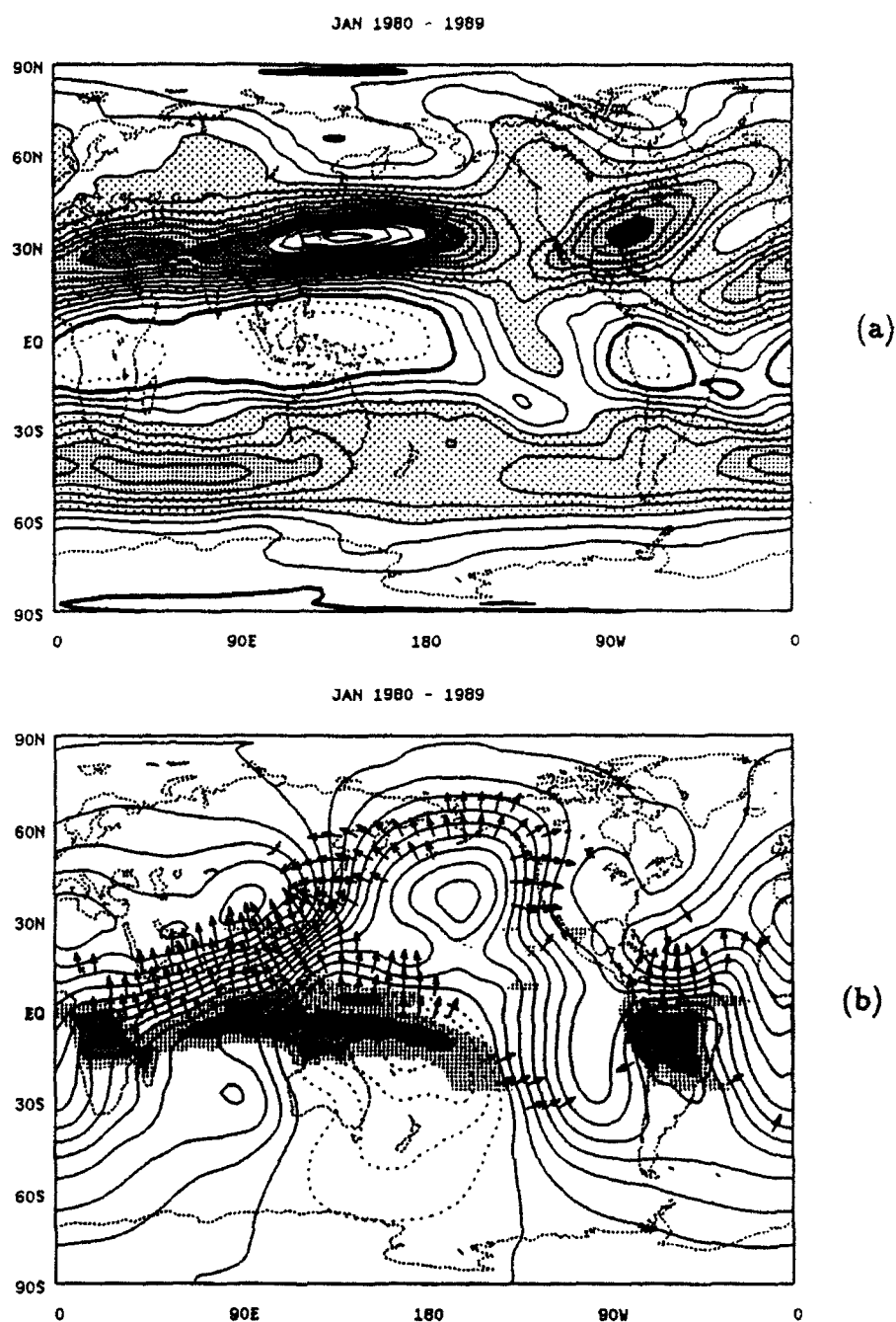
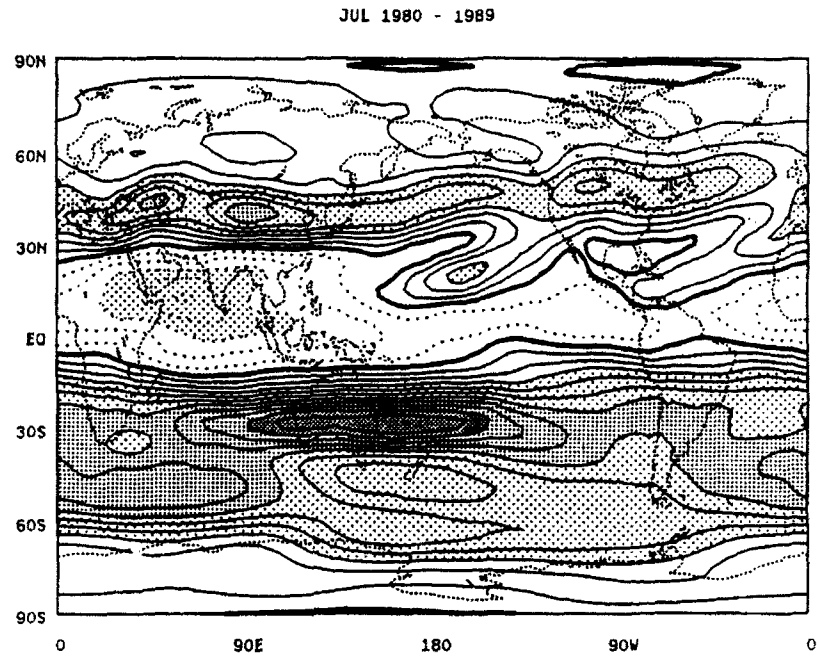
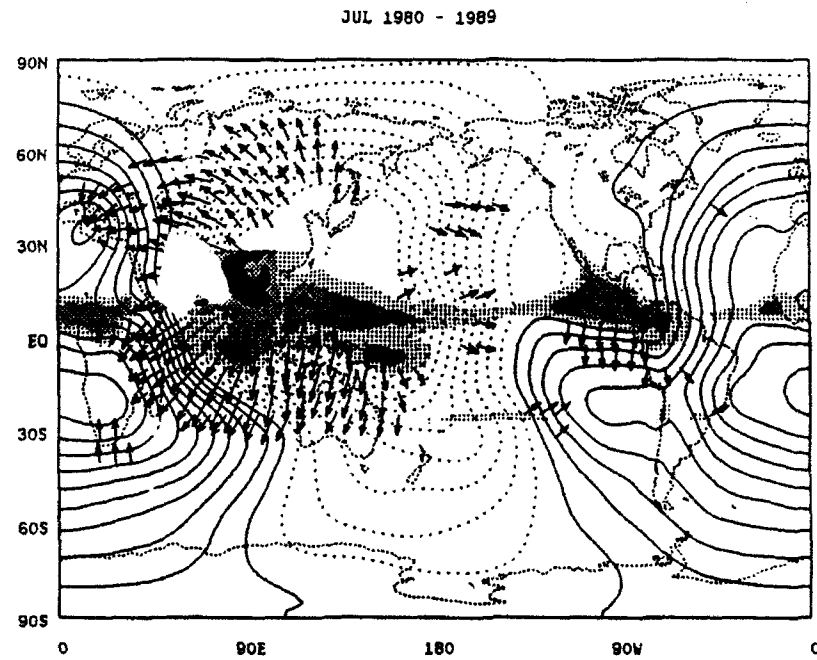


Figure 3.3. January and July 1980-1989. Zonal wind shown in (a,c). Contour interval is 5 m s^{-1} with light, medium and dark shading for speeds of 15-30 m s^{-1} , 30-45 m s^{-1} , and 45-60 m s^{-1} . OLR, velocity potential and divergent winds are shown in (b,d). OLR shading discussed in text. Maximum winds are 5.4 m s^{-1} near 23° N, 124° E in (b) and 4.6 m s^{-1} near 18° N, 90° E in (d). Wind less than 2 m s^{-1} are not plotted in (b,d).



(c)



(d)

the Indian monsoon.

A representation of the seasonal evolution of the OLR fields is shown in Fig. 3.4 with time-longitude cross-section of 200 mb and 850 mb zonal wind at 15° N. The atmospheric response to convective forcing between 10–20° N exhibits a vertically reversing circulation with maximum easterlies over the Indian Ocean associated with the monsoon. Increases in convective activity (indicated by decreasing OLR values) in these latitudes are followed by 200 mb zonal wind changing from westerly to easterly, at similar longitudes, with only minor time lags. As the convection decays, there is a rapid decrease in the strength of the easterly winds. A similar, but opposite response occurs at lower levels and it is seen as an increase in the westerly winds at 850 mb. This evolution in the zonal wind repeats itself off the west coast of South America.

Figure 3.3 also shows a dominant wave one in the subtropical SH zonal wind during July and a wave two pattern in January in the NH. The amplitude of these wind and other height waves are quantified in the next section by projecting height and wind fields onto Fourier functions.

3.2 Seasonal Wave Cycle

3.2.1 Stationary Waves

Stationary waves partly result from the atmospheric response to various surface and mid-atmospheric forcing. The vertical structure and tilt of the zonally asymmetric component of the geopotential height field indicate the nature of the forcing. For example, topographically forced waves which propagate vertically tilt westward with height (e.g., Held 1983). An equivalent barotropic response in the extratropics may indicate a tropical source embedded in a zonal flow with vertical shear (Simmons 1982; Kasahara and Silva Dias 1989). A vertically reversing

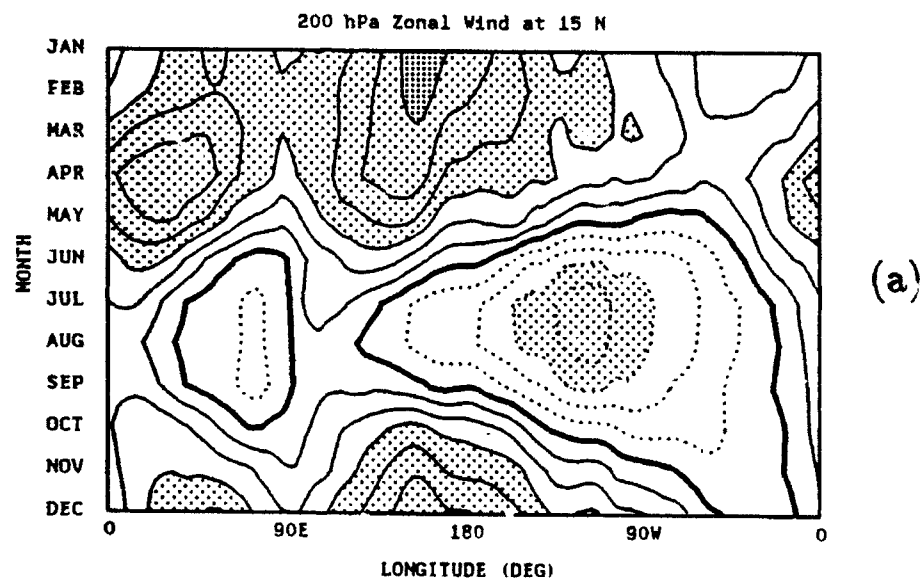
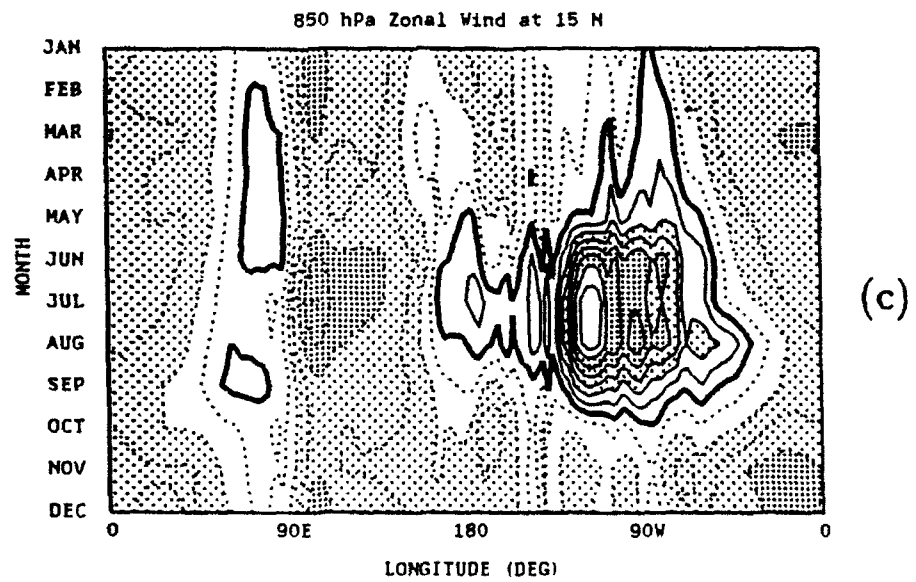
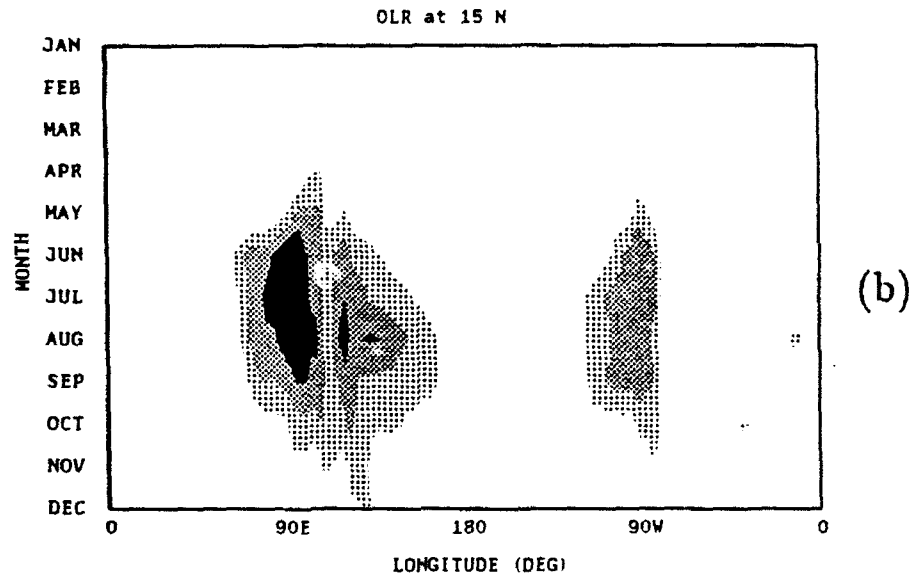


Figure 3.4. Time-longitude sections of (a) 200 mb zonal wind, (b) OLR, and (c) 850 mb zonal wind at 15° N. Contour interval for (a) and (c) are 5 m s^{-1} and 2 m s^{-1} . OLR shading follows the same convention described in text.



structure such as that shown in Fig. 3.4 indicates mid-atmospheric local forcing (such as latent heat release).

The vertical structure of the winter and summer standing waves in the NH, seen in Fig. 3.5a-c, indicates an amplitude that maximizes near 200 mb and shows a slight westward tilt. This tilt, suggestive of vertically propagating wave modes, together with the strong indication of a wavenumber two pattern seen in the amplitude, suggest that the orographic forcing from the Himalayan Plateau and Rocky Mountains is the dominant factor in determining the positions of the major troughs and ridges during winter. Therefore, we do not expect to be able to reproduce this feature of the stationary waves in the model integrations forced only with tropical heating.

During boreal summer, the amplitude of the stationary waves decreases significantly (Fig. 3.5d-f). The westward tilt is no longer apparent and the near vertical appearance, with amplitude increasing with increasing height, suggests an equivalent barotropic component. A strong, distinct phase reversal can be seen at 25° N between the upper and lower tropospheric geopotential height fields, centered near 90° E, indicating the Indian monsoon. Thus, the monsoon circulation, driven by diabatic heating, appears to account for the prominent summertime maximum in the stationary wave pattern. With the exception of White (1982), the role of mechanical forcing by orography during the NH summer has received relatively little emphasis, probably due to the lack of a westward tilt. However, Wallace (1983) points out that when thermal and orographic forcing are simultaneously present, the vertical structure of the waves may not be a reliable indicator as to the dominant type of forcing.

The seasonal variation in the SH stationary waves is much less pronounced than in the NH. Tropical latitudes exhibit weak amplitudes with similar patterns in summer and winter (Fig. 3.6). At higher latitudes a wave one pattern is dominant.

Figure 3.5. Height-longitude cross-section of the stationary wave geopotential height for December–February 1980–1989 at (a) 60° N, (b) 45° N, and (c) 25° N and for June–August 1980–1989 at (d) 60° N, (e) 45° N, and (f) 25° N. Contour interval is 30 m.

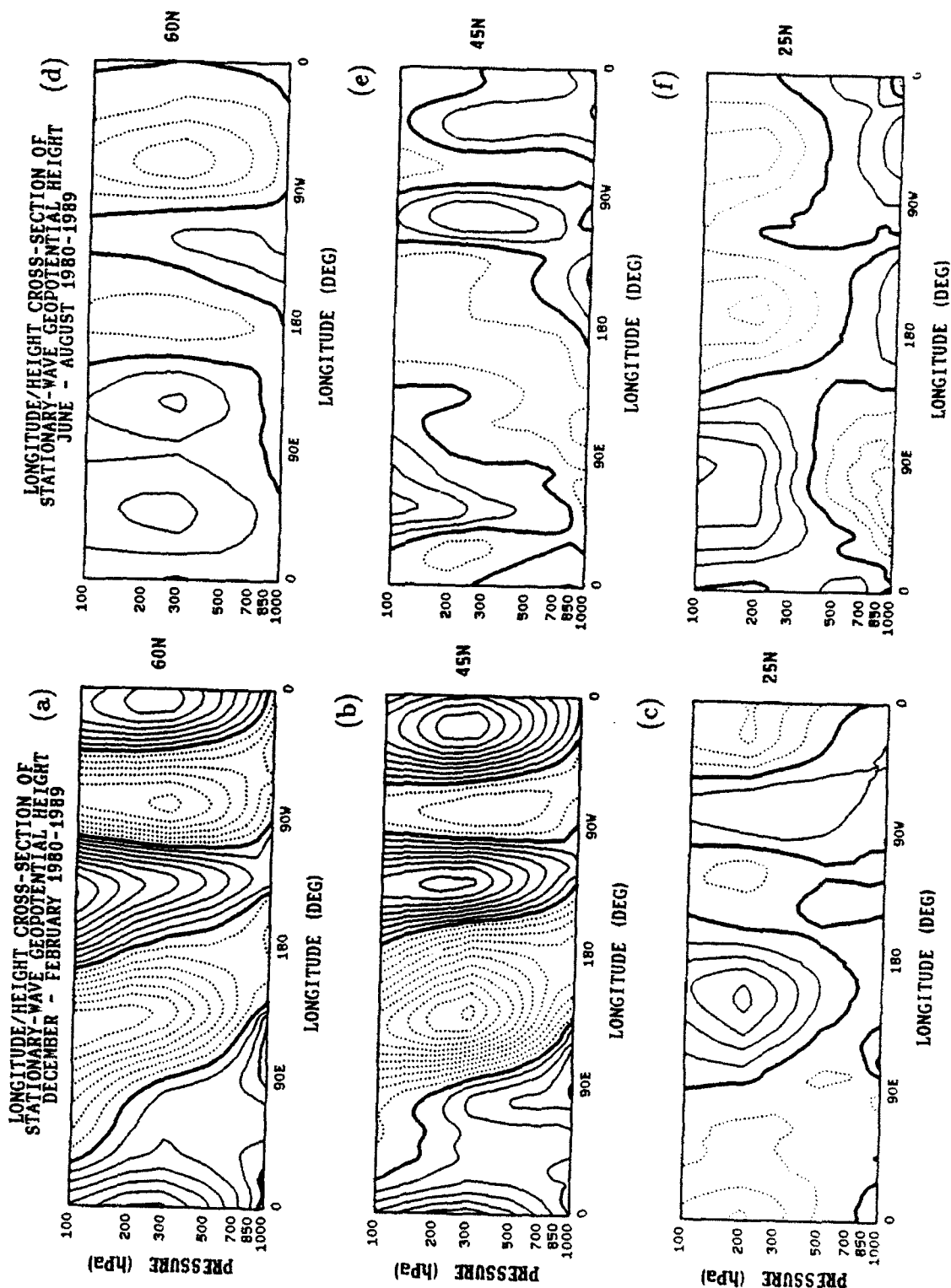
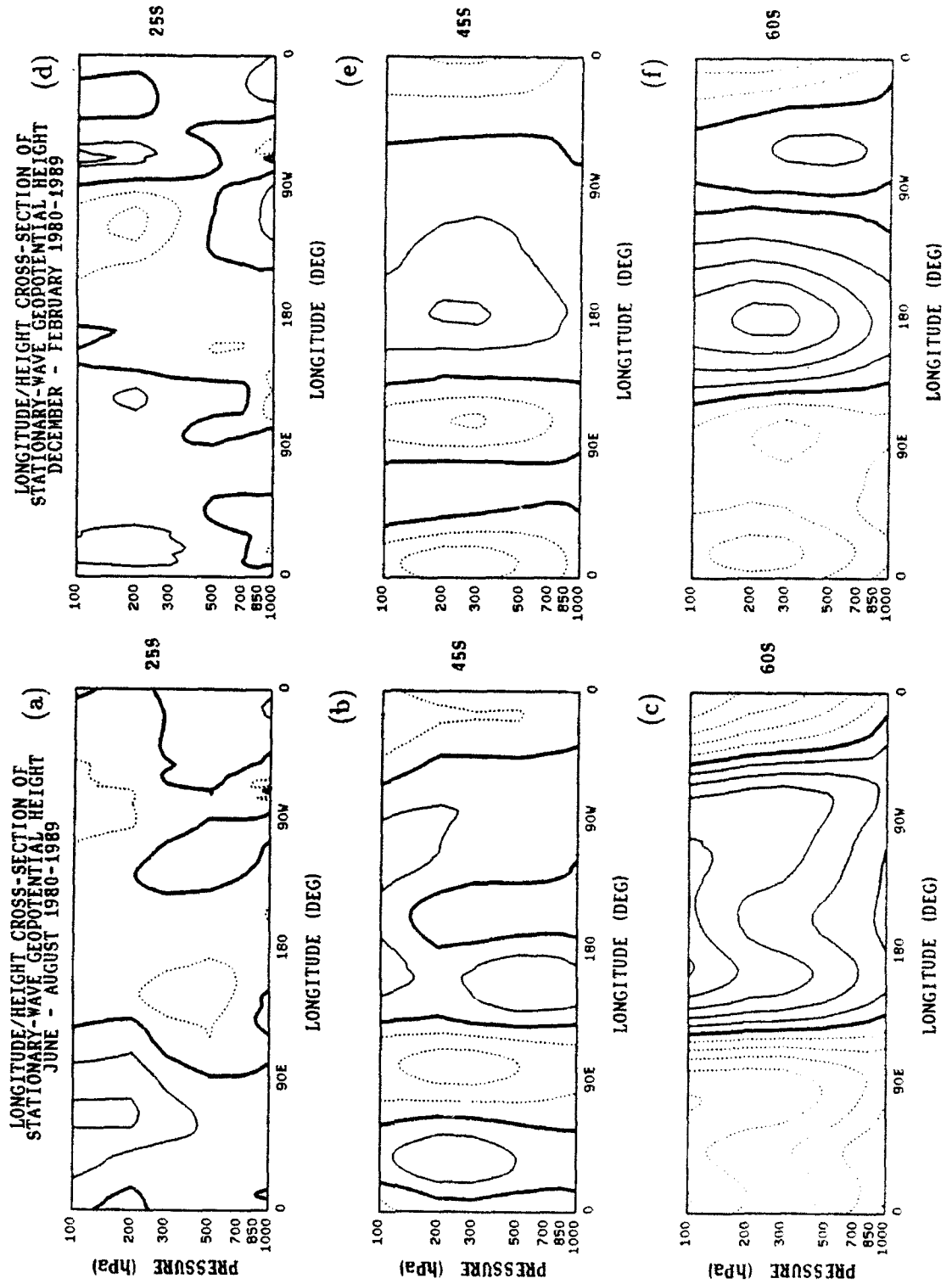


Figure 3.6. Height-longitude cross-section of the stationary wave geopotential height for June–August 1980–1989 at (a) 25° S, (b) 45° S, and (c) 60° S and for December–February 1980–1989 at (d) 25° S, (e) 45° S, and (f) 60° S. Contour interval is 30 m.



Wave amplitudes maximize between 300–200 mb, and have no vertical tilt. During SH summer (Fig. 3.6d–f) the high latitudes show evidence of a wavenumber one, barotropic structure. A smaller, and much weaker area of phase reversal, as compared the the NH, is seen off the coast of South America in the tropical region. This is accompanied by an even smaller region, but of opposite sign, over the South American continent.

During the transition seasons, the structure of the NH standing waves are remarkably similar (Fig. 3.7). A near barotropic response is present in the NH at mid- and high latitudes with a slight westward tilt at low levels over the western Pacific, which decreases rapidly with height. The tilt is slightly more pronounced during autumn. The height of the maximum amplitudes at these latitudes changes slightly from near 300 mb for spring to 300–200 mb during fall, with autumn values slightly higher. This is consistent with Fleming (1987), who found many of the features of the NH autumn pattern to be somewhat stronger. The phase reversal over the region of the Indian monsoon is present during both seasons, with the maximum low level amplitude slightly further eastward during spring.

Unlike the NH, the structure of the SH geopotential height standing waves, shown in Fig. 3.8, is quite different during the two transition seasons. The maximum wave amplitude is much greater, particularly at high latitudes, during the austral spring. Therefore, the stronger of the two transition seasons is different for the hemispheres, but they occur during the same actual months of September–November.

These differences in the transition seasons may also be seen in the poleward momentum transport, $([\bar{u}^* \bar{v}^*])$, and meridional heat transport, $([\bar{v}^* \bar{T}^*])$. These are shown in Fig. 3.9.

The largest values of both heat and momentum transport occur in the NH during DJF (Fig. 3.9a,b) as expected from the westward tilt of the waves with height. There is meridional convergence of momentum transport between 30° and 60° N

Figure 3.7. Height-longitude cross-section of the stationary wave geopotential height for March-May 1980-1989 at (a) 60° N, (b) 45° N, and (c) 25° N and for September-November 1980-1989 at (d) 60° N, (e) 45° N, and (f) 25° N. Contour interval is 30 m.

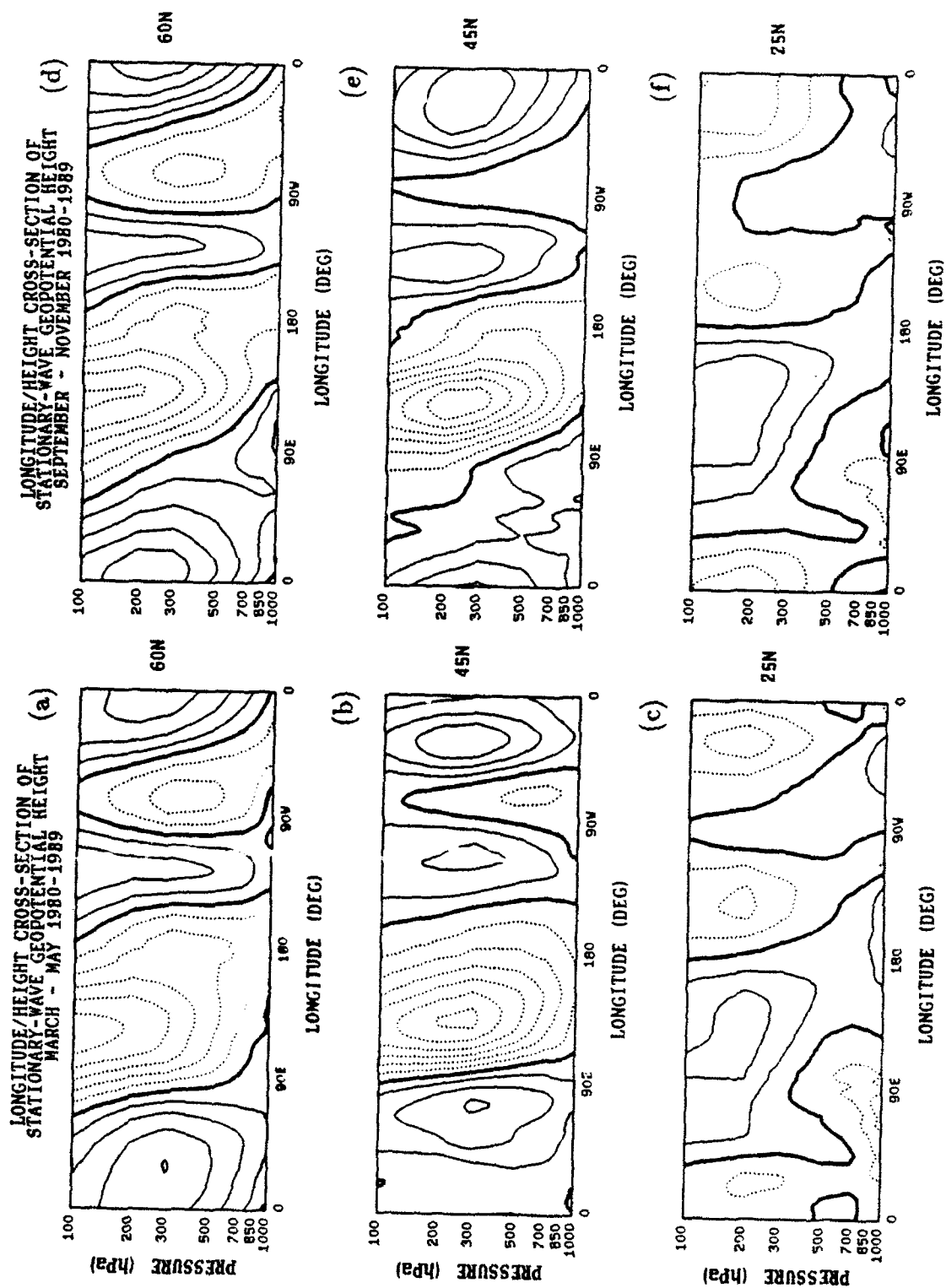
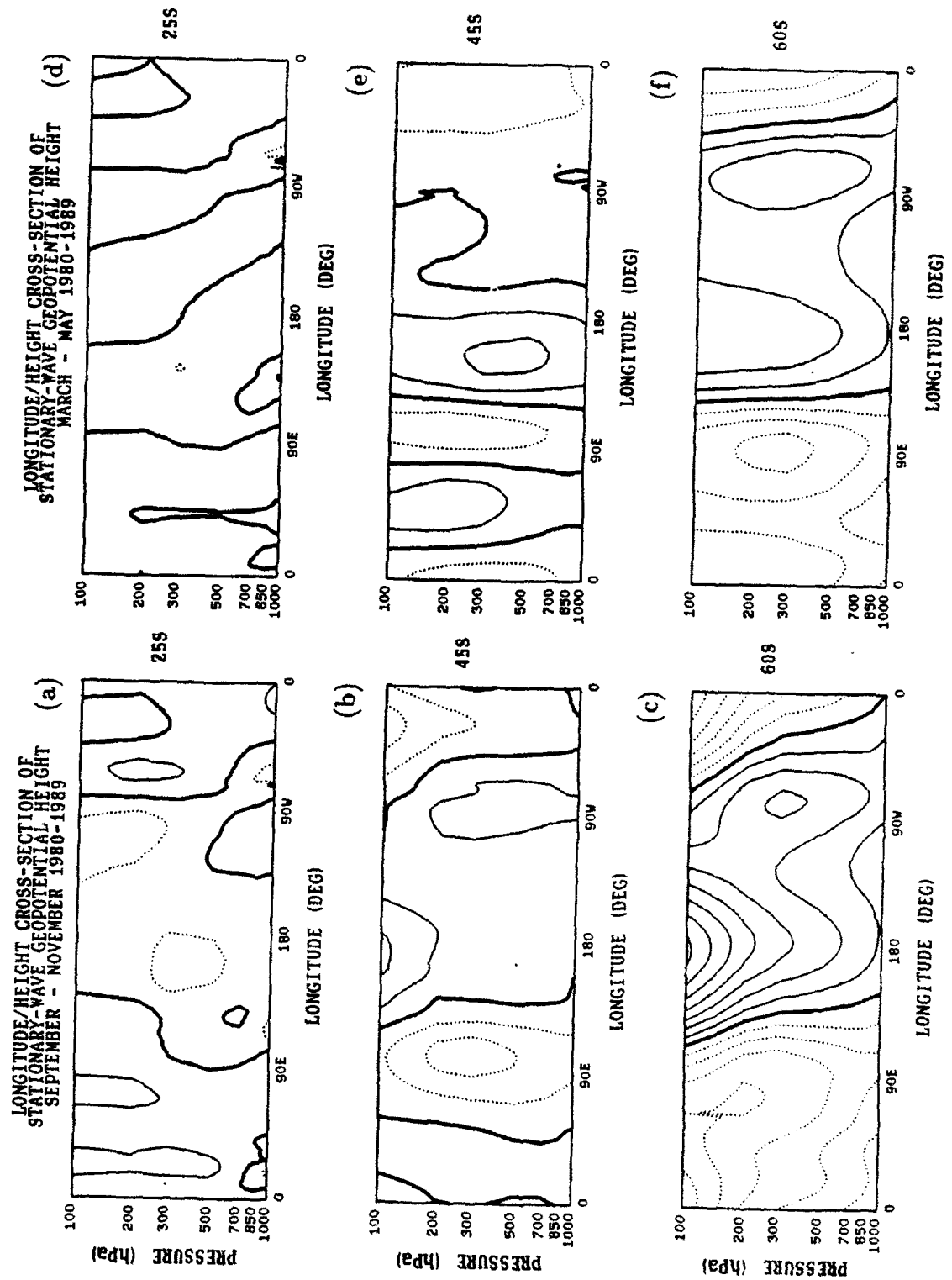


Figure 3.8. Height-longitude cross-section of the stationary wave geopotential height for September–November 1980–1989 at (a) 25° S, (b) 45° S, and (c) 60° S and for March–May 1980–1989 at (d) 25° S, (e) 45° S, and (f) 60° S. Contour interval is 30 m.



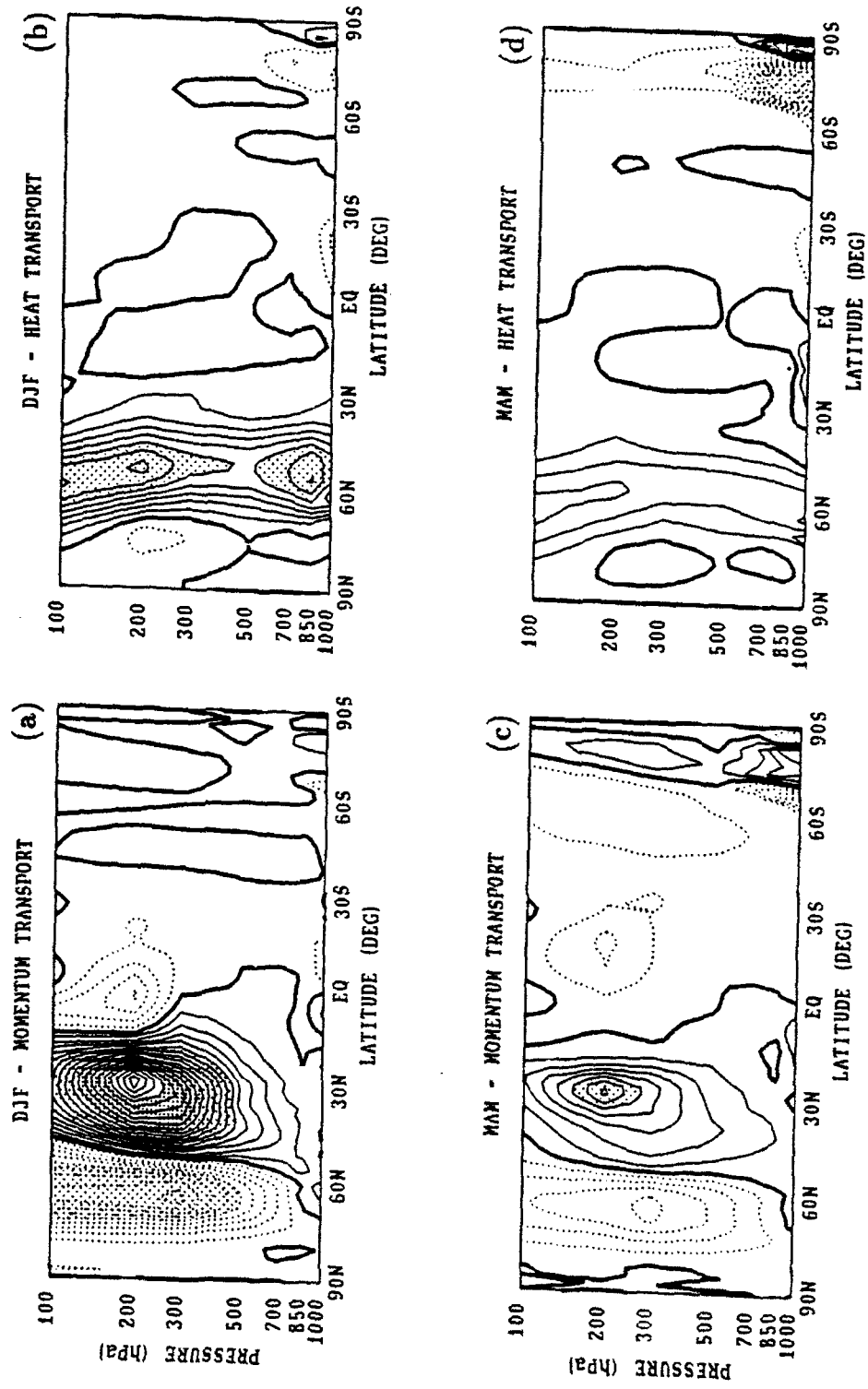
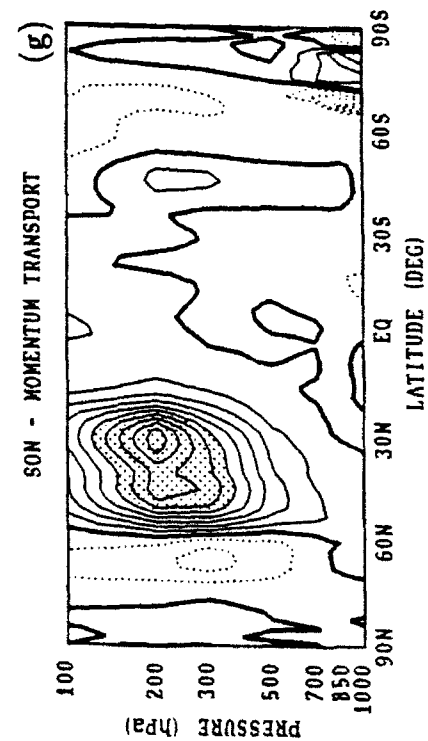
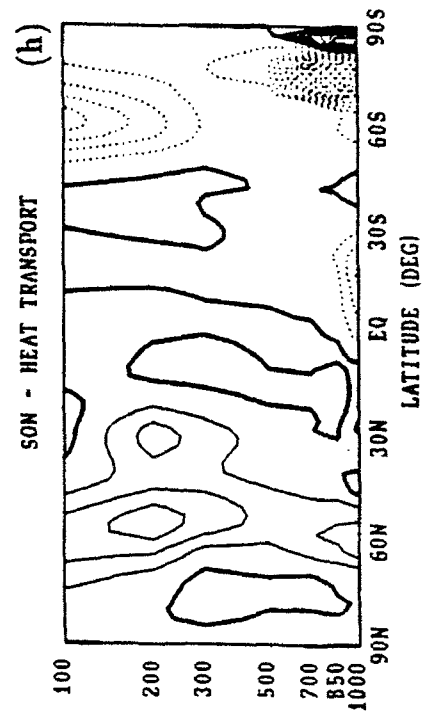
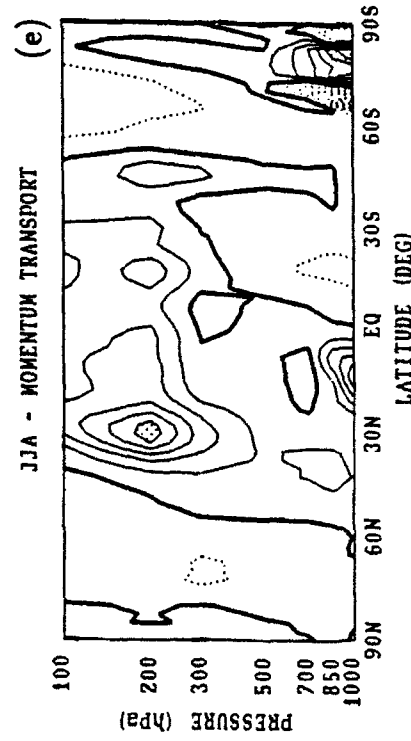
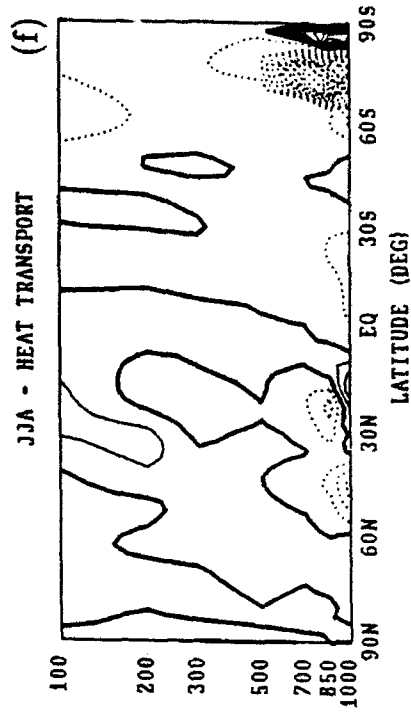


Figure 3.9. Zonally averaged seasonal momentum and heat transport for DJF (a,b), MAM (c,d), JJA (e,f) and SON (g,h). Contour interval is $2 \text{ m}^2 \text{ s}^{-2}$ in (a) and $2 \text{ }^\circ\text{K m s}^{-1}$ in (b). Shading is for values of ± 10 units.



indicating the stationary wave role in maintaining the zonally averaged circulation against dissipation. The heat transport maximum throughout the troposphere is centered over $50\text{--}60^\circ$ N. Momentum transport at upper levels in the SH never approaches the magnitude of the NH, even during austral winter (JJA). This is also consistent with the relatively small magnitude of the SH waves compared with those in the NH. Maximum values in the SH are limited to lower layers of the atmosphere and poleward of 60° S. However, these values are close to the Antarctic continent and may not be reliable. Another area of significant momentum flux near the surface occurs during JJA between the equator and 30° N. The pattern of heat transport mimics the momentum transport. The exception occurs during SON in the SH where a stratospheric intrusion of heat flux is present in the upper troposphere between approximately $60\text{--}80^\circ$ S.

In summary, the results presented in this subsection quantify the vertical and horizontal structure of stationary waves. These are found to tilt westward with height in the NH winter, they exhibit pronounced northwest to southeast tilts at high latitudes and from northeast to southwest at mid-latitudes. These meridional tilts are inferred from the momentum transports. Wave amplitudes are larger in the NH than in the SH and they exhibit a pronounced seasonal variation. The internal structure typical of heat driven circulations is observed in the tropics during NH summer and to a much lesser extent over tropical South America during austral summer.

3.2.2 Fourier Analysis

Quantification of the amplitude of the dominant planetary waves shown in the previous subsection is now presented. Fourier analysis of geopotential heights reveals that wave one is the main contributor to the 200 mb height field (Fig. 3.10).

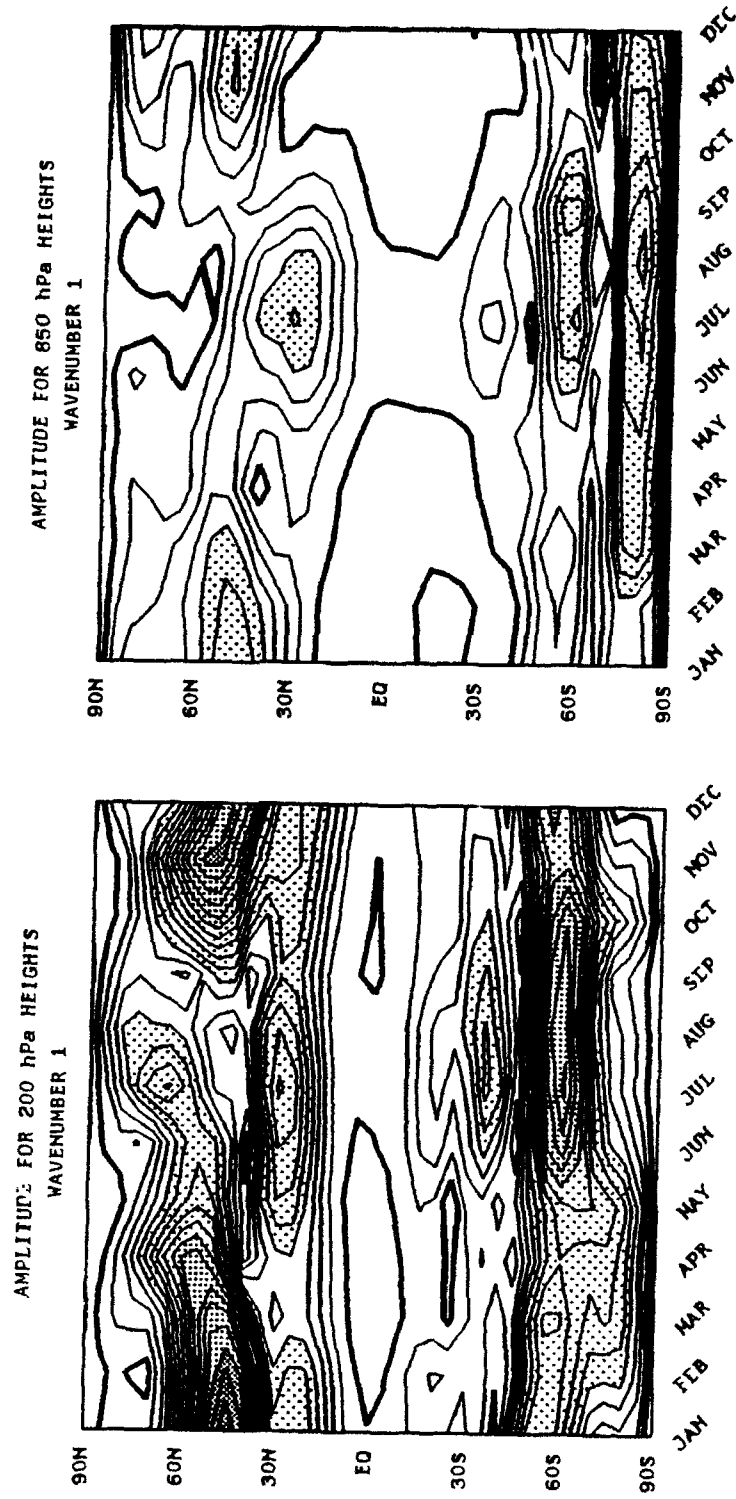
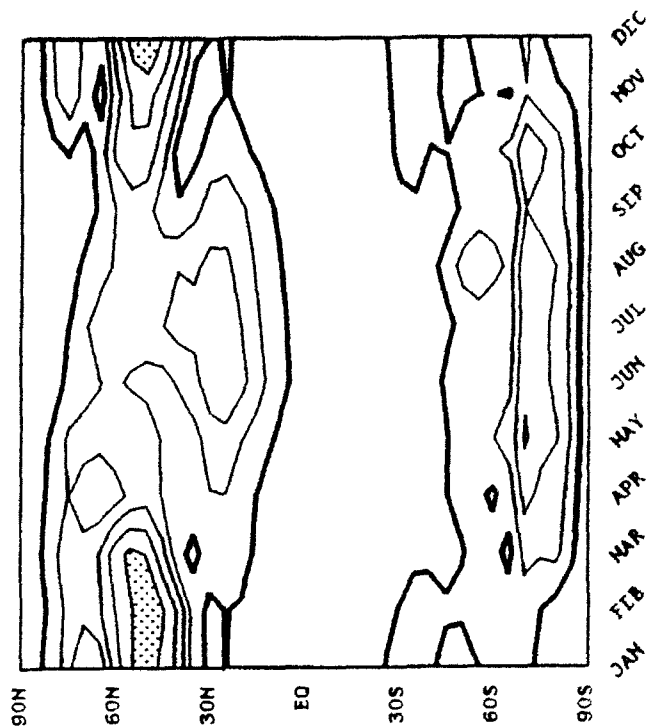
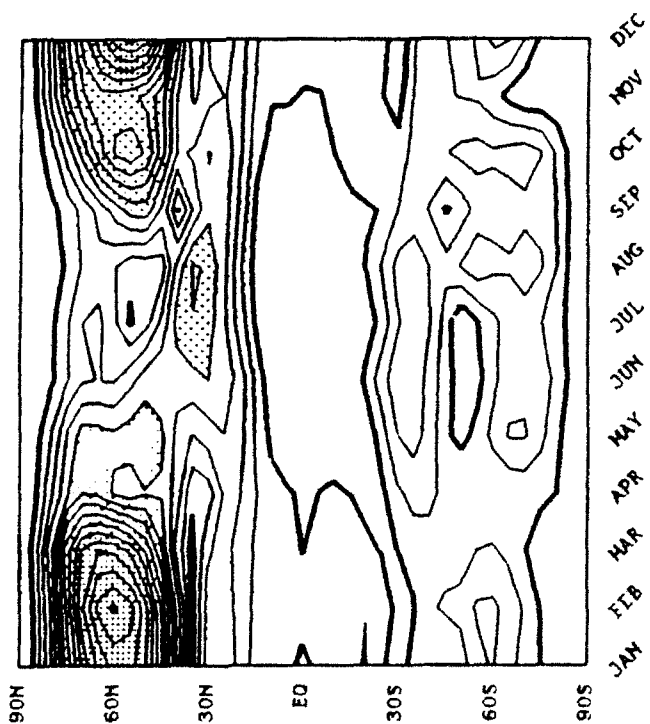


Figure 3.10. Latitude/time cross-section of amplitude for the 200 and 850 mb heights for wavenumbers one, two, and three. Contour interval is 10 m. and heights from 50–100 m are shaded with light dots, 100–150 m are shaded with medium dots, and 150+ m are shaded with heavy dots. The 10 m contour is highlighted.

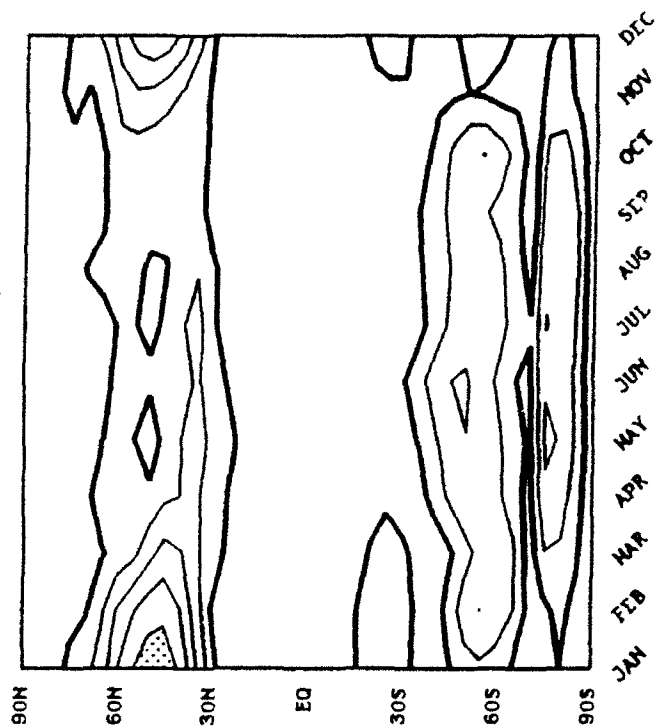
AMPLITUDE FOR 850 hPa HEIGHTS
WAVENUMBER 2



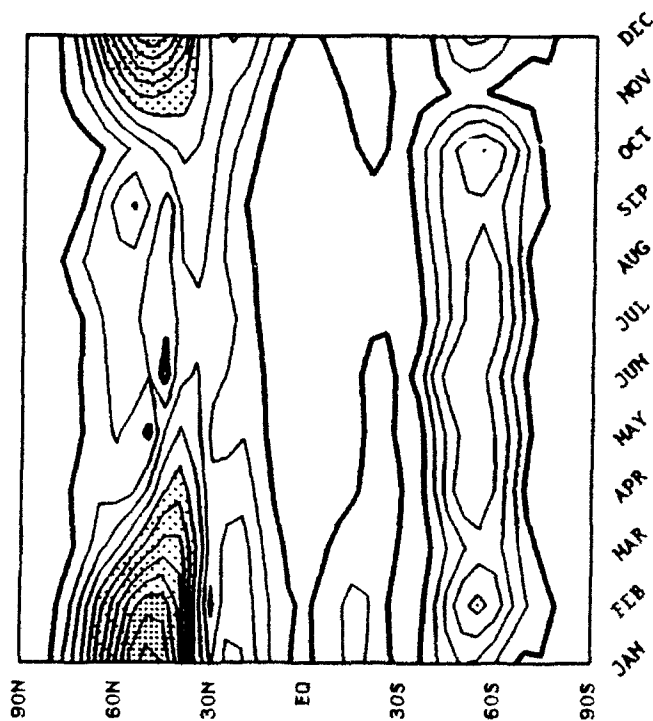
AMPLITUDE FOR 200 hPa HEIGHTS
WAVENUMBER 2



AMPLITUDE FOR 850 hPa HEIGHTS
WAVENUMBER 3



AMPLITUDE FOR 200 hPa HEIGHTS
WAVENUMBER 3



Maximum values in the northern hemisphere occur in winter, near 45° N for wave one, and near 60° N for wave two. Maximum values in the SH are found for wave one during austral winter, centered near 60° S. Waves shorter than wavenumber three contribute comparatively little to the zonal flow variations at 200 mb and are not shown. Waves decrease in summer to 25 to 30% of their winter amplitude. During boreal summer a relative maximum is found at about 30° N both in waves one and two reflecting the effect of the Asian monsoon in the height field. In the SH late spring and summer wavenumber three exhibits a relative maximum amplitude in the subtropics. This is expected from the three dominant centers of convection previously discussed during this season. Wave three also appears to attain maximum amplitude during October and February at these latitudes. While the February maximum may be attributed to meridional propagation from the tropics, causes for the October maximum are not clear.

The height waves at 850 mb mirror the upper tropospheric flow in the NH and SH with the exception of much decreased amplitude. Also, the maximum amplitude is now observed for wave two during boreal winter.

3.3 Wavenumber Vertical Structure

The previous section focused on the height field which exhibits maximum wave amplitude in the extratropics. In this section, winds are considered instead of heights, and their vertical structure is quantified in terms of the contribution to the rotational and divergent wind by different vertical modes as explained in Chapter 2.

3.3.1 The Zonal Rotational Wind

As described in Chapter 2, the Fourier coefficients, \hat{S}_k , are projected onto the vertical structure functions, $\psi_n(\sigma)$, to obtain the contributions to the Fourier

coefficients by the different vertical modes, \hat{S}_k^n . Values are normalized using the maximum value for each wavenumber, within the latitudinal belts of 90° S–30° S, 30° S–30° N, and 30° N–90° N. This is done so that features in the vertical structure of the SH and tropics are not normalized by values from the dominant NH. Also, within the latitudinal belts, grid points whose total normalized vertical variability does not exceed 0.25 for a given wavenumber are not plotted. As described in Section 2.2.2, the modes are represented in rosette fashion, using the following format: mode 1 (\rightarrow), mode 2 (\nearrow), mode 3 (\uparrow), mode 4 (\nwarrow), and mode 5 (\leftarrow). These arrows represent the contribution from the different vertical modes to the total wave field. The discussion is limited to the first seven wavenumbers, since for all but the meridional rotational wind, the first seven wavenumbers account for approximately 75% of the total wind variability during all seasons (see Fig. 3.11). Tables 3.1 through 3.4 present the maximum values within each of the latitudinal belts, by wavenumber, used to normalize the grid point values for each of the rotational and divergent wind components. The total contribution by each mode, for each wavenumber, for latitudes from 80° N to 80° S, at 10° intervals, is shown next for the midpoint of each season.

During January (Fig. 3.12a) the vertical structure for the first five wavenumbers, outside the tropics, is composed primarily of a combination of the external and second internal modes (modes one and three). This is the combination which results in an equivalent barotropic structure (refer to Fig. 2.2). The tropics, from the equator to approximately 20° S, yield a composite of mode two and three. This results in a vertical reversing structure, typical of that found associated with deep convection (Fig. 2.3). Wavenumbers six and seven, the shorter wavelengths, still have a significant external mode, but also more of a complex vertical structure. This is due to more variability at lower levels which result in significant contributions from modes four and five.

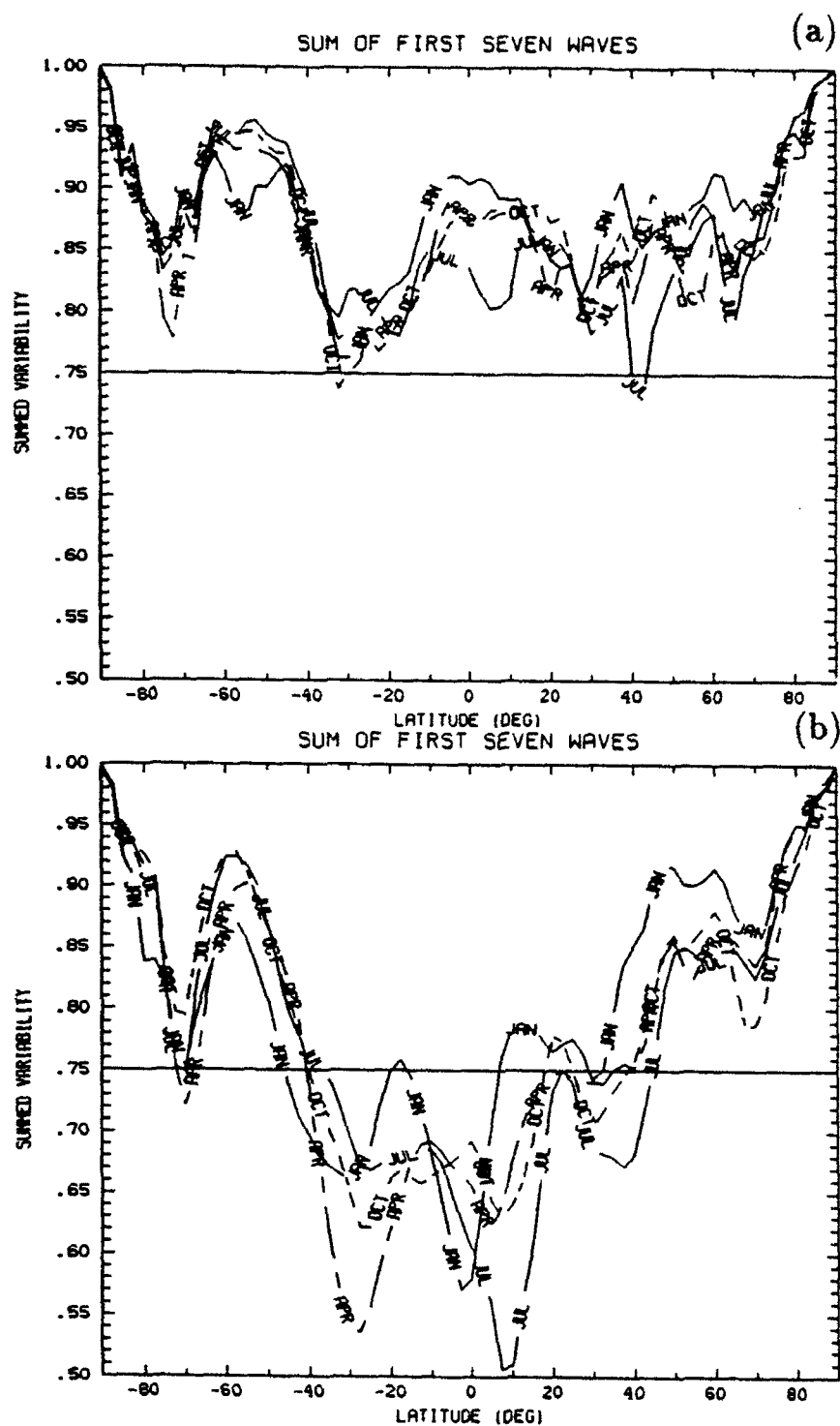


Figure 3.11. Contribution of the first seven wavenumbers to the total wind variability during each season for the (a) zonal rotational, (b) meridional rotational, (c) zonal divergent, and (d) meridional divergent wind components.

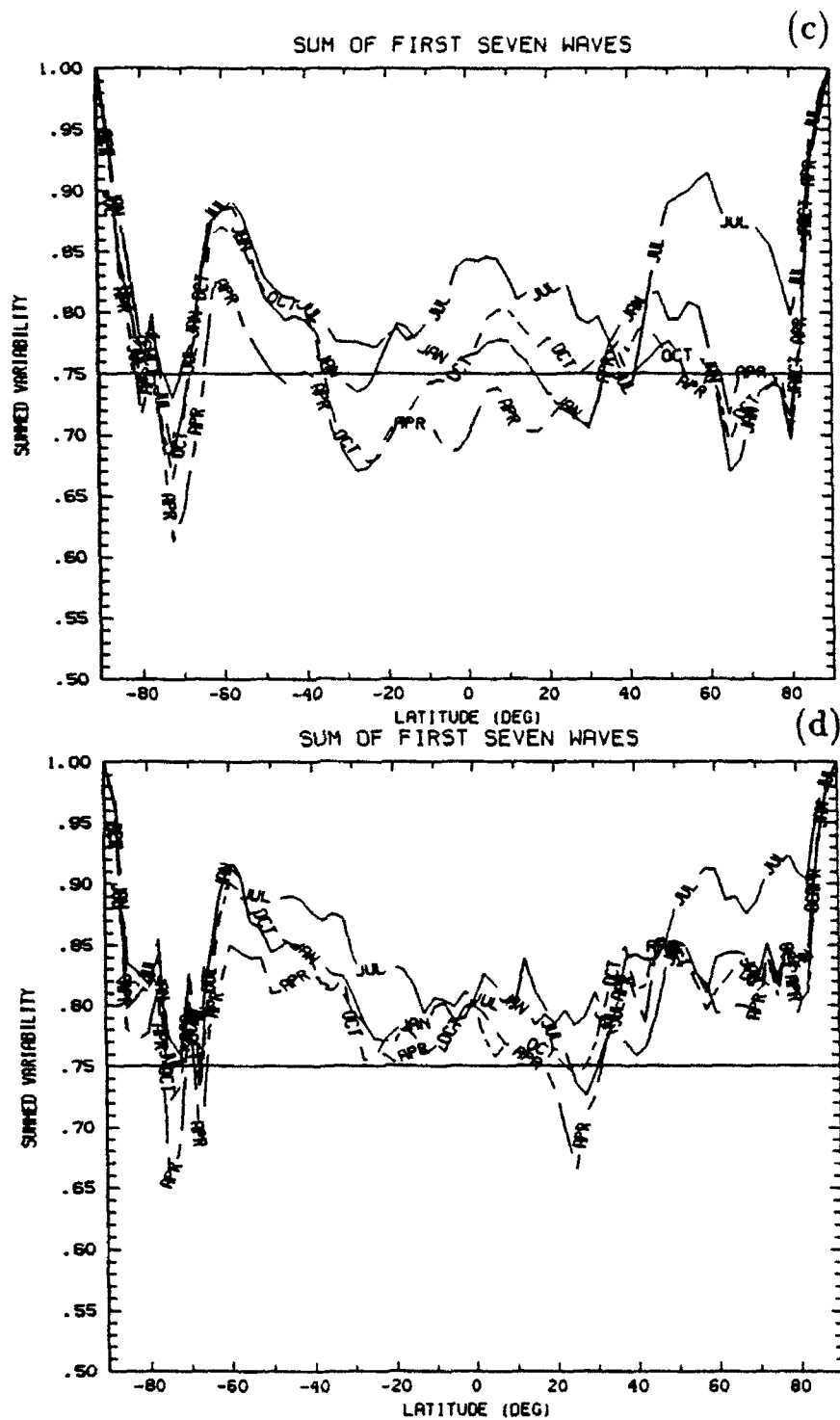


Table 3.1. Maxima (ms^{-1}) for zonal rotational wind summed for the first seven wavenumbers over the latitudinal belts for January, April, July and October 1980-1989.

ZONAL ROTATIONAL WIND			
January 1980-1989			
Wavenumber	90° S - 30° S	30° S - 30° N	30° N - 90° N
1	4.74	11.95	12.15
2	2.35	3.38	5.33
3	1.76	6.96	7.71
4	1.94	3.35	3.35
5	0.48	1.58	1.58
6	0.49	1.15	1.15
7	0.90	1.69	1.69
April 1980-1989			
Wavenumber	90° S - 30° S	30° S - 30° N	30° N - 90° N
1	4.57	4.73	6.39
2	1.85	3.32	3.18
3	2.24	4.41	4.41
4	1.76	2.03	1.87
5	0.74	1.08	1.31
6	0.41	0.71	0.75
7	0.65	1.04	1.24
July 1980-1989			
Wavenumber	90° S - 30° S	30° S - 30° N	30° N - 90° N
1	7.94	7.07	5.25
2	2.10	3.47	2.30
3	2.11	2.24	2.48
4	1.41	1.99	1.48
5	0.69	0.85	1.92
6	0.58	1.16	1.20
7	0.48	1.19	1.40
October 1980-1989			
Wavenumber	90° S - 30° S	30° S - 30° N	30° N - 90° N
1	6.08	5.50	7.20
2	2.62	4.10	4.93
3	1.87	3.10	3.10
4	1.47	1.83	1.58
5	0.84	1.18	1.25
6	0.57	0.78	0.88
7	0.91	1.47	1.57

Table 3.2. Maxima (m s^{-1}) for meridional rotational wind summed for the first seven wavenumbers over the latitudinal belts for January and July 1980-1989.

MERIDIONAL ROTATIONAL WIND			
January 1980-1989			
Wavenumber	90° S - 30° S	30° S - 30° N	30° N - 90° N
1	2.33	1.69	2.88
2	1.07	1.56	5.29
3	1.59	3.14	5.78
4	1.35	1.95	3.60
5	0.84	0.70	1.88
6	0.64	0.91	1.25
7	1.06	1.05	0.83
July 1980-1989			
Wavenumber	90° S - 30° S	30° S - 30° N	30° N - 90° N
1	3.15	2.23	2.28
2	2.05	2.34	2.39
3	2.67	0.91	1.47
4	1.27	1.06	1.54
5	0.81	0.80	1.98
6	0.48	0.64	1.72
7	0.44	0.94	2.06

Table 3.3. Maxima (m s^{-1}) for zonal divergent wind summed for the first seven wavenumbers over the latitudinal belts for January and July 1980–1989.

ZONAL DIVERGENT WIND			
January 1980–1989			
Wavenumber	90° S – 30° S	30° S – 30° N	30° N – 90° N
1	0.63	0.57	0.75
2	0.30	0.39	0.58
3	0.43	0.48	0.55
4	0.40	0.43	0.24
5	0.07	0.17	0.19
6	0.09	0.19	0.17
7	0.15	0.17	0.15
July 1980–1989			
Wavenumber	90° S – 30° S	30° S – 30° N	30° N – 90° N
1	0.89	1.10	1.14
2	0.29	0.90	0.91
3	0.29	0.25	0.36
4	0.24	0.31	0.31
5	0.19	0.25	0.17
6	0.13	0.16	0.12
7	0.10	0.24	0.25

Table 3.4. Maxima (m s^{-1}) for meridional divergent wind summed for the first seven wavenumbers over the latitudinal belts for January and July 1980–1989.

MERIDIONAL DIVERGENT WIND			
January 1980–1989			
Wavenumber	90° S ~ 30° S	30° S ~ 30° N	30° N ~ 90° N
1	0.56	0.69	0.75
2	0.24	0.43	0.43
3	0.32	0.58	0.54
4	0.26	0.28	0.20
5	0.07	0.24	0.22
6	0.10	0.16	0.11
7	0.10	0.21	0.13
July 1980–1989			
Wavenumber	90° S ~ 30° S	30° S ~ 30° N	30° N ~ 90° N
1	0.79	0.88	1.13
2	0.27	0.53	0.65
3	0.26	0.38	0.23
4	0.22	0.29	0.20
5	0.16	0.22	0.14
6	0.10	0.16	0.14
7	0.10	0.15	0.13

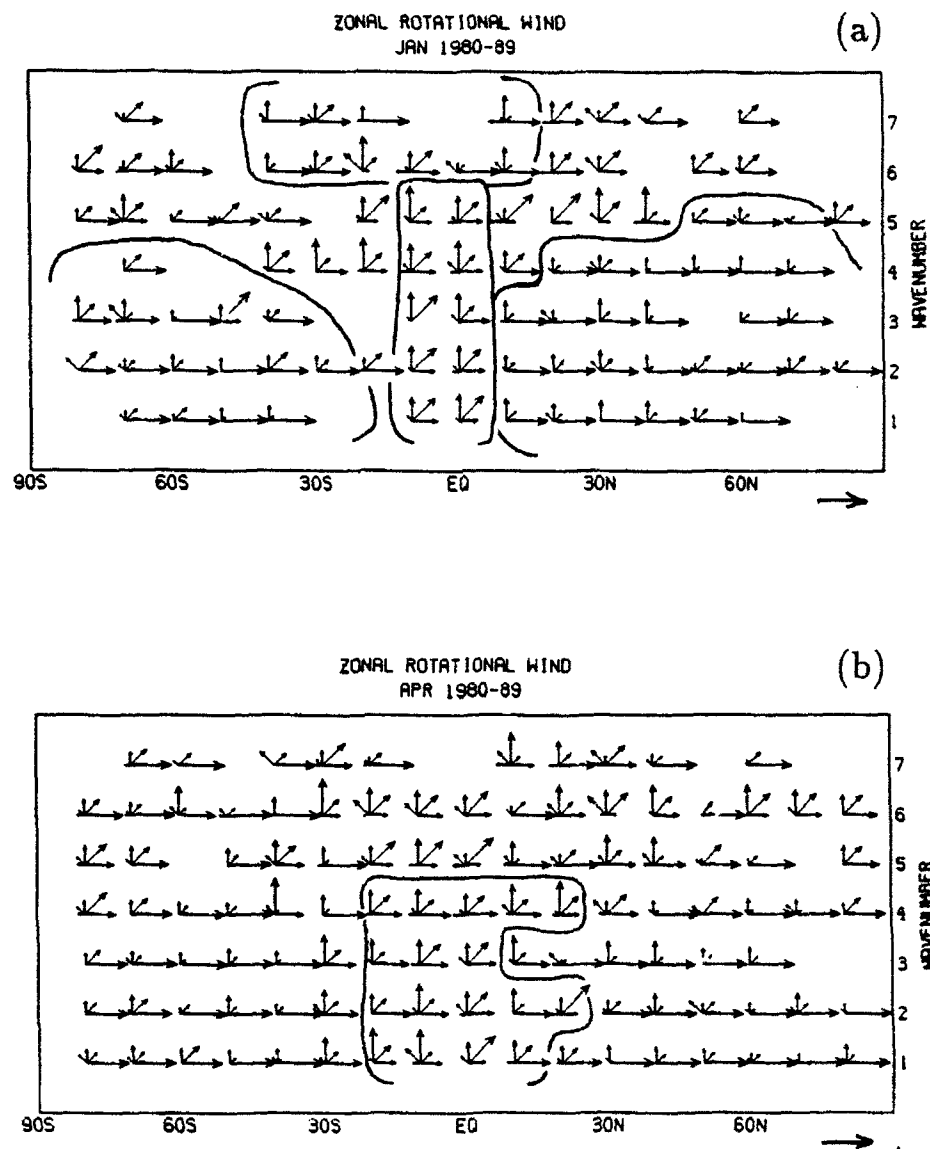


Figure 3.12. Contribution by the first five vertical modes for the zonal rotational wind during (a) January and (b) April 1980-1989 for waves one through seven. Mode representation by arrows described in text. Maximum normalized vector shown in bottom right of each panel.

At mid- and high latitudes, little has changed for the month of April (Fig. 3.12b) for wavenumbers one through five. The vertically reversing structure, a result of the mode two and three combination, has spread into the NH to 20° N for wavenumbers two and four. While little of the mode composition has changed at the higher wavenumbers, more latitudes now exhibit total vertical variances larger than the threshold value.

The month of July (as seen in Fig. 3.13a) shows the mode one/three combination of an equivalent barotropic atmosphere for most of the extratropics all the way through wavenumber seven. In the SH tropics, the mode two vertical contribution has dropped off sharply for wavenumbers one through three and it is now found in the NH, up to 10° N, at wavenumbers one through five, indicative of the Asian monsoon. The first seven wavenumbers continue to account for at least 75% of the total variance of the vertical structure.

The same holds true for the wavenumber total during October (Fig. 3.13b). However, a distinction now exists between NH and SH extratropical regions. The NH shows a strong external/second internal mode, while the SH is more comprised of a strong external mode which overshadows the minor contributions from the internal modes. This holds true, with few exceptions, at all latitudes and for the first six wavenumbers. The strong convective mode combination has died off in the NH, but continues in the tropics and SH, reaching as far as 40° S for wavenumbers four through six.

3.3.2 The Meridional Rotational Wind

The vertical structure of the meridional rotational wind exhibit some similarities with that of the zonal wind, with some notable exceptions. These are discussed next for the months of January and July.

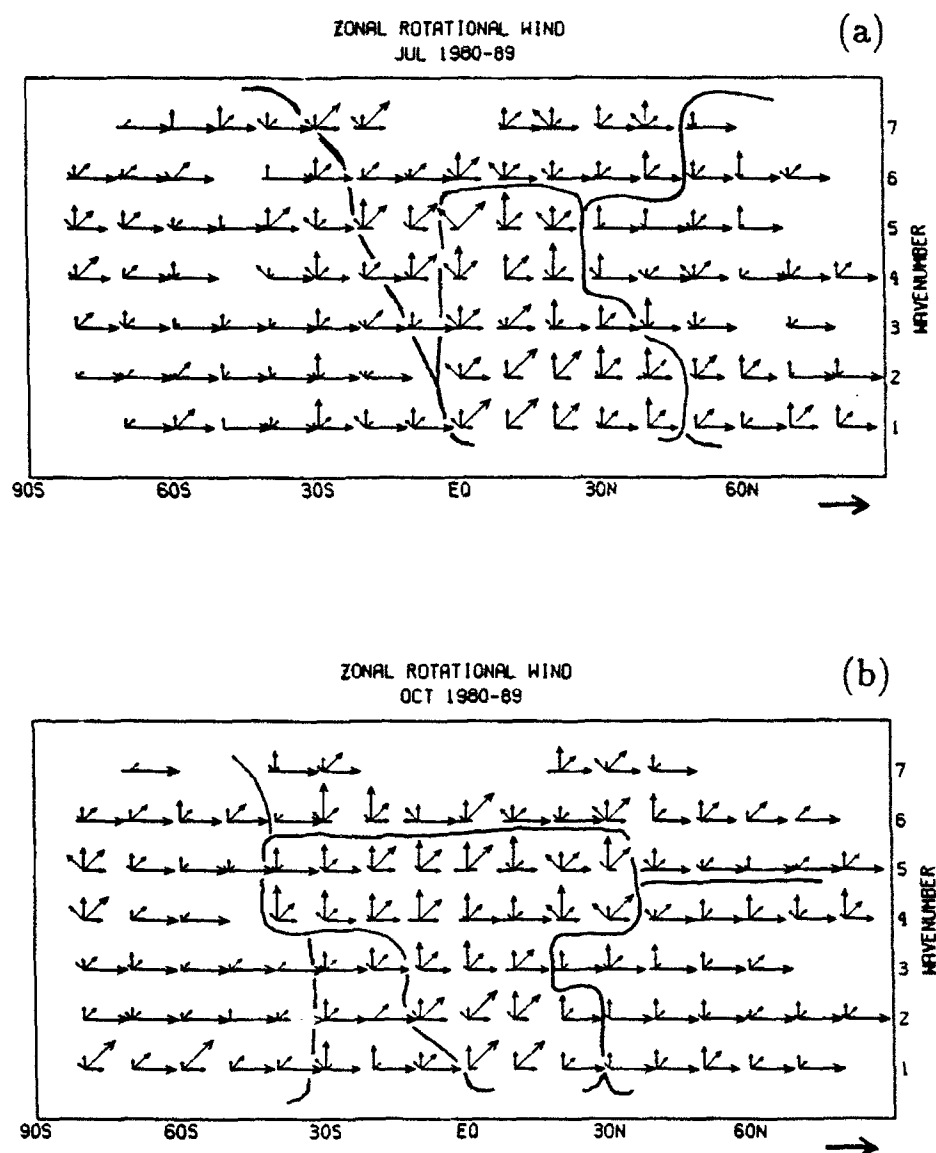


Figure 3.13. Contribution by the first five vertical modes for the zonal rotational wind during (a) July and (b) October 1980-1989 for waves one through seven. Mode representation by arrows described in text. Maximum normalized vector shown in bottom right of each panel.

Recall from Fig. 3.11b that the first seven wavenumbers do not explain at least 75% of the total longitudinal variance for the meridional rotational wind at most latitudes. It is necessary to include at least the first eight, and possibly as many as ten wavenumbers, to achieve the same level of completeness in the representation of the variance. This is expected from the geostrophic approximation.

The most notable mode structure differences for the meridional rotational wind during January (Fig. 3.14a), when compared to the zonal component, are the lack of a significant contribution at the equator, due to the prevalent zonality of the tropical rotational flow, and the strong internal mode contribution in the SH to 30° S for the first six wavenumbers. As with the zonal rotational wind, the external mode dominates outside the tropics, mixed with the second internal (third) mode.

By July (Fig. 3.14b) important contributions from the internal modes have spread to 50° N for wavenumbers one and two and as far as 30° N for wavenumbers three through six. The exception appears to be for wavenumber one, where internal modes appear to remain strong in the tropical NH, and also in the tropical and extratropical SH. The combination of modes one and two found in the SH would indicate a wind profile that continuously increases with height, reaching its maximum value at or above the top layer of the data.

The rotational wind analysis has shown, in summary, that there is a pronounced change in the vertical structure of the rotational wind planetary waves from the tropical internal to the extratropical equivalent barotropic structure. Though this result is not new, the fact that this change takes place for the long waves within $10\text{--}15^{\circ}$ poleward of latitudes of organized convection has not been previously documented. The vertical mode decomposition of zonal divergent wind is discussed next.

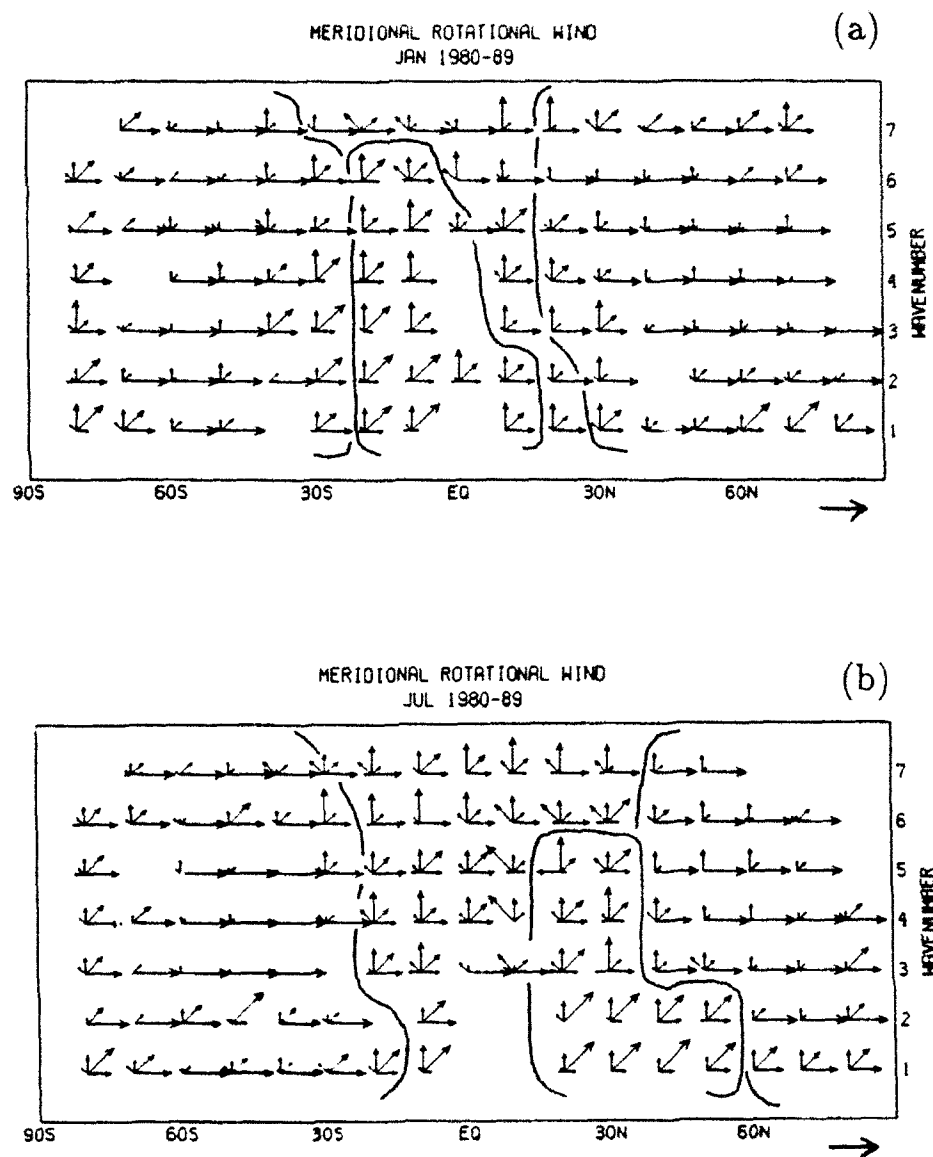


Figure 3.14. Contribution by the first five vertical modes for the meridional rotational wind during (a) January and (b) July 1980-1989 for waves one through seven. Mode representation by arrows described in text. Maximum normalized vector shown in bottom right of each panel.

3.3.3 The Zonal Divergent Wind

The longitudinal-vertical overturnings of the Walker circulation are reflected in this wind component.

The most readily apparent difference between the vertical structure of the rotational and divergent winds is the contribution made by the internal modes, as seen in January (see Fig. 3.15a), particularly the higher internal modes, indicating the existence of shallower layers at lower altitudes. The changes in the vertical structure of the divergent wind are more subtle than those of the rotational wind and they are more readily apparent when examining the plots on a wavenumber by wavenumber basis. Wavenumber two in the SH subtropics is dominated by mode two during January, but shifts to a near equal contribution by all modes during April (not shown), and a return to a strong mode two during July (Fig. 3.15b). The NH response is almost seasonally mirrored, with modes one through three strongest in January and modes two and three strongest during July.

At wavenumber three the tropics from 10° N to 10° S exhibit a strong mode five response during all months. This annual consistency in the tropics also holds for a mode two/four combination at wavenumber four, whereas a strong mode five response is apparent in this region for wavenumbers five through seven (except during July where it is found in wavenumbers five and six).

3.3.4 The Meridional Divergent Wind

As with the zonal divergent wind, the meridional divergent wind can be almost totally explained by looking at the first seven wavenumbers. The meridional divergent wind has a strong zonally averaged component, the Hadley cell, which is not included in the following discussion.

Beginning with wavenumber one, the tropics, between 10° N and 10° S, and SH show little change throughout the year with modes two and five playing the major

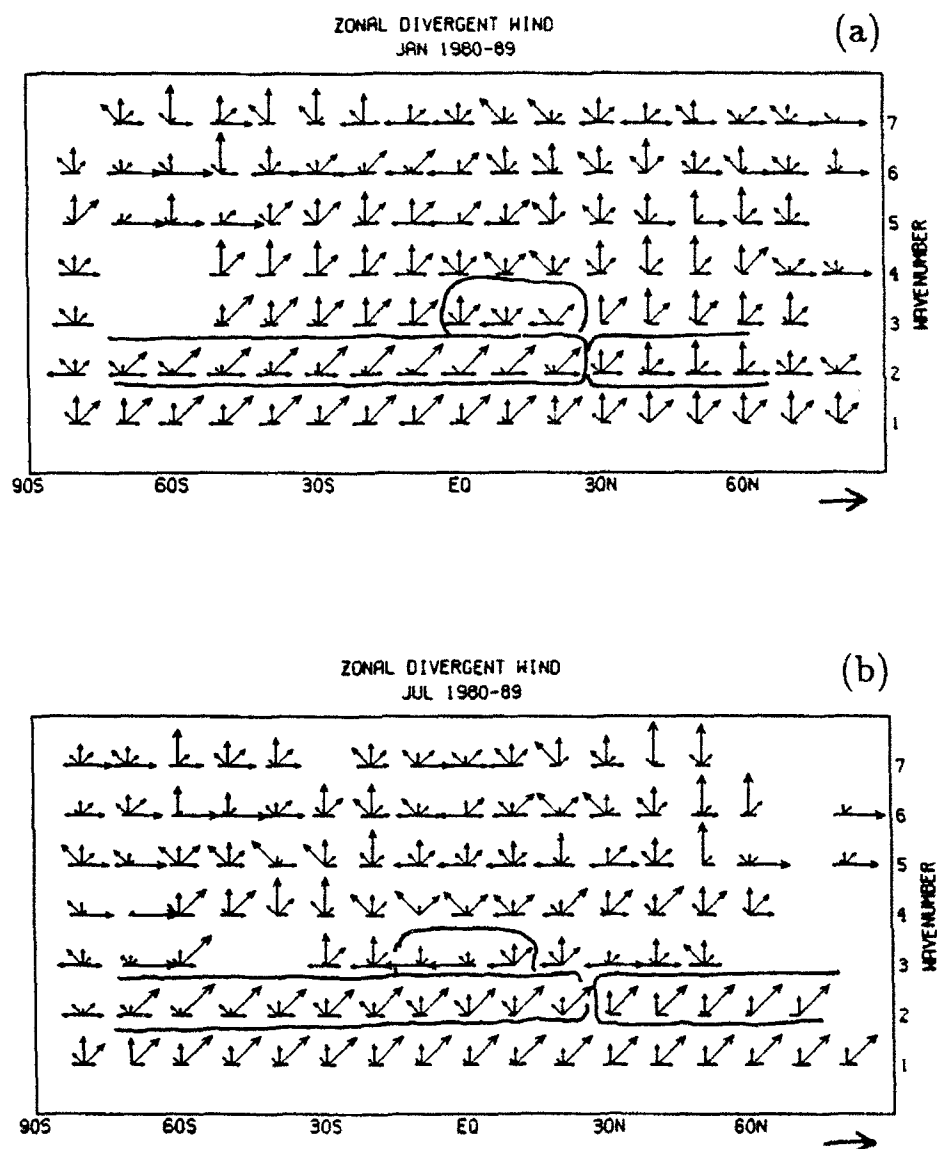


Figure 3.15. Contribution by the first five vertical modes for the zonal divergent wind during (a) January and (b) July 1980-1989 for waves one through seven. Mode representation by arrows described in text. Maximum normalized vector shown in bottom right of each panel.

role (Fig. 3.16). In the NH, mid-latitudes show a mode two/three combination during January which slowly becomes a dominant mode two by October.

Wavenumber two echos wavenumber one in the tropics and SH during January with modes two and five providing the largest contributions. However, during July, mode five weakens and mode three dominates. The NH undergoes a transition from a near equal contribution by modes one, two, and three, during the first half of the year, to an almost exclusive mode two/three combination for July.

The third mode gives dominant contributions for wavenumber three throughout most of the year in the NH, whereas mode five has this dominant annual role in the tropics, shared at times by modes two and three.

The above results indicate, that in general, the Walker circulation, as represented by planetary waves one and two in zonal divergent wind in the tropics, exhibits a deeper vertical structure than does the meridional divergent wind. This structure extends into higher latitudes without the pronounced meridional changes apparent in the structure of the meridional divergent component close to the equator. The above discussion presented contributions by different vertical modes normalized by the total vertical variance for each wavenumber. Therefore, no description was given of the actual magnitude of the contributions by different modes. This is done next, focusing on the main contributors to the variance of the rotational zonal wind (modes one, two, and three) and the meridional and zonal divergent wind component (modes two through five) to the planetary waves.

3.3.5 Seasonal March of Selected Waves and Modes

The discussion in the previous sections has emphasized differences in the vertical structure of the tropics and the extratropics. In spite of these differences, a linkage between the reversing divergent tropical circulations and the extratropical equivalent barotropic rotational flow is apparent in the seasonal flow evolution.

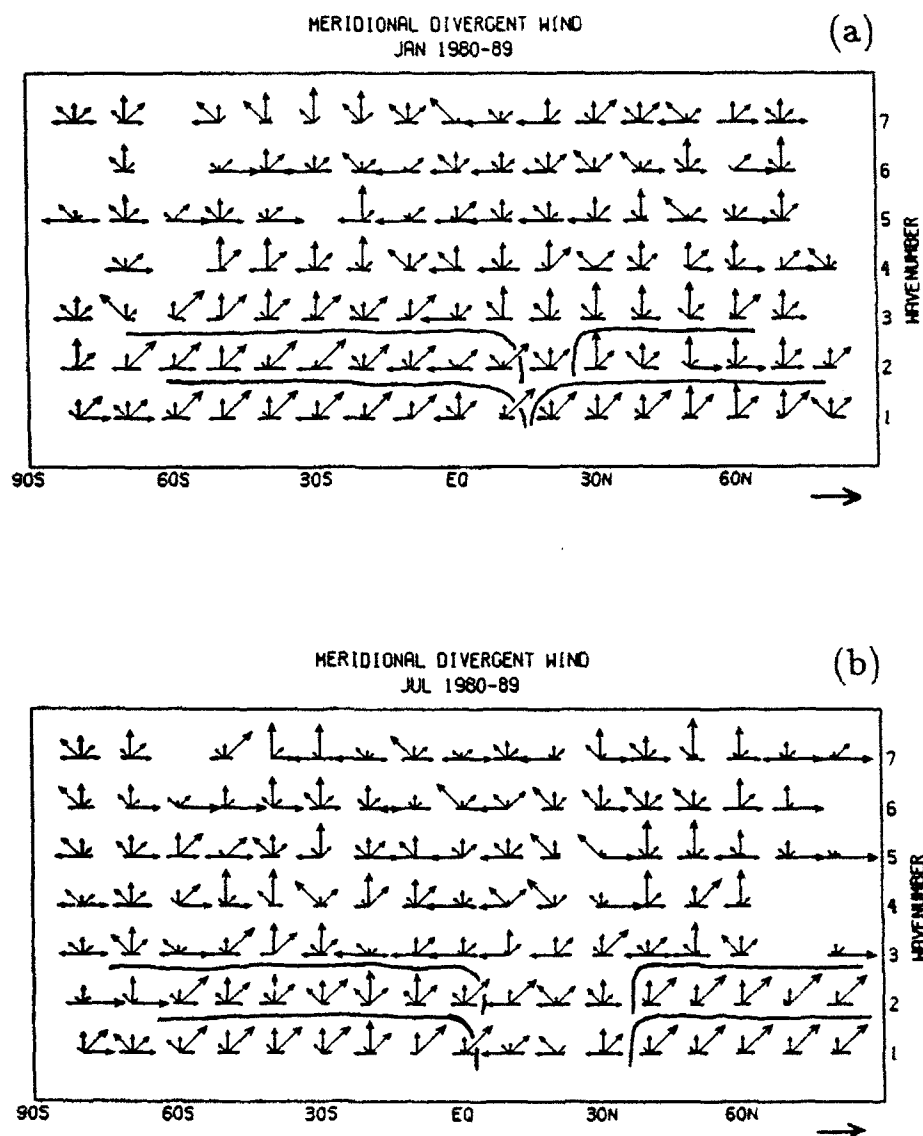


Figure 3.16. Contribution by the first five vertical modes for the meridional divergent wind during (a) January and (b) July 1980-1989 for waves one through seven. Mode representation by arrows described in text. Maximum normalized vector shown in bottom right of each panel.

Figure 3.17 shows large contributions from waves one (a,b,c) and two (d,e,f) in the extratropics with an equivalent barotropic structure, as discussed before. Panels (g) and (i) also clearly show an important contribution by zonal wave three to the NH winter subtropical zonal rotational wave field.

Inspection of Fig. 3.18 reveals marked contributions to the meridional divergent wind by waves two and three in the internal modes during NH winter. The meridional overturnings associated with the three convective maxima located in the SH tropics in January produce a wave three meridional divergent pattern modulated with a wave two which maximizes in the NH subtropics. This is reflected in the Dec-Jan maxima of Fig. 3.18e and h. During NH summer, the main contributions to the meridional divergent wind are seen in waves one and two (maximizing in July) in response to the Asian and North American monsoonal circulations. At the same time, a wave one response is seen in the subtropical jet of the SH. These features are easily interpreted considering that the release of latent heat in the tropics is compensated by the adiabatic cooling of rising motions. The rising air results in the divergent meridional overturning in the Hadley cell and wave components. Though the link between the Hadley circulation and the zonally-averaged zonal wind has been extensively discussed in the literature, the link between the divergent wave meridional overturnings and wave patterns in the extratropics has received less attention. At least two mechanisms may be involved to explain this link. Sardeshmukh and Hoskins (1988) have argued that the advection of vorticity by the meridional divergent wind may produce a Rossby wave source. Nevertheless, they emphasize that the resulting wave train would be relatively insensitive to the longitudinal location of the tropical heating. Another possibility is that the local Hadley cell causes local zonal wind accelerations similar to those of the zonally-averaged circulations.

Further inspection of Fig. 3.18 reveals that the contributions by the second mode

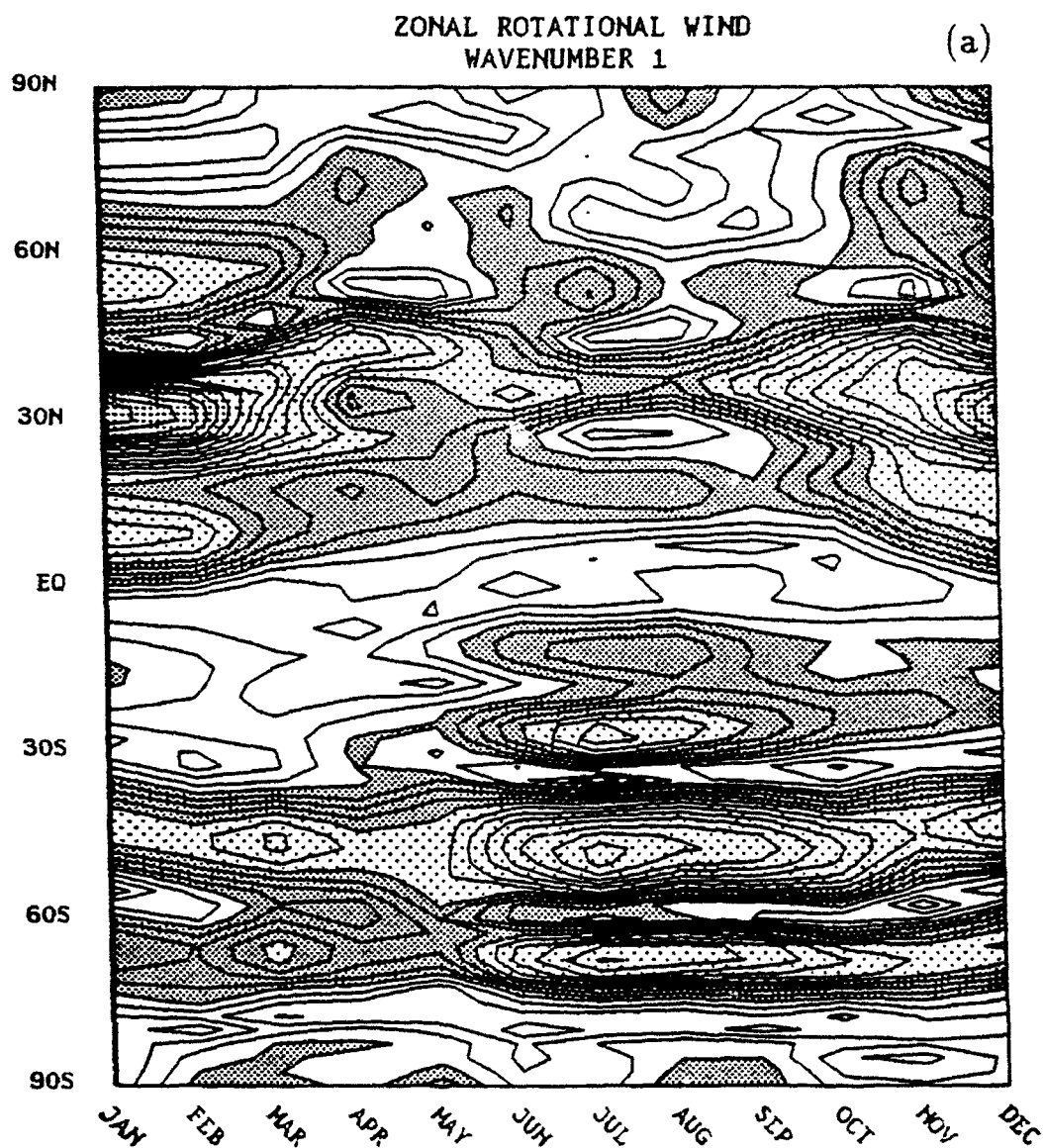
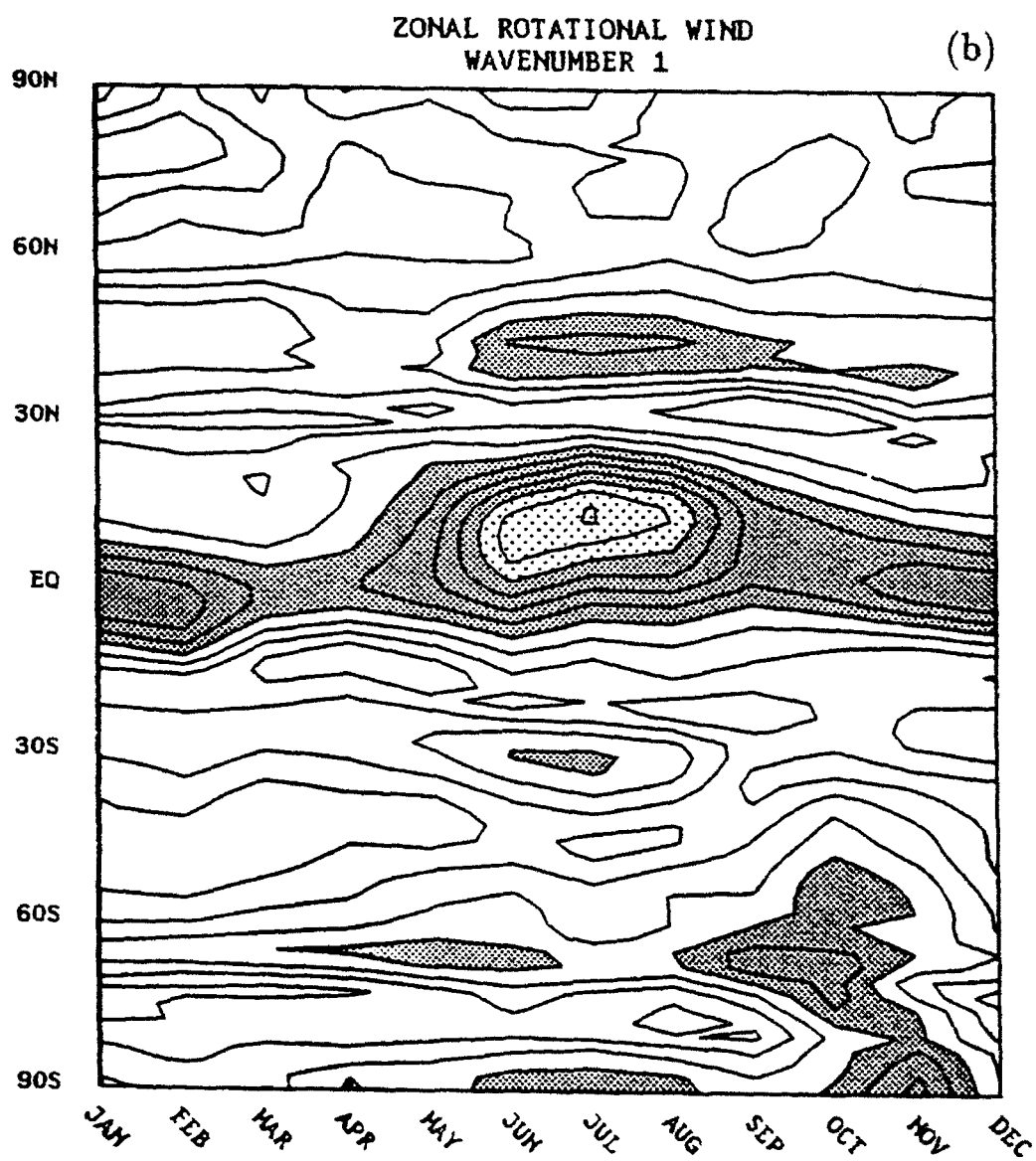
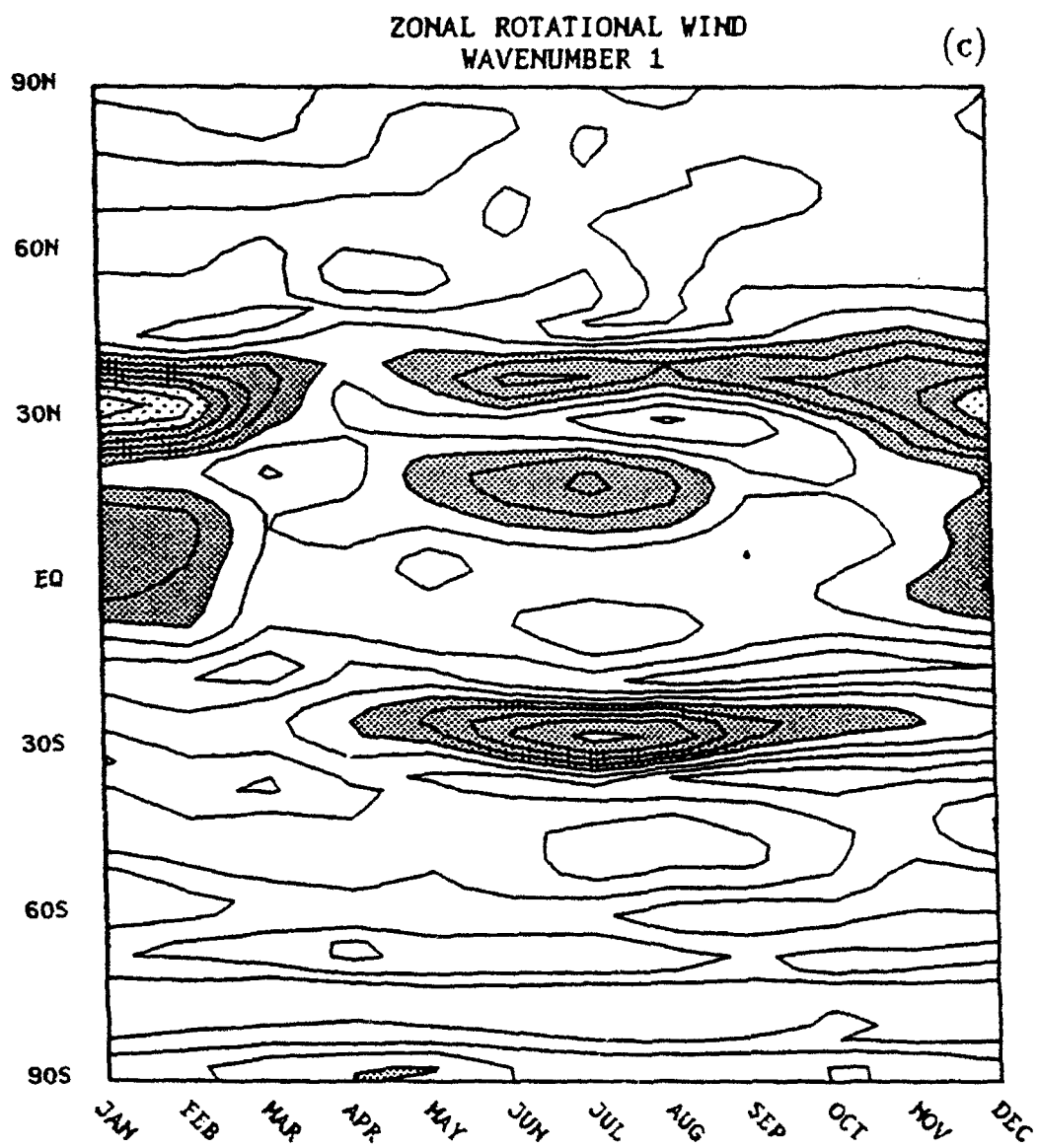
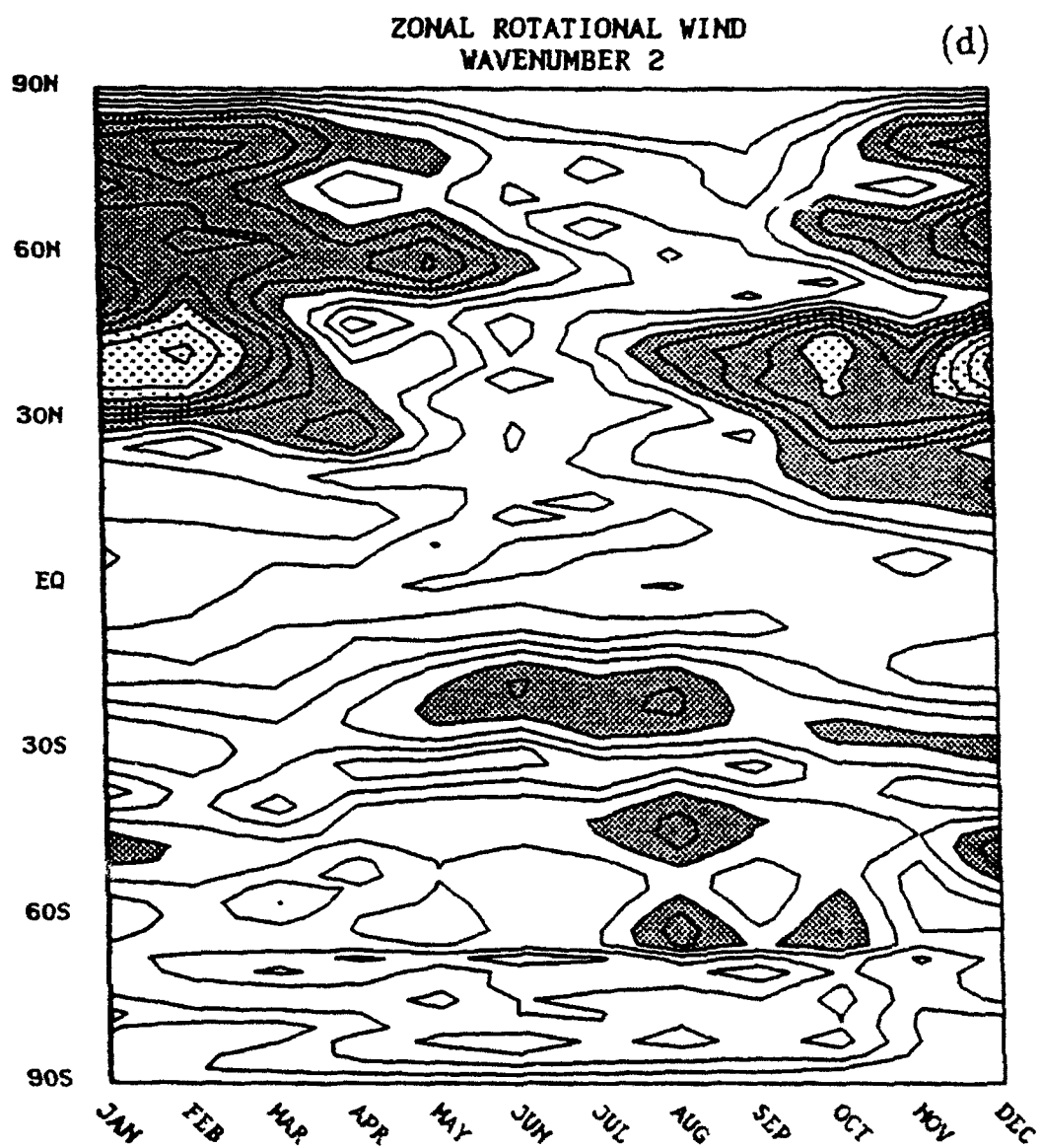
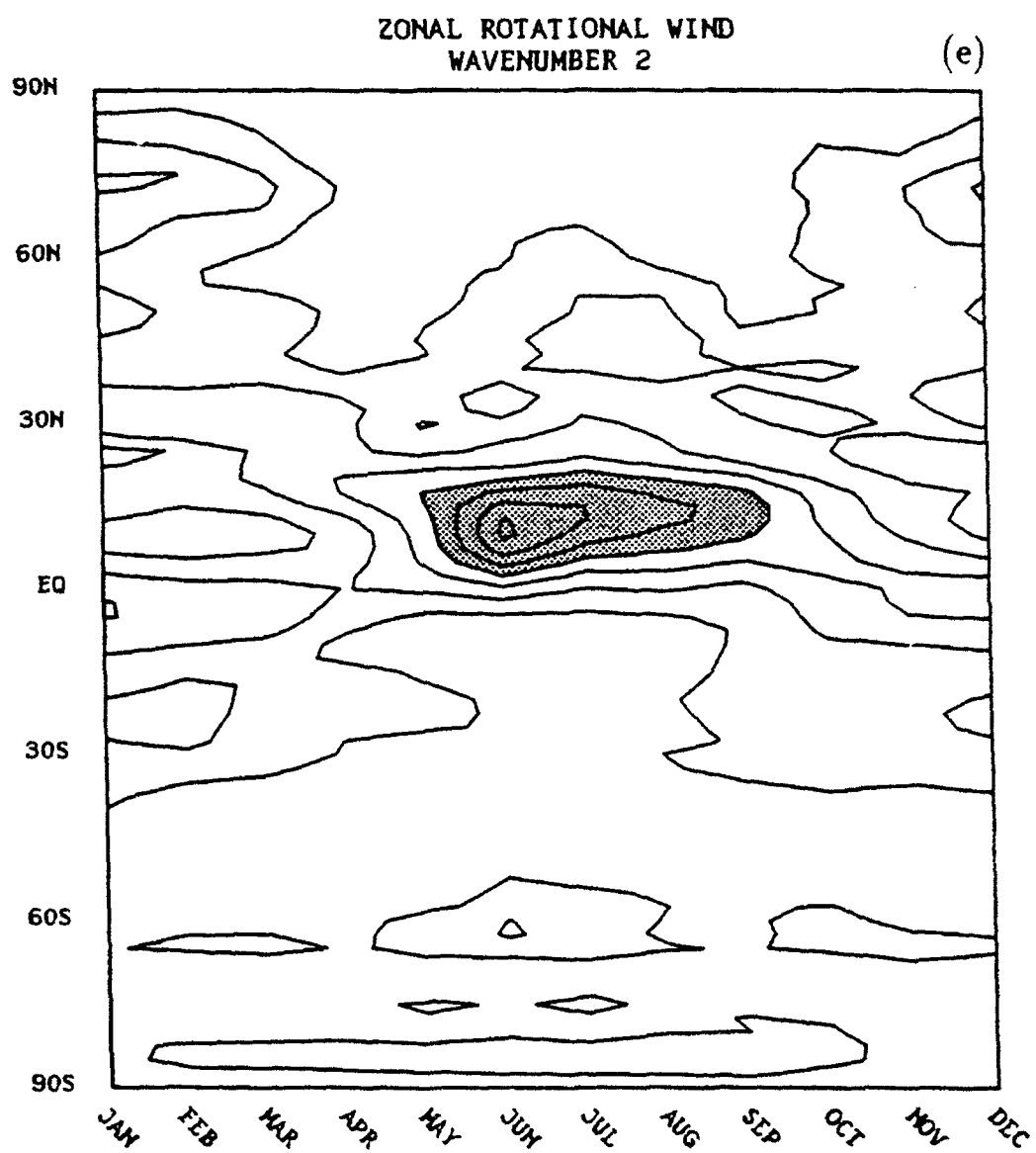


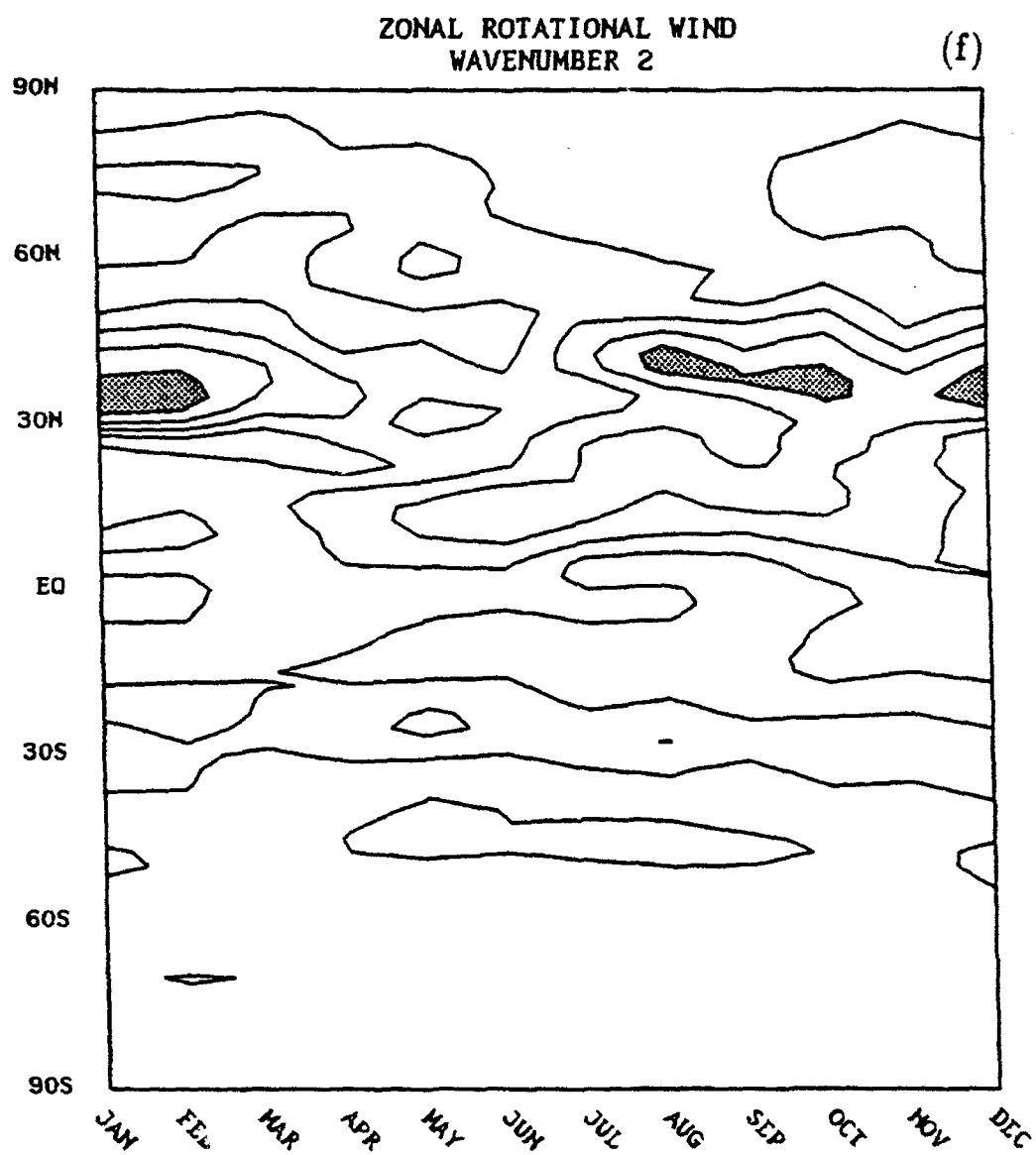
Figure 3.17. Latitude/time cross-section of the vertical modes for long wave contributions to the zonal rotational wind. The first three modes for wave number one are shown in (a), (b), and (c), for wavenumber two in (d), (e), and (f), and lastly for wavenumber three in (g), (h), and (i). Contour interval is 0.5 m s^{-1} . Dark shading represents speed from $2\text{--}4 \text{ m s}^{-1}$, medium dots are for speeds between $4\text{--}8 \text{ m s}^{-1}$, and light dots are for speeds ranging from $8\text{--}12 \text{ m s}^{-1}$. Regions with speeds greater than 12 m s^{-1} are clear.

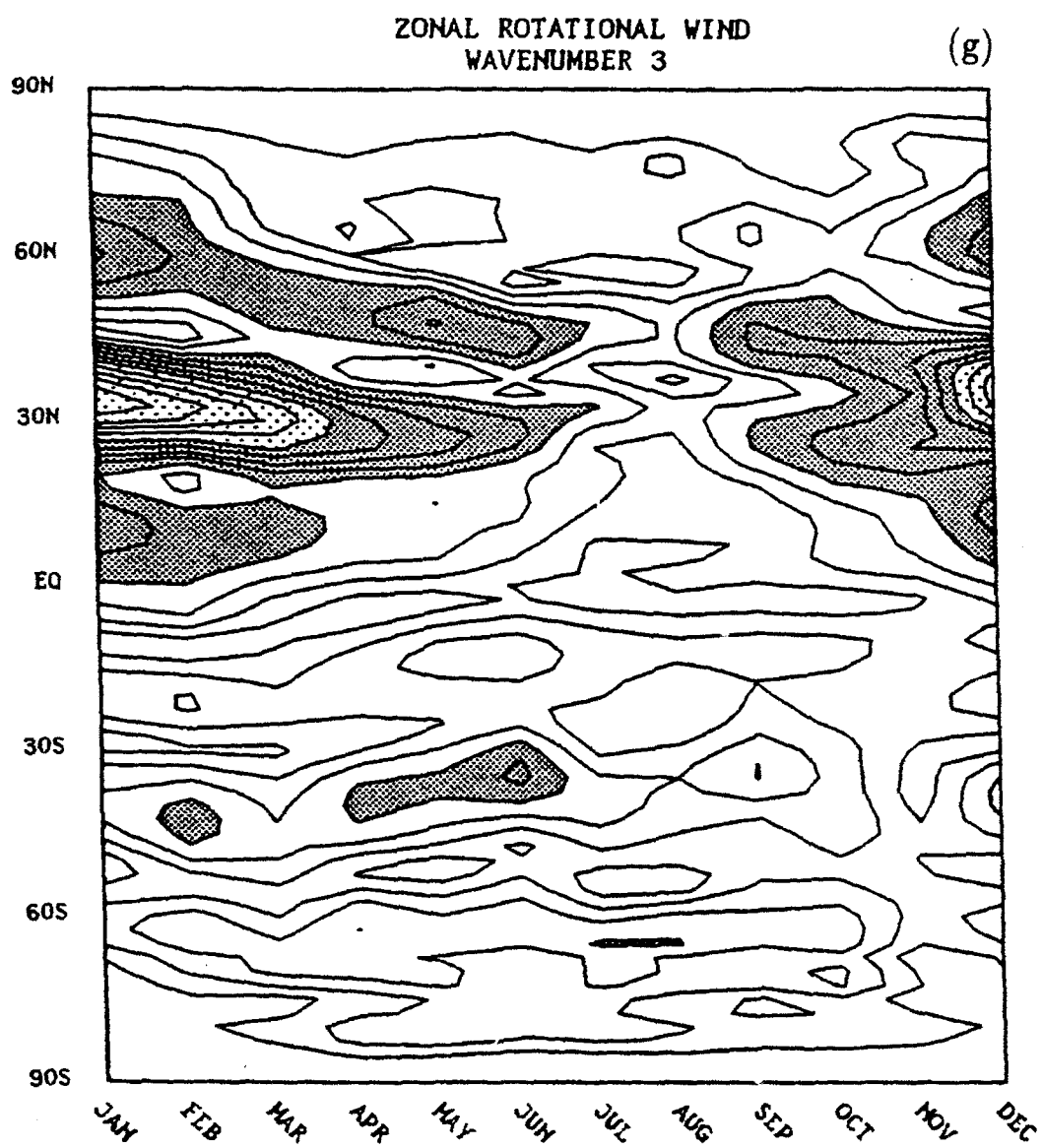


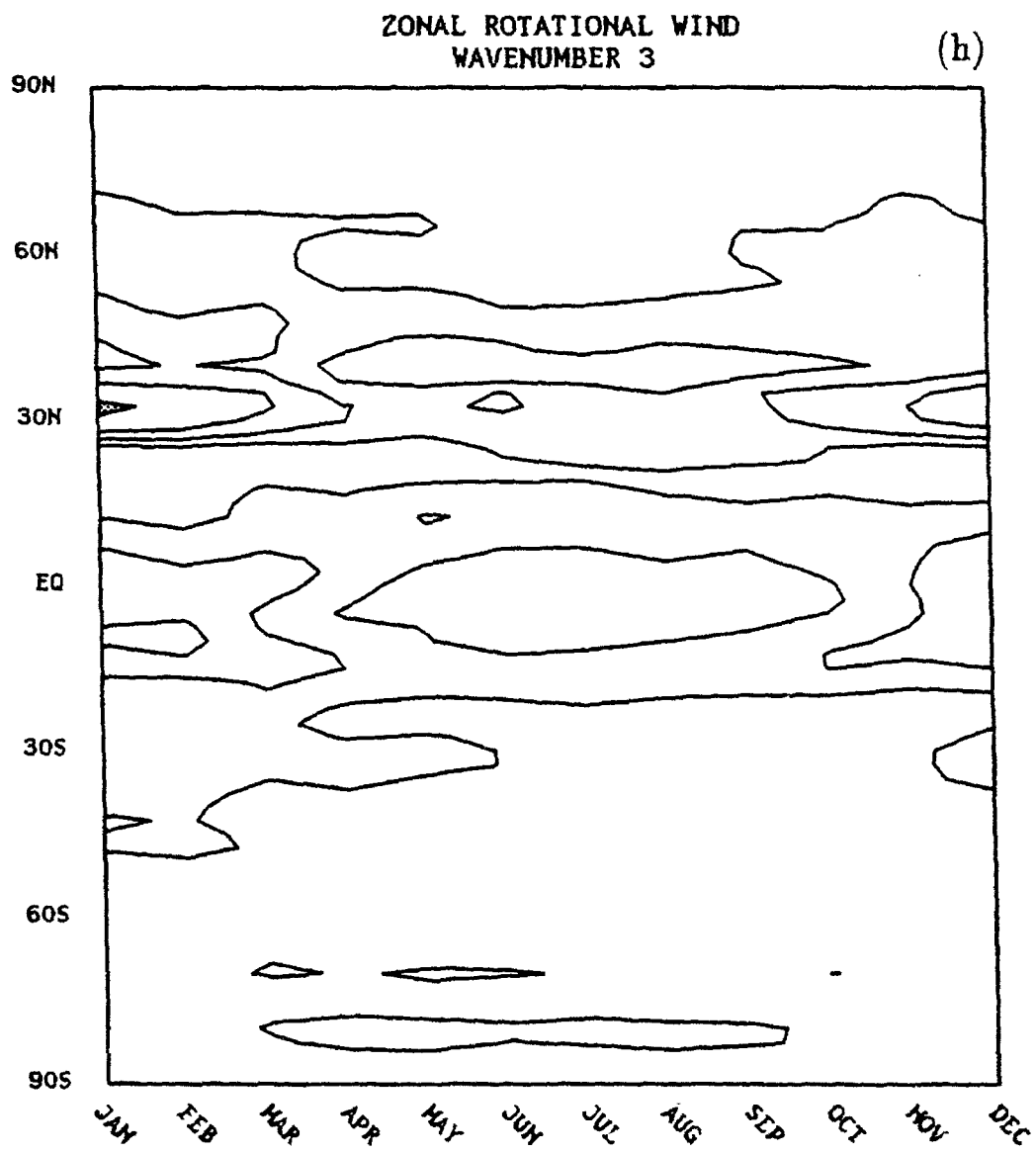






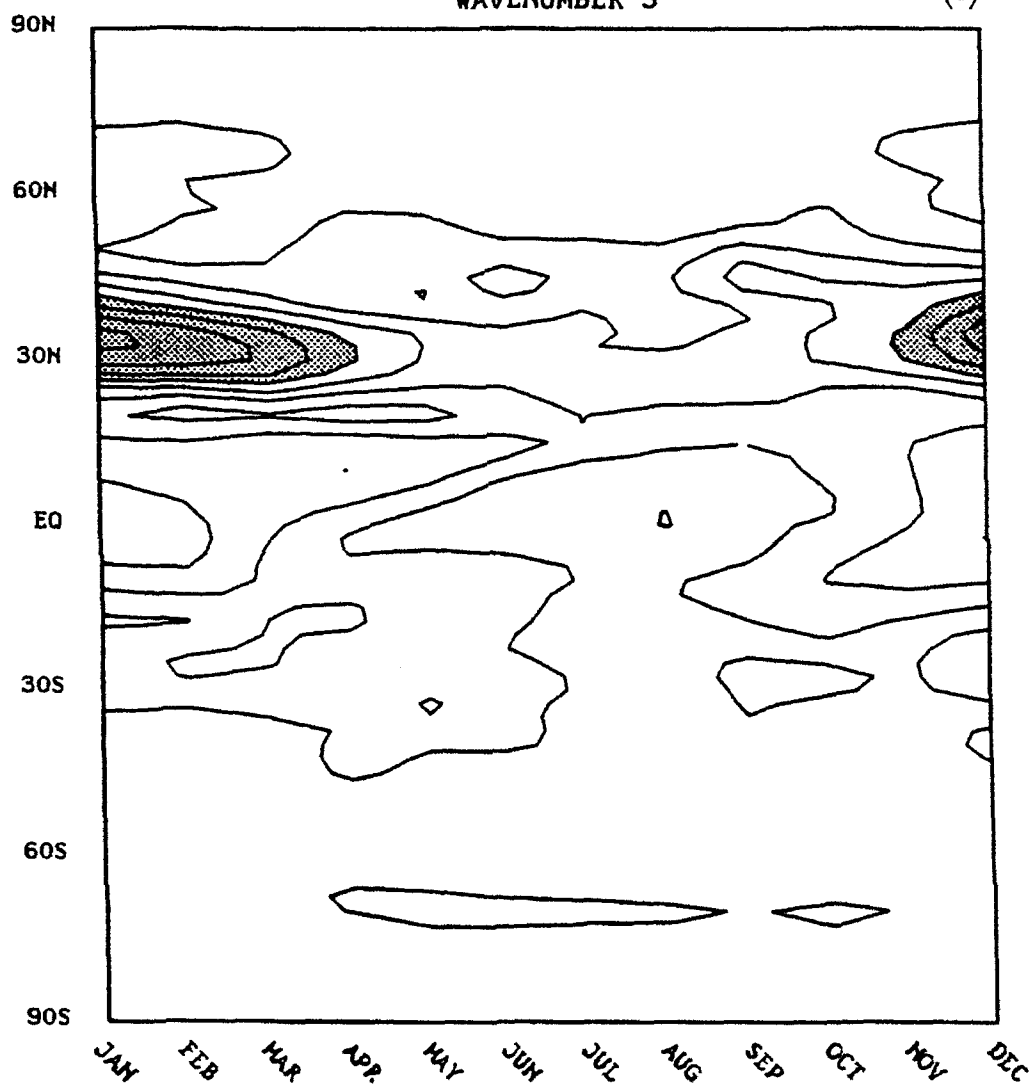






ZONAL ROTATIONAL WIND
WAVENUMBER 3

(i)



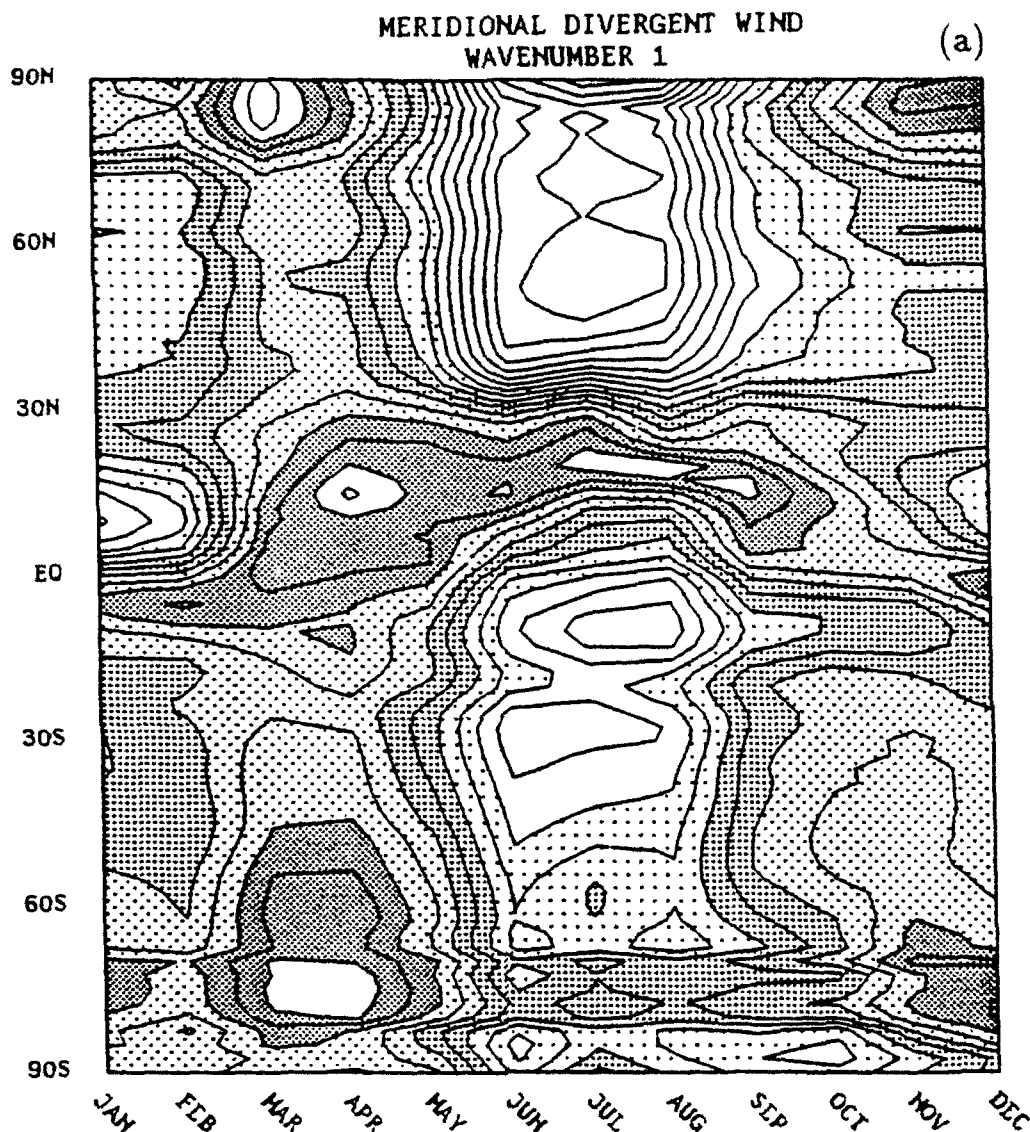
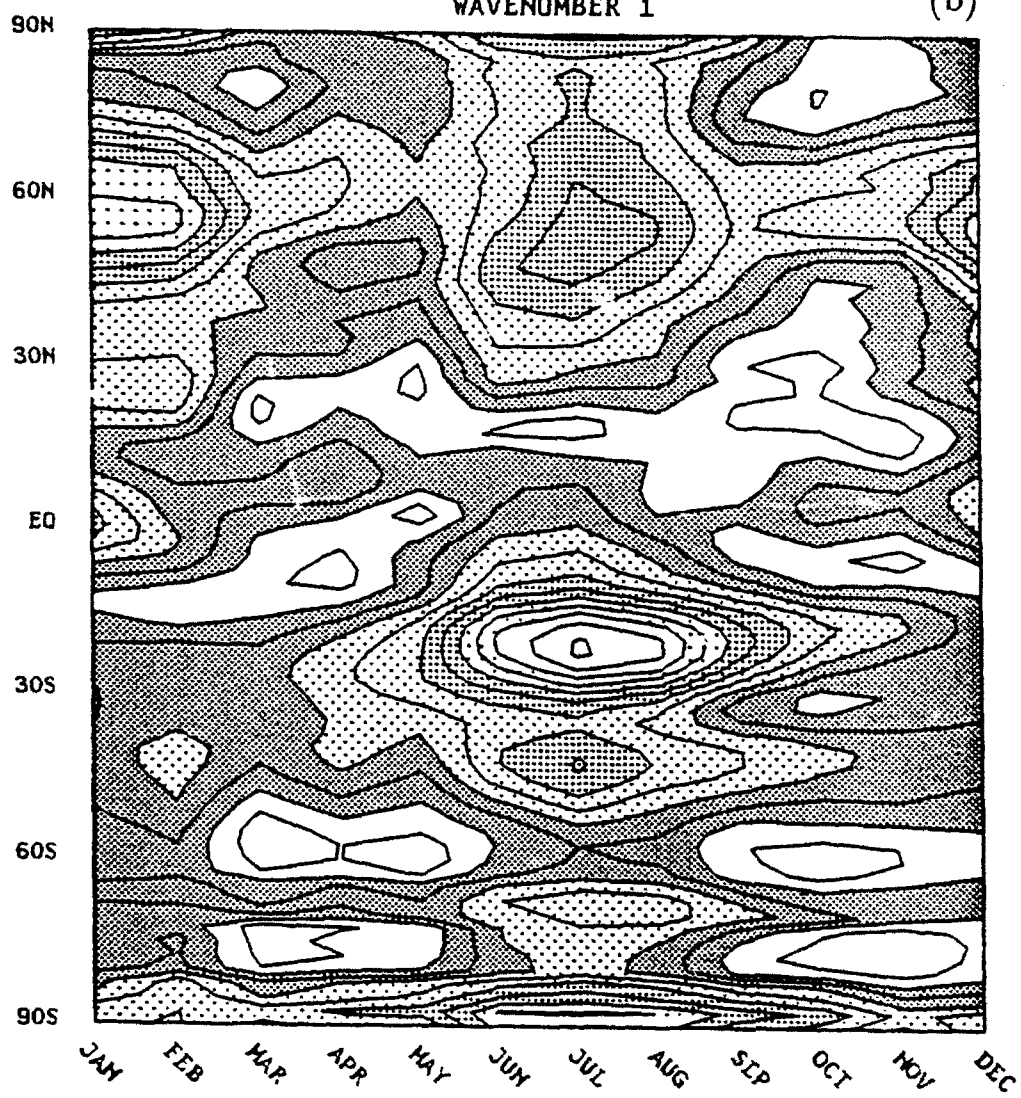
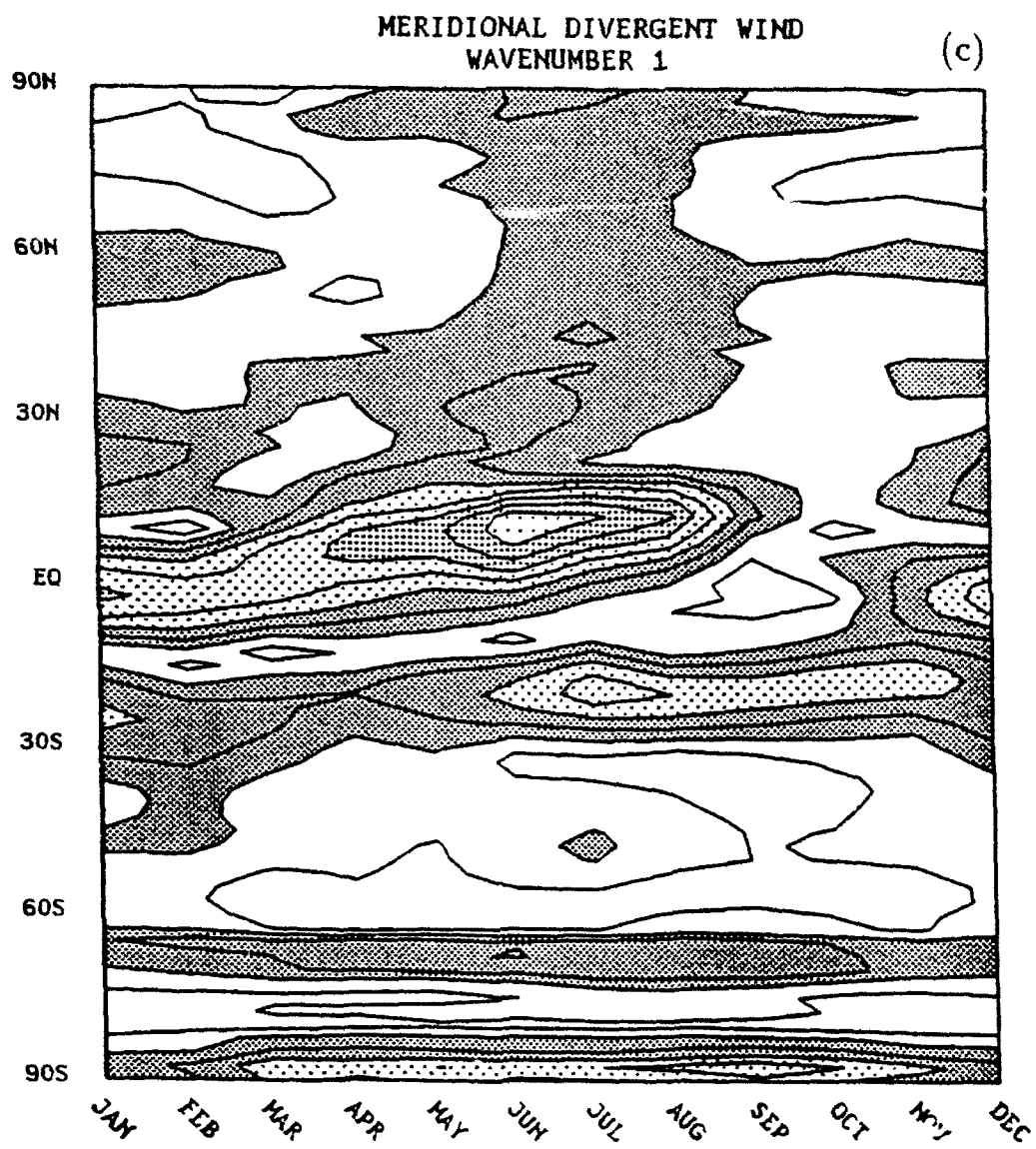


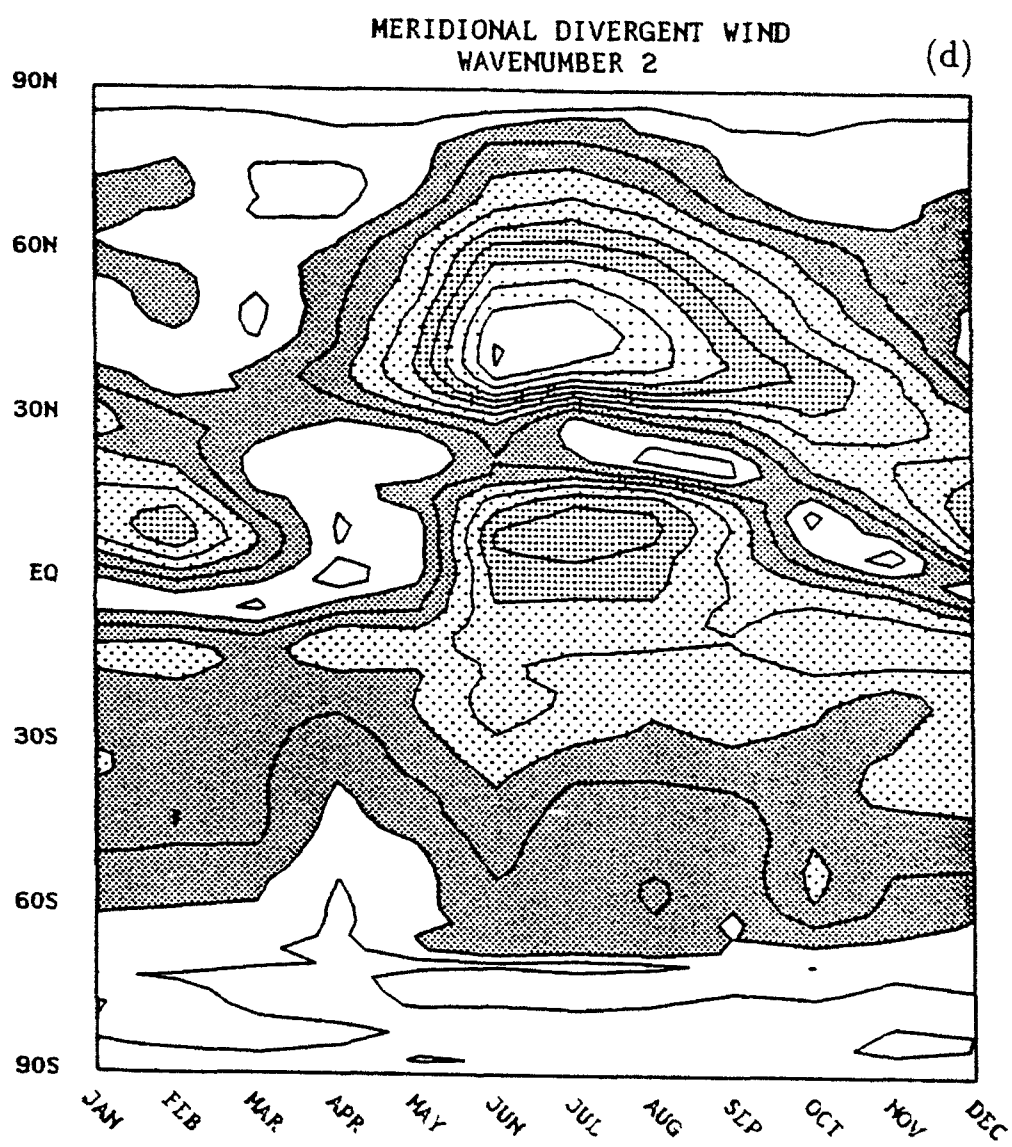
Figure 3.18. Latitude/time cross-section of the vertical modes for long wave contributions to the meridional divergent wind. The internal modes two, three, and five for wavenumber one are shown in (a), (b), and (c), for wavenumber two in (d), (e), and (f), and lastly for wavenumber three in (g), (h), and (i). Contour interval is 0.05 m s^{-1} . Dark shading represents speed from $0.1\text{--}0.2 \text{ m s}^{-1}$, medium dots are for speeds between $0.2\text{--}0.4 \text{ m s}^{-1}$, heavy dots delineate speed of $0.3\text{--}0.4 \text{ m s}^{-1}$, and light dots are for speeds ranging from $0.4\text{--}0.5 \text{ m s}^{-1}$. Regions with speeds greater than 0.5 m s^{-1} are clear.

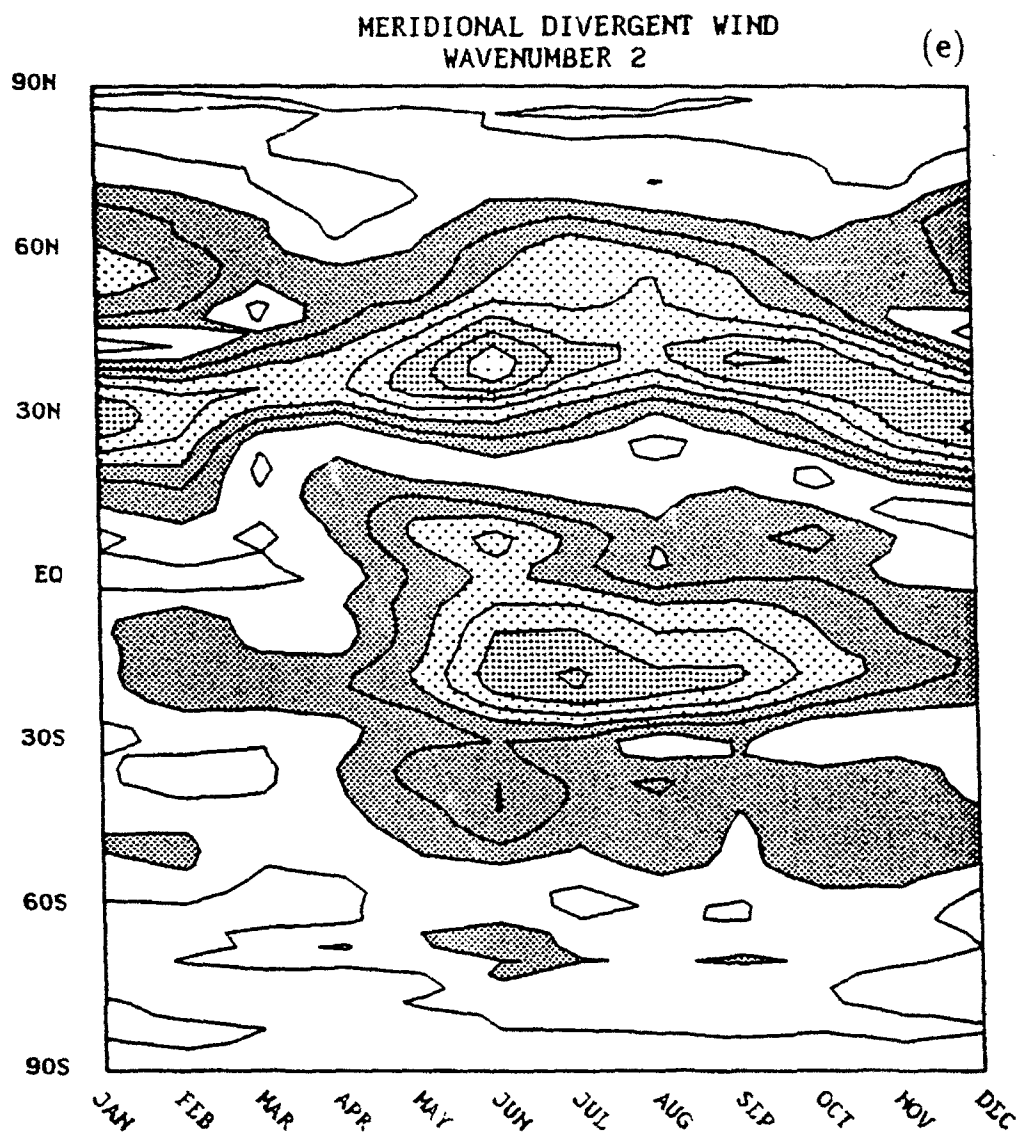
MERIDIONAL DIVERGENT WIND
WAVENUMBER 1

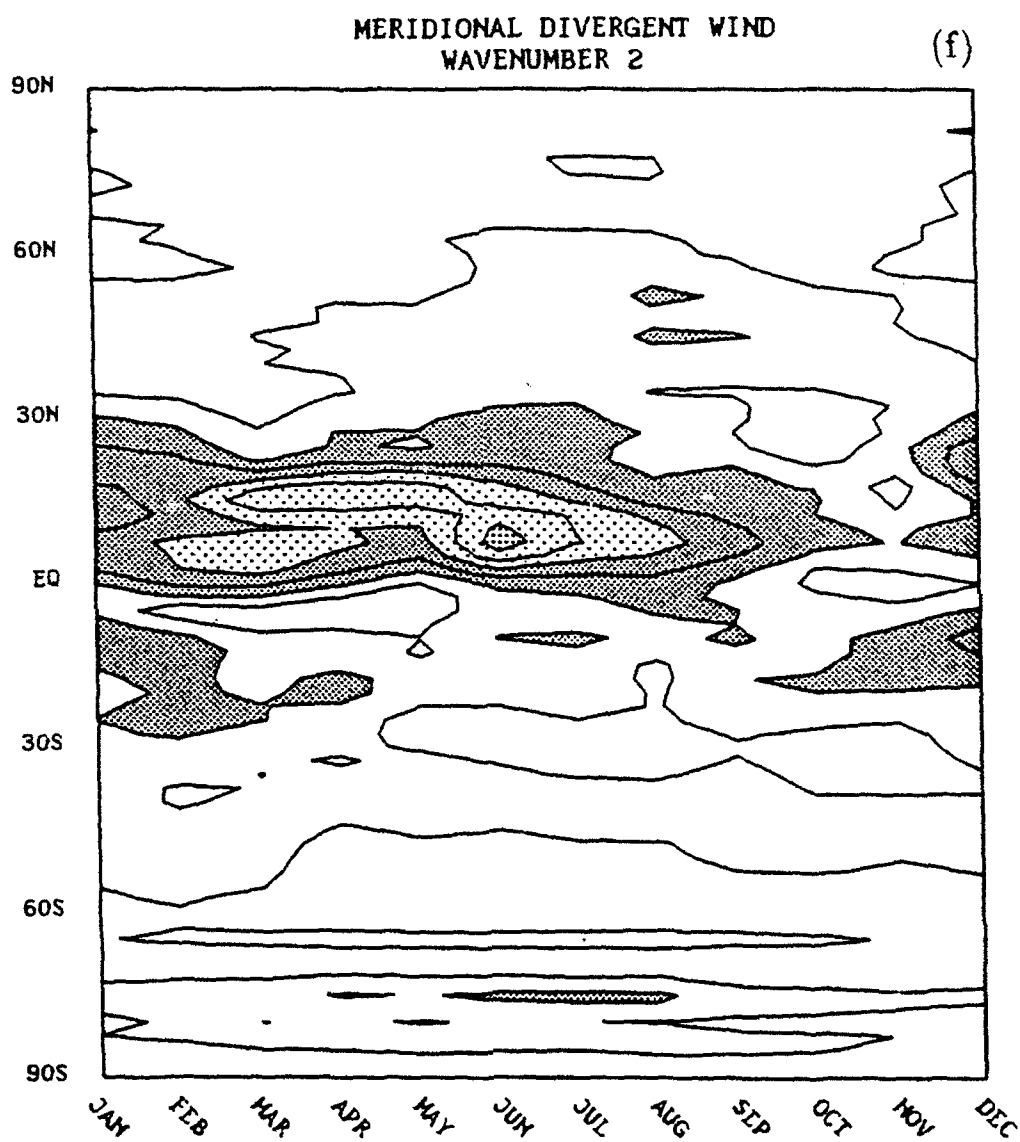
(b)





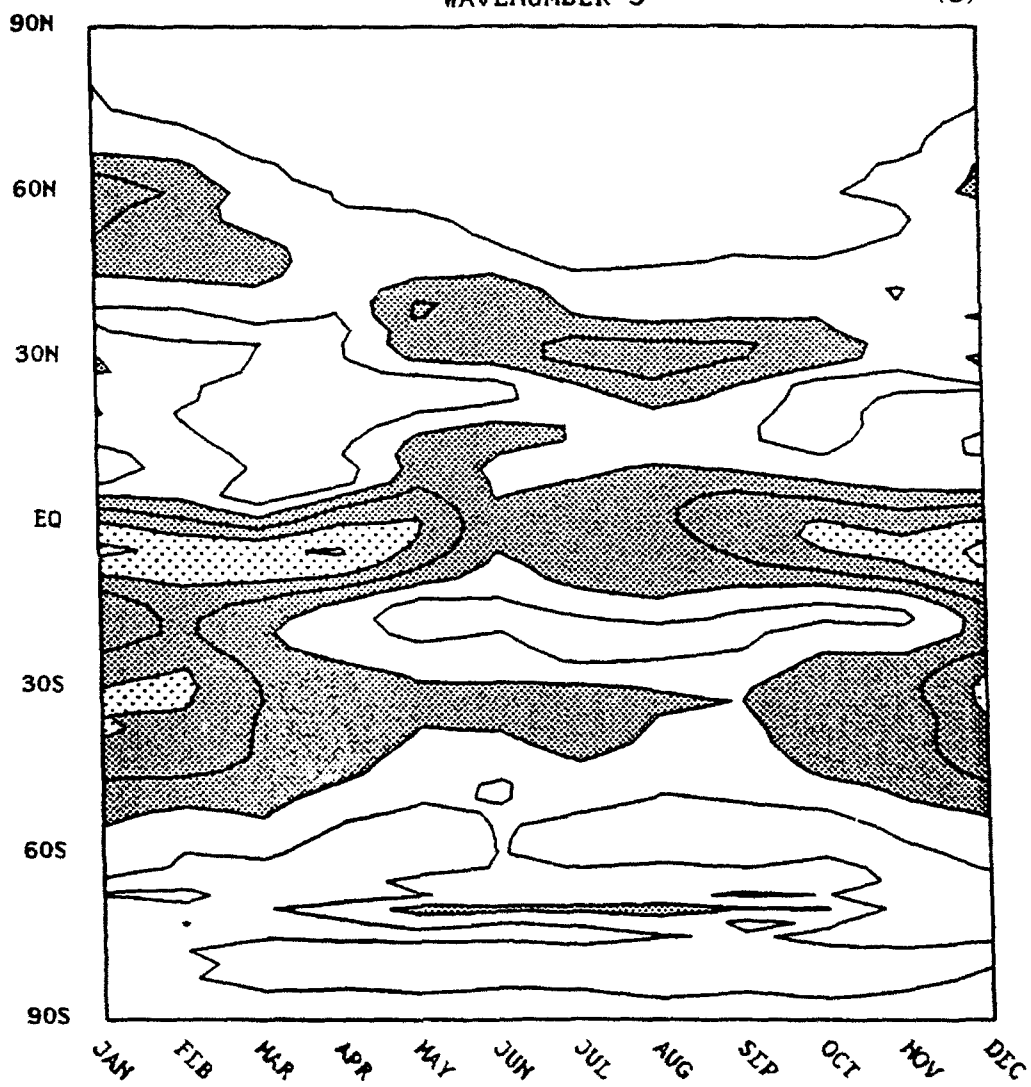






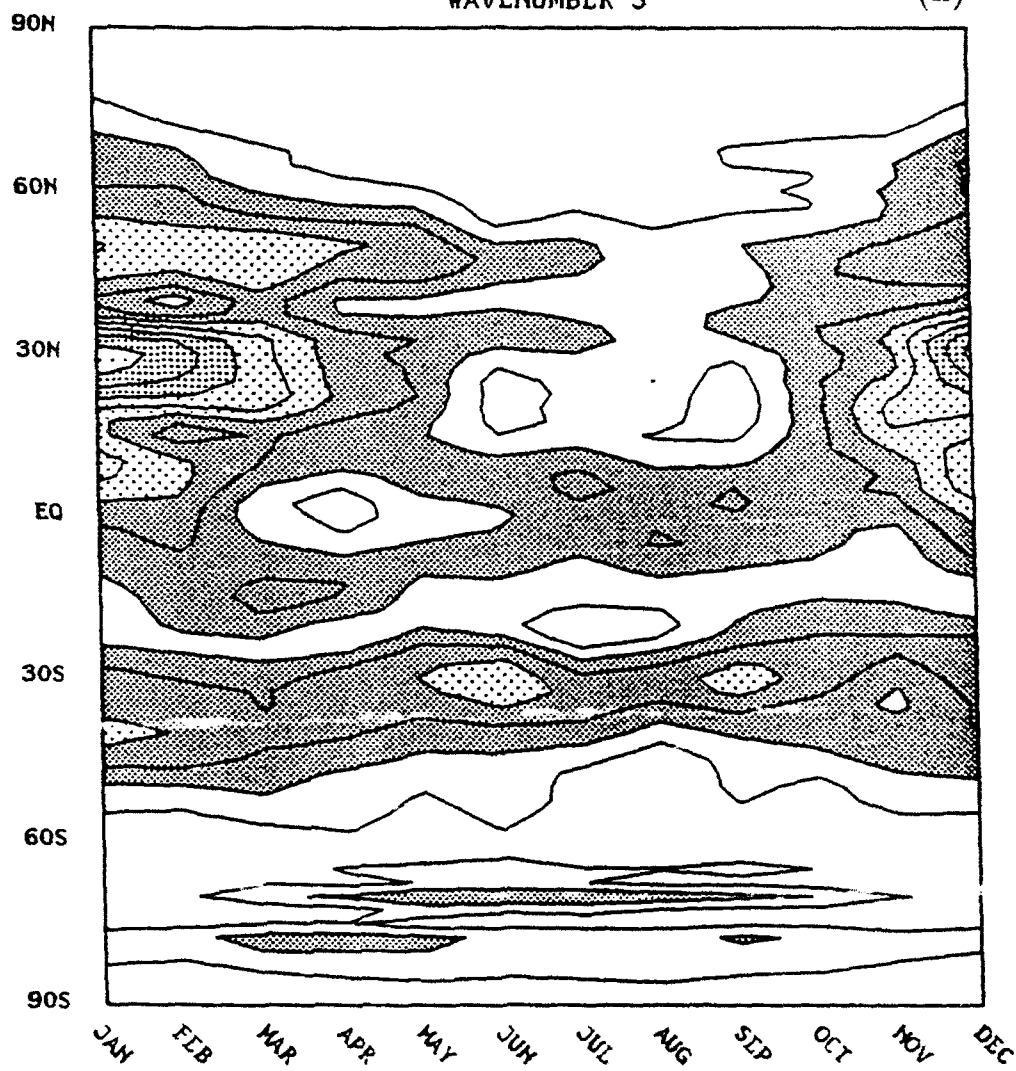
MERIDIONAL DIVERGENT WIND
WAVENUMBER 3

(g)



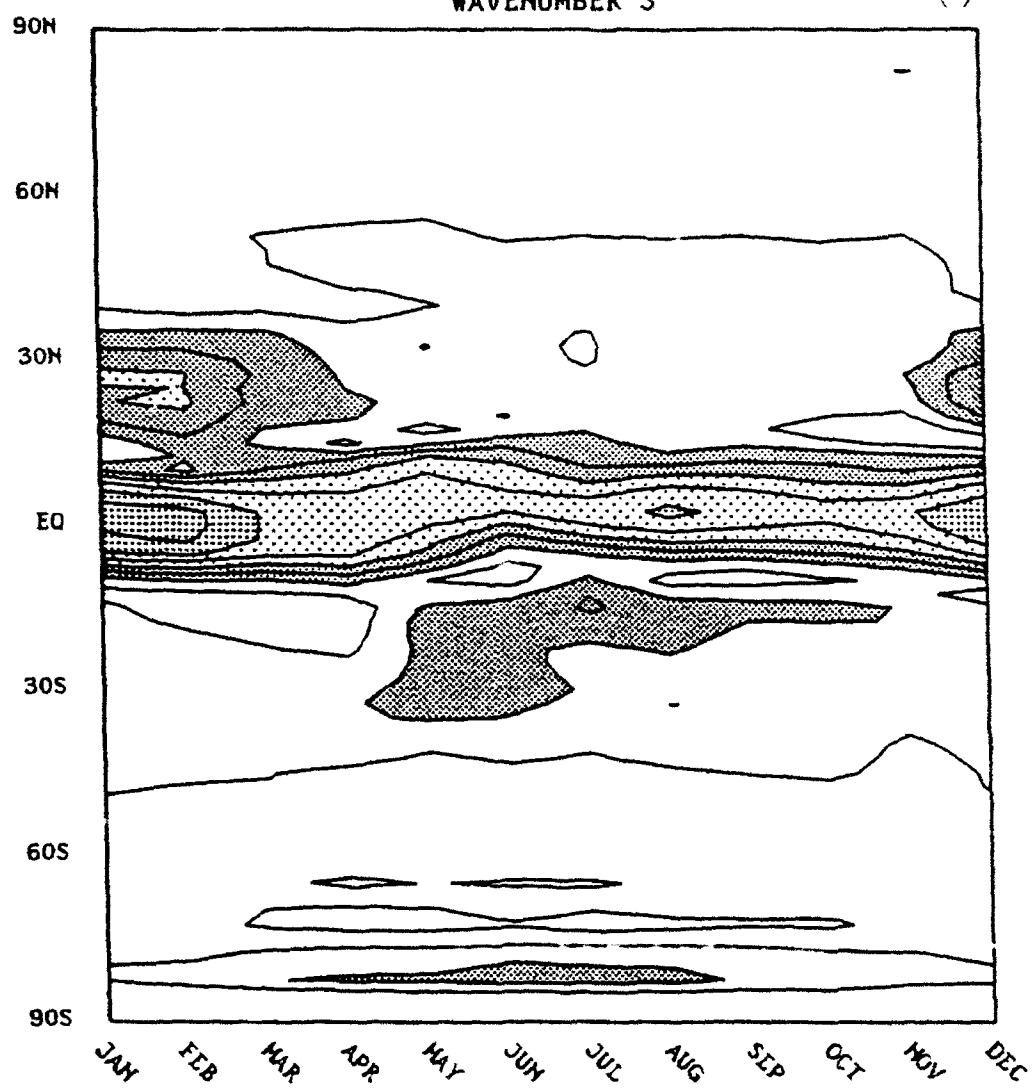
MERIDIONAL DIVERGENT WIND
WAVENUMBER 3

(h)



MERIDIONAL DIVERGENT WIND
WAVENUMBER 3

(i)



to the meridional divergent wind are mostly confined to the summer hemisphere for wave two, three during NH/SH summer. On the other hand, contributions by the third mode are more symmetric about the equator, with maximum values found in the winter hemisphere (Fig. 3.18b,h). Important contributions to the long waves are also given by mode five as seen in Fig. 3.18c,f,i.

Figure 3.19 shows the vertical mode decomposition of the longitudinal divergent overturning described by the long waves. This figure indicates that the NH summer exhibits dominant waves one and two, while the SH summer exhibits strong wave three components in the zonal divergent wind. This may also be inferred from Fig. 3.3. Maximum contributions to the longitudinal overturnings by the deeper vertical modes (internal modes two and three) maximize close to 30° latitude. This is different from what is observed for the meridional wind component, which shows relative maxima close to the equator (Fig. 3.19d,g). The different vertical structures for the zonal and meridional divergent wind components suggest lack of horizontal isotropy on the divergent circulations induced by latent heat release.

3.4 Model Response to Tropical Heating

The extent to which observed extratropical wave patterns result from the tropical heating is examined next through the use of linear and nonlinear numerical models. The previous discussion indicates that the minimum vertical resolution capable of describing the seasonal evolution should contain at least three vertical levels. It has already been shown that the first three modes contain most of the vertical structure, therefore, the three levels are chosen to capture features where these modes maximize. As a result, Paegle's (1989) primitive equation (PE) model is run with three vertical levels centered at $\sigma = 0.2, 0.5$, and 0.8 . The PE model forcing is accomplished by using a parabolic heating profile with the peak heating rate fixed

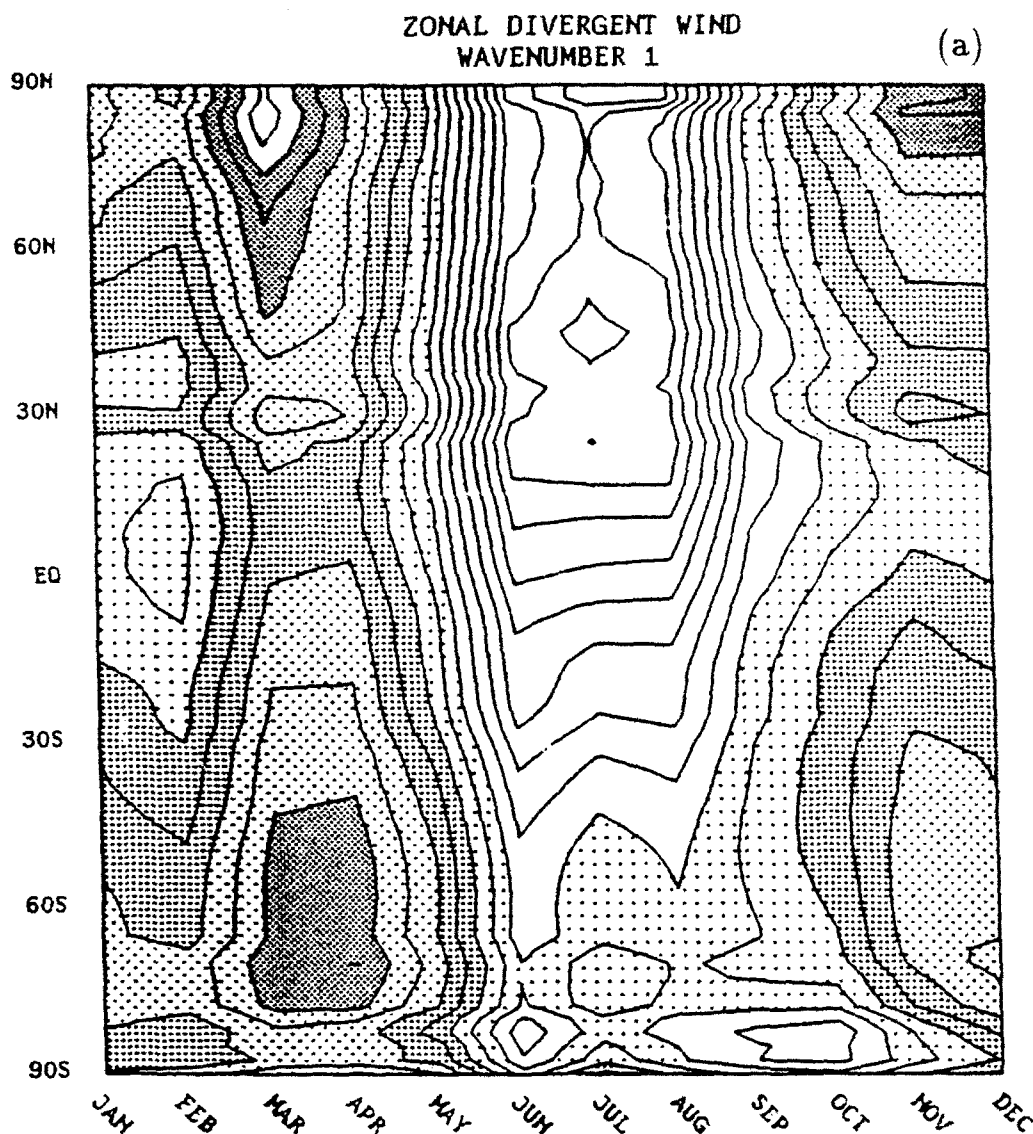
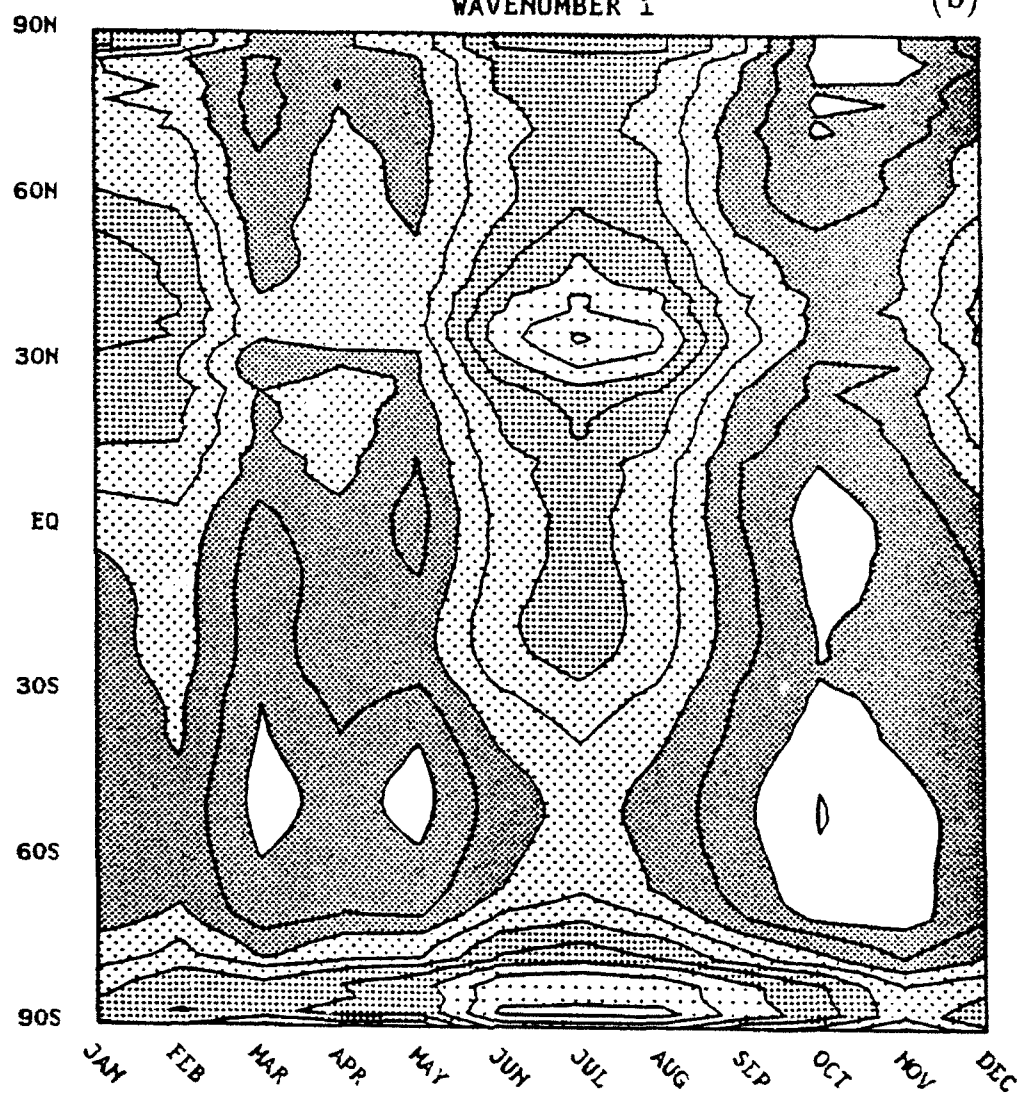
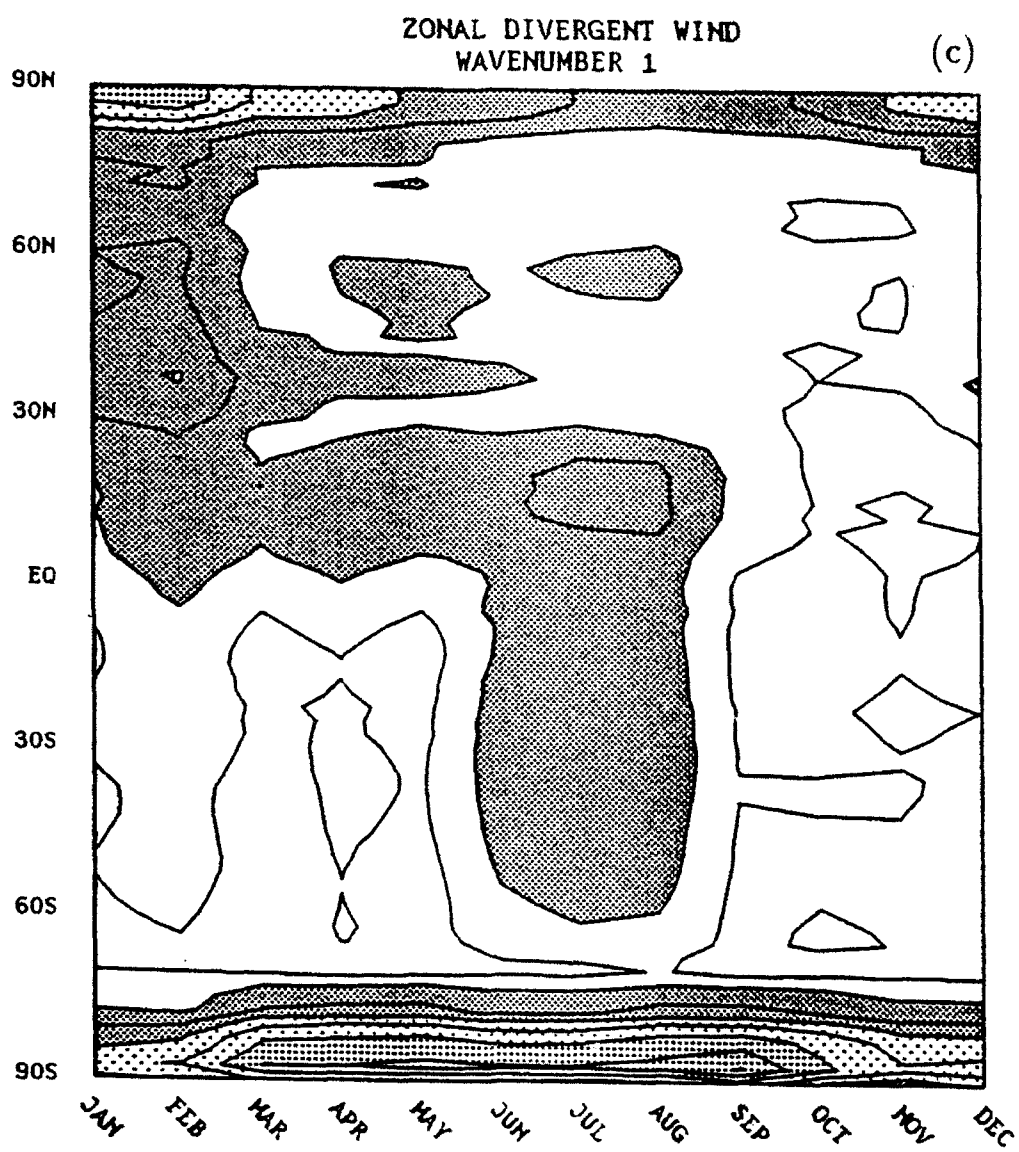


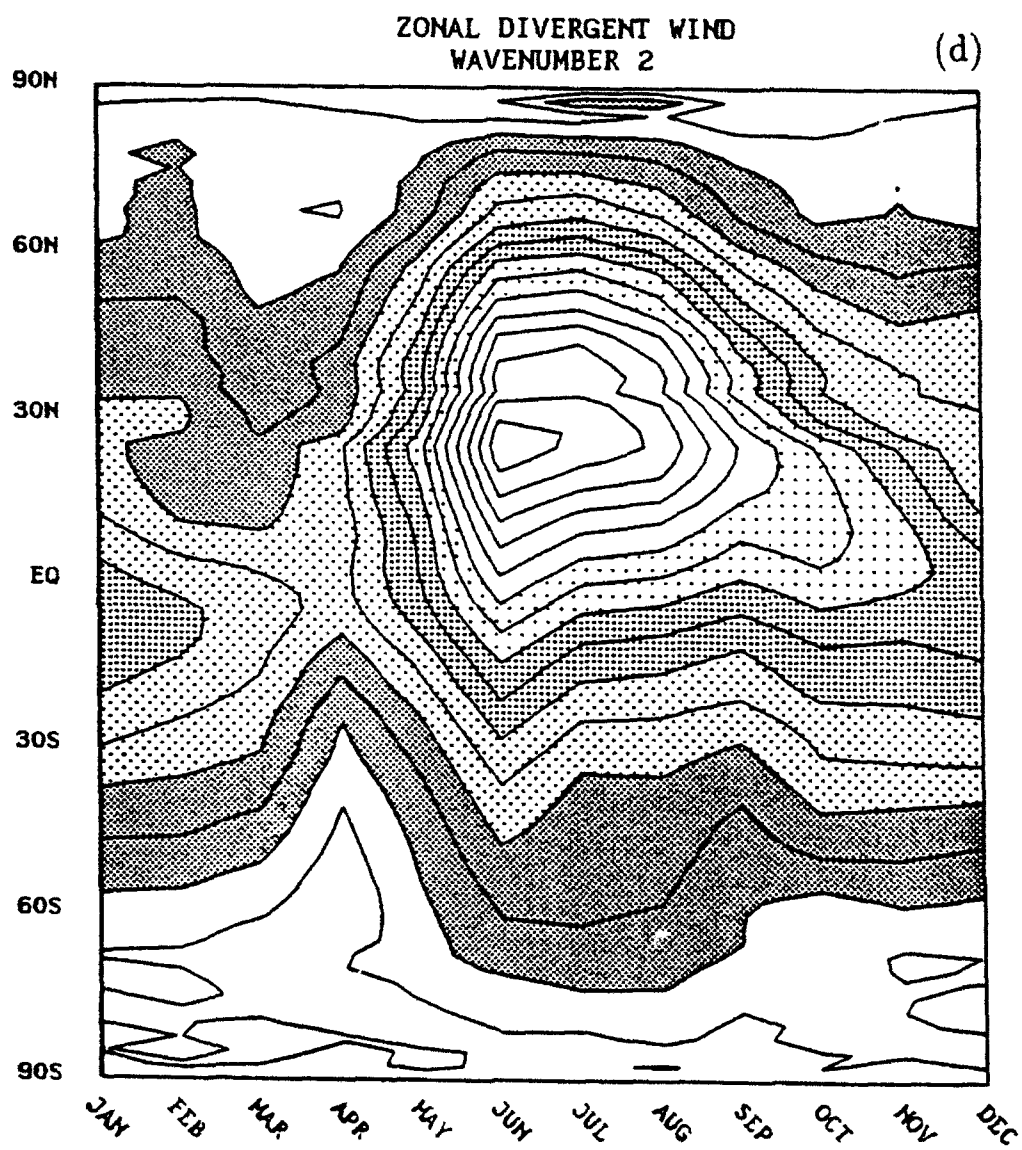
Figure 3.19. Latitude/time cross-section of the vertical modes for long wave contributions to the zonal divergent wind. The internal modes two, three, and four for wavenumber one are shown in (a), (b), and (c), for wavenumber two in (d), (e), and (f), and lastly for wavenumber three in (g), (g), and (i). Contour interval is 0.05 m s^{-1} . Dark shading represents speed from $0.1\text{--}0.2 \text{ m s}^{-1}$, medium dots are for speeds between $0.2\text{--}0.4 \text{ m s}^{-1}$, heavy dots delineate speed of $0.3\text{--}0.4 \text{ m s}^{-1}$, and light dots are for speeds ranging from $0.4\text{--}0.5 \text{ m s}^{-1}$. Regions with speeds greater than 0.5 m s^{-1} are clear.

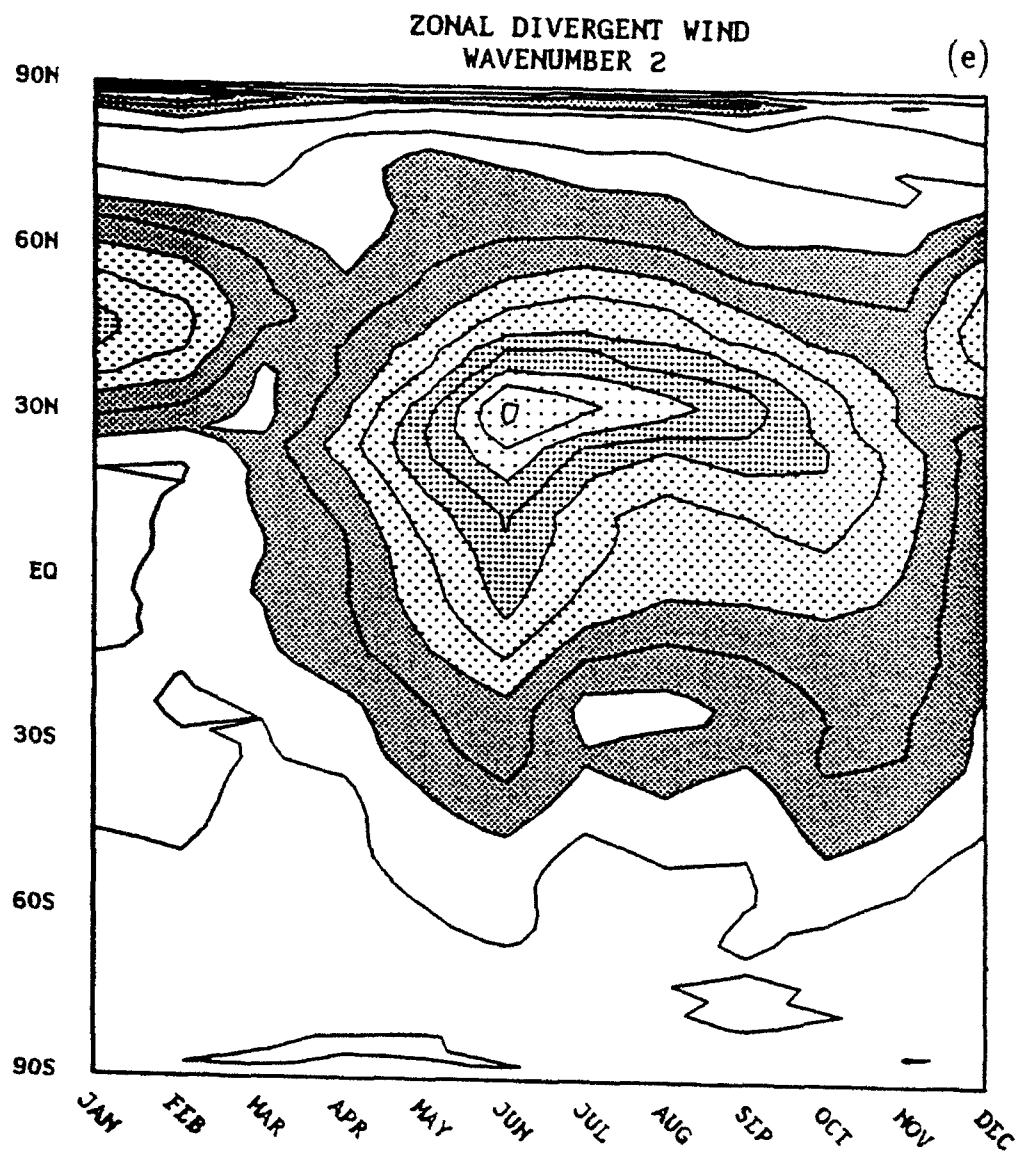
ZONAL DIVERGENT WIND
WAVENUMBER 1

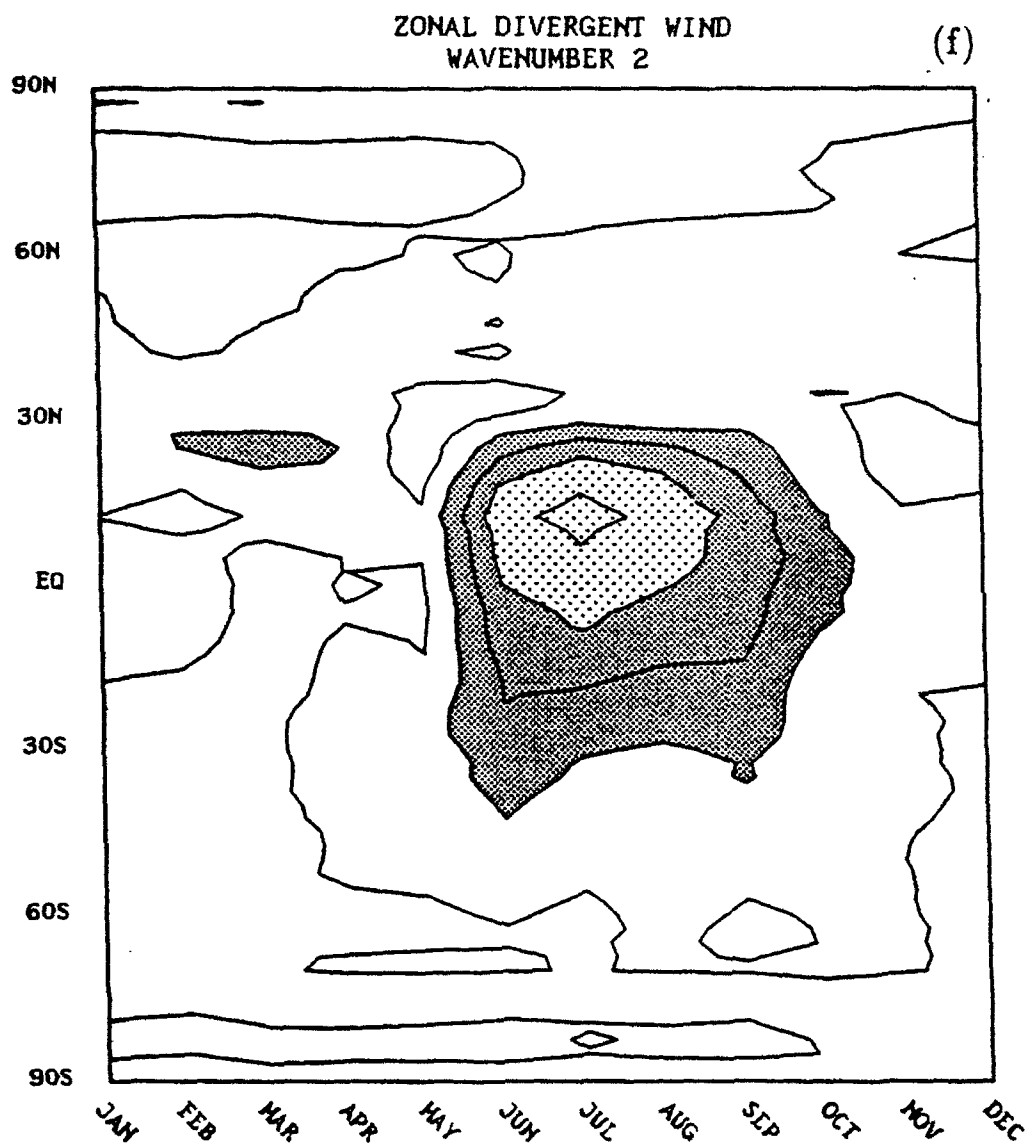
(b)





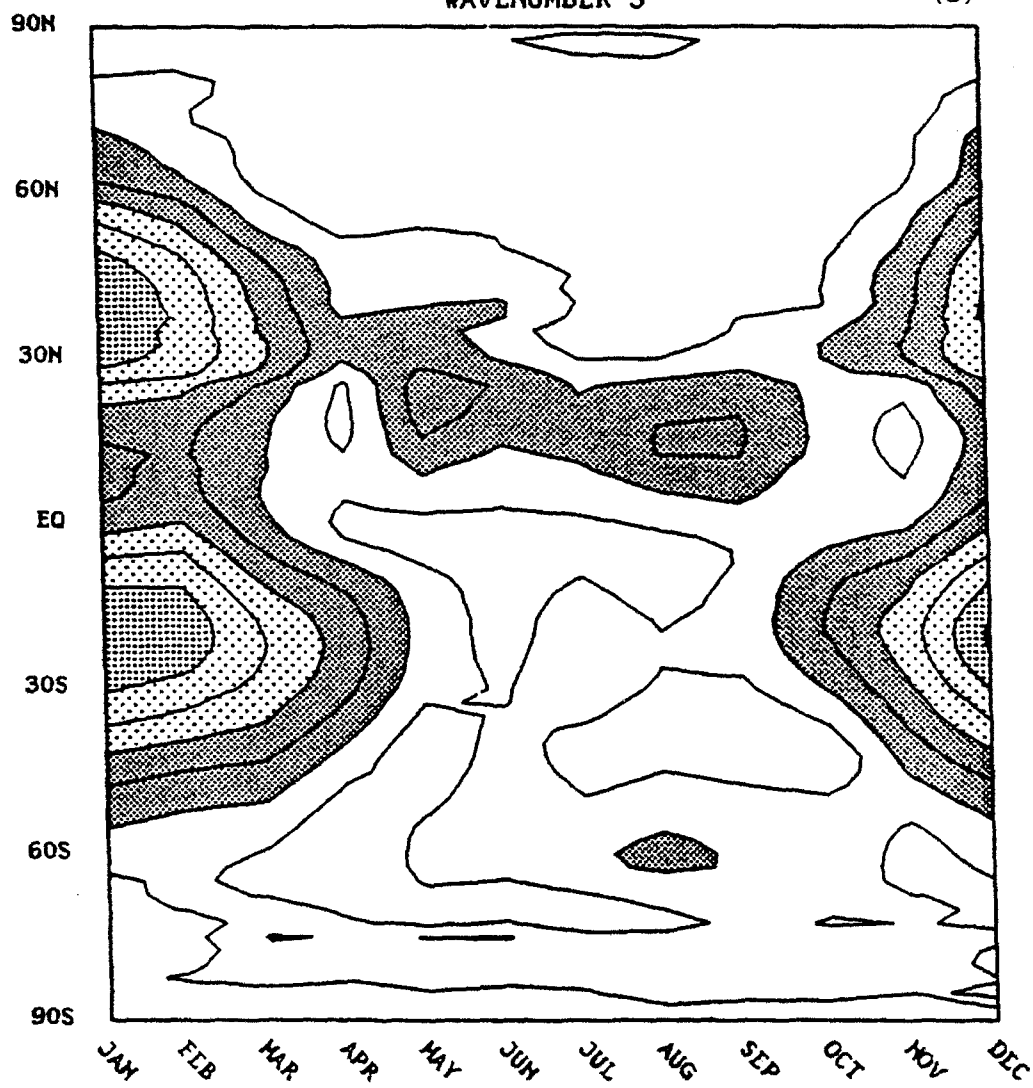


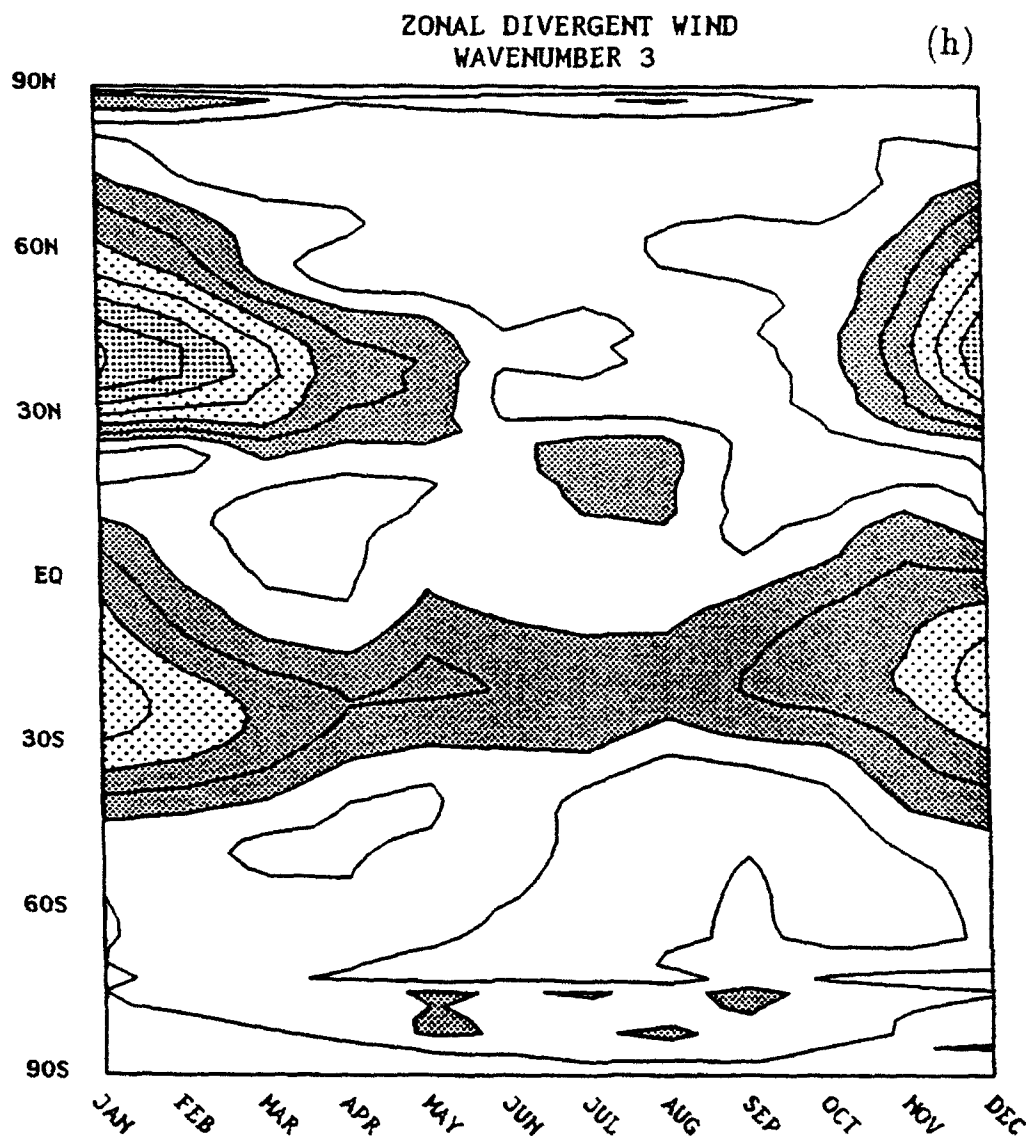




ZONAL DIVERGENT WIND
WAVENUMBER 3

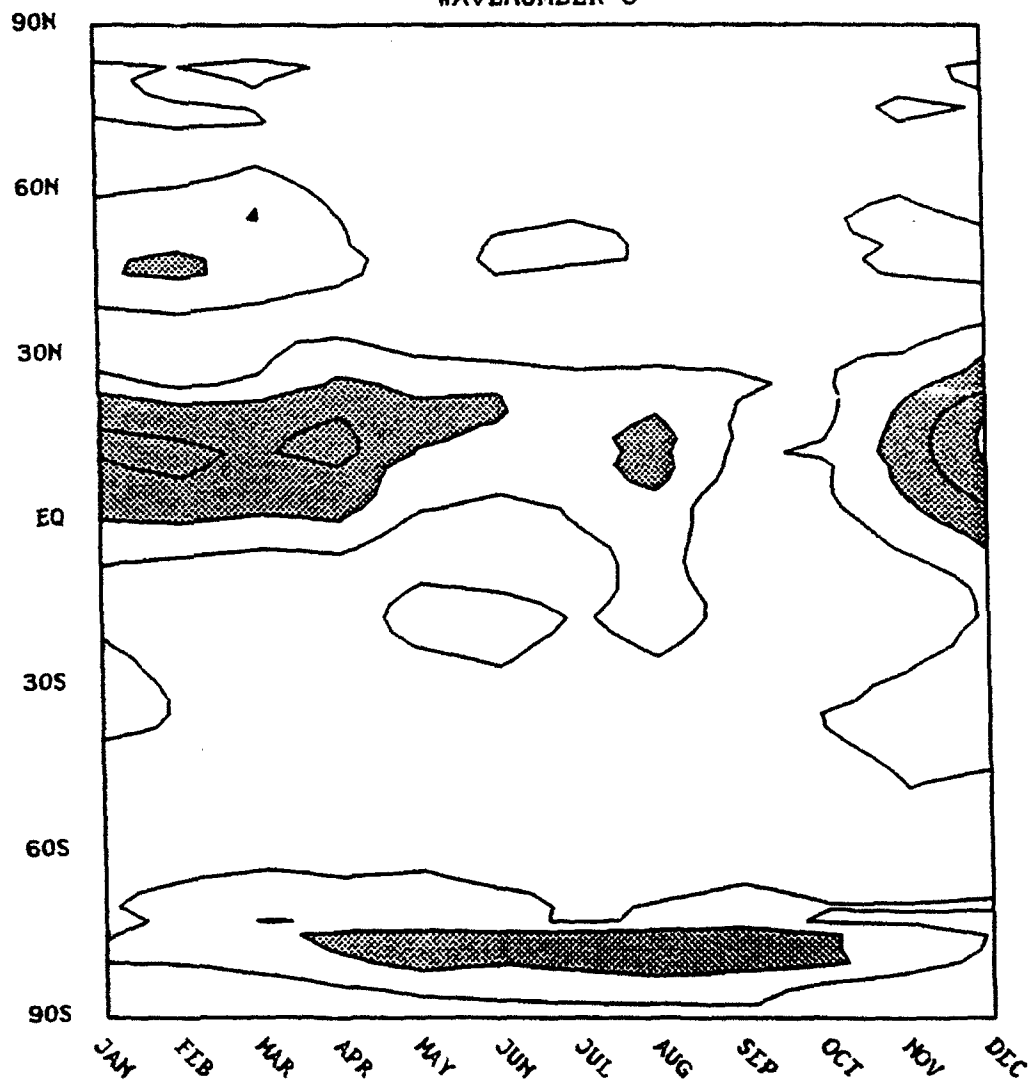
(g)





ZONAL DIVERGENT WIND
WAVENUMBER 3

(i)



at the 0.5σ level. These heating rates are derived from the OLR values, considering only values smaller than 240 W m^{-2} . This threshold value of 240 W m^{-2} is then subtracted from the OLR grid point value and the resulting number is divided by 10. This is then considered to be the heating in $^{\circ}\text{K day}^{-1}$. Compensating cooling is prescribed over the remaining grid points, so that there is no net cooling or heating. The validity of this approach can be demonstrated by comparing Figs. 3.20a,b and 3.21a,d. Maximum mean monthly rainfall rates for January and July in excess of 22 mm are found over the maritime continent and Bay of Bengal. It can be shown that 20 mm of rainfall equates to approximately $6^{\circ} \text{ K day}^{-1}$. The maximum values of $5.4^{\circ} \text{ K day}^{-1}$ for January and $5.2^{\circ} \text{ K day}^{-1}$ for July, obtained close to 90° E from Fig. 3.21a,d, are in good agreement with the values extracted from the precipitation data.

The PE model is integrated for 90 days and the results are averaged for the last two weeks. The initial conditions are given by the zonally- and annually-averaged zonal wind as shown in Fig. 2.4. The model is nudged to relax to this zonal wind with a relaxation coefficient given by $(4\Delta t)^{-1}$, where Δt , the time step, is equal to six minutes. As discussed in Section 2.2.5, this assures that the zonally averaged wind remains that of the annual average through the integration. This implementation of the PE model is designed to provide a response to diabatic heating intermediate between a full GCM simulation and a linear model. The PE design in the current integration mode excludes topographic feedback and wave mean-flow interactions. It retains linear mechanics and includes some nonlinear processes, such as Hadley cell transports (Schneider 1987) which are not included in most linear treatments as well as vertical shear effects and local barotropic instability to the extent that the basic state is produced by tropical heating.

These experiments are designed to address the question of how much of the observed wave structure may be attributed to atmospheric response to tropical

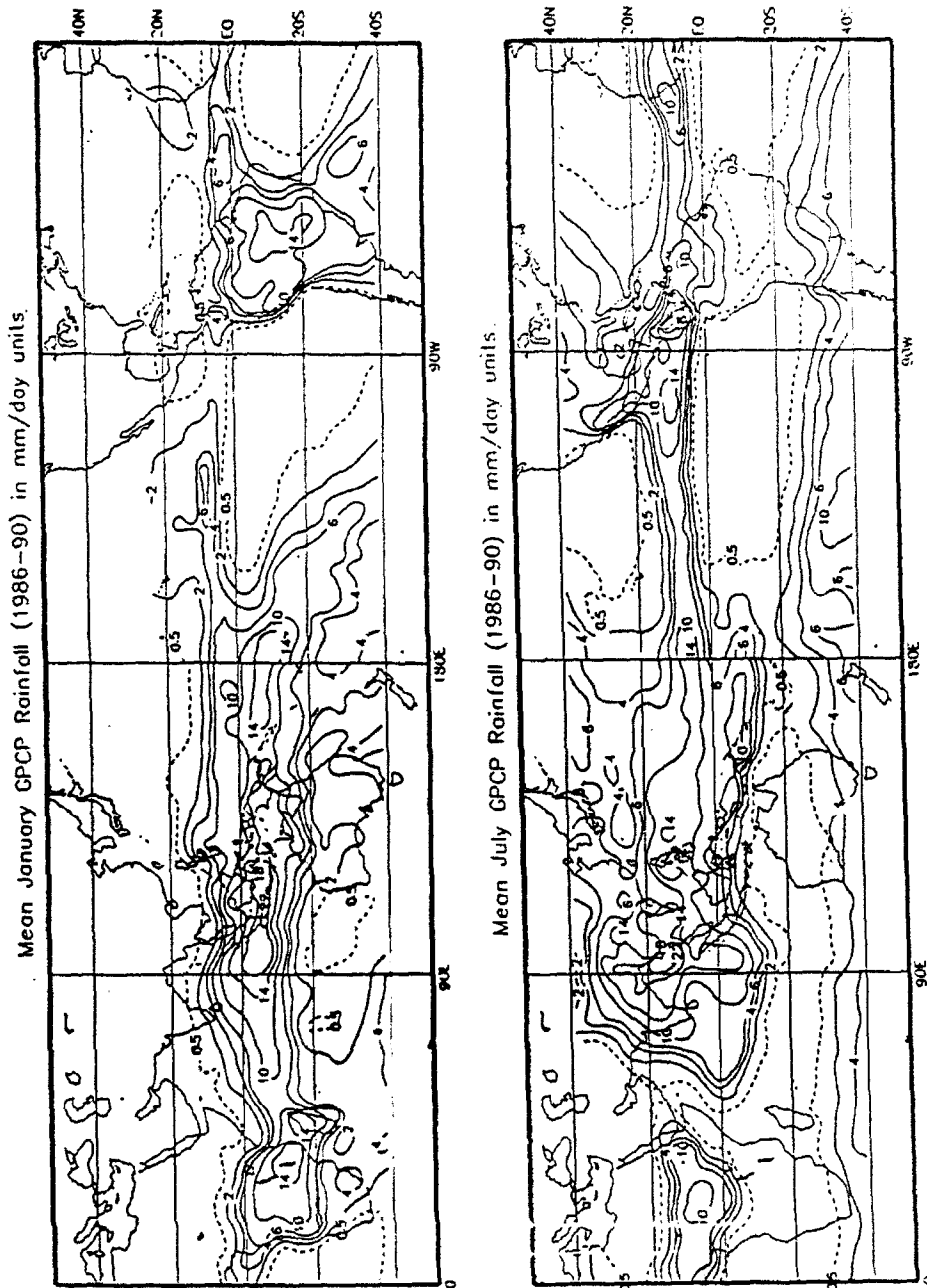


Figure 3.20. Satellite derived (GPCP) mean monthly rainfall rates for the period 1986-1990 in mm/day for January and July. Graphs provided courtesy of Kingtse Mo.

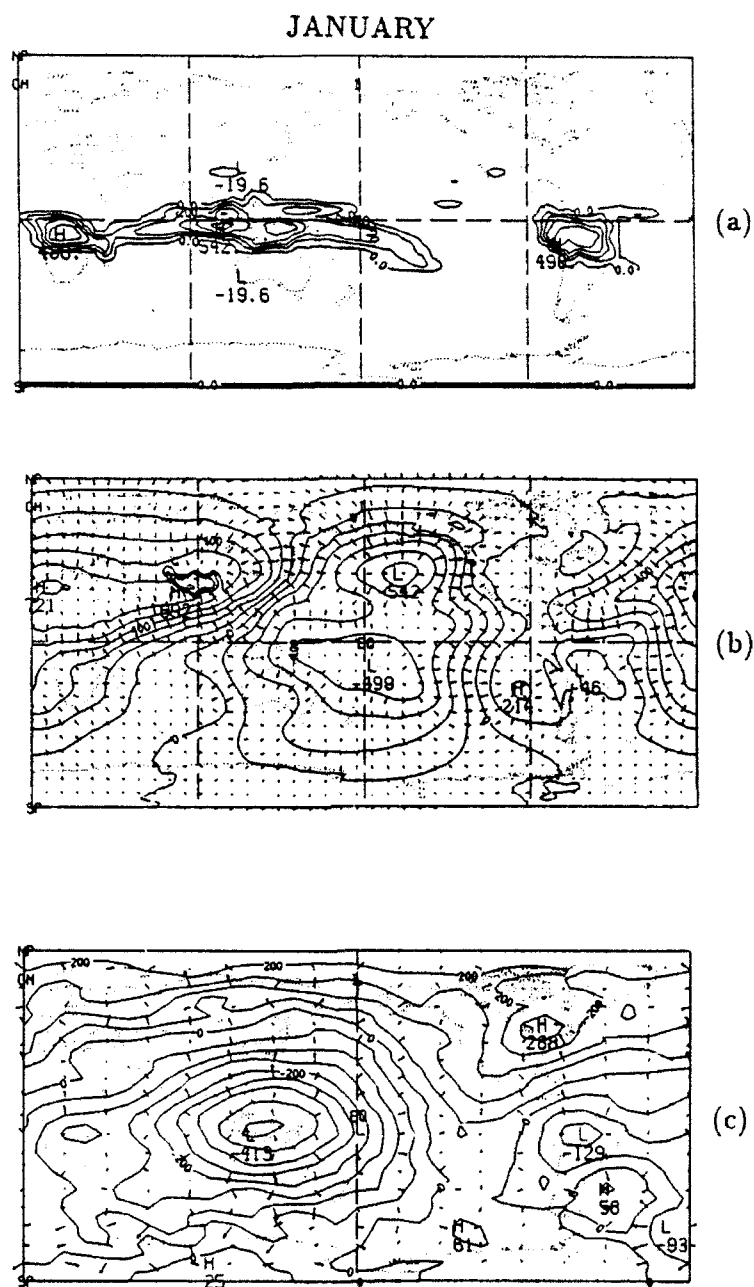
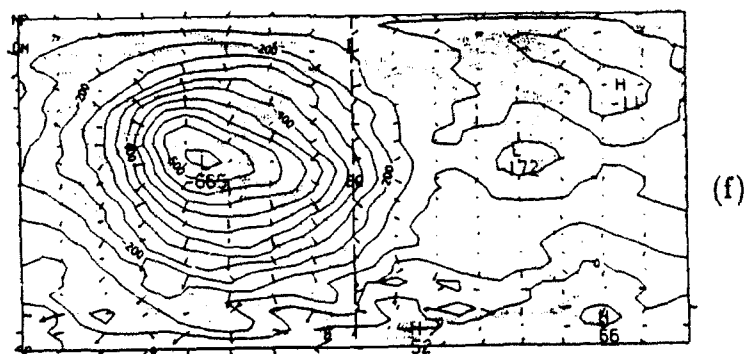
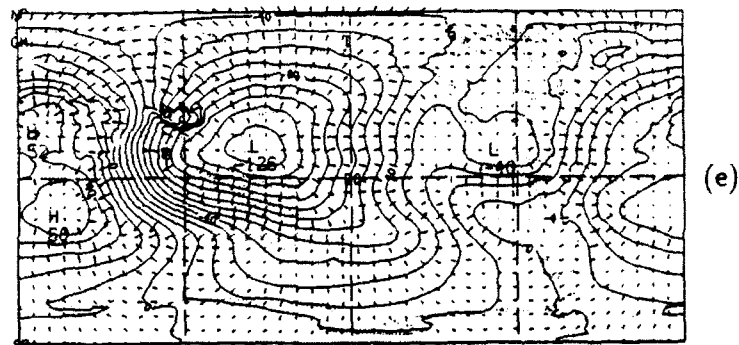
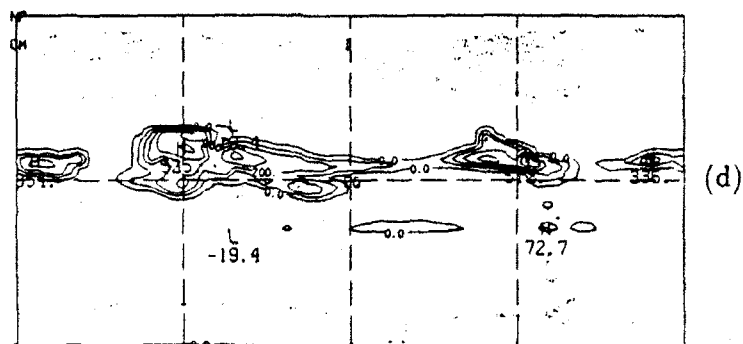


Figure 3.21. Heating rates in $^{\circ}\text{K day}^{-1}$ multiplied by 100 and contoured every $100^{\circ}\text{K day}^{-1}$ for January (a) and July (d); observed velocity potential contoured every $10^6 \text{ m}^2 \text{ s}^{-1}$ and divergent wind truncated to include only the first and second internal modes (b,e), velocity potential and divergent wind obtained as the average of the last 15 days of a 90 day PE integration (c,f). The level for (c)-(f) is $\sigma = 0.2$ and the maximum wind vectors are set at 2.5 m s^{-1} .

JULY



heating and those features that are not reproduced by the simulations will be interpreted as due to mechanisms not included in the model. Again, the emphasis is on the model being a diagnostic tool and it is assumed that the model is capable of adequately simulating the orographic response. Results are presented at the upper tropospheric level only ($\sigma = 0.2$).

The velocity potential and divergent winds obtained from the decade averages for January and July are also shown for $\sigma = 0.2$ (Fig. 3.21b,e). These fields only include the contributions from the second and third modes. Compare these to Fig. 3.21c,f which show the resulting divergent circulations from the PE model runs. The July heating induces fairly realistic divergent circulations. In January, the main difference is found in the North Pacific, where a divergent outflow present in the analysis is not reproduced by the model. This outflow is probably associated with quasi-geostrophic extratropical perturbations not directly linked with tropical forcing.

The primary purpose of the linear model is to aid in the determination of when the nonlinear PE model response makes its way into the opposite hemisphere. The linear model is forced through a function whose horizontal structure is identical to that of the PE model as shown in Fig. 3.21.a,d. However, because the linear model contains no thermodynamic energy equation, the heating is put into the divergence equation (2.15) of the shallow water model in the Q term. The results of forcing the linear model with the same heating rate as the PE model are shown in Figure 3.22a,d. Note that the linear stationary response is mostly confined to the summer hemisphere, where the majority of the heating is applied, as a result of the basic state equatorial easterlies. The 90 day PE integrations show similar response to that of the linear model in the summer hemisphere. Thirty days earlier in the integrations the wave pattern over south of Australia (Fig. 3.22b) and eastern Asia (Fig. 3.22e) is quite different from that of the linear model and that shown by the

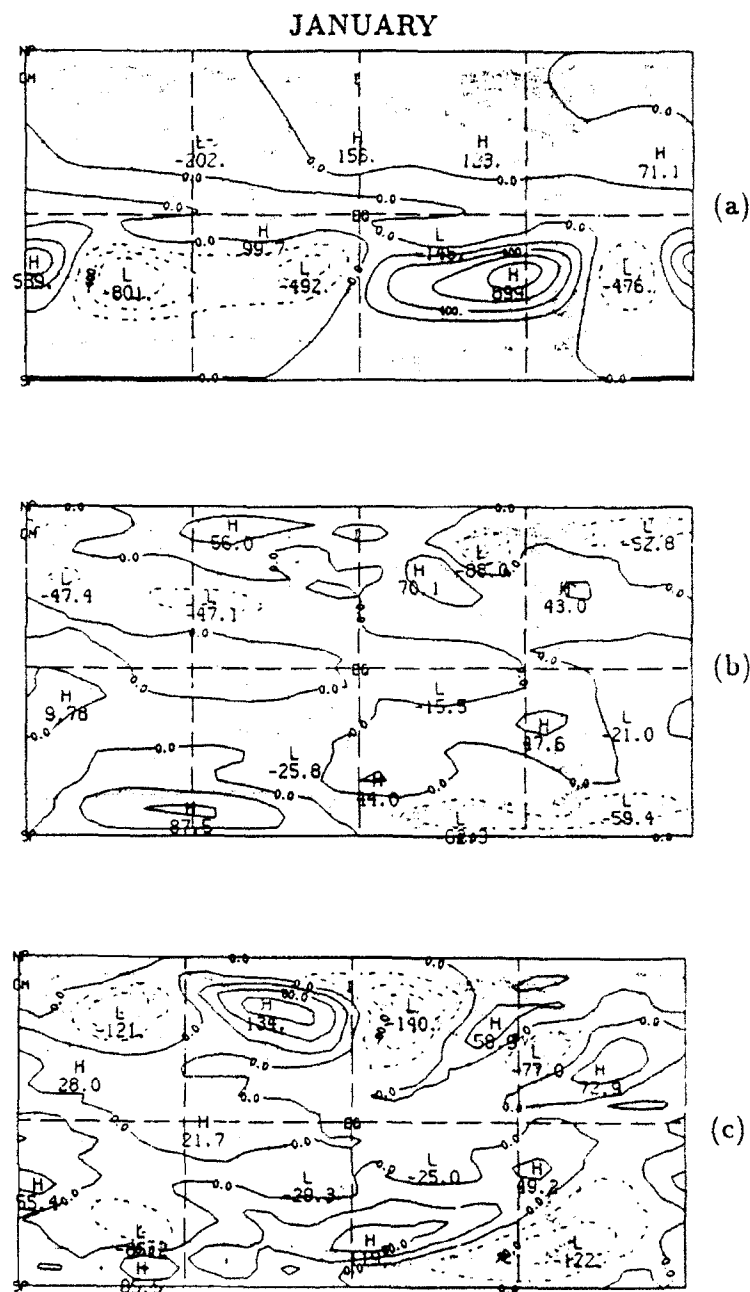
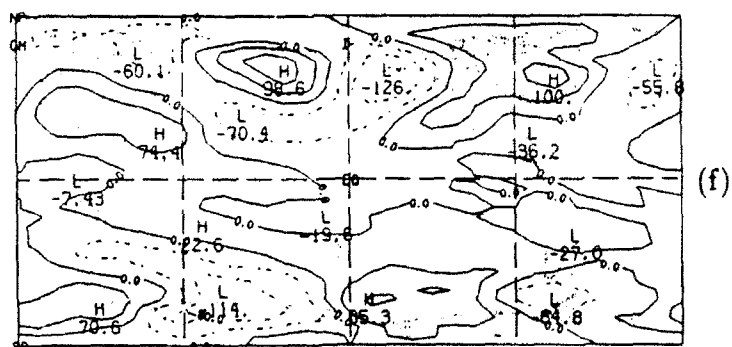
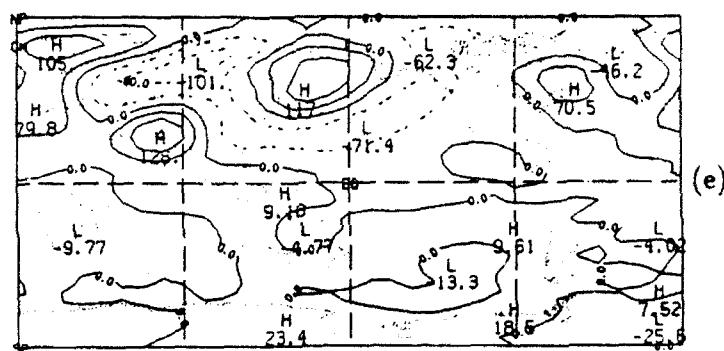
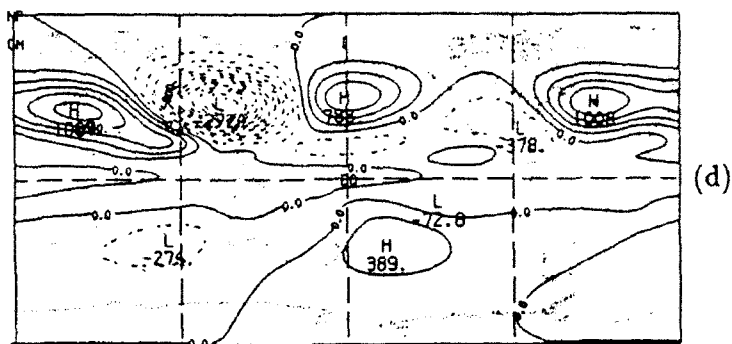


Figure 3.22. Height wave response to tropical heating obtained from the linear shallow water equation model, contoured every 20 m (a, d). Height waves at $\sigma = 0.2$ averaged for the last 15 days of the second (b, d) and third (d, f) month integrations of the PE model. Contour interval is 40 m in panels b, c, e, and f.

JULY



PE model 30 days later. These results indicate that at 60 days the response is still evolving, and that 90 day integrations are adequate in reproducing the stationary response of the waves. That is, after three months integration time the amplitude of the PE response in the winter hemisphere are of similar magnitude to those in the summer hemisphere.

The wind response predicted by the PE model is next examined in conjunction with the climatology at $\sigma = 0.2$ in Figs. 3.23 and 3.24. Comparison of Fig. 3.23a,b suggests that the westerlies over the eastern equatorial Pacific in January are due to the tropical response to mid-latitude forcing, since they are not reproduced by the PE integrations. The PE response displays the westerlies straddling the equator at approximately 25% of the analysis value. The PE integrations exhibit westerly maxima north of the Arabian peninsula (5.54 m s^{-1}) and off the North American coast (6.14 m s^{-1}). These features are also present in the observations with over twice the amplitude given by the PE model (2.4 and 2.3 times greater for the Arabian and North American maxima, respectively). In contrast, the westerly jet off the Asian coast is not reproduced by the numerical integration, indicating the need to include orography and land-sea contrasts to account for this pronounced feature of the NH winter circulation. The austral summer zonal wind maxima near 90° E is represented by the PE at 56% of its observed value.

The wave response is most easily seen in the meridional wind. Figure 3.23d shows a wave three response in the NH winter as expected from the January forcing which contains a pronounced wave three component. The observations instead present a dominant wave two component which may be linked with the orography. The average strength of the three PE northerly wind maxima in the NH (7.86 m s^{-1}) are about 60% of the average strength of the two climatological wind maxima (13.3 m s^{-1}). Similar results are found for the southerly wind maxima (55%).

Figure 3.24a shows the typical structure for the zonal wind in the SH during July,

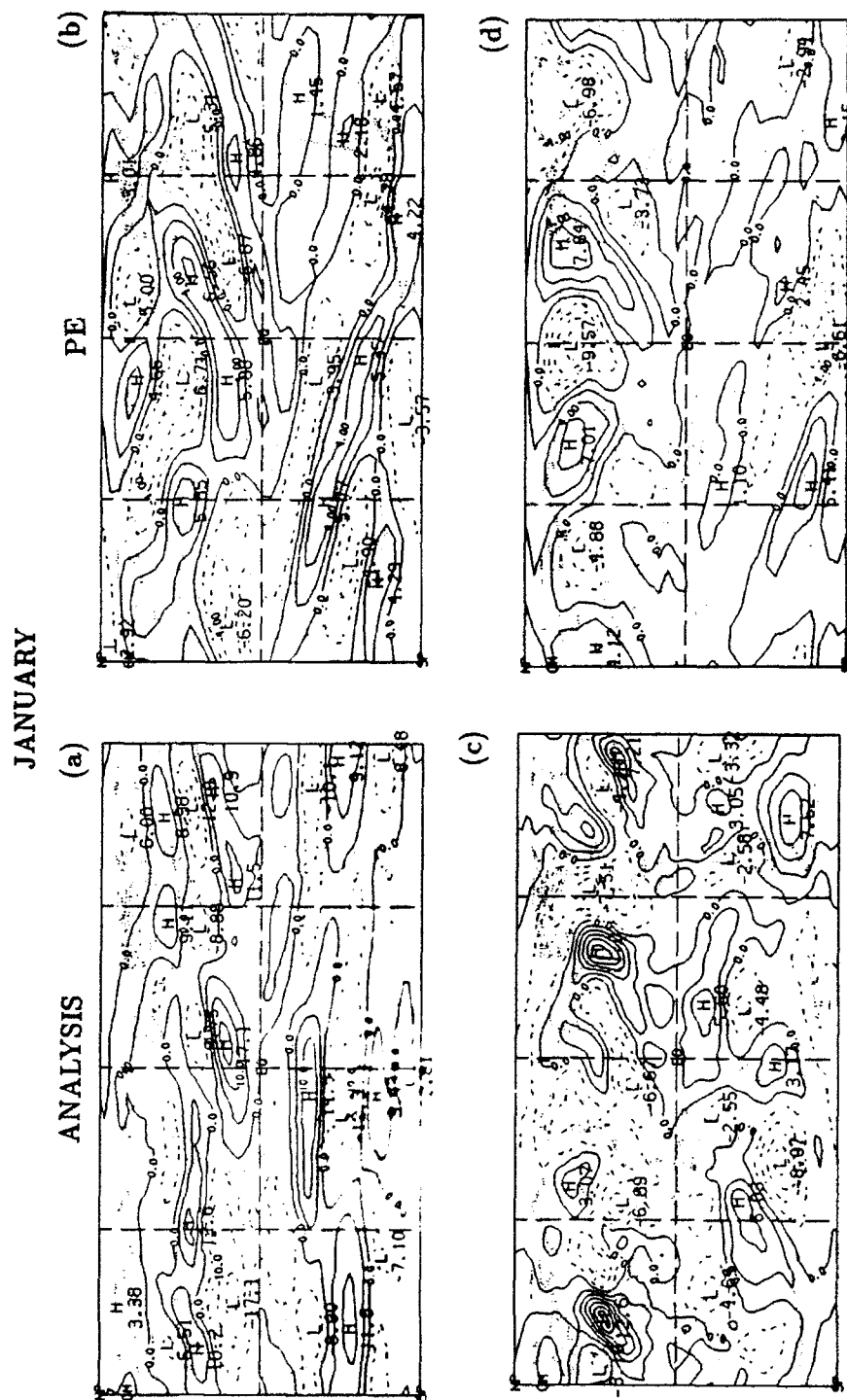


Figure 3.23. Zonal wind wave component from analysis (a, contoured every 5 m s^{-1}) and from the PE simulation (b, contoured every 2 m s^{-1}) and meridional wind component from analysis (c) and PE simulation (d) contoured every 2 m s^{-1} for January.

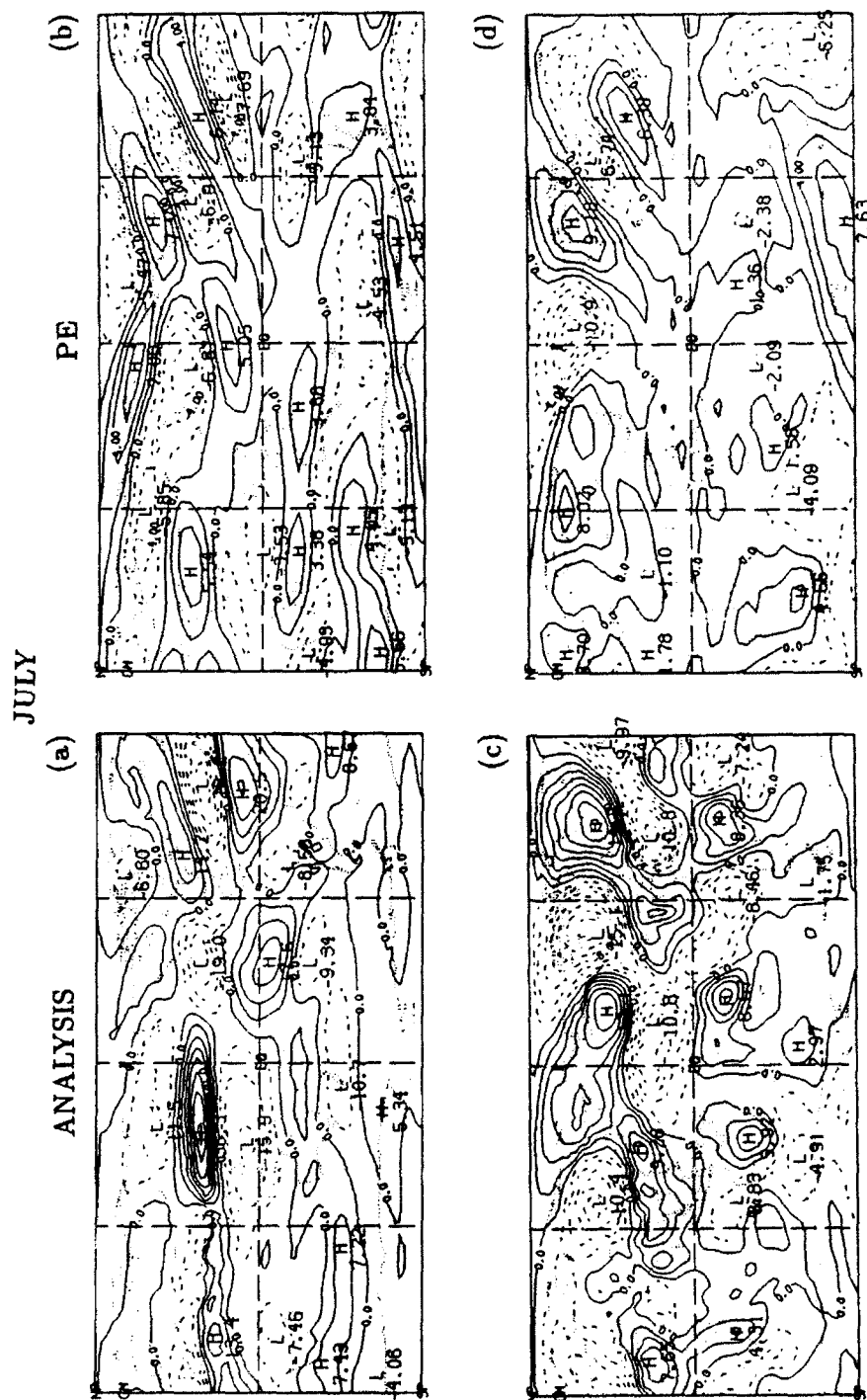


Figure 3.24. Zonal wind wave component from analysis (a, contoured every 5 m s^{-1}) and from the PE simulation (b, contoured every 2 m s^{-1}) and meridional wind component from analysis (c) and PE simulation (d) contoured every 2 m s^{-1} for July.

with a subtropical wind maximum over Australia spiraling southeasterly, circling the Antarctic continent. A double jet is observed at $\sim 160^\circ$ E, with maximum values near 25° (14.5 m s^{-1}) and 60° S (9.43 m s^{-1}). This feature is reproduced by the PE model, but it is displaced about 90° west of the observations with the double jet structure now present at about 60° E. Simulated values for the subtropical zonal wind waves are near 45% of the observed values. The observed positive and negative zonal wind bands of the NH summer have some counterparts in the PE model whose maxima are about 35 to 45% of the observed values (42% Tibet, 36% central Pacific, and 43% Central America). The observations (Fig. 3.24c) show a wave train that appears to emanate in the Indian Ocean and propagates toward the Pacific Ocean. A similar wave pattern with the right amplitude is predicted by the PE integrations (see thick dashed lines in Fig. 3.24c,d), but it is further south and of longer wavelength in the simulations. The PE model produces a meridional overturning (Fig. 3.21f) that extends about 30° further south in the SH than is observed (Fig. 3.21d). This may account for the southward shift of the Rossby wave source discussed by Sardeshmukh and Hoskins (1988) and cause the Rossby wave response to be shifted southward. Nevertheless, these results suggest that the interpretation that the wave pattern in Fig. 3.24c may have a tropical origin is still valid.

In summary, this chapter views the climatology of the vertical structure of the seasonal cycle using 10 years of operational analyses from the ECMWF. In doing so, the dominant wave patterns of the Northern and Southern Hemispheres are seen to exhibit wave one and two structures, with those in the NH containing larger amplitudes and a westward tilt with height. The seasonal linkage between the divergent and rotational wave patterns is also reviewed. Finally, simulations from a three-level PE model are examined to quantify, within the framework of this model, how much the tropical forcing translates into the observed extratropical

response. Results suggest that over 40% of the observed midlatitude waves in the SH can be attributed to tropical heating. The next step is to focus attention on the interannual and intraseasonal variations.

CHAPTER 4

LOW-FREQUENCY OSCILLATIONS

Studies of tropical convection using OLR data (e.g., Lau and Chan 1988) have revealed the existence of multiple time scales in the most dominant patterns of convective variability. These time scales are those of i) the seasonal cycle, ii) interannual changes associated with ENSO episodes, and iii) the 30-60 day or intraseasonal oscillation.

The previous chapter focussed on the seasonal cycle and explored the extent to which stationary extratropical patterns result from the annual changes of tropical convection. The most dramatic seasonal changes were found associated with the shift in convection from the monsoon region over eastern Asia, during NH summer, to the western Pacific (Australia and the maritime continent) during winter. This region also exhibits anomalous convection patterns associated with the other two time scales of tropical variability (ENSO and intraseasonal oscillation). Weickmann (1983) has noted the spatial similarity of patterns associated with these time scales. Recent studies (e.g., Hendon and Liebmann 1990) have described the global character of the intraseasonal oscillations which includes a tropical internal structure and an extratropical equivalent barotropic response. In this chapter we examine the vertical structure of interannual and intraseasonal variations. The goals are 1) to determine whether the vertical structures of these global patterns depend on the phase of the oscillations, and 2) to quantify how much of the observed response may be directly linked to the tropical heating.

4.1 El Niño – Southern Oscillation Phenomenon

The Southern Oscillation (SO) is the name given by Sir Gilbert Walker to the most prominent interannual atmospheric signal of the earth's climate. Originally, it was detected in the sea level pressure difference between two centers located thousands of kilometer apart; one over the maritime continent and the second over the tropical southeastern Pacific. In collaboration with Bliss (Walker and Bliss 1932,1937), they determined that the SO was also associated with major changes in the precipitation and wind fields of the tropical Pacific and could be correlated to fluctuations in meteorological variables around the globe, such as rainfall rates in the Hawaiian Islands, sea level pressure changes over the Southeast US, and temperature in western Canada (Horel and Wallace 1981).

Analyses have determined the time scale of the SO to be between 2-7 years with a duration of between 1-2 years (Lau and Chan 1988). There are two phases to the SO which are termed warm, or El Niño, and cold. The El Niño events are characterized by high surface pressure over the Indonesian center and low pressure over the southeastern Pacific. This pressure gradient results in relaxed trade winds in the central and eastern tropical Pacific. The Indian Ocean has been suggested as the site where impulses for the ENSO originate, and it is also the region where significant 30-60 day oscillation signals are found (Lau and Chan 1988). The wind and surface pressure anomalies slowly propagate eastward from this region, into the central Pacific. Once east of the maritime continent, the anomalies are over the region of warm SSTs and, where the SSTs are sufficiently warm, convection develops (Barnett 1983). The region of warm SSTs progresses eastward, bringing heavy rainfall to the otherwise dry central and eastern Pacific. In contrast, the cold phase is described by relatively lower/higher pressure over the maritime continent/southeastern Pacific. Trade winds are intense and rainfall rates and SSTs are lower in the central and eastern tropical Pacific. Both horizontal and

vertical gradients of diabatic heating are required to maintain the pattern of these large-scale thermally driven circulations.

The dominant pattern of the SO is one of two poles (see Fig. 4.1) which are closely related to changes in SSTs in the tropical Pacific. This important link was made by Bjerknes (1969) who, in describing the large-scale west-east circulations that develop in this region, introduced the term "Walker Circulation." The zonal counterpart to the Hadley Cell, this thermally-direct circulation is described by rising motion and convection forming over the warm SSTs of the western Pacific, upper level outflow moving to the east, subsidence in the eastern Pacific, and easterly return flow at low levels back to the western Pacific.

The heat driven tropical circulations, on the seasonal time scales described in Chapter 3, were shown to have internal mode structure given by a combination

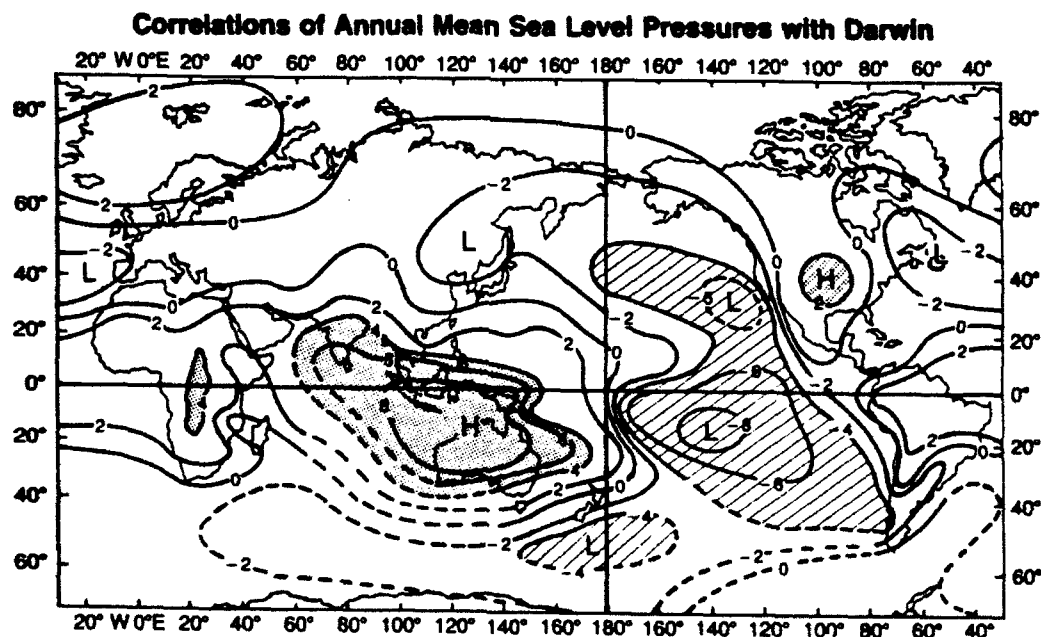


Figure 4.1. Composite assessment of the correlations of annual mean sea level pressures with Darwin, Australia (taken from Trenberth and Shea, 1987).

of vertical modes two and three. Waves in the meridional divergent wind (v_D) were observed to reach maximum amplitude for the same months which exhibit maximum amplitude in the extratropical zonal wind waves (u_R). This relationship was best observed between the contributions from the third internal mode to v_D and those of the equivalent barotropic structure to u_R . This relationship was documented in Chapter 3 for the seasonal changes in convection. The current chapter discusses whether similar relationships are found for the intraseasonal and interannual changes.

In particular, the vertical structure of the flow is expected to exhibit longitudinal variations due to different air-sea interactive processes acting over the Indian Ocean, western Pacific regions, and the eastern Pacific. Over the warm pool of the western Pacific, the static stability is relatively low and the rising motion and resulting convection are in phase with the surface low pressure, and out of phase with the surface zonal wind. Over the eastern Pacific, SST gradients are large (e.g., Horel 1982) and induce a pressure gradient force which drives relatively strong low level westerlies below the convection center. In this case, the "beta" convergence mechanism (Lindzen and Nigam, 1987), due to meridional motions, determine the heating distribution. These different vertical flow configurations were found by Wang (1992) to be typical of the cold/warm phases of the 82/83 and 86/87 ENSO episodes. His study was based on 200 and 850 mb winds and surface data. These two ENSO episodes are discussed next based on a more complete data set.

4.1.1 1983 – 1985 ENSO

Low values of OLR have long been used as an indicator for areas of deep convection in the tropics. The months of February 1983/1987 and February 1985/1989 represent the warm/cold phases of the SO, respectively. Figure 4.2 depicts for February 1983 the monthly mean OLR in panel (a), the streamfunction and velocity

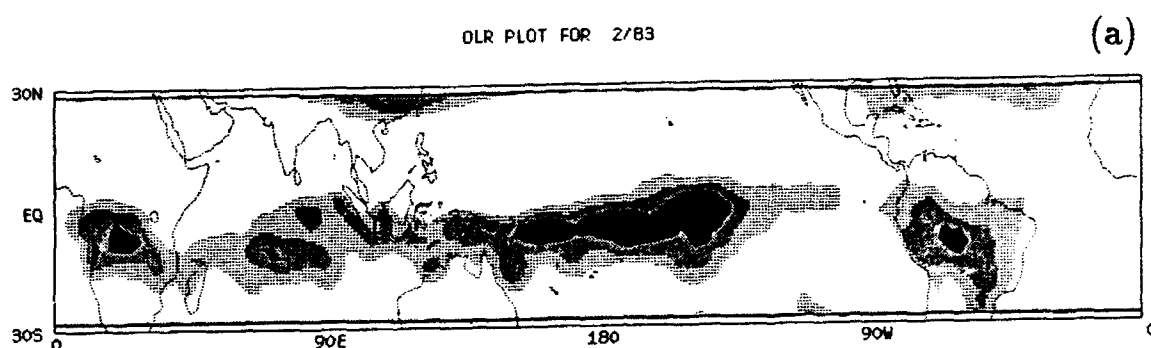
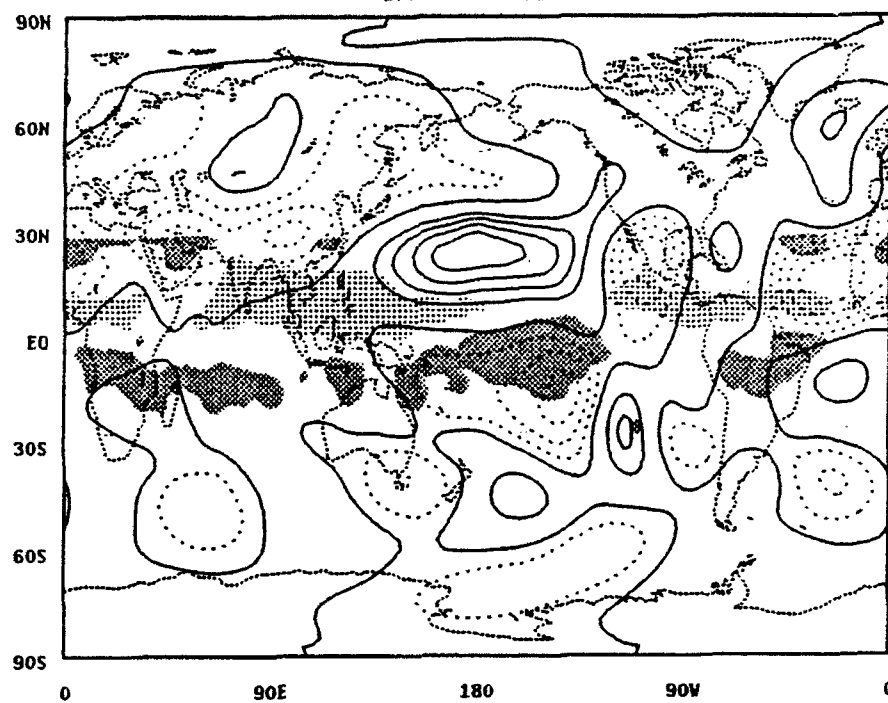


Figure 4.2. Monthly mean OLR (a), 200 mb streamfunction (b) and velocity potential (c) with OLR anomaly superimposed for February 1983, as well as PE simulations averaged for days 60-74 for the streamfunction (d) and velocity potential (e). Shading for OLR described in text. Contours intervals are $0.5 \times 10^7 \text{ m}^2 \text{ s}^{-1}$ in (b,d), and $1 \times 10^6 \text{ m}^2 \text{ s}^{-1}$ in (c,e). Maximum wind value in (e) of 3.35 m s^{-1} near 75° S , 157° W .

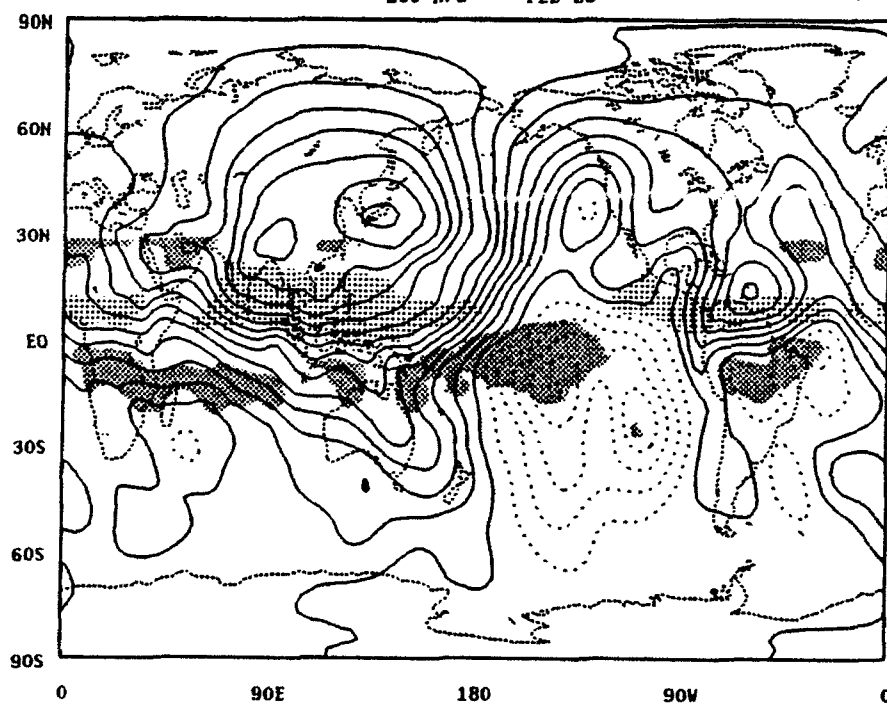
Streamfunction Perturbation and OLR Anomaly
200 hPa FEB 83

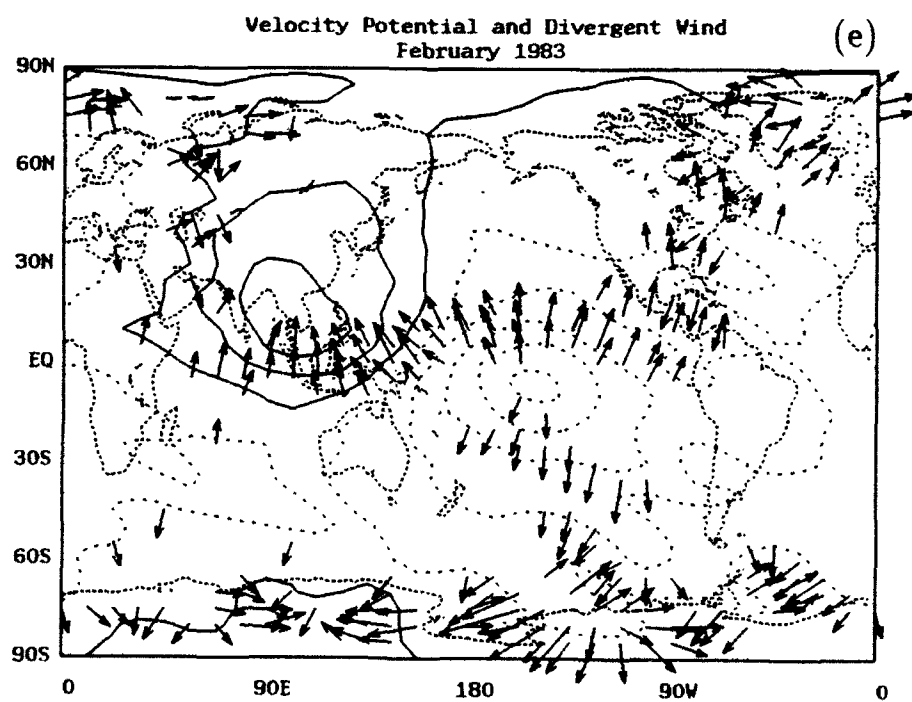
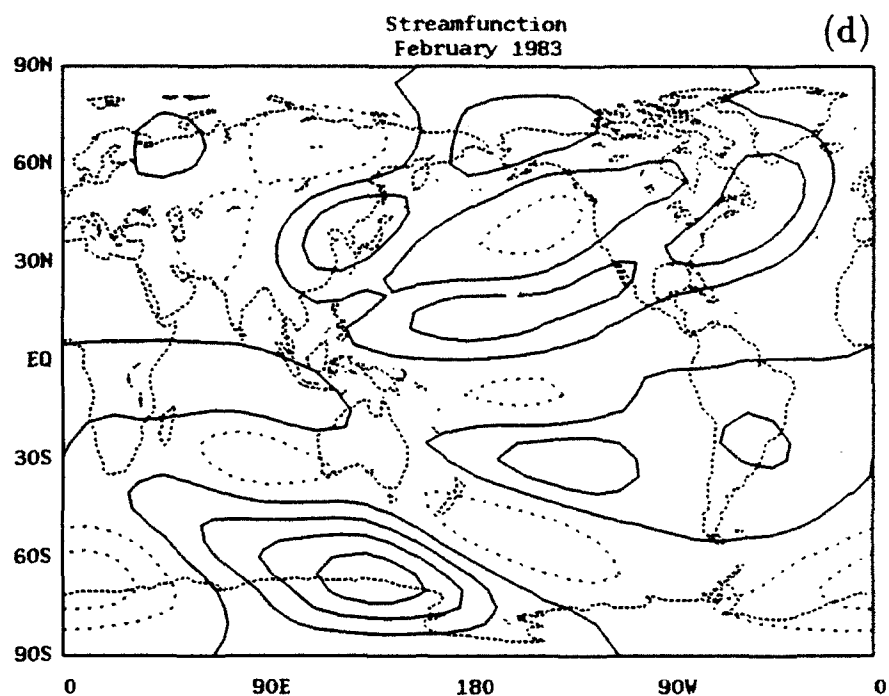
(b)



Velocity Potential and OLR Anomaly
200 hPa FEB 83

(c)





potential anomalies with OLR anomalies superimposed are in panels (b) and (c), respectively. The primitive equation model was run by forcing with a heating rate in $^{\circ}\text{K day}^{-1}$ which is proportional to the negative OLR anomaly $((\text{OLR anomaly} - 240) / 10)$. The model is initialized and relaxed to the annual zonal wind average as described in Chapter 3. The 15 day averaged model response in the streamfunction and velocity potential are shown in panels (d) and (e), respectively. Shading for the OLR in (a) indicates areas $< 200 \text{ W m}^{-2}$ (dark), $200\text{--}220 \text{ W m}^{-2}$ (heavy dots), and $220\text{--}240 \text{ W m}^{-2}$ (medium dots). The OLR anomaly in (b) and (c) is shaded with heavy dots in areas with values $< -20 \text{ W m}^{-2}$ and with medium dots for values $> 20 \text{ W m}^{-2}$. The same shading will be seen in Figs. 4.3, 4.9 and 4.10.

Three main regions of convection are seen in Fig. 4.2a; one over south central Africa, a second is the ITCZ which straddles the equator in the central Pacific, and the third area over central South America. The departure of the monthly average from the annual mean is shaded in Fig. 4.2b,c with anomalous low OLR values (representing mid-atmospheric heating) highlighted with dark shading. The streamfunction anomaly exhibits two well defined circulation centers poleward of the Pacific heating anomaly. Though a similar anticyclonic response is predicted by the study of Gill (1980), the observed streamfunction and OLR anomalies do not exhibit the longitudinal shift typical of Gill's model. The observed longitudinal phasing of the anticyclonic centers is captured on the PE response to the heating anomaly (Fig. 4.2d)

The main divergent outflows which are perpendicular to the gradient of the velocity potential shown in Fig. 4.2c appear in the PE integrations (Fig. 4.2e). During February 1983 minimum OLR values are found at about 150° W while SSTs larger than 29° C are found east of 145° W at this time and surface westerly wind anomalies extend from the dateline to the South American coast at the equator (Philander 1990). The maximum westerly wind anomaly is found at about 150° W ,

in the location of maximum heating. At the upper levels this is manifested in easterly anomalies in the central Pacific. This feature is well reproduced in the PE simulations (Fig. 4.2d). The SH wave train that appears to emanate from the Pacific convective center also appears in the PE simulation. The model did not reproduce the divergent outflow off the coast of North America. The reasons for this model's strong response at the very high latitudes need to be further investigated.

Similar features are found in Fig. 4.3 for February 1985 during the cold phase of the SO. The areas of convection over central Africa and South America are essentially unchanged; however, the convection areas in the central Pacific, implied via the OLR, are much further west, over northern Australia, the maritime continent, and the Indian Ocean. During this phase a Rossby top wave train exists, which extends from about 145° E into North America. This wave train is also seen in the PE simulations although it is displaced about 15° northward from the observed field. This displacement is consistent with the PE simulations of the meridional outflows over the maritime continent, which are found about 15° further north in the simulations than in the observations (Fig. 4.3d).

Further information can be gleaned from examination of the vertical mode structure of the zonal and meridional rotational wind. These are shown in Figs. 4.4 through 4.7 for February 1983/85 for the monthly averages.

The total vertical variability of the zonal rotational wind, shown in Fig. 4.4a, stretches almost continuously around the NH with a maximum north of the anomaly in the central Pacific. The SH response is similar, but more diffuse with maxima between 30° to 60° S associated with the OLR anomalies in the tropics. It is readily apparent from Fig. 4.4b that the external mode accounts for most of the variability in the zonal rotational wind north of about 15° N and south of 30° S. Also, note the concentration in the tropics of the negative bands. All but modes four and five are positive at $\sigma = 0.2$ so that the negative regions indicate areas of easterly winds

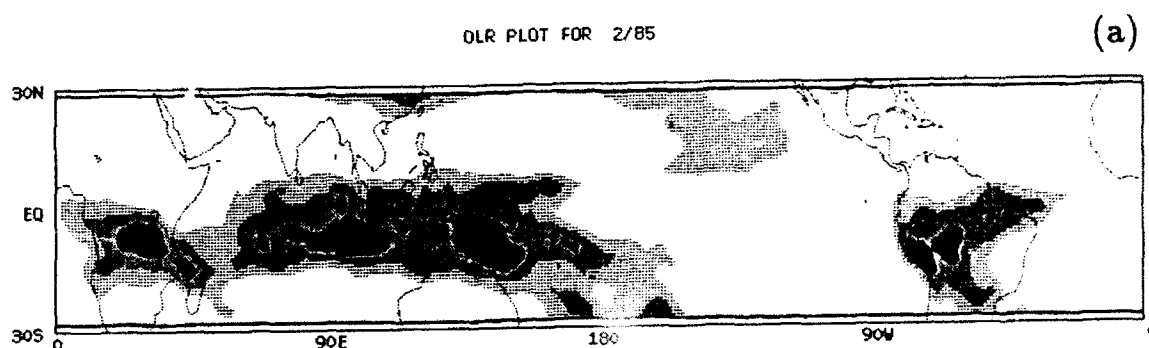
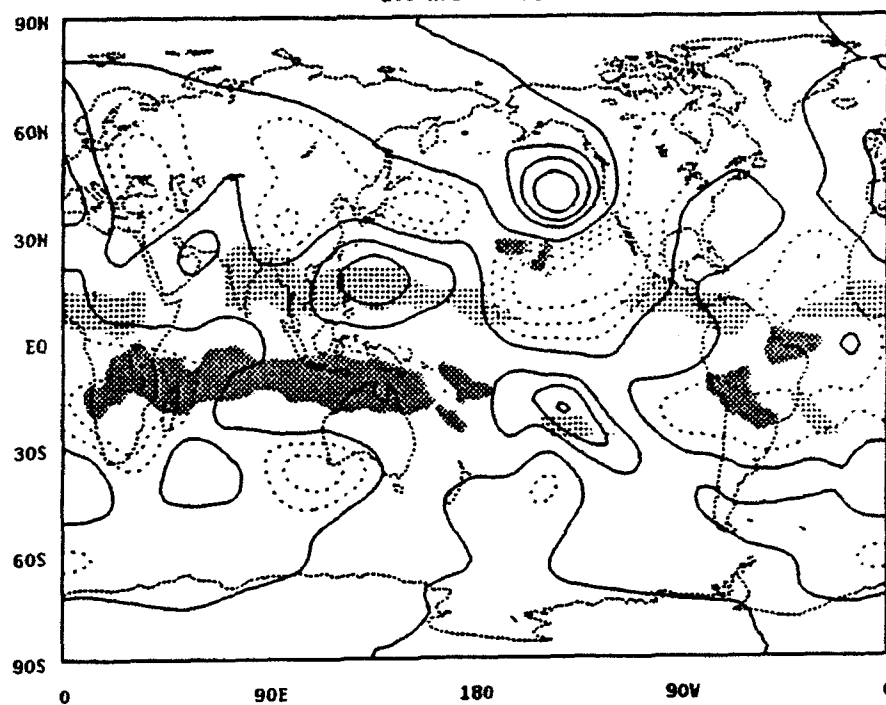
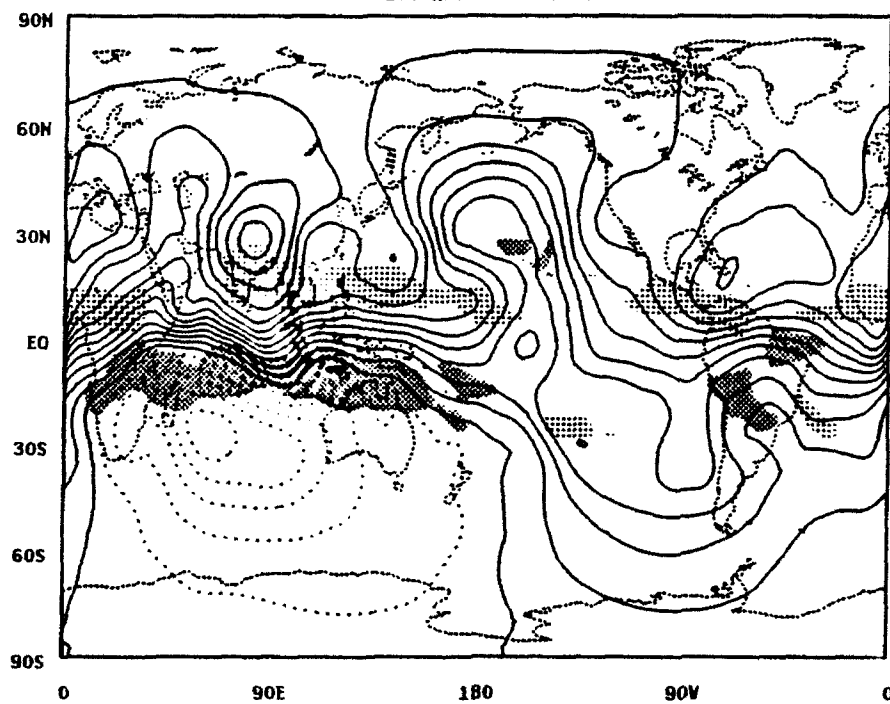


Figure 4.3. Monthly mean OLR (a), 200 mb streamfunction (b) and velocity potential (c) with OLR anomaly superimposed for February 1985, as well as PE simulations averaged for days 60-74 for the streamfunction (d) and velocity potential (e). Shading for OLR described in text. Contours intervals are $0.5 \times 10^7 \text{ m}^2 \text{ s}^{-1}$ in (b,d) and, $1 \times 10^6 \text{ m}^2 \text{ s}^{-1}$ in (c,e). Maximum wind value in (e) of 3.18 m s^{-1} near 75° S , 113° W .

Streamfunction Perturbation and OLR Anomaly
200 hPa FEB 85 (b)



Velocity Potential and OLR Anomaly
200 hPa FEB 85 (c)



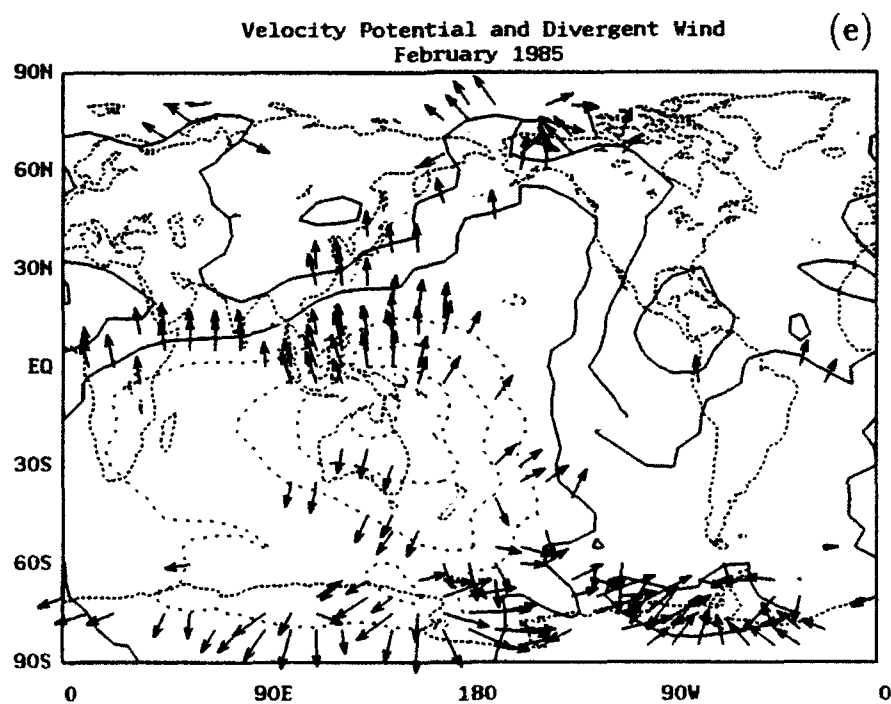
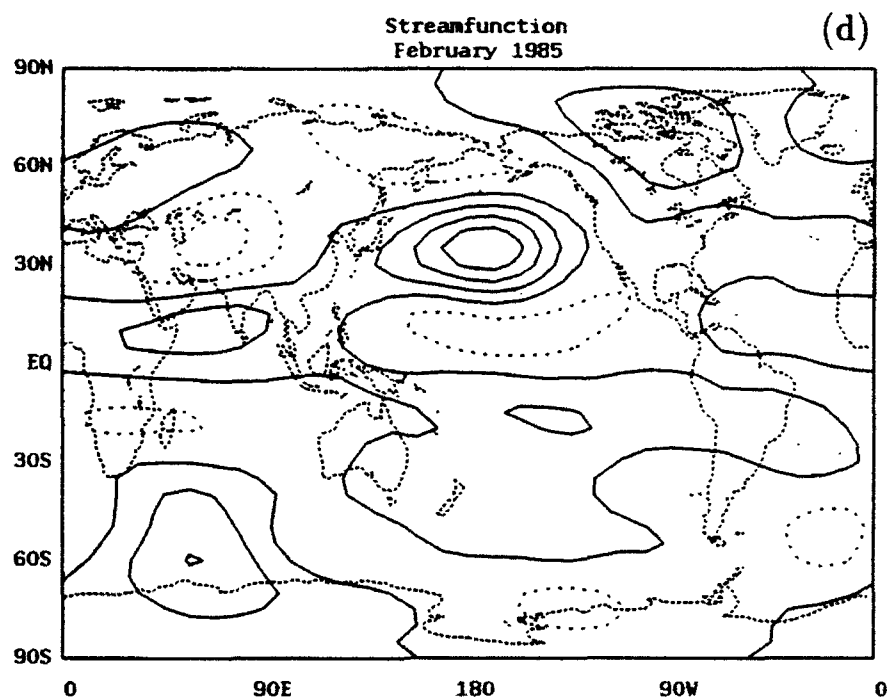
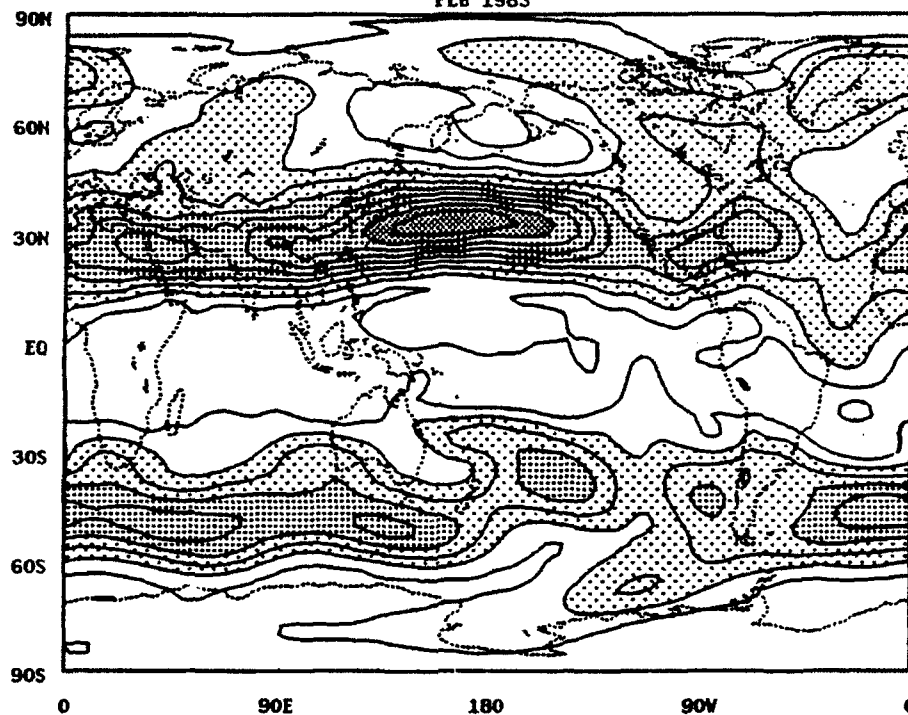


Figure 4.4. Total root mean square value (a) and normalized modes one (b), two (c), and three (d) for February 1983 zonal rotational wind. Mode contributions in (b-d) are normalized using the total root mean square value in (a). Contour interval in (a) 5 m s^{-1} with light shading in area of $10\text{--}20 \text{ m s}^{-1}$, medium shading for $20\text{--}40 \text{ m s}^{-1}$, and heavy shading for $40\text{--}60 \text{ m s}^{-1}$. Contour interval in (b)–(d) is 0.25 with heavy shading for areas > 0.50 and light shading for regions < -0.50 .

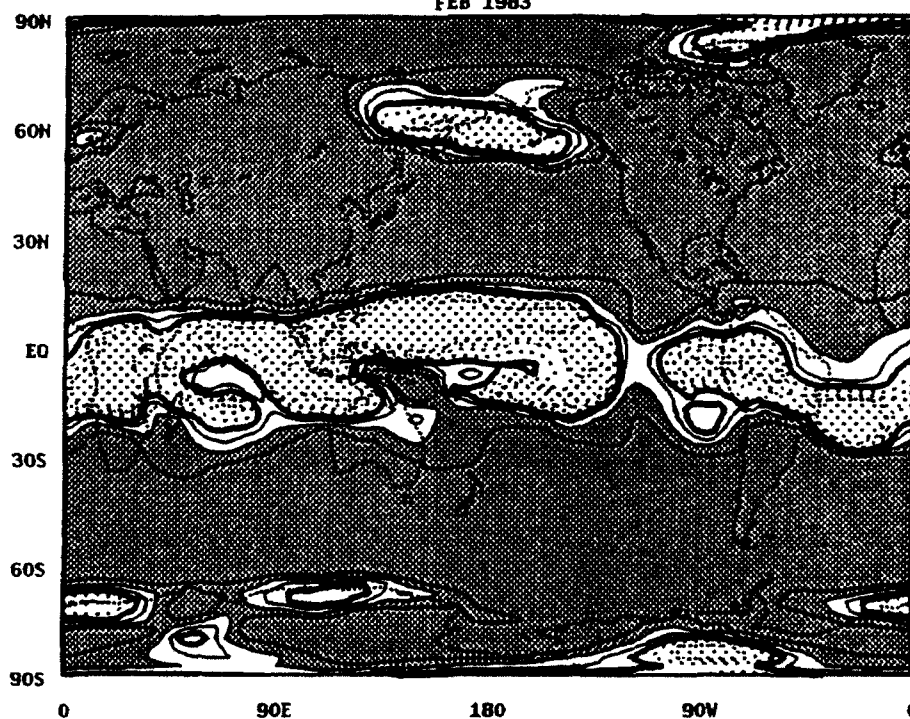
U COMPONENT OF ROTATIONAL WIND
Sum of Vertical Variability
FEB 1983

(a)



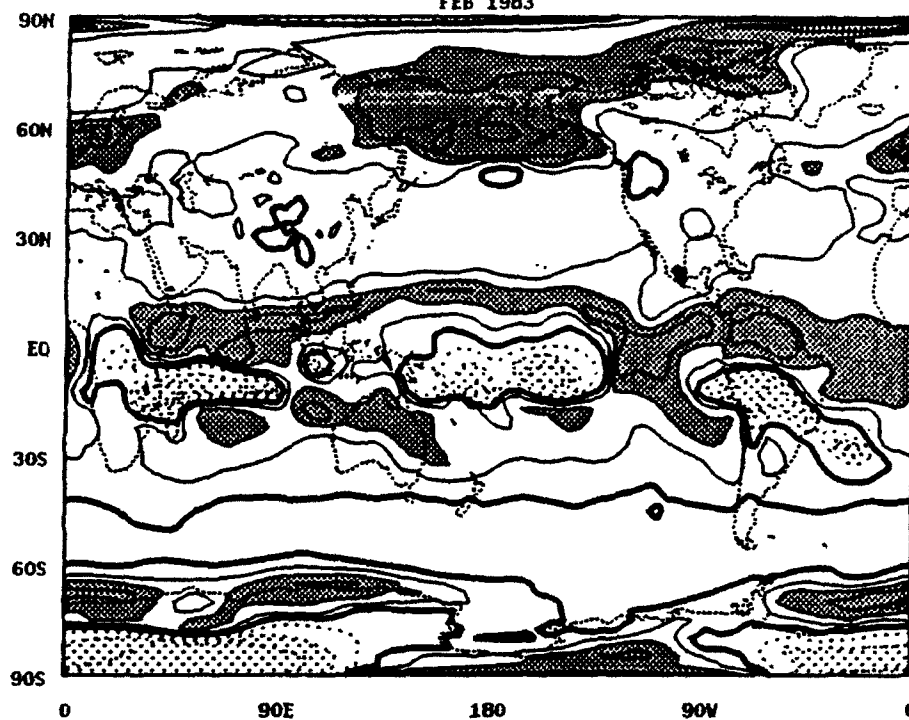
U COMPONENT OF ROTATIONAL WIND
Normalized Mode 1
FEB 1983

(b)



U COMPONENT OF ROTATIONAL WIND
Normalized Mode 2
FEB 1983

(c)



U COMPONENT OF ROTATIONAL WIND
Normalized Mode 3
FEB 1983

(d)

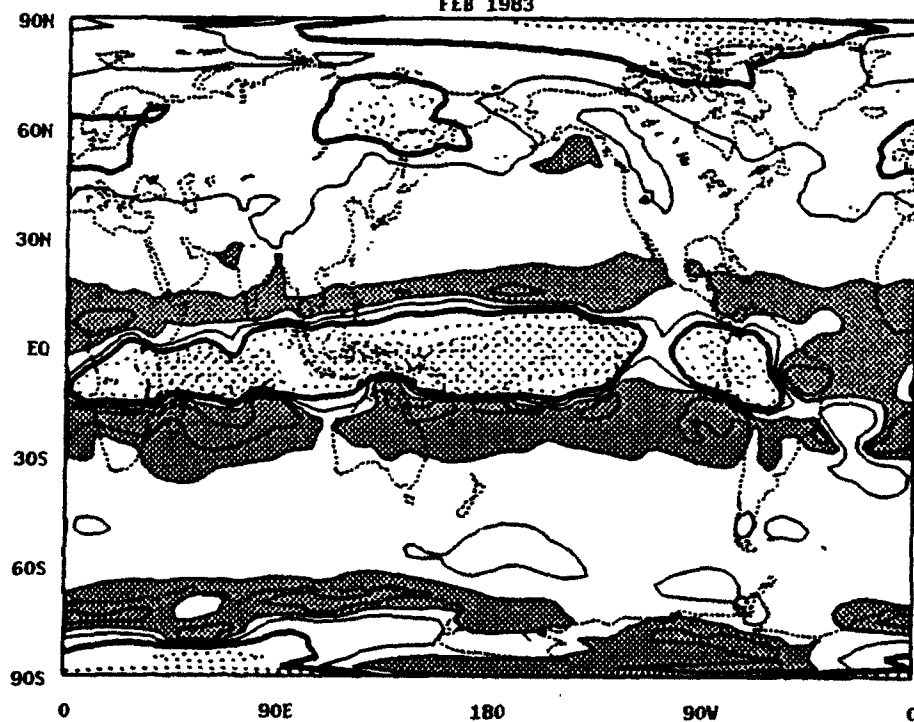
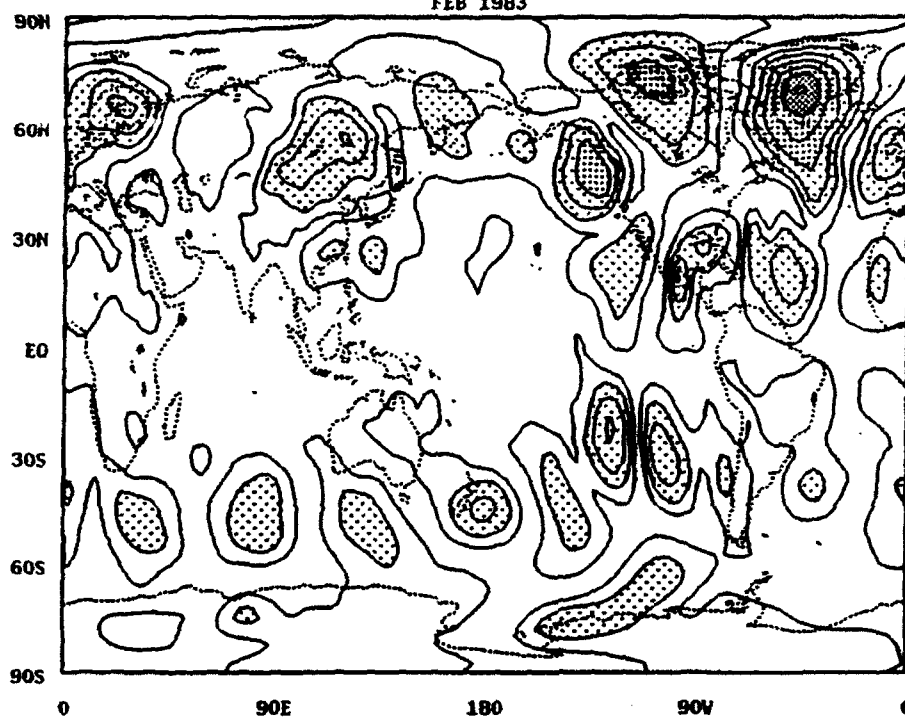


Figure 4.5. Total root mean square value (a) and normalized modes one (b), two (c), and three (d) for February 1983 meridional rotational wind. Mode contributions in (b-d) are normalized using the total root mean square value in (a). Contour interval in (a) 2.5 m s^{-1} with light shading in area of $5\text{--}10 \text{ m s}^{-1}$, medium shading for $10\text{--}15 \text{ m s}^{-1}$, and heavy shading for $15\text{--}20 \text{ m s}^{-1}$. Contour interval in (b)–(d) is 0.25 with heavy shading for areas > 0.50 and light shading for regions < -0.50 .

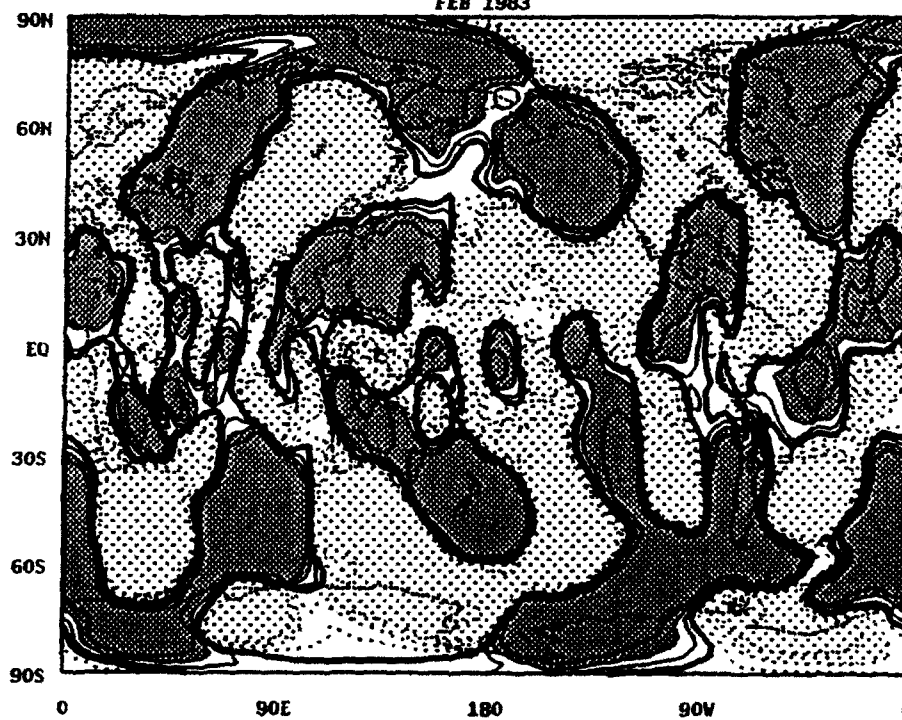
V COMPONENT OF ROTATIONAL WIND
Sum of Vertical Variability
FEB 1983

(a)



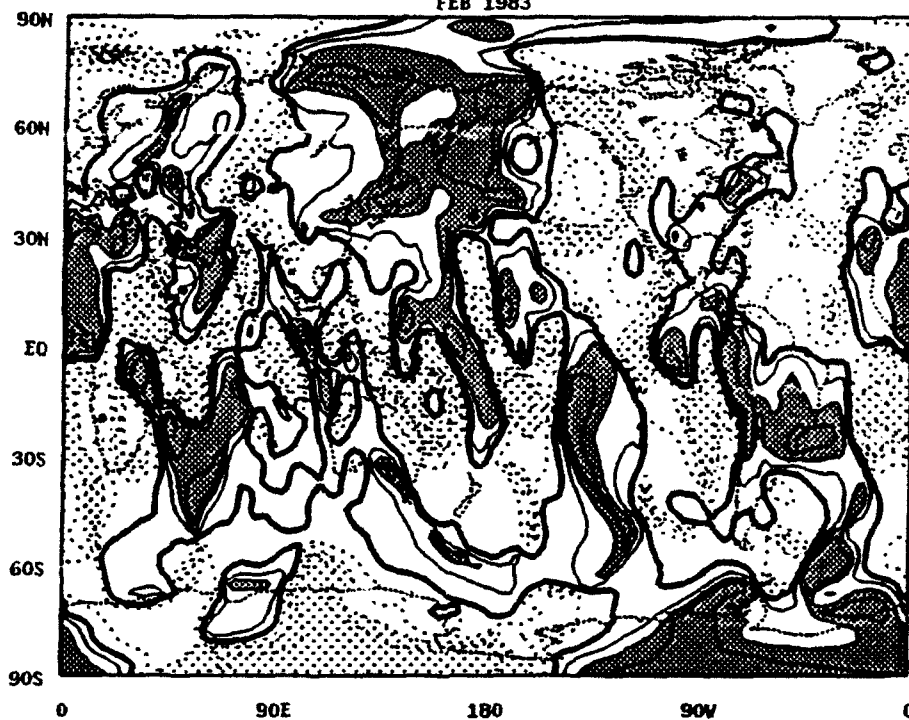
V COMPONENT OF ROTATIONAL WIND
Normalized Mode 1
FEB 1983

(b)



V COMPONENT OF ROTATIONAL WIND
Normalized Mode 2
FEB 1983

(c)



V COMPONENT OF ROTATIONAL WIND
Normalized Mode 3
FEB 1983

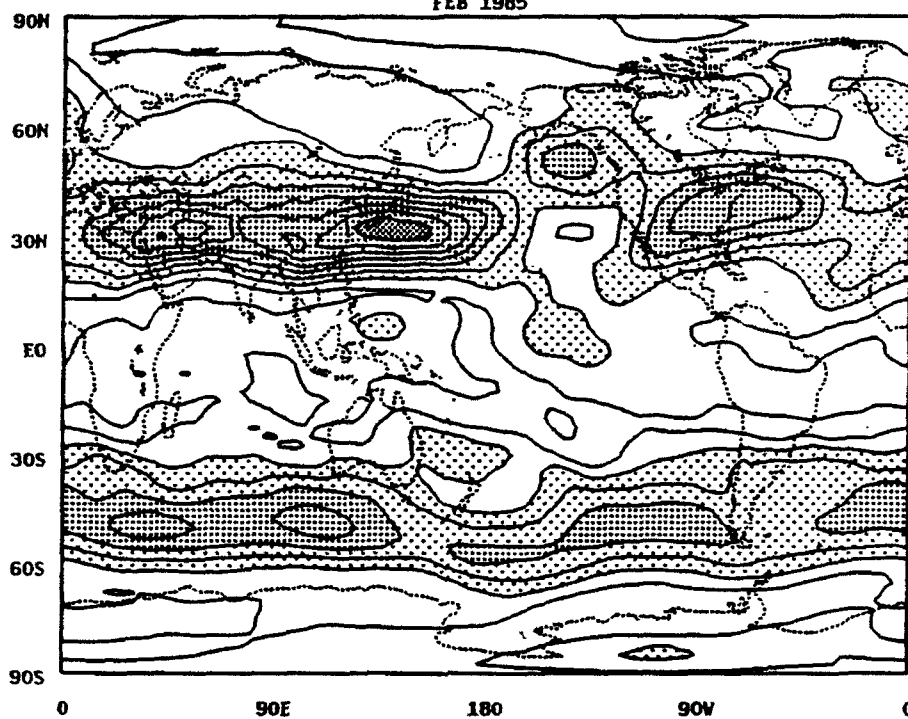
(d)



Figure 4.6. Total root mean square value (a) and normalized modes one (b), two (c), and three (d) for February 1985 zonal rotational wind. Mode contributions in (b-d) are normalized using the total root mean square value in (a). Contour interval in (a) 5 m s^{-1} with light shading in area of $10\text{--}20 \text{ m s}^{-1}$, medium shading for $20\text{--}40 \text{ m s}^{-1}$, and heavy shading for $40\text{--}60 \text{ m s}^{-1}$. Contour interval in (b)-(d) is 0.25 with heavy shading for areas > 0.50 and light shading for regions < -0.50 .

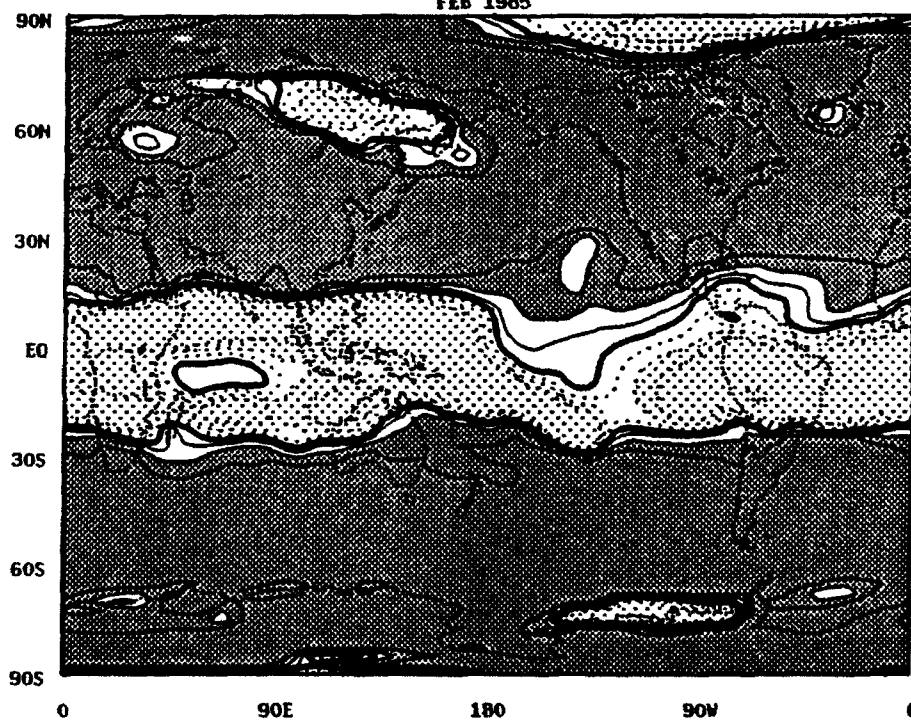
U COMPONENT OF ROTATIONAL WIND
Sum of Vertical Variability
FEB 1985

(a)



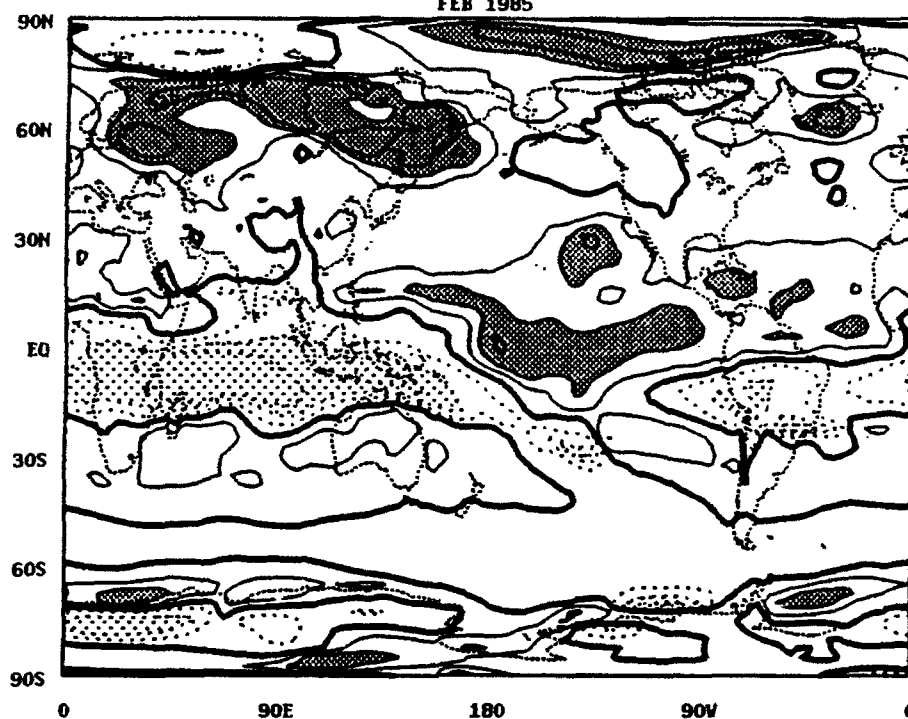
U COMPONENT OF ROTATIONAL WIND
Normalized Mode 1
FEB 1985

(b)



U COMPONENT OF ROTATIONAL WIND
Normalized Mode 2
FEB 1985

(c)



U COMPONENT OF ROTATIONAL WIND
Normalized Mode 3
FEB 1985

(d)

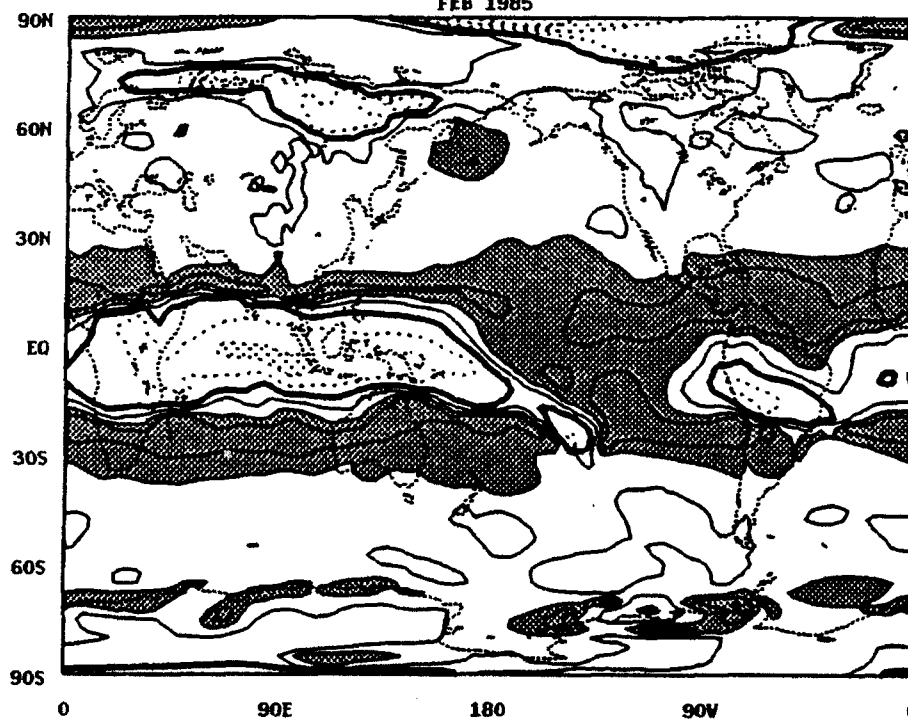
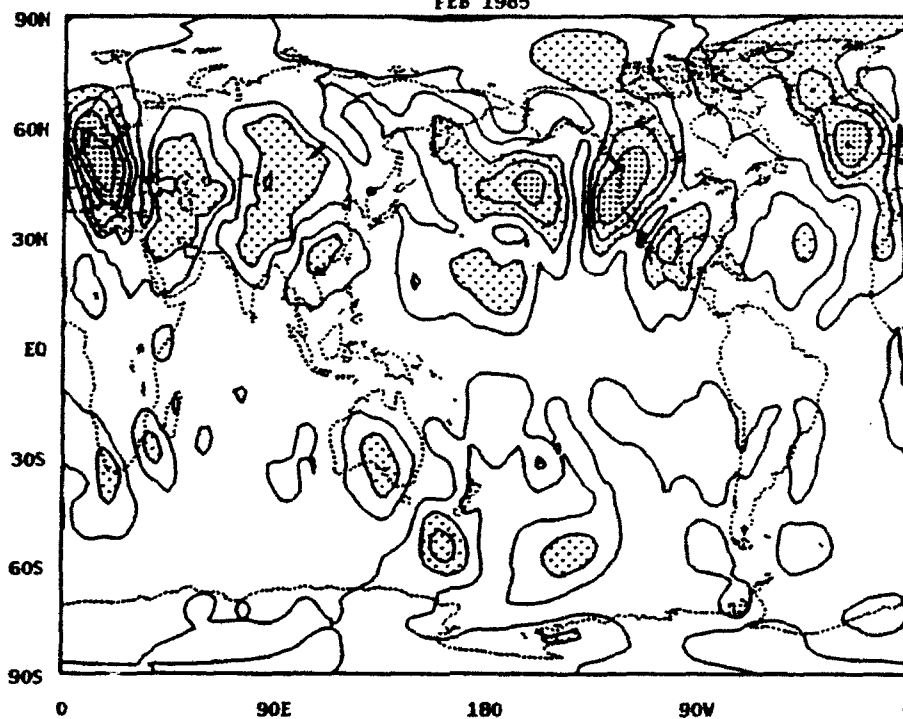


Figure 4.7. Total root mean square value (a) and normalized modes one (b), two (c), and three (d) for February 1985 meridional rotational wind. Mode contributions in (b-d) are normalized using the total root mean square value in (a). Contour interval in (a) 2.5 m s^{-1} with light shading in area of $5\text{--}10 \text{ m s}^{-1}$, medium shading for $10\text{--}15 \text{ m s}^{-1}$, and heavy shading for $15\text{--}20 \text{ m s}^{-1}$. Contour interval in (b)-(d) is 0.25 with heavy shading for areas > 0.50 and light shading for regions < -0.50 .

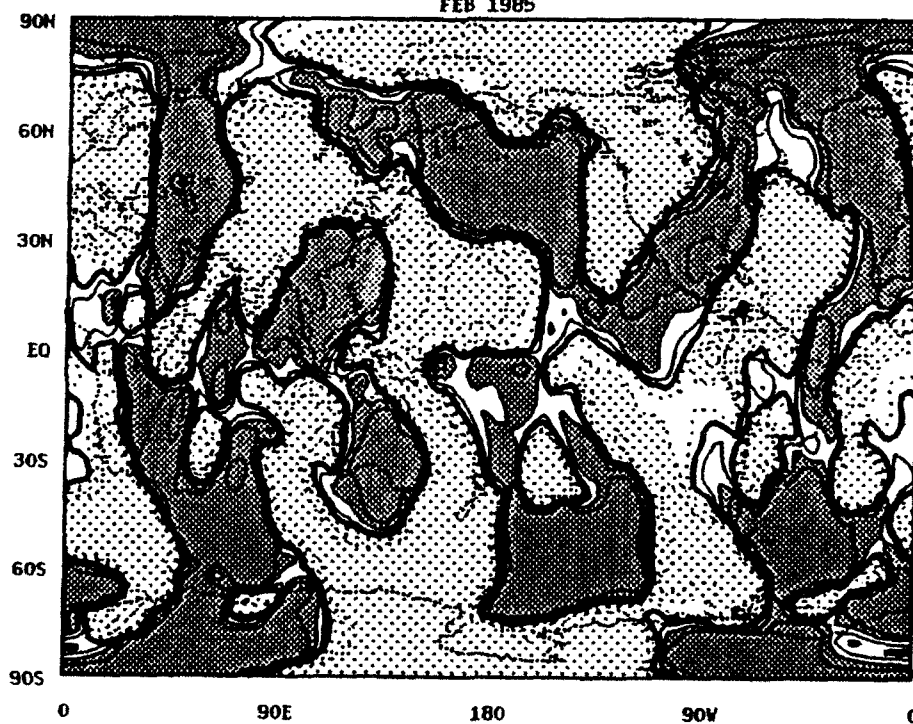
V COMPONENT OF ROTATIONAL WIND
Sum of Vertical Variability
FEB 1985

(a)



V COMPONENT OF ROTATIONAL WIND
Normalized Mode 1
FEB 1985

(b)



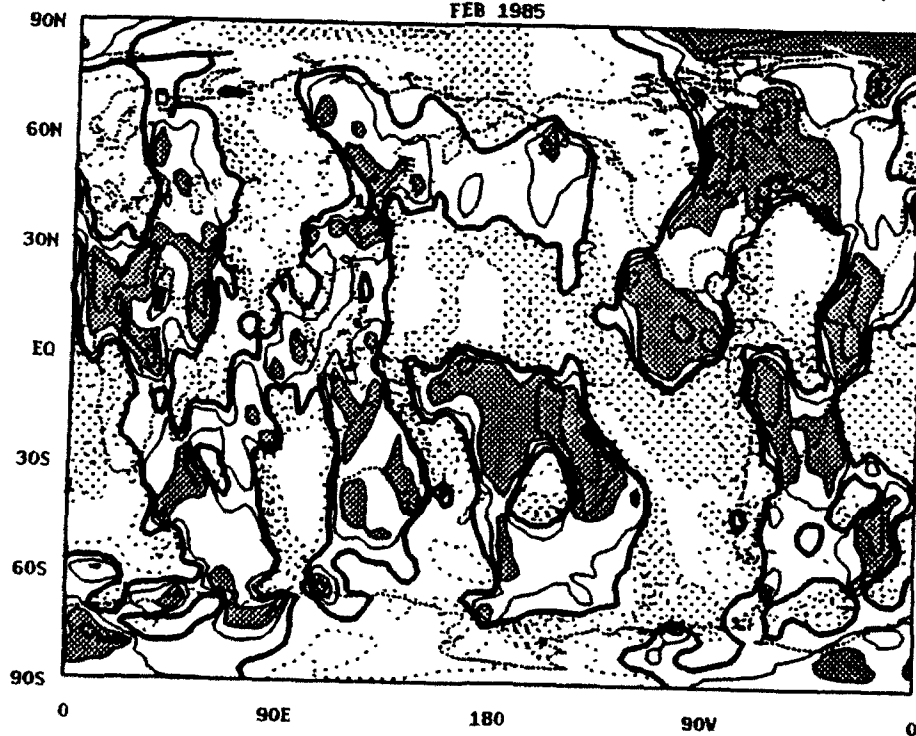
V COMPONENT OF ROTATIONAL WIND
Normalized Mode 2
FEB 1985

(c)



V COMPONENT OF ROTATIONAL WIND
Normalized Mode 3
FEB 1985

(d)



for the modes one, two, and three, which contribute most to the vertical structure.

In Fig. 4.5a there are two sets of "bull's-eyes" in the tropical meridional rotational wind. The first is between the equator and 30° N over the southwestern US and Central America, and the second is between 30° S and the equator in the eastern Pacific, off the west coast of South America. These features of the monthly averages are similar to those implied by the streamfunction anomalies in Fig. 4.2b. As with the zonal component, the second and third modes, a signature of convection, are found concentrated between 15° N and 30° S.

In the changes of the SO phases between 1983 and 1985, the center of convection shifts from the central Pacific to the maritime continent, as shown in the OLR field. The major difference in the cold phase variability (Fig. 4.6a) is the break in the NH over the eastern Pacific. This is reflected in the mode contributions from first, second, and third modes. All three modes show the signature of the SPCZ between 90° E and the dateline. Also typical of the cold phase, the maximum over North America is further north and westerlies at 200 mb are present over the eastern Pacific in the tropics. During the cold phase the internal modes extend further poleward over the eastern Pacific, off the west coasts of North and South America.

The vertical structure of the meridional rotational wind also reflects the differences between the warm and cold phases as seen by comparing Figs. 4.5 and 4.7. There is little of the total variability accounted for in the tropics and the PNA pattern is displaced towards the west (see Fig. 4.7a). This shift of the PNA pattern with the tropical convection indicates a sensitivity of the Rossby wave trains to the longitudinal location of the tropical heating. This appears to be different from the conclusions reached by Sardeshmukh and Hoskins (1988) who argued that the Rossby wave source, created through the advection of vorticity by the divergent wind, primarily depends on the location of the subtropical jet stream. In particular, the tight vorticity gradients associated with the Asian subtropical jet would render

the Rossby wave source relatively insensitive to the precise locations of the heating anomalies. The current results may be reconciled with this interpretation, if the subtropical jet streams are considered to be part of the basic state rather than part of the atmospheric response to the heating anomaly. In this case, the westward shift of the PNA pattern with the tropical convection may be ascribed to the westward shift of the subtropical jet. Nevertheless, the PE response to the tropical heating clearly indicates that both the westerly displacement of the subtropical jet and mid-latitude wave train position depends on the location of the tropical heating.

Internal structures are found to have a more important role during the cold phase than during the warm phase of the ENSO episode. This is consistent with the analysis of ENSO events by Wang (1992) who finds atmospheric flow both in the free atmosphere and boundary layer to be controlled by the convective heating during this phase. He also finds that changes in the vertical structure of the ENSO anomalies for the cold and warm phases are similar to the longitudinal variations of vertical structures typical of the equatorial Pacific Ocean. Therefore, it may be argued that the vertical structure changes observed for the cold/warm phase are due to the longitudinal migrations of the OLR anomaly.

These changes may be interpreted considering the low relative values of the static stability over the warm waters of the western Pacific and the relative high static stability values over the cold waters of the eastern Pacific. Over the western Pacific, adiabatic cooling is relatively ineffective in compensating for the convective heating, and mid-atmospheric warming takes place. This excites the internal modes, with boundary layer convergence driven by the convective overturnings. In contrast, over the eastern Pacific a well-mixed boundary layer exists under the trade wind inversion. The equatorial zonal wind responds to the zonal pressure gradients (induced by SST zonal gradients) and the boundary layer convergence is mostly due to the meridional wind convergence. It has been shown by Lindzen and Nigam

(1987) that the latitudinal variation of the Coriolis parameter plays an important role in producing meridional wind convergence in the boundary layer with boundary layer westerlies. In this case the convection is in phase with strong boundary layer westerly winds and the adiabatic cooling associated with rising motion nearly compensates the warming due to latent heat release. Then there is little or no net atmospheric warming. This results in a more complex vertical structure at lower levels with more contribution expected from higher order vertical modes.

4.1.2 1987 - 1989 ENSO

The ENSO event of 1987 was very different from the 1983 event. While the peak for the 1983 ENSO occurred in February 1983, the 1987 event did not reach its maximum until May 1987 and differed in amplitude (see Fig. 4.8). Similarly, the duration of this ENSO was on the order of 24+ months, versus 12-18 months for the former.

A direct comparison of the peak warm phases would, therefore, be difficult because of the different seasonal timing of the two episodes. However, the SO Index, upper level flow patterns, and convective activity during the NH winter season were similar to those of other ENSO events and indicate that all characteristics of the warm phase are present by February 1987. By using the same months for both the warm and cold phase, a better comparison can be made without the interference of the seasonal cycle. The atmospheric response to tropical heating can be seen in the streamfunction standing wave and velocity potential anomaly fields (Fig. 4.9) consistent with that of previous figures. Positive/negative values in the streamfunction field coincide with negative/positive values of OLR anomalies. The velocity potential anomaly field is much weaker during this period, exhibiting a wavenumber one in the tropics, but the general relationship of divergent winds —

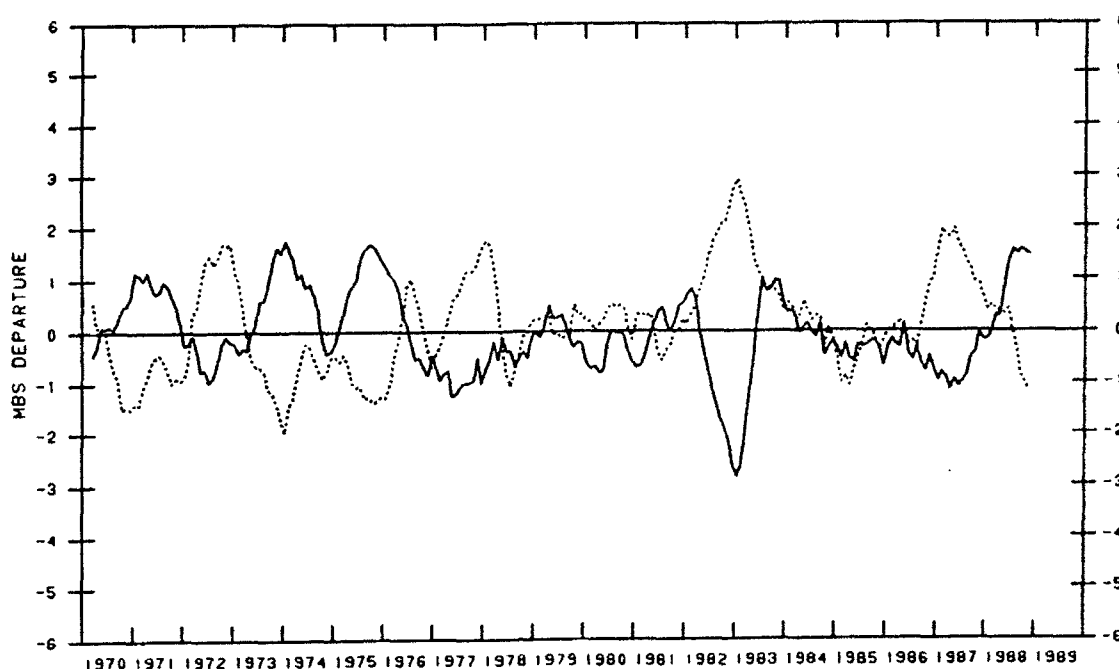


Figure 4.8. Five-month running mean of the sea level pressure anomalies at Darwin (dashed) and Tahiti (solid). Taken from *Climate Diagnostics Bulletin*, January 1989, No. 89-1, US Department of Commerce.

flowing across the gradient from regions of high OLR into regions of low OLR — still holds.

OLR anomalies are not included in Fig. 4.10. A minor problem in either the data or the processing, results in unusually high values on the equator between $\sim 100^\circ$ to 150° E (see Fig. 4.10a). However, from the pattern of the OLR, the centers of the negative anomalies can be inferred to be in much the same location as seen in Fig. 4.3. A wave train in the streamfunction field can be seen emanating from the OLR maximum over the maritime continent, reminiscent of February 1985. The general pattern of the velocity potential anomaly, however, looks more like that of February 1983. This again points to the high degree of variability between individual ENSO events.

The vertical structure of the warm phase for 1987 has features both similar and

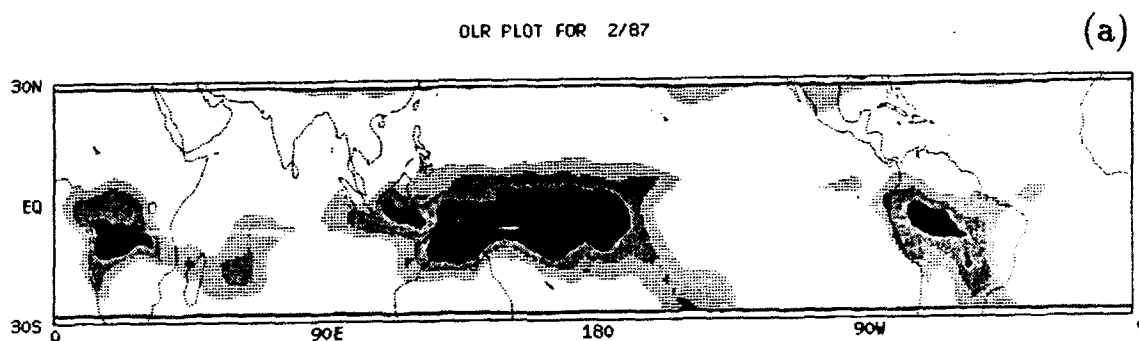
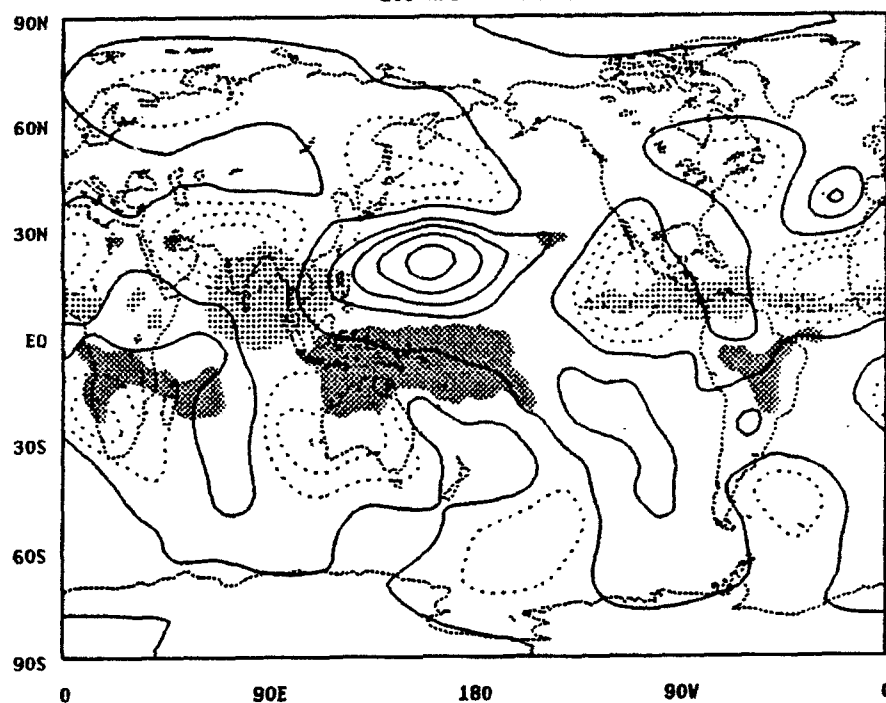


Figure 4.9. Monthly mean OLR (a), 200 mb streamfunction (b) and velocity potential (c) with OLR anomaly superimposed for February 1987. Shading for OLR described in text. Contours intervals are $0.5 \times 10^7 \text{ m}^2 \text{ s}^{-1}$ in (b) and $1 \times 10^6 \text{ m}^2 \text{ s}^{-1}$ in (c).

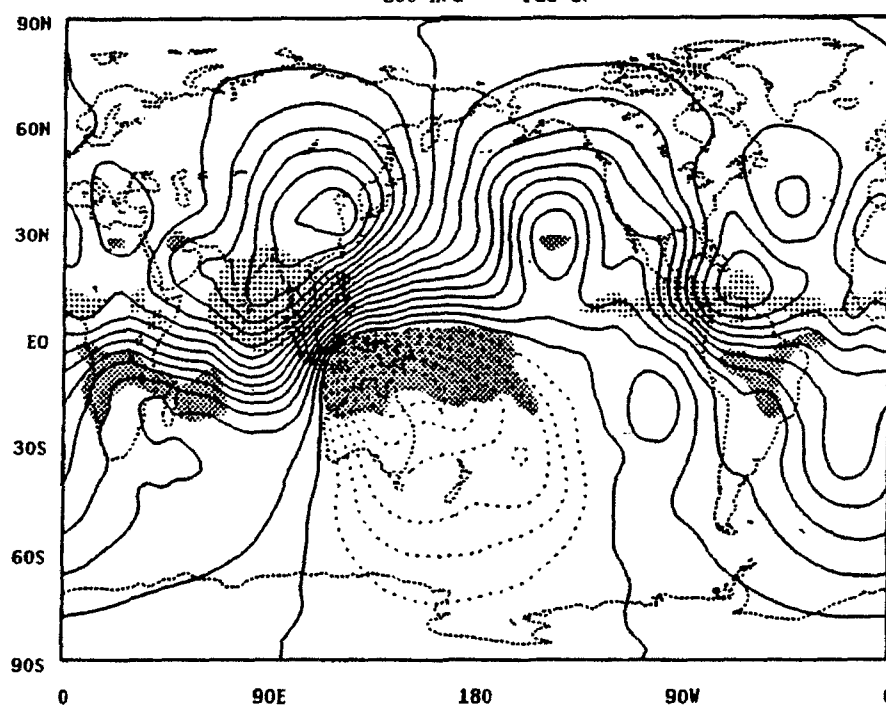
Streamfunction Perturbation and OLR Anomaly
200 hPa FEB 87

(b)



Velocity Potential and OLR Anomaly
200 hPa FEB 87

(c)



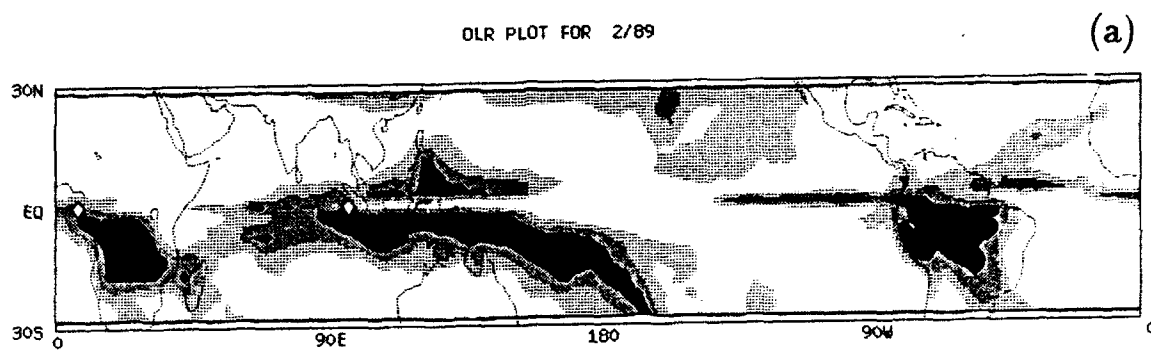
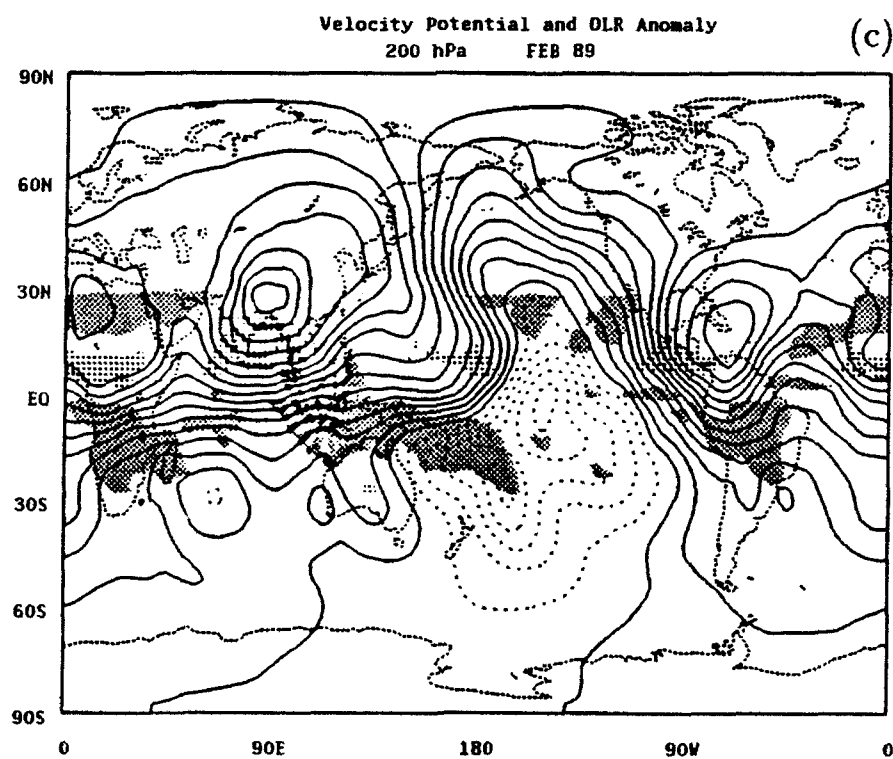
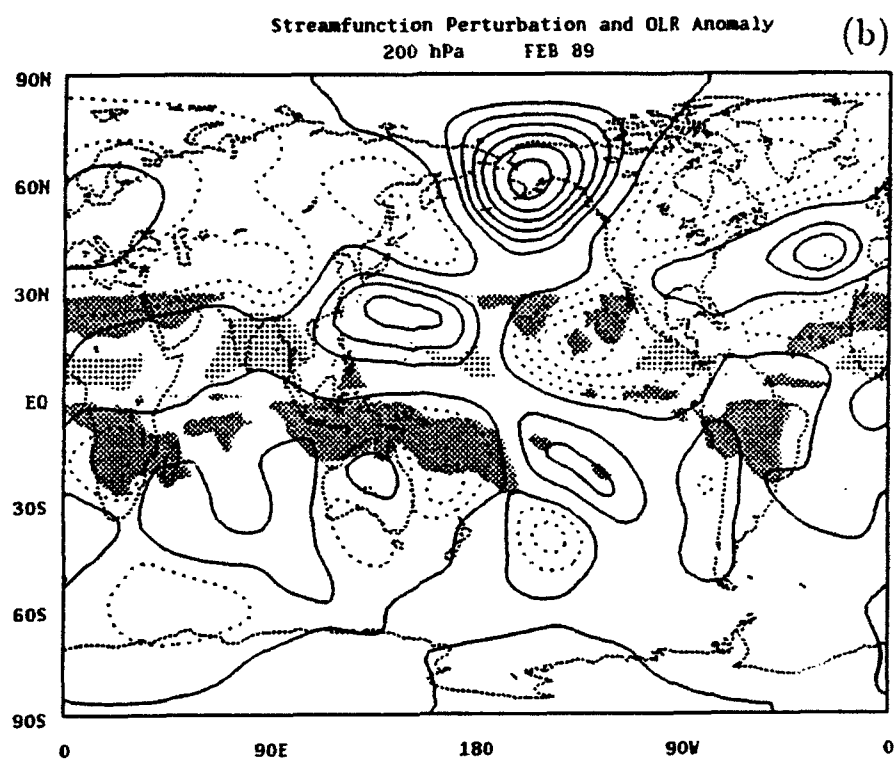


Figure 4.10. Monthly mean OLR (a), 200 mb streamfunction (b) and velocity potential (c) with OLR anomaly superimposed for February 1989. Shading for OLR described in text. Contours intervals are $0.5 \times 10^7 \text{ m}^2 \text{ s}^{-1}$ in (b) and $1 \times 10^6 \text{ m}^2 \text{ s}^{-1}$ in (c).



dissimilar to those of 1983. As stated previously, some of the dissimilarity may be due to the difference in the timing of maximum amplitude of the ENSO events (May 87 vs. February 83). The external mode contribution in the zonal rotational wind (Fig. 4.11b) is again significant over most of the globe, with the exception of the eastern tropical Pacific. The response in the internal modes (Fig. 4.11c,d) reflect the migrating convection. The pattern of the second mode is unlike that for the 83 warm phase in that the easterly and westerly winds are confined to the western and eastern Pacific, respectively, instead of a belt of tropical easterlies stretching across the tropical Pacific and straddled by westerlies. It is also interesting to note the strong response at high latitudes in the external and first internal modes. These could be indicative of the influence of the stratospheric polar jets being felt in the upper troposphere. The first internal mode possesses a vertical profile that rapidly increases with height, necessary for the structure of the stratospheric jet.

The vertical structure of the meridional rotational component (Fig. 4.12) is similar to that of February 1983. The vertically reversing circulation of the mode two/three combination is seen off the coast of South America. Additionally, the shift from internal to external modes occurs in most locations not only longitudinally, but latitudinally as well.

This is also seen in the cold phase of this ENSO event. The pattern of the zonal rotational wind in Fig. 4.13 looks nearly identical to that February 1985. The exceptions are the strength of the internal modes at high latitudes and the extent of the vertically reversing mode three in the central and eastern Pacific. The meridional flow (Fig. 4.14) depicts more structure in the tropics than any other period, except that of February 1983, with the strongest responses at high latitudes.

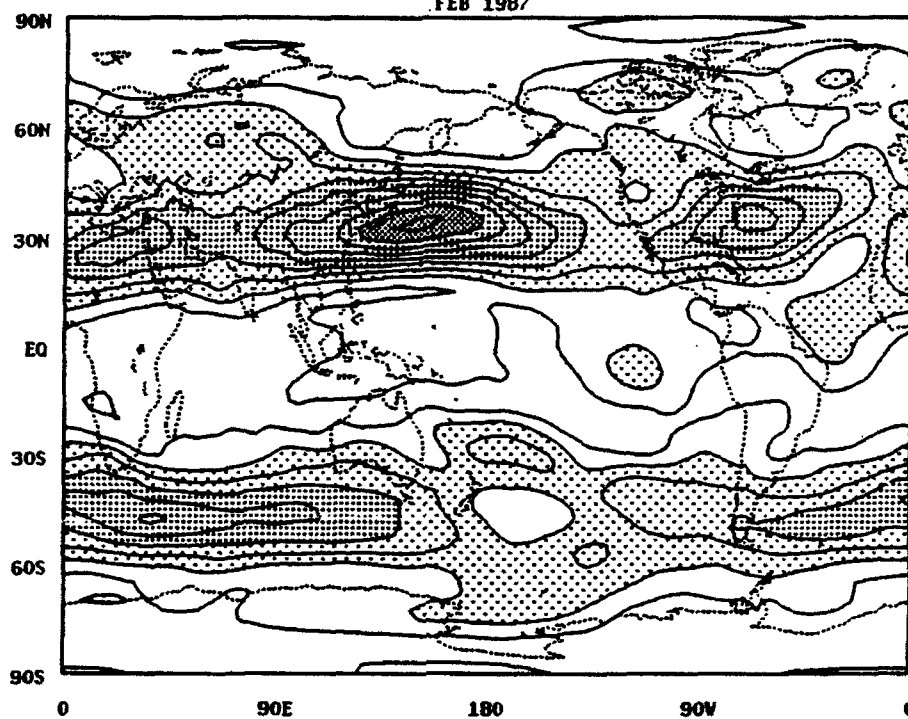
Internal modes on smaller zonal scales for the meridional component (i.e. at much higher wavenumbers), particularly in the tropics.

Up to this point, the focus for El Niño years has been on the excess heating

Figure 4.11. Total root mean square value (a) and normalized modes one (b), two (c), and three (d) for February 1987 zonal rotational wind. Mode contributions in (b-d) are normalized using the total root mean square value in (a). Contour interval in (a) 5 m s^{-1} with light shading in area of $10\text{--}20 \text{ m s}^{-1}$, medium shading for $20\text{--}40 \text{ m s}^{-1}$, and heavy shading for $40\text{--}60 \text{ m s}^{-1}$. Contour interval in (b)-(d) is 0.25 with heavy shading for areas > 0.50 and light shading for regions < -0.50 .

U COMPONENT OF ROTATIONAL WIND
Sum of Vertical Variability
FEB 1987

(a)



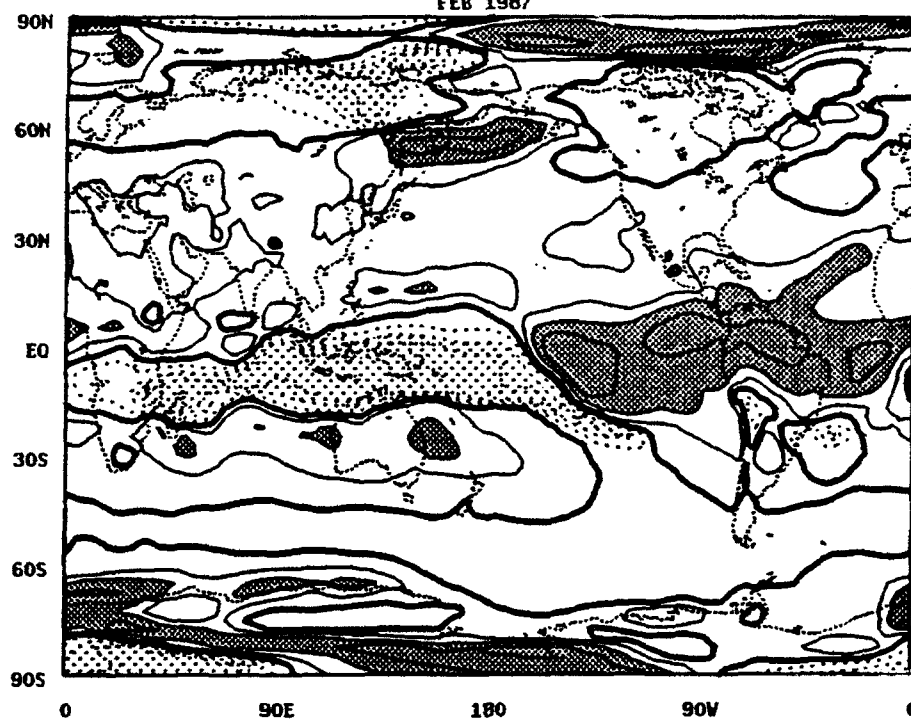
U COMPONENT OF ROTATIONAL WIND
Normalized Mode 1
FEB 1987

(b)



U COMPONENT OF ROTATIONAL WIND
Normalized Mode 2
FEB 1987

(c)



U COMPONENT OF ROTATIONAL WIND
Normalized Mode 3
FEB 1987

(d)

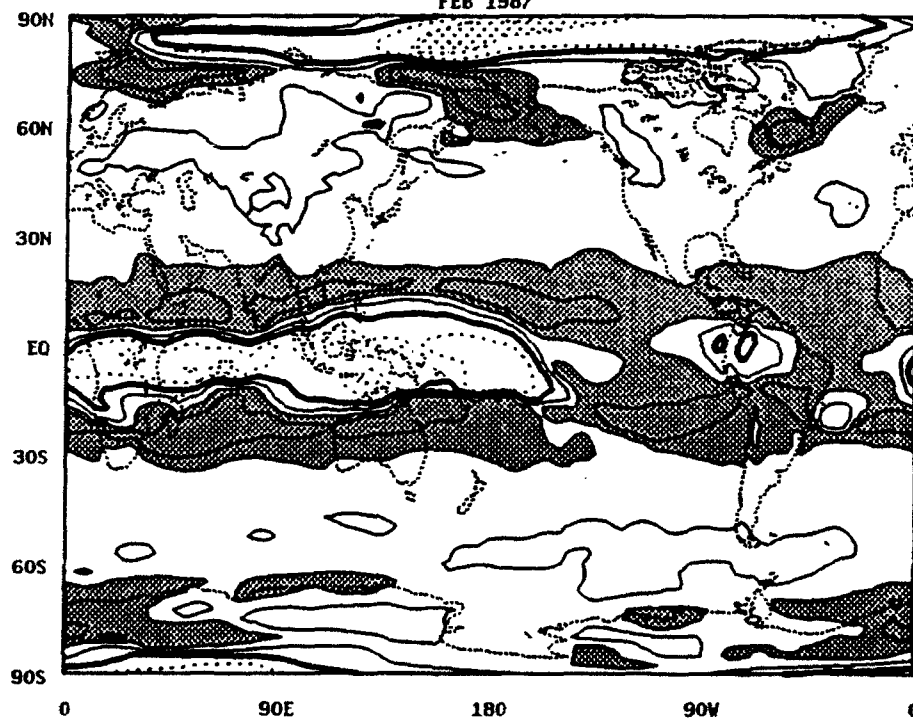
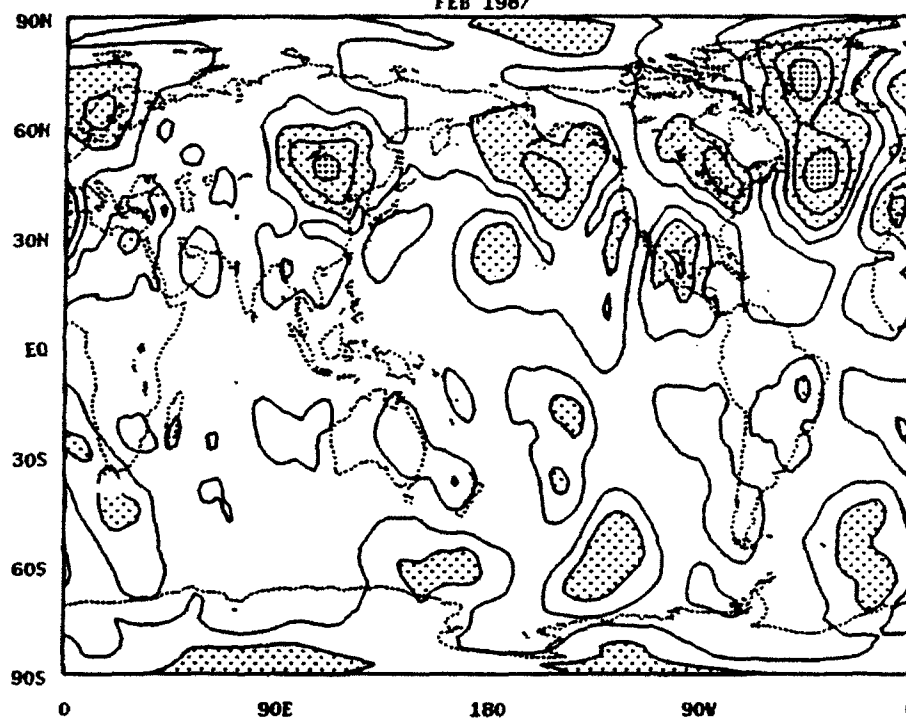


Figure 4.12. Total root mean square value (a) and normalized modes one (b), two (c), and three (d) for February 1987 meridional rotational wind. Mode contributions in (b-d) are normalized using the total root mean square value in (a). Contour interval in (a) 2.5 m s^{-1} with light shading in area of $5\text{--}10 \text{ m s}^{-1}$, medium shading for $10\text{--}15 \text{ m s}^{-1}$, and heavy shading for $15\text{--}20 \text{ m s}^{-1}$. Contour interval in (b)-(d) is 0.25 with heavy shading for areas > 0.50 and light shading for regions < -0.50 .

V COMPONENT OF ROTATIONAL WIND
Sum of Vertical Variability
FEB 1987

(a)



V COMPONENT OF ROTATIONAL WIND
Normalized Mode 1
FEB 1987

(b)



V COMPONENT OF ROTATIONAL WIND
Normalized Mode 2
FEB 1987

(c)



V COMPONENT OF ROTATIONAL WIND
Normalized Mode 3
FEB 1987

(d)

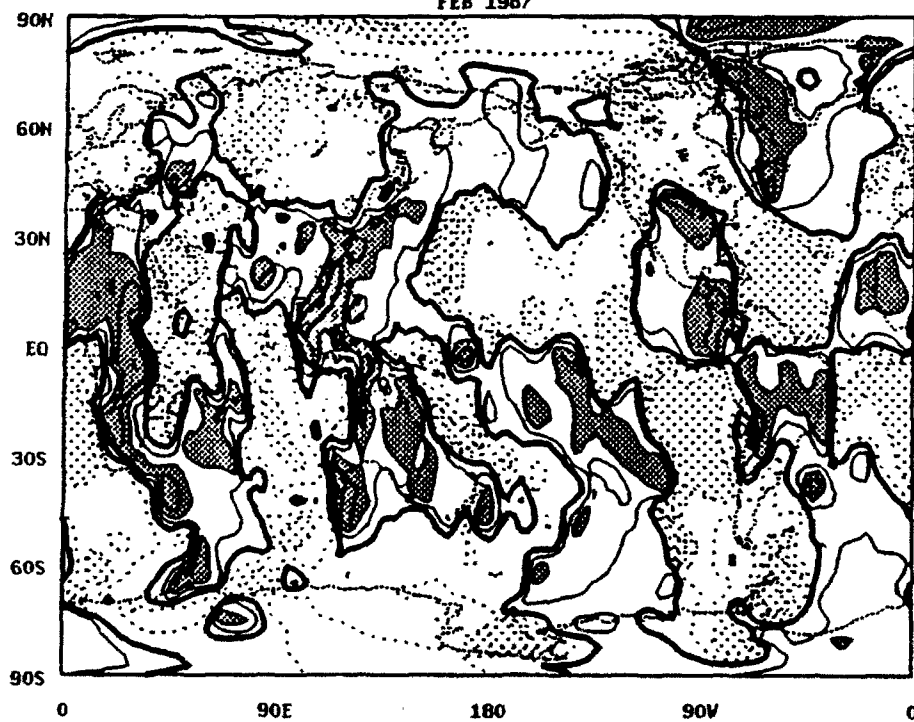
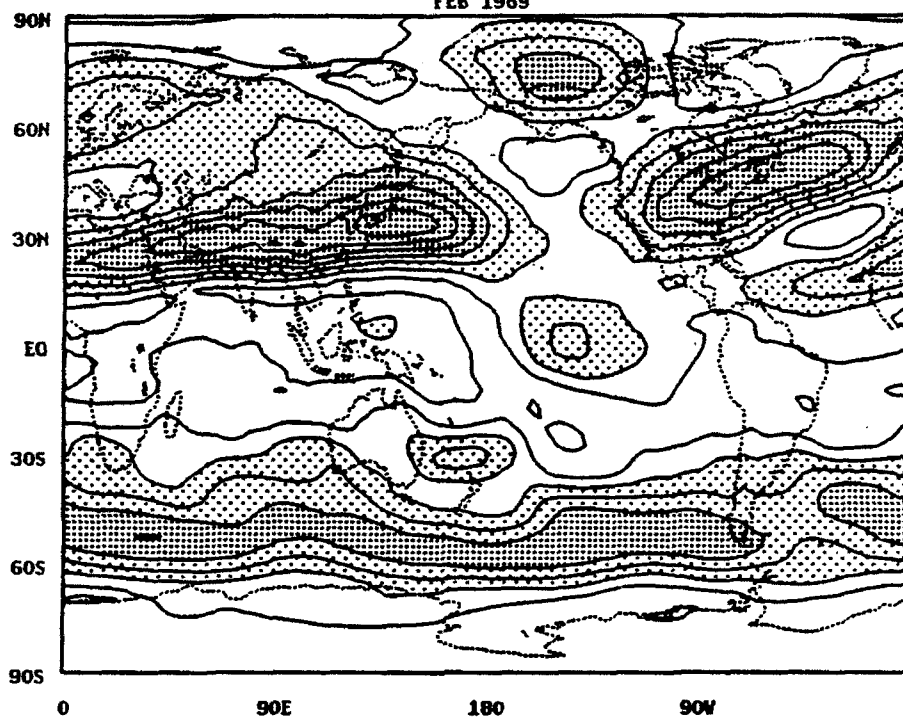


Figure 4.13. Total root mean square value (a) and normalized modes one (b), two (c), and three (d) for February 1989 zonal rotational wind. Mode contributions in (b-d) are normalized using the total root mean square value in (a). Contour interval in (a) 5 m s^{-1} with light shading in area of $10\text{--}20 \text{ m s}^{-1}$, medium shading for $20\text{--}40 \text{ m s}^{-1}$, and heavy shading for $40\text{--}60 \text{ m s}^{-1}$. Contour interval in (b)–(d) is 0.25 with heavy shading for areas > 0.50 and light shading for regions < -0.50 .

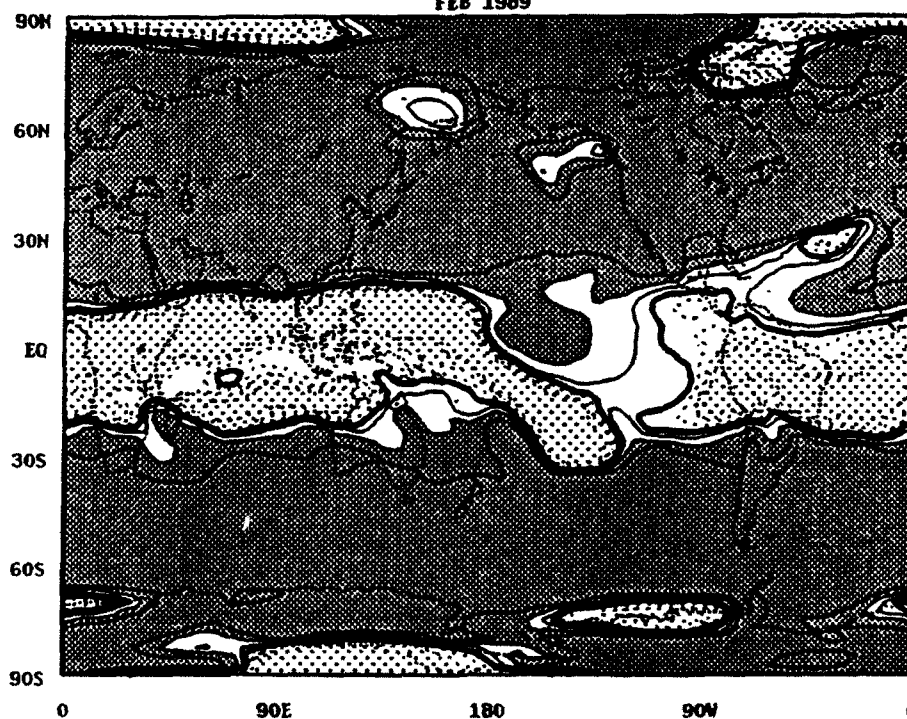
U COMPONENT OF ROTATIONAL WIND
Sum of Vertical Variability
FEB 1989

(a)



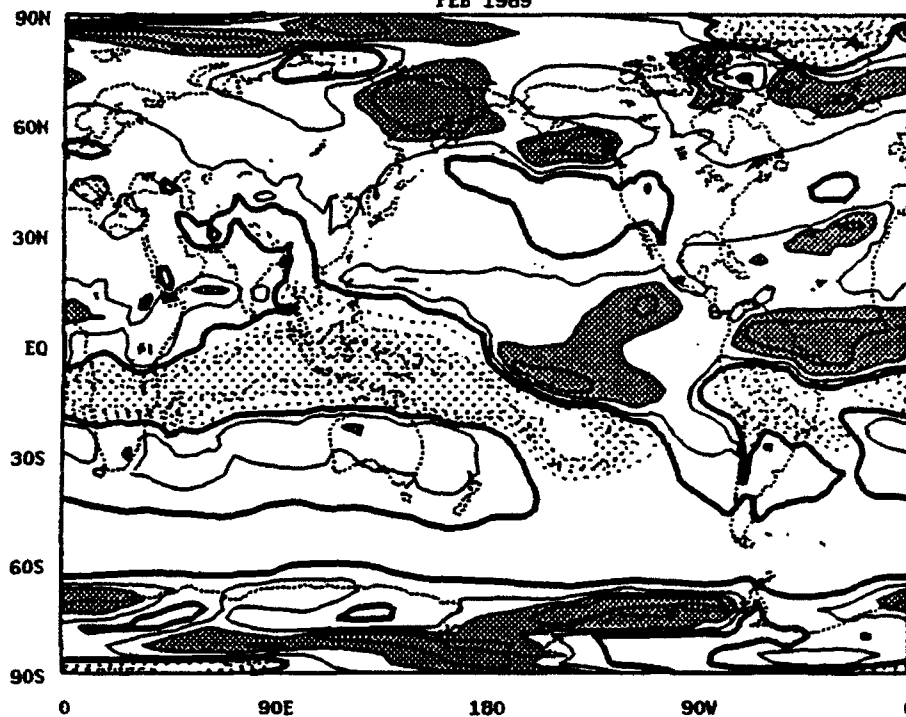
U COMPONENT OF ROTATIONAL WIND
Normalized Mode 1
FEB 1989

(b)



U COMPONENT OF ROTATIONAL WIND
Normalized Mode 2
FEB 1989

(c)



U COMPONENT OF ROTATIONAL WIND
Normalized Mode 3
FEB 1989

(d)

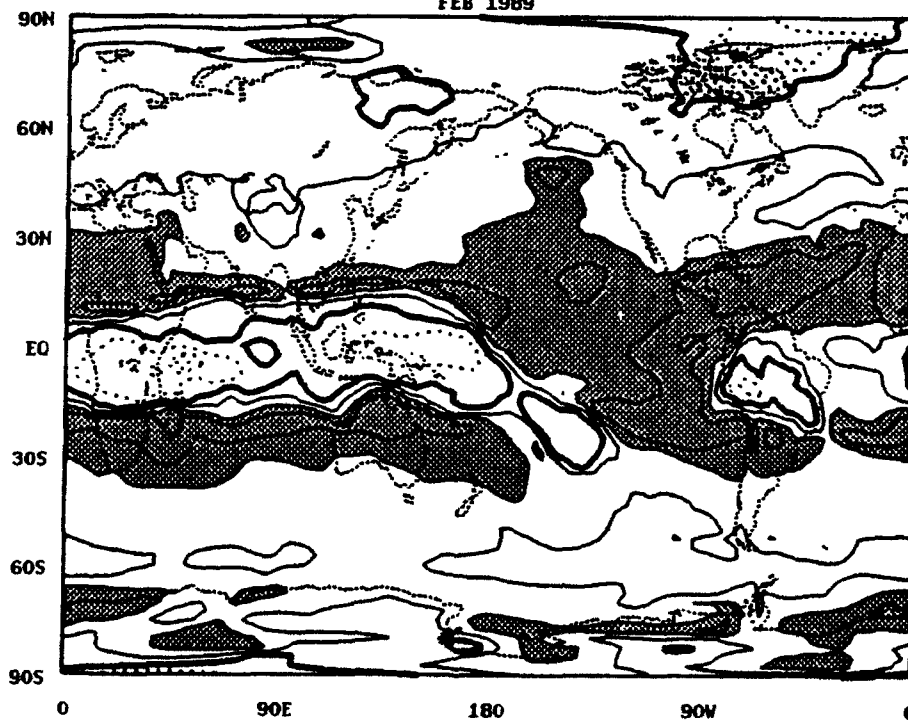
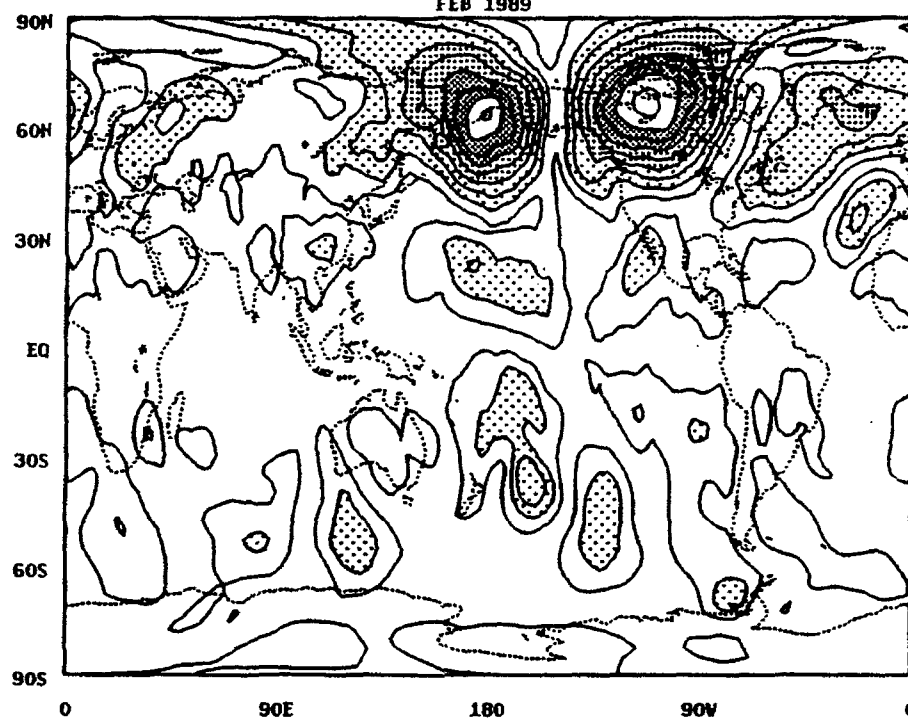


Figure 4.14. Total root mean square value (a) and normalized modes one (b), two (c), and three (d) for February 1989 meridional rotational wind. Mode contributions in (b-d) are normalized using the total root mean square value in (a). Contour interval in (a) 2.5 m s^{-1} with light shading in area of $5\text{--}10 \text{ m s}^{-1}$, medium shading for $10\text{--}15 \text{ m s}^{-1}$, and heavy shading for $15\text{--}20 \text{ m s}^{-1}$. Contour interval in (b)-(d) is 0.25 with heavy shading for areas > 0.50 and light shading for regions < -0.50 .

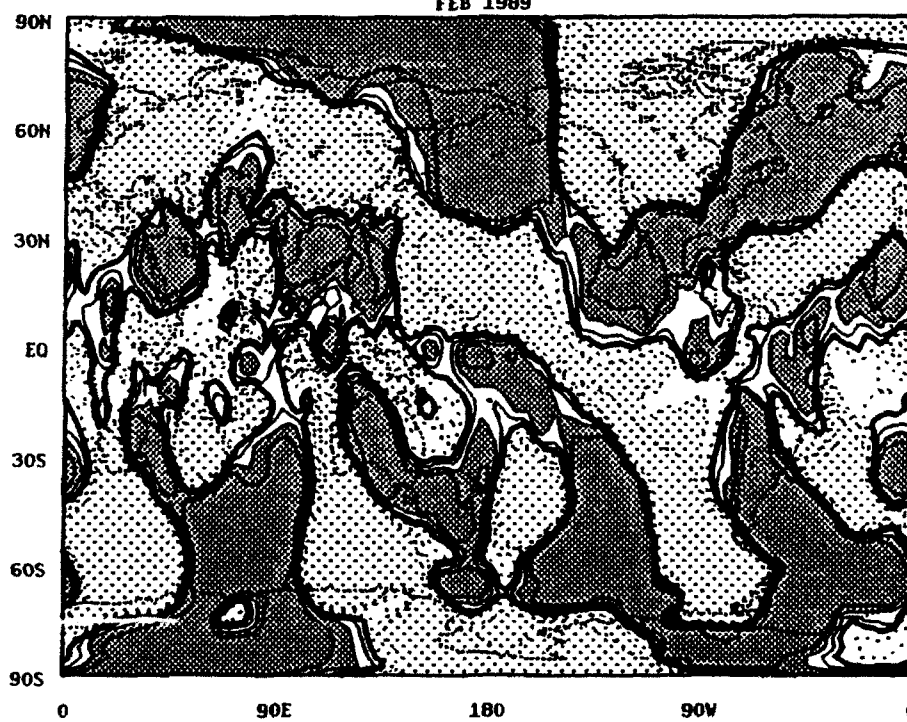
V COMPONENT OF ROTATIONAL WIND
Sum of Vertical Variability
FEB 1989

(a)



V COMPONENT OF ROTATIONAL WIND
Normalized Mode 1
FEB 1989

(b)



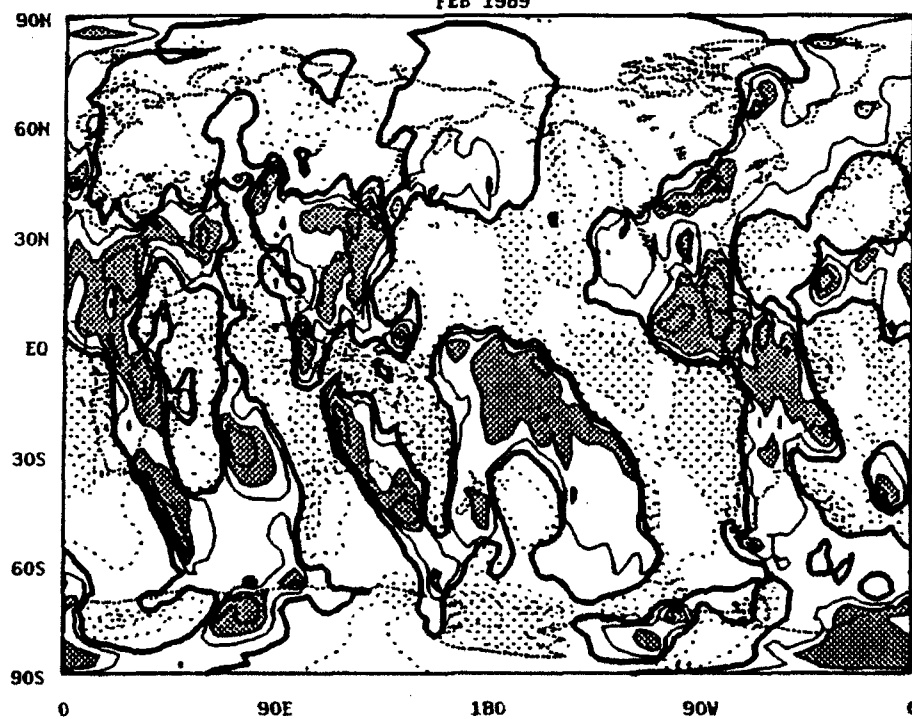
V COMPONENT OF ROTATIONAL WIND
Normalized Mode 2
FEB 1989

(c)



V COMPONENT OF ROTATIONAL WIND
Normalized Mode 3
FEB 1989

(d)



inferred from the OLR and the resulting Rossby waves emanating from the tropics and their associated vertical structure. However, this heating tends to strengthen the Hadley Cell, as seen in the velocity potential field of Figs. 4.2c, 4.3c, 4.9c and 4.10c. Using a simple form of the u-momentum equation,

$$\frac{d\bar{u}}{dt} - f\bar{v} = 0, \quad (4.1)$$

and the conservation of angular momentum, it is apparent that any increase in the strength of the Hadley Cell will lead to an increase in the subtropical zonally-averaged wind. The impact of the 1983 ENSO event on the zonally-averaged wind is shown in Fig. 4.15.

Because the Hadley Cell is strongest in the winter hemisphere, the effect will be most pronounced north of the equator at this time. The difference between the warm and cold phase is on the order of 15 m s^{-1} between $20\text{--}30^\circ \text{ N}$. Outside the tropics, differences between the two phases are smaller. Within the framework of linear theory, excitation of waves on a constant basic state depends on the nature of the forcing. Figure 4.15 shows no anomalous zonally-averaged zonal wind at latitudes with significant orographic relief. We may tentatively conclude, within this interpretation, that the observed anomalous patterns in the extratropics may not be directly linked with orographic forcing, and are, instead, more directly related to tropical forcing which changes from the warm to cold phase of the ENSO. This is also consistent with the conclusions already stated in conjunction with the PE model integrations. Although the magnitude does not approach that of the NH, the effect of the tropical forcing can also be seen in the SH.

In summary, this section has discussed the vertical structure of the warm and cold phase of the ENSO episodes, linking the more dominant contributions of the lower vertical modes to the vertical structure during the cold phase of the oscillation to the location of the convection over the warm pool of the western Pacific. Also,

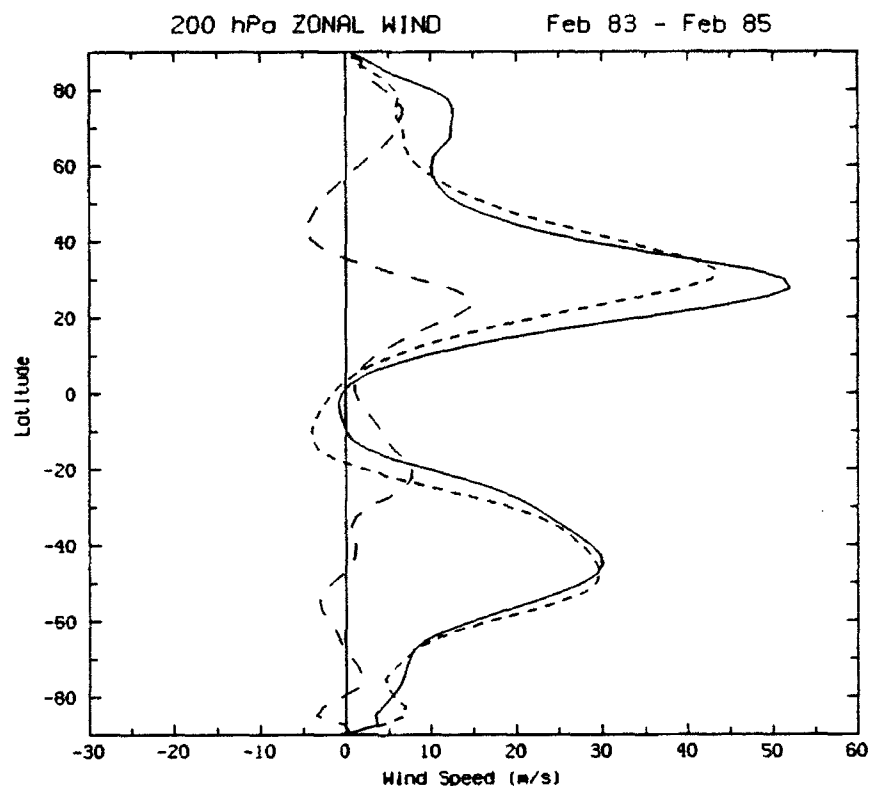


Figure 4.15. 200 mb zonal wind representing the warm phase of February 1983 (solid), the cold phase of February 85 (short dashed), and their difference [83 - 85](medium dash).

the longitudinal shift of the subtropical jet and the extratropical wave patterns were linked to the observed longitudinal shifts in convection. In the next section we focus on the third scale of pronounced convective variability; the intraseasonal oscillation and consider its dependence on the seasonal cycle and interannual variations.

4.2 Intraseasonal Oscillations

The 30–60 day oscillation, and related slow oscillations of the tropics and extratropics have received increased attention since the early papers of Madden and Julian (1971, 1972) (e.g., Krishnamurti and Gadgil 1985; Weickmann et al. 1985; Lau and Chan 1985; Knutson et al. 1986; Nogués-Paegle et al. 1989; Ghil and Mo

1991a,b) and several theories about its origin and maintenance have been offered (e.g., Yamagata and Hayashi 1984; Chao 1987; Lau and Peng 1987; Emanuel 1987; Neelin et al. 1987). Several of these studies have pointed out the existence of a dominant wave one in the tropical velocity potential. The study of Murakami (1988), among others, points out the erratic behavior of the 30-60 day oscillation, with periods of well defined easterly propagation associated with pronounced extra-tropical response, embedded in periods of stagnant or irregular zonal propagation. In contrast, Liebmann and Hartmann (1984) conclude that on this time scale the tropics do not influence mid-latitudes in a systematic fashion. The recent study of Gutzler and Madden (1989) has described this oscillation with a "two-regime" character in the global tropics. Across the western Pacific and Indian Ocean the oscillation is found during all seasons and it is coupled to convection. In other locations, the oscillation is present only in the upper troposphere, it is seasonally dependent (maximizing during boreal winter) and it is not coupled with convection — their "dry" regime. The purpose of this section is to isolate cases when the "convective" regime is well defined. This is done based on the wave one component of the upper tropospheric computations of the velocity potential.

4.2.1 Equatorial Wave One Statistics

As mentioned, from year to year the intraseasonal oscillations exhibit large variations in phase, amplitude and frequency. Even within the same year, the 30-60 day oscillations contain short-term, irregular high-frequency variations. To see this, the pentad values of the amplitude and phase of the 200 mb velocity potential for wavenumber one, averaged between 5° N to 5° S, were plotted on a dial diagram for each season for the years 1982 through 1988. The annual maximum values for each season are included in Table 4.1. The amplitude is strongest during the boreal summer, with a secondary maximum during winter. The minima occur during

Table 4.1. Pentad (PTD) for which annual seasonal maxima (in units of $10^6 \text{ m}^2 \text{ s}^{-1}$), amplitude (AMP), and phase occurred for wave one component of the 200 mb velocity potential field. Velocity potential is averaged between 5° N - 5° S .

YR	DJF			MAM			JJA			SON		
	AMP	PHASE	PTD	AMP	PHASE	PTD	AMP	PHASE	PTD	AMP	PHASE	PTD
82	91	20	12	84	7	13	115	140	45	80	112	54
83	79	102	11	87	135	30	114	116	35	78	104	57
84	138	130	10	125	122	30	178	130	34	131	131	49
85	154	139	3	130	143	16	186	124	35	144	128	51
86	146	103	11	79	70	21	130	128	47	111	101	49
87	98	137	5	155	133	17	146	151	39	118	144	53
88	109	152	4	93	109	21	112	153	39	53	155	58
AVG	116	112	8	108	103	21	140	135	39	102	125	53

the spring and fall transitions. Maximum summer amplitudes are found between 116° and 153° E, within the convective region of Gutzler and Madden (1989).

With the exception of the El Niño years, the 30–60 day oscillation signal in the OLR data of Lau and Chan (1986) disappears east of the dateline. However, with the ENSO, as precipitation migrates away from the maritime continent into the central Pacific, the 30–60 day signal moves across the dateline, to the west coast regions of North/South America. As a result, over the last few years observational studies have led researchers to try to establish a connection between the 30–60 day oscillation and ENSO (e.g., Lau and Chan, 1985, 1986, 1988). The statistics presented in Table 4.1 do not reflect Lau and Chan's (1988) results which suggest an intensification of the 30–60 day oscillation prior to the onset and suppression during the decay phase of the ENSO.

The movement and variability of these impulses can also be seen in the 200 mb velocity potential field, averaged between 5° N to 5° S (Figs. 4.16, 4.17, 4.18). Examination of the annual departures of wave one components to the χ_{200} reveals that the 30–60 day oscillation signal is most easily identifiable during the months of March, April, and May (Fig. 4.16), taking an average of 11 pentads, or 55 days to circle the globe. During JJA, the χ_{200} exhibits a dipole structure, and like the OLR, impulses generated in the Indian Ocean do not persist past 180° . During the last months of the year, the impulses, for the most part, go full circle around the globe, but at an average speed of 40 days. These three distinct patterns in the 200 mb velocity potential were composited to examine global patterns at the times of pronounced convection for different seasons. Although only three pentads are used for each composite, the oscillations are chosen over different years so as to be in phase with one another.

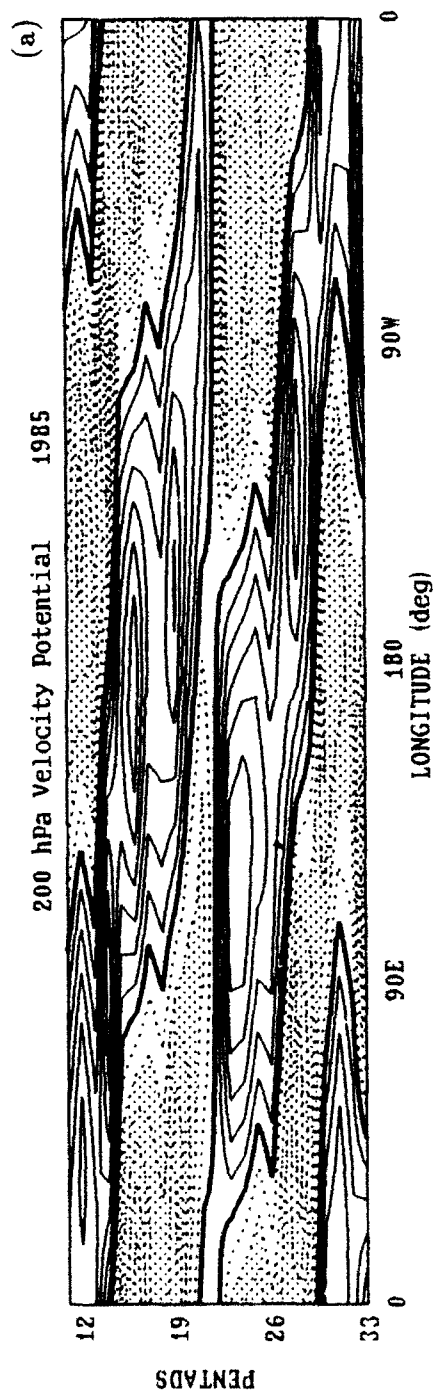
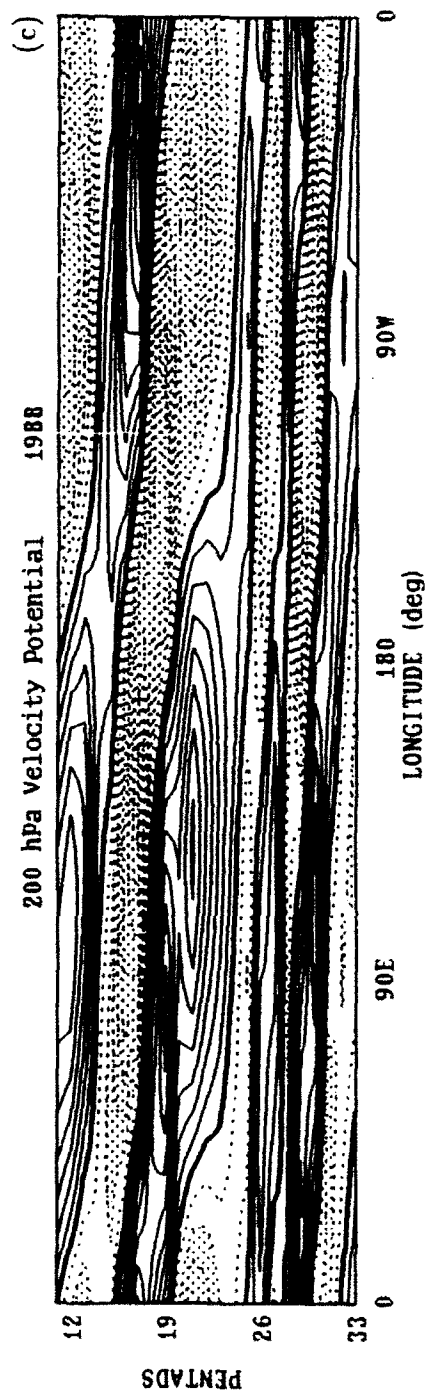
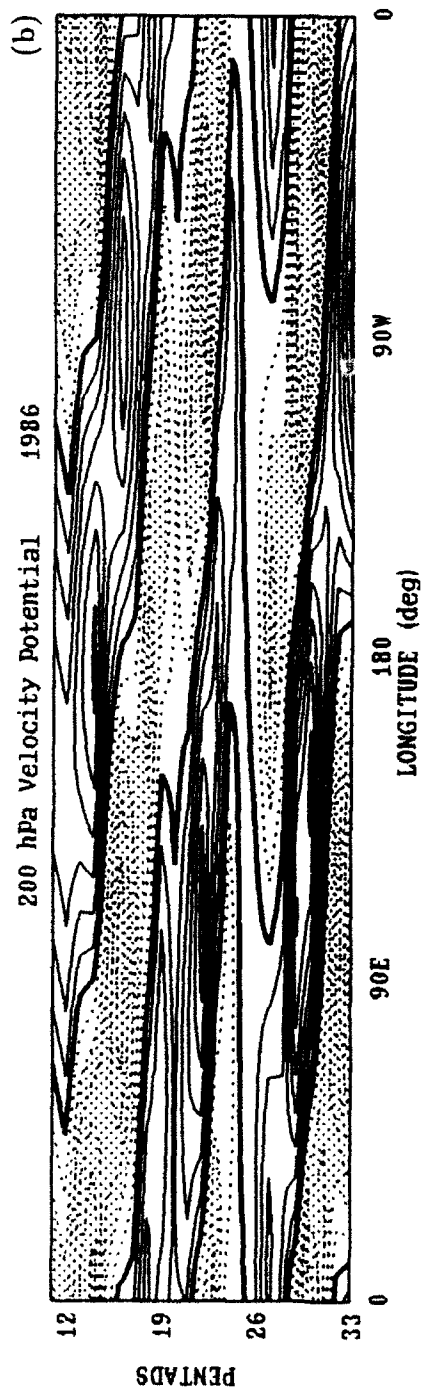


Figure 4.16. Wave one contribution of mean equatorial 200 mb velocity potential (averaged from 5° N to 5° S) during pentads 11–33 for (a) 1985, (b) 1986, and (c) 1988. Contour interval $1 \times 10^7 \text{ m}^2 \text{ s}^{-1}$ and shading for areas less than $-2 \times 10^7 \text{ m}^2 \text{ s}^{-1}$.



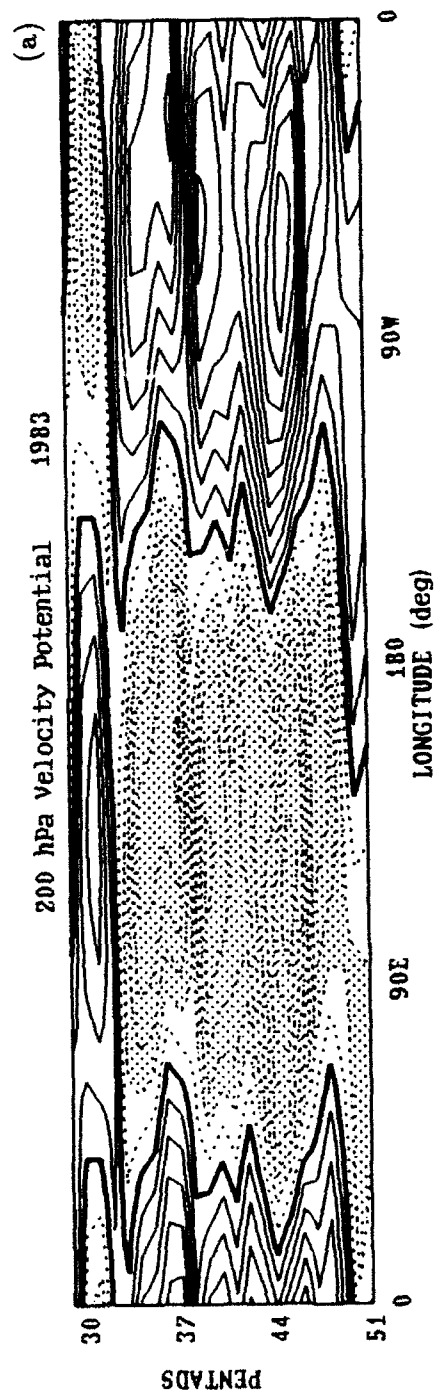
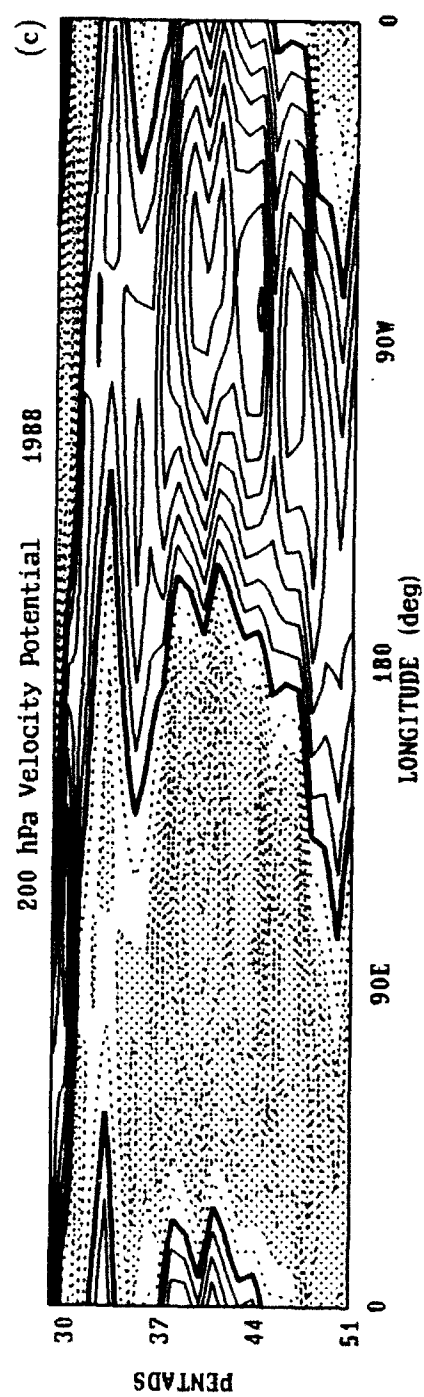
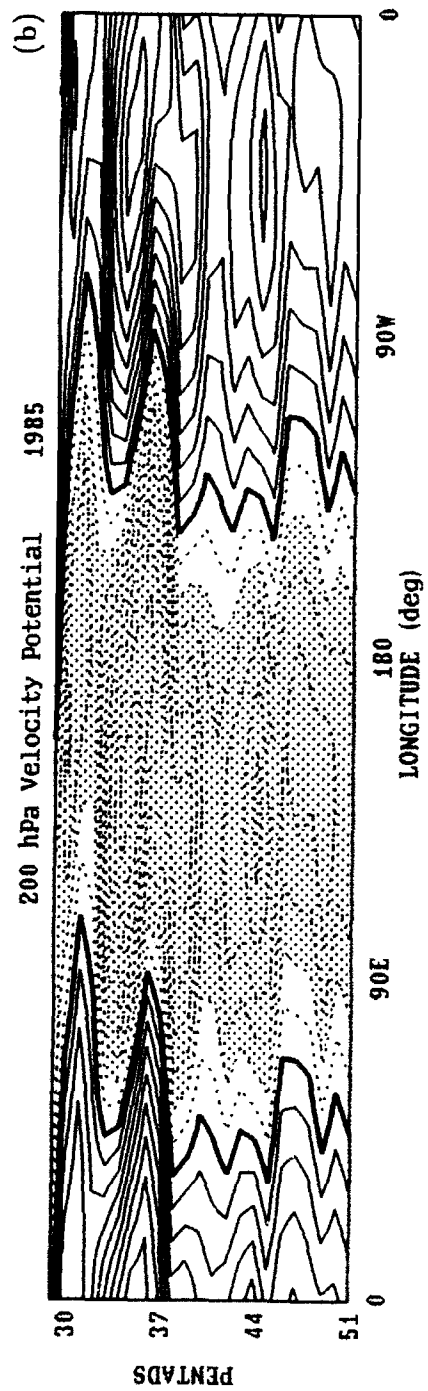


Figure 4.17. Wave one contribution of mean equatorial 200 mb velocity potential (averaged from 5° N to 5° S) during pentads 29–51 for (a) 1983, (b) 1985, and (c) 1988. Contour interval $1 \times 10^7 \text{ m}^2 \text{ s}^{-1}$ and shading for areas less than $-2 \times 10^7 \text{ m}^2 \text{ s}^{-1}$.



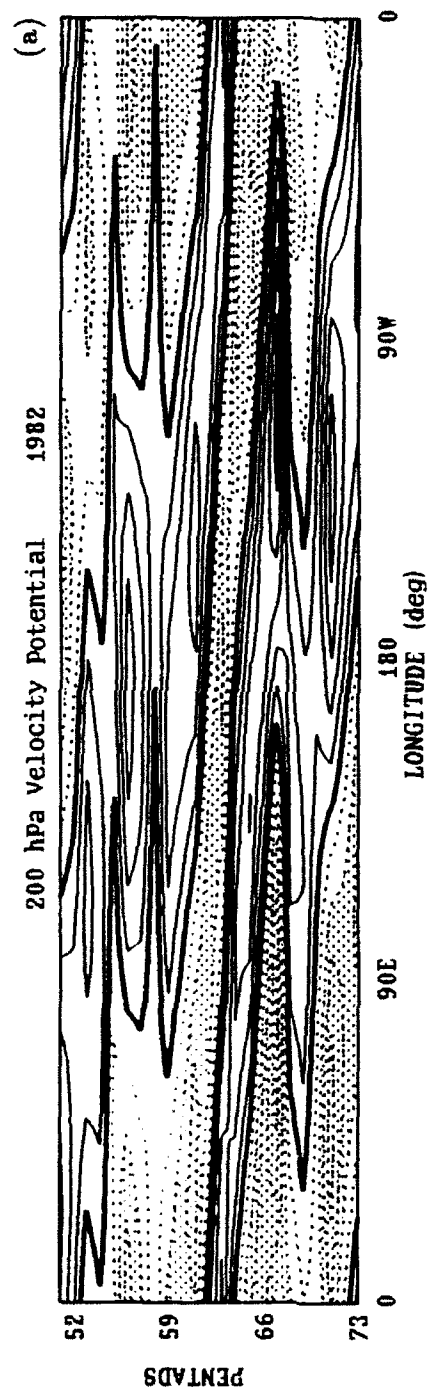
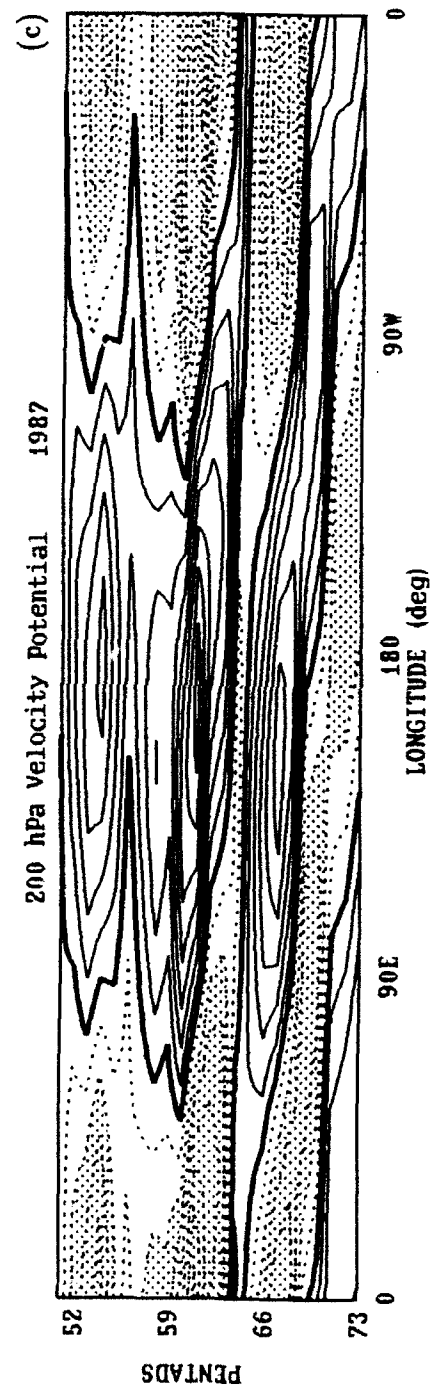
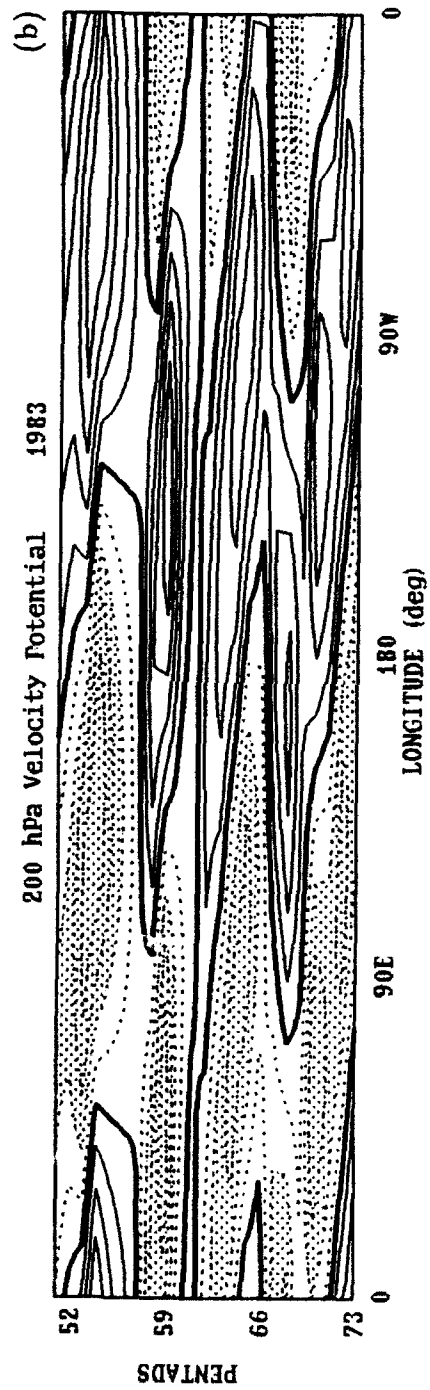


Figure 4.18. Wave one contribution of mean equatorial 200 mb velocity potential (averaged from 5° N to 5° S) during pentads 51–73 for (a) 1982, (b) 1983, and (c) 1987. Contour interval $1 \times 10^7 \text{ m}^2 \text{ s}^{-1}$ and shading for areas less than $-2 \times 10^7 \text{ m}^2 \text{ s}^{-1}$.



4.2.2 Global Departures from the Annual Mean

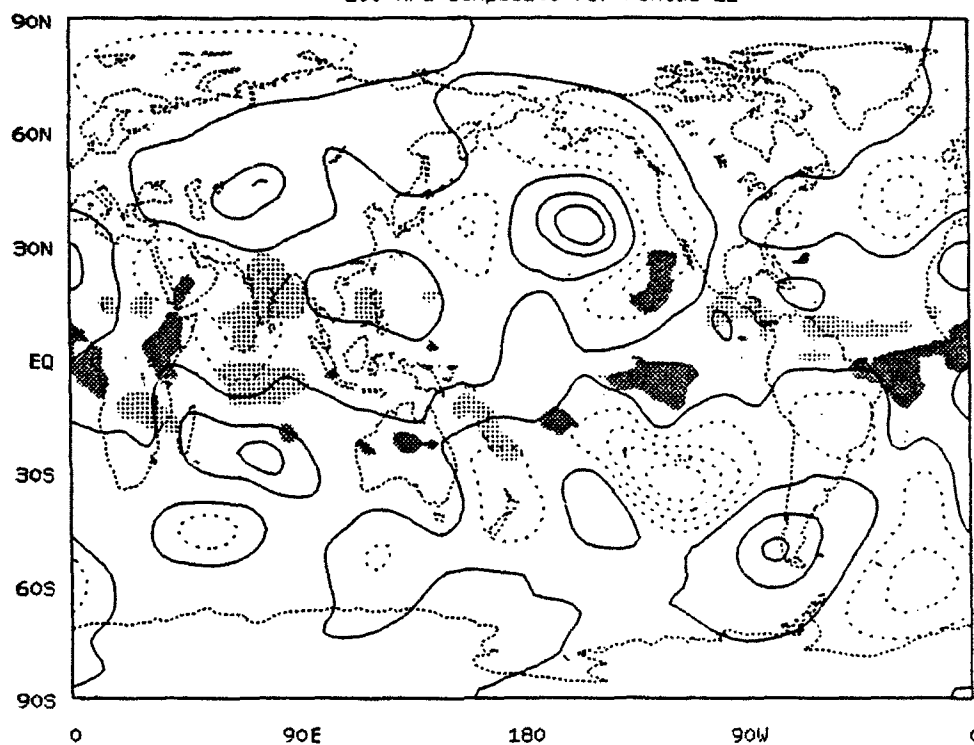
Three composites were formed for the three different phases of the 30-60 day oscillation as discussed above; pentad 22 to represent the transition season, pentad 40 to represent the summer monsoon, and pentad 67 to represent the boreal winter. The annual mean has been removed to filter out interannual variations discussed in the previous section. The remaining "anomalies" contain both seasonal and intraseasonal signals. In Chapter 3, the extent to which the seasonally varying tropical convection may be invoked to explain the observed global response on an annually-averaged basic state was discussed. In the previous section we discussed the interannual flow variations and interpreted the results in terms of propagation of ENSO anomalies (annual average removed) in the same basic state. In the present section, a different approach is taken. We consider now, for each season, a composite of cases with active tropical convection for each season. Because seasonal changes are strongly modulated by the intraseasonal oscillations in the tropics we use instances with well defined "convective" phases to select cases for the composites, and consider deviations from that year's average. We study these composites to assess whether the added signal of the intraseasonal oscillation to the seasonal signal modifies our previous conclusions.

The same relationships found earlier in Chapter 3 for seasonal variations in the streamfunction perturbation, velocity potential anomaly, and OLR anomaly in relation to the warm and cold phases of ENSO still hold for the composite pentads (Figs. 4.19, 4.20, 4.21). Excess heating, inferred from the negative OLR anomalies, force a response in the streamfunction and velocity potential fields at 200 mb. In the composite for pentad 22 (see Fig. 4.19) the main sources of heating in the tropics are over southern Africa, the eastern Pacific, and stretching across the Atlantic from the east coast of South America to west Africa. The ITCZ and summer monsoon have yet to reach their peak and the SPCZ is weakening as

Figure 4.19. Streamfunction (a) and velocity potential (b) anomalies with OLR anomalies superimposed for composite pentad 22. OLR anomaly shading describe in text. Contours in (a) every $0.5 \times 10^7 \text{ m}^2 \text{ s}^{-1}$ and in (b) every $1 \times 10^6 \text{ m}^2 \text{ s}^{-1}$. Maximum value of divergent wind in (b) of 4.5 m s^{-1} near 3° N , 48° E .

Streamfunction Perturbation and OLR Anomaly
200 hPa Composite for Pentad 22

(a)



Velocity Potential and Divergent Wind Anomaly
200 hPa Composite for Pentad 22

(b)

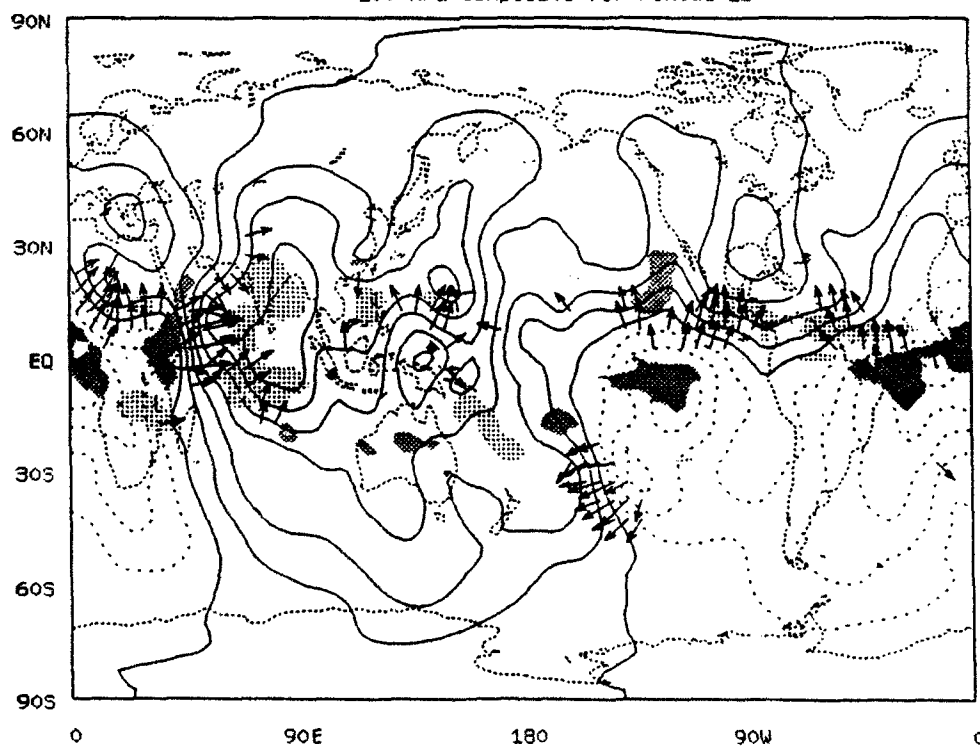
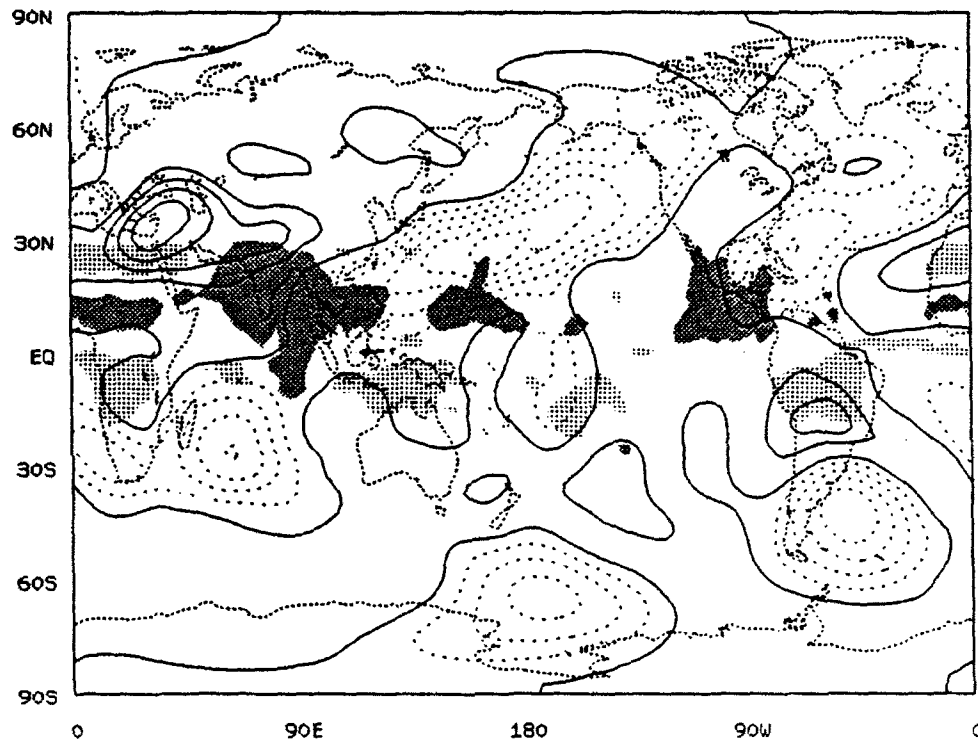


Figure 4.20. Streamfunction (a) and velocity potential (b) anomalies with OLR anomalies superimposed for composite pentad 40. OLR anomaly shading describe in text. Contours in (a) every $0.5 \times 10^7 \text{ m}^2 \text{ s}^{-1}$ and in (b) every $1 \times 10^6 \text{ m}^2 \text{ s}^{-1}$. Maximum value of divergent wind in (b) of 4.7 m s^{-1} near 3° N , 34° E .

Streamfunction Perturbation and OLR Anomaly
200 hPa Composite for Pentad 40

(a)



Velocity Potential and Divergent Wind Anomaly
200 hPa Composite for Pentad 40

(b)

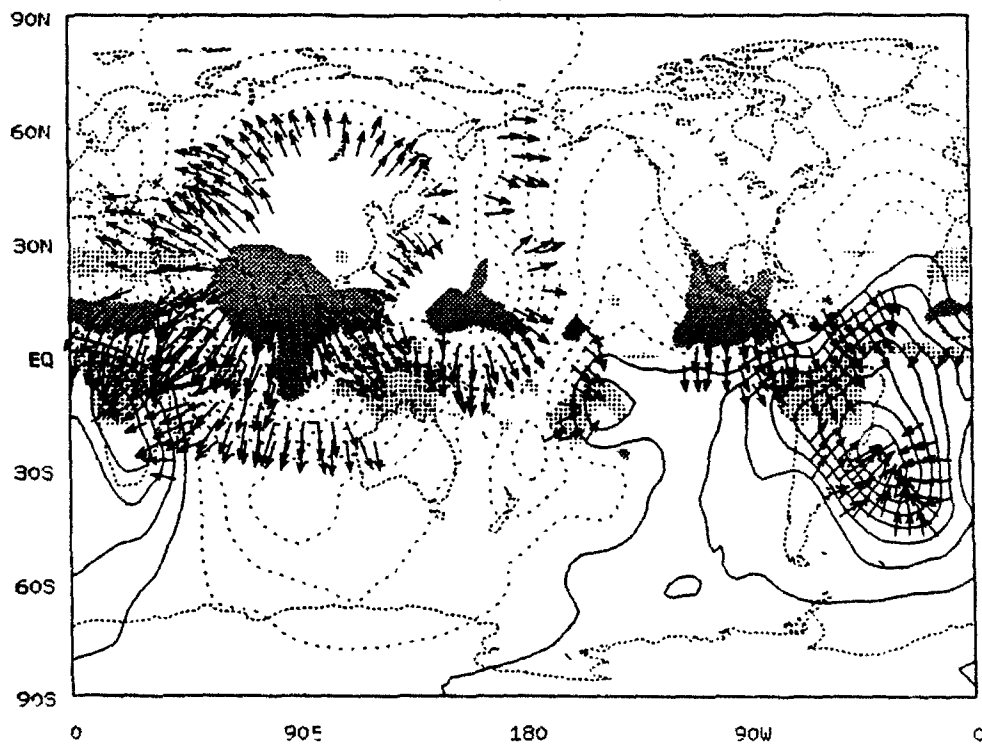
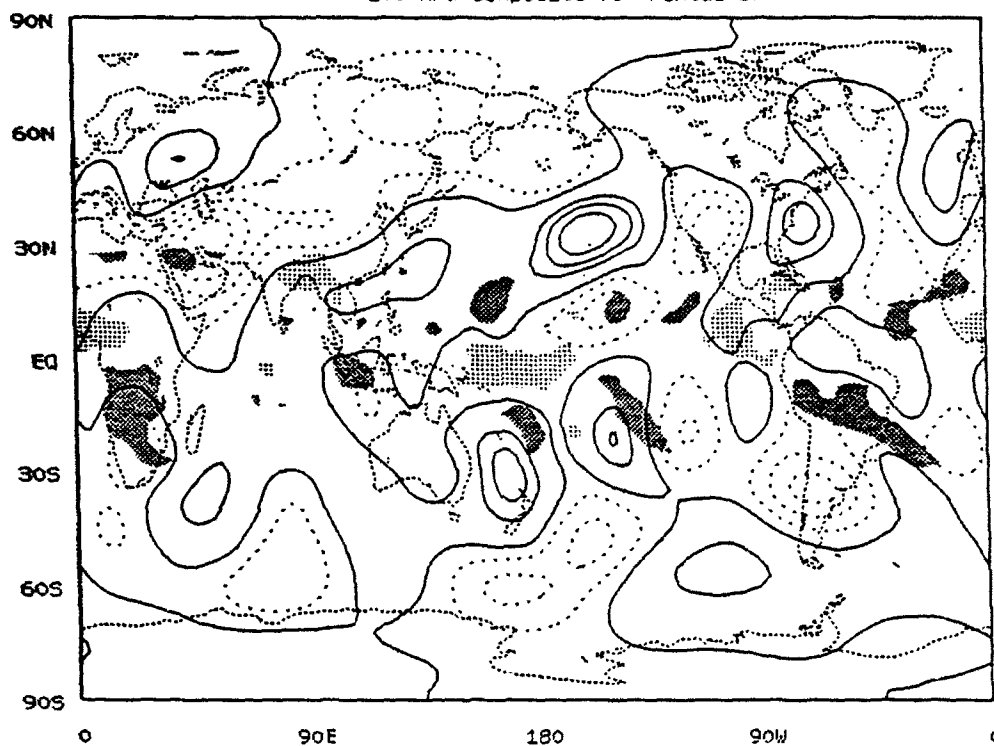


Figure 4.21. Streamfunction (a) and velocity potential(b) anomalies with OLR anomalies superimposed for composite pentad 67. OLR anomaly shading describe in text. Contours in (a) every $0.5 \times 10^7 \text{ m}^2 \text{ s}^{-1}$ and in (b) every $1 \times 10^6 \text{ m}^2 \text{ s}^{-1}$.Maximum value of divergent wind in (b) of 3.4 m s^{-1} near 13° N , 87° E .

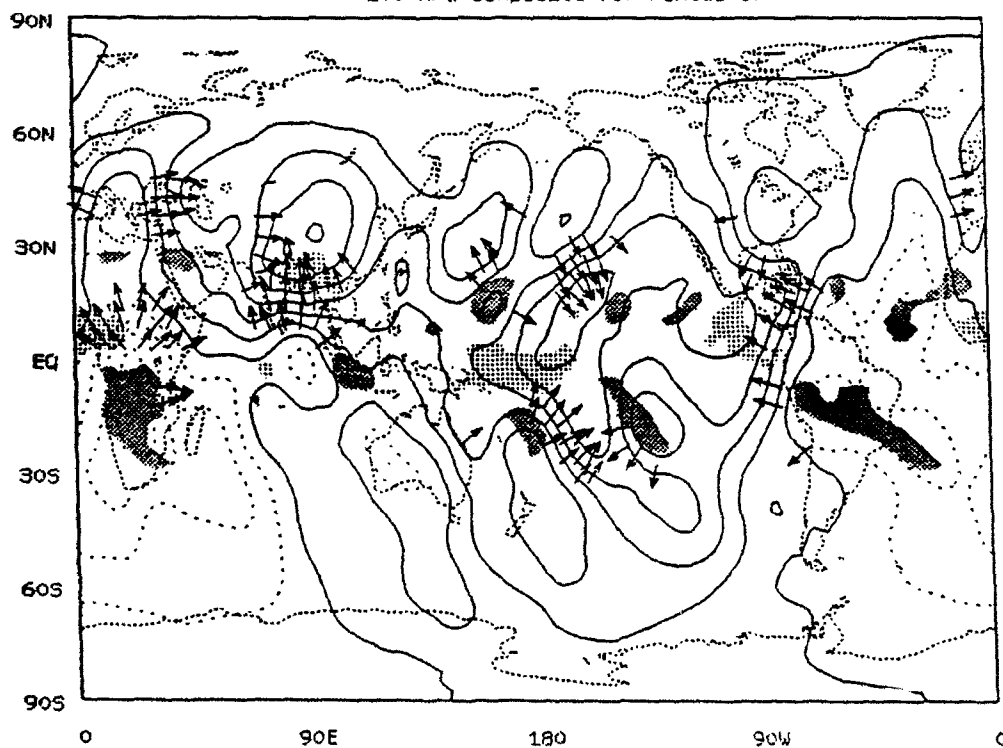
Streamfunction Perturbation and OLR Anomaly
200 hPa Composite for Pentad 67

(a)



Velocity Potential and Divergent Wind Anomaly
200 hPa Composite for Pentad 67

(b)



it moves to the northwest. The resulting flow, shown in the divergent winds, is correspondingly weak.

By pentad 40 (Fig. 4.20), the Asian monsoon is in full swing, and both the ITCZ and convective zone over Central America are active. The strongest positive perturbation in ψ is seen over southwest Asia and to a lesser extent over central South America. Large meridional wind anomalies are evident in the divergent wind associated principally with the monsoon, adding to the strength of the Hadley Cell in the Southern Hemisphere. While the Asian monsoon dominates in areal extent, each of the convective regions exhibits wind anomalies of almost equal magnitude. Comparison of Fig. 4.20b with Fig. 3.3d reveals some differences from those of the decadal July average, notably in the convection center just west of the dateline and the convergence center east of South America at about 30° S. These differences are considered here to be the signature of the intraseasonal oscillation, though, they may also be due to sampling fluctuations.

The wind anomalies have decreased substantially by pentad 67 (Fig. 4.21) as mid-year convection activity subsides in the NH. The convective anomalies have changed from three coherent centers into scattered spots either side of the equator. As would be expected, the response is likewise disorganized and weak, and in a much higher wavenumber pattern than the composite for pentad 40. Over South America, the South Atlantic convergence zone is more evident than in the January average, which shows most of the convection over the Bolivian Plateau. The anomaly of OLR and divergent wind in the SH close to the dateline indicates an eastward displacement of the SPCZ. The composites for pentad 40 and 67 indicate, in general, convection enhancements in regions where convection is found on seasonal averages. If this result holds for a larger number of composites, it would suggest a modulation of the seasonal cycle by the intraseasonal oscillation with amplification of the seasonal convection signature over the global tropics during the "convective"

phase of the oscillation.

4.2.3 Vertical Structure of Divergent Winds

Next, the contribution of the divergent wind for each mode at $\sigma = 0.2$ (~ 200 mb) was calculated for each of the composite pentads using the vertical structure components in the following manner.

$$X_{\sigma=0.2}^n = \bar{X}^n(\sigma) \psi_{\sigma=0.2}^n \quad (4.2)$$

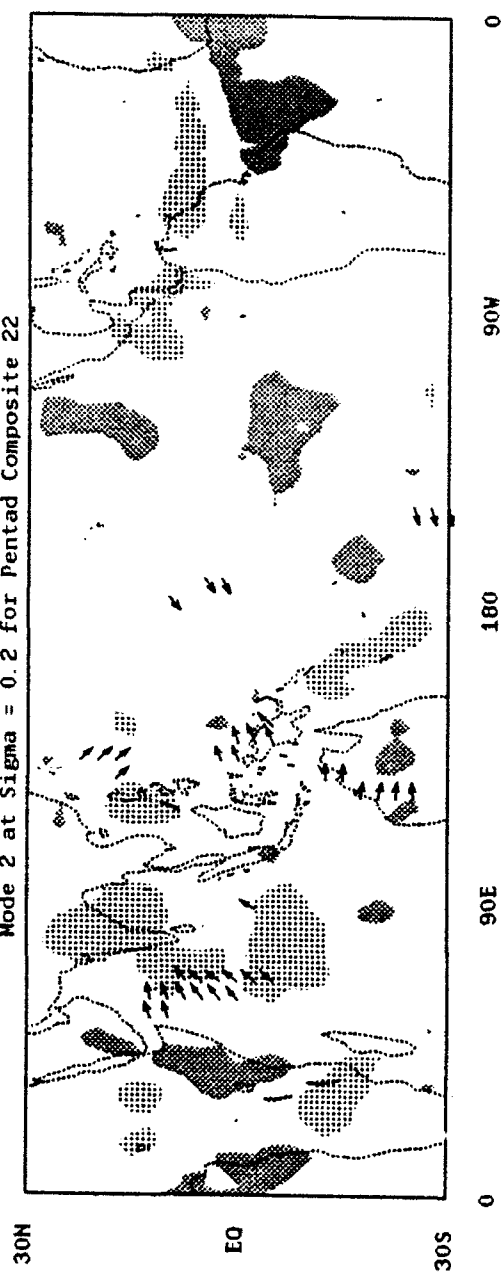
where X is one of the horizontal divergent wind components, n is the vertical mode number, and ψ is the vertical structure function for the given mode number and σ level.

The composite for pentad 22 (see Fig. 4.22) has little contribution from the first internal mode at 200 mb, but very strong inputs from the higher internal modes, as seen in 4.21b-d. This is consistent with the transition season. Typically, the ITCZ at this time is diminishing in the western Pacific and the SPCZ has not yet fully developed. Convective activity is present, as represented by the OLR anomalies, but not throughout the depth of the tropics, hence, the lack of a strong mode two contribution. The only regions indicating deep convective overturning are in the western Indian Ocean, western Australia, and over the maritime continent.

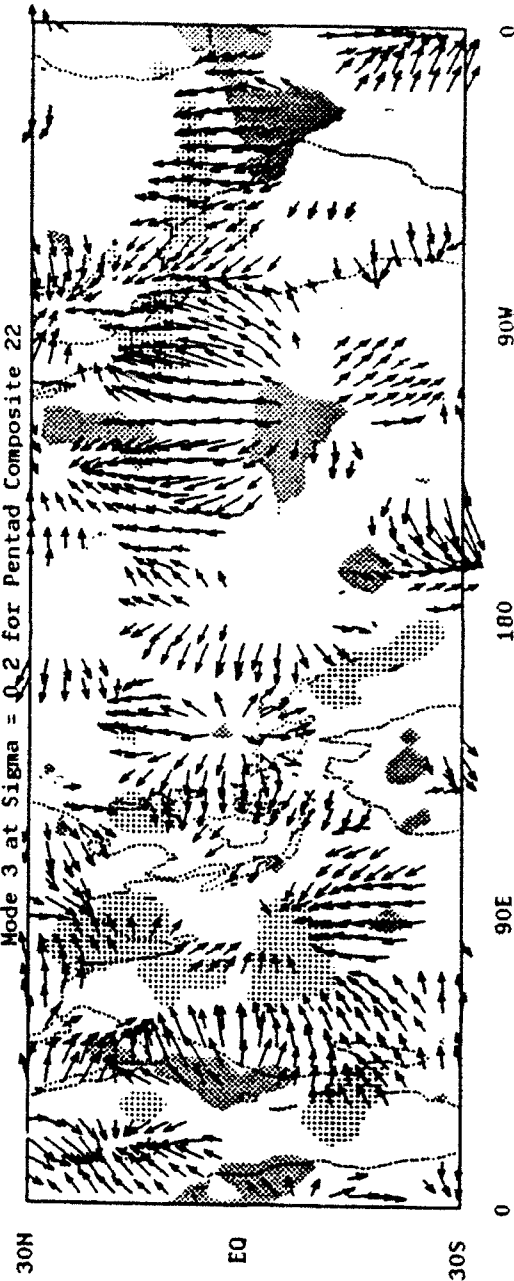
The change in the depth of tropical convection is readily apparent in the composite of pentad 40 (Fig. 4.23). The summer monsoon is well established and significant divergent winds are seen emanating from the OLR anomaly over India. Throughout the tropics each of the internal modes makes a substantially stronger contribution than has been seen previously for pentad 22. There is also an appreciable difference in the vertical structure of the divergent winds emanating from the Indian monsoon region compared to those due to the intraseasonal oscillation signal referred to previously. Although the former reflects deep convection by modes two

Figure 4.22. OLR anomaly and vertical mode contribution to divergent wind anomaly at $\sigma = 0.2$ for composite of pentad 22 for (a) mode 2 (first internal mode), (b) mode 3, (c) mode 4, and (d) mode 5. OLR dark shading for areas $< -20 \text{ W m}^{-2}$, and light shading for areas $> 20 \text{ W m}^{-2}$. Divergent winds only shown when in excess of 0.5 m s^{-1} . Maximum wind values are 0.6 m s^{-1} near 3° S , 138° E in (a), 1.7 m s^{-1} near 5° N , 105° W in (b), 1.6 m s^{-1} near 8° N , 8° E , and 1.2 m s^{-1} near 3° N , 48° E .

(a)

OLR and Divergent Wind Anomaly
Mode 2 at Sigma = 0.2 for Pentad Composite 22

(b)

OLR and Divergent Wind Anomaly
Mode 3 at Sigma = 0.2 for Pentad Composite 22

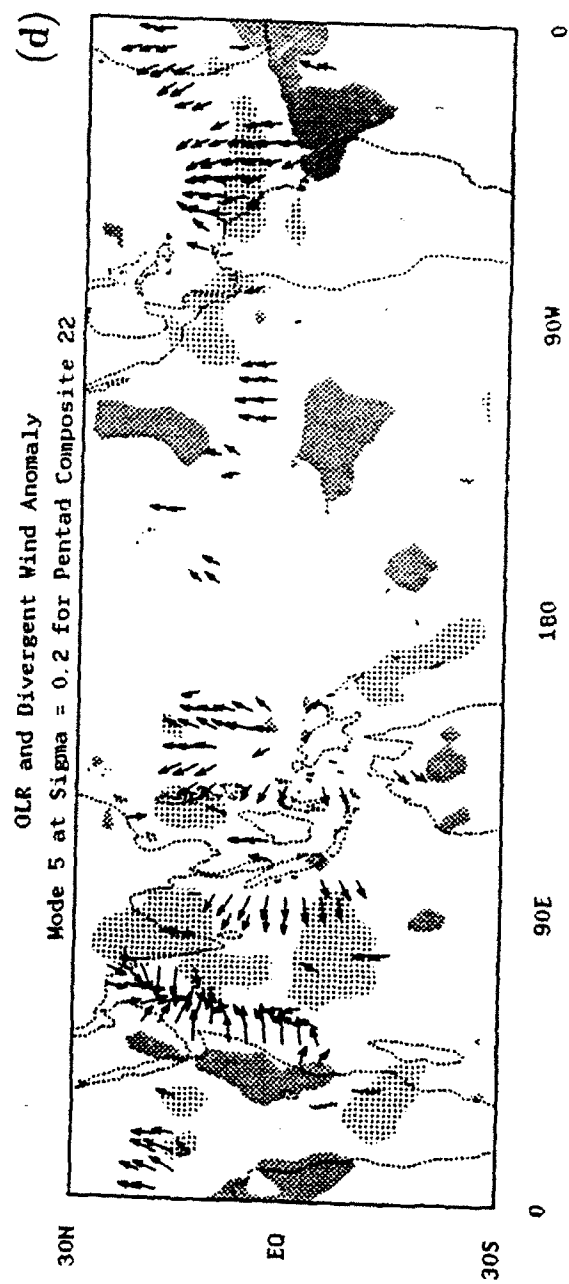
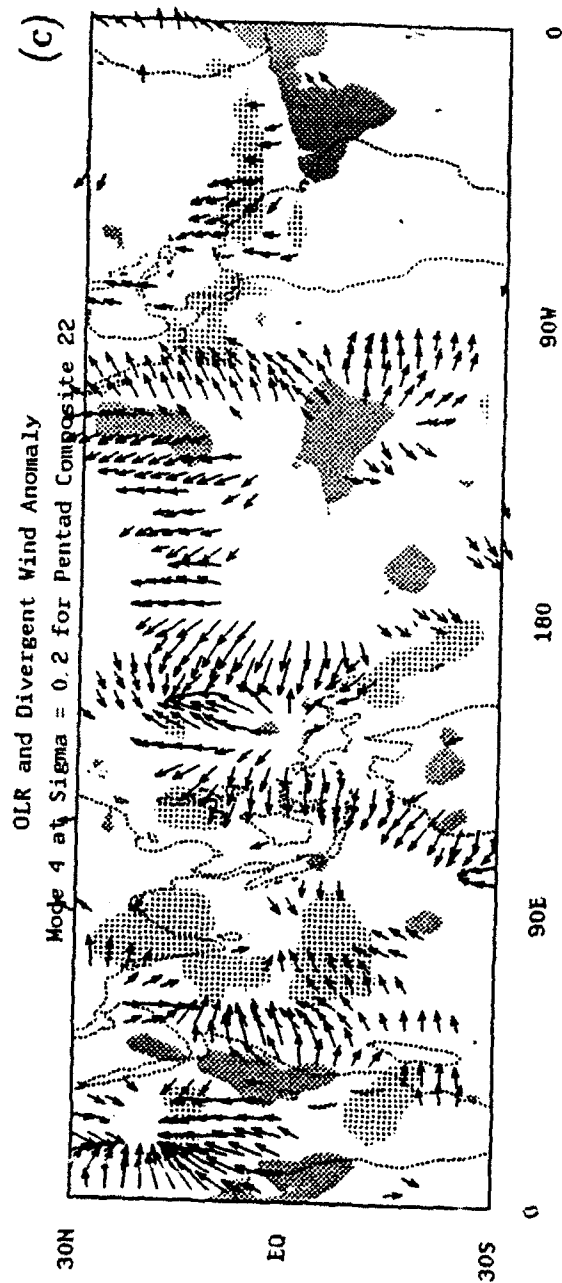
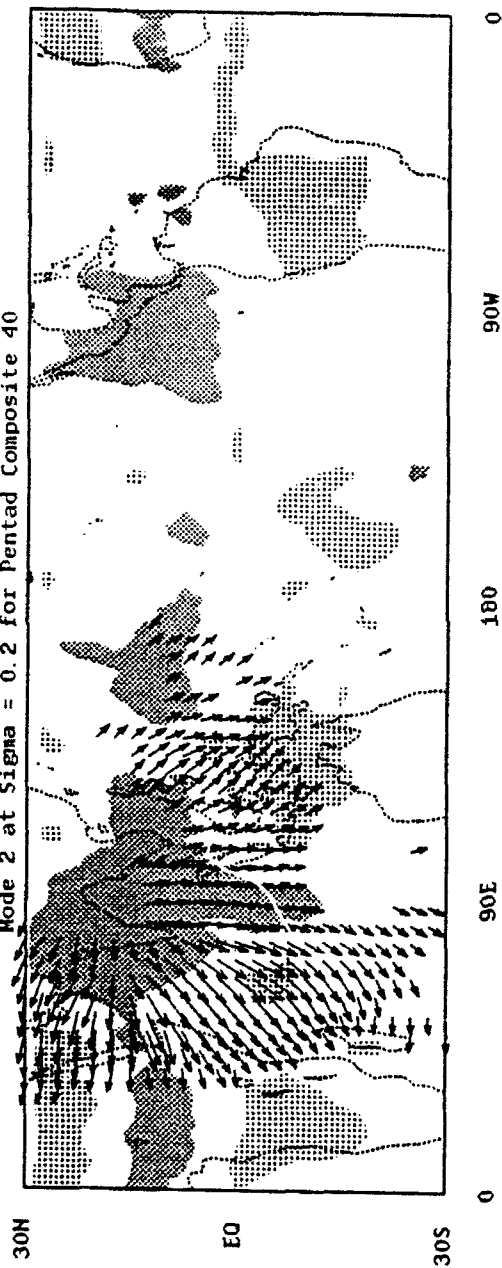


Figure 4.23. OLR anomaly and vertical mode contribution to divergent wind anomaly at $\sigma = 0.2$ for composite of pentad 40 for (a) mode 2 (first internal mode), (b) mode 3, (c) mode 4, and (d) mode 5. OLR dark shading for areas $< -20 \text{ W m}^{-2}$, and light shading for areas $> 20 \text{ W m}^{-2}$. Divergent winds only shown when in excess of 0.5 m s^{-1} . Maximum wind values are 1.3 m s^{-1} near 8° N , 53° E in (a), 2.2 m s^{-1} near 30° S , 15° W in (b), 1.2 m s^{-1} near 18° N , 70° E , and 1.1 m s^{-1} near 10° N , 70° E .

(a)

OLR and Divergent Wind Anomaly

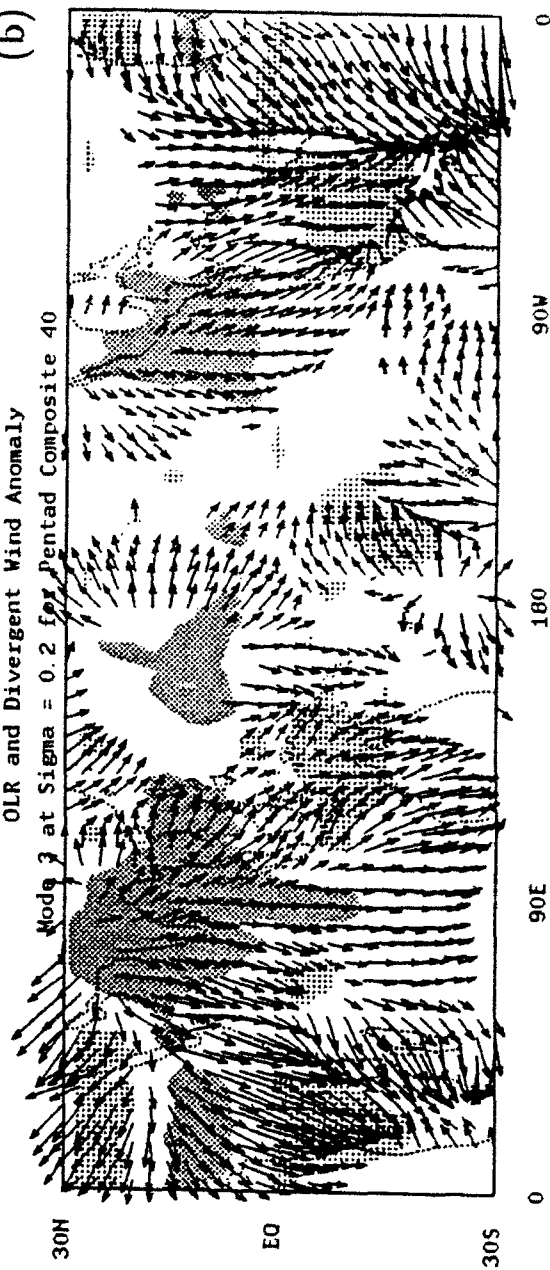
Mode 2 at Sigma = 0.2 for Pentad Composite 40



(b)

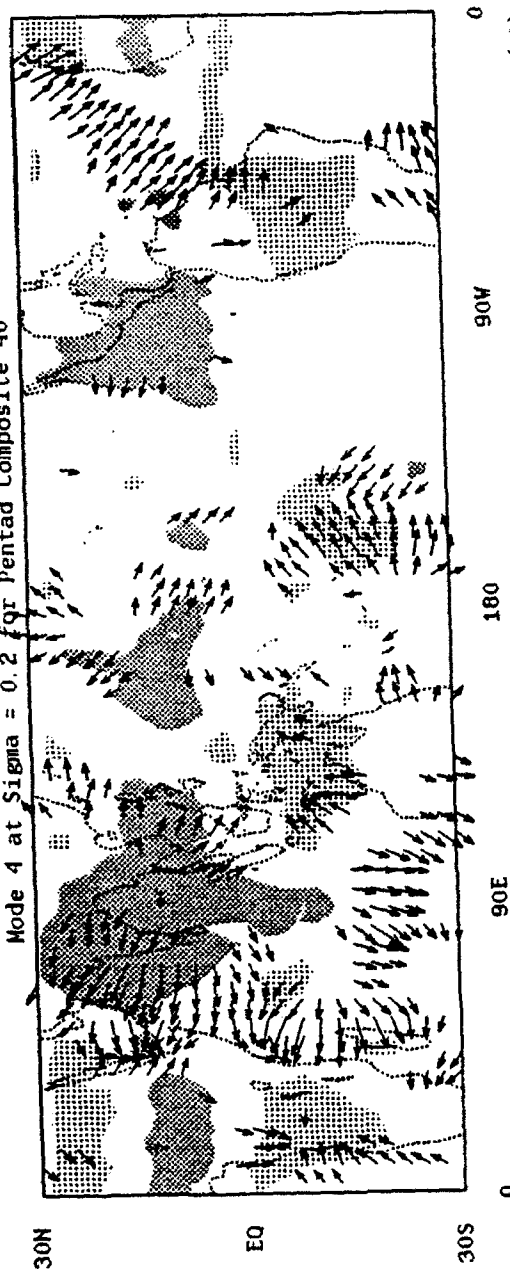
OLR and Divergent Wind Anomaly

Mode 3 at Sigma = 0.2 for Pentad Composite 40



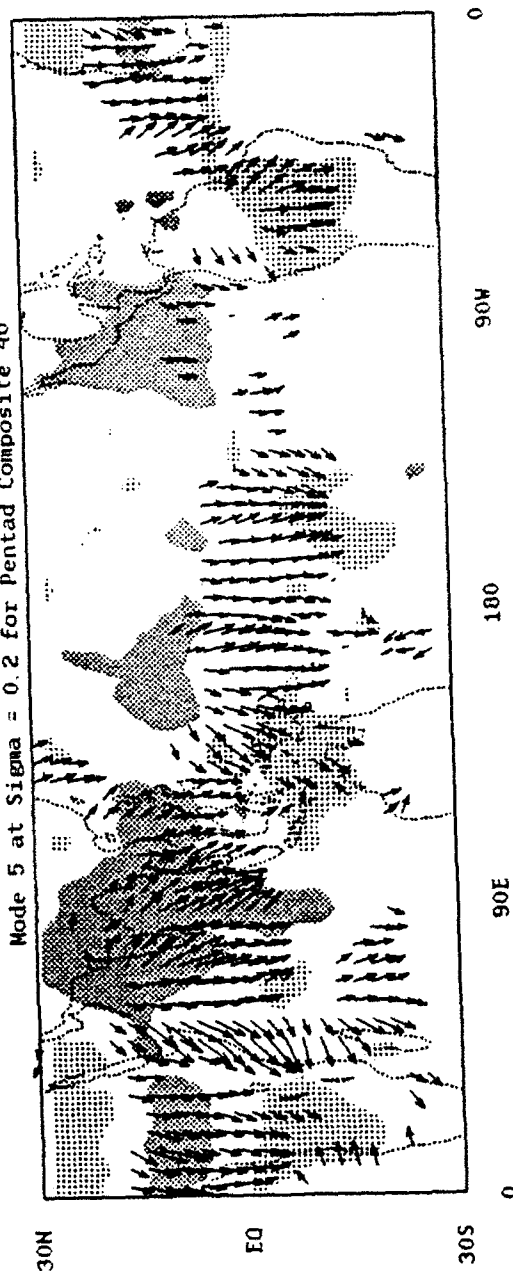
(c)

OLR and Divergent Wind Anomaly
Mode 4 at $\text{Sigma} = 0.2$ for Pentad Composite 40



(d)

OLR and Divergent Wind Anomaly
Mode 5 at $\text{Sigma} = 0.2$ for Pentad Composite 40



and three, the intraseasonal divergent winds emanating from the anomaly center west of the dateline, as well as those converging off the eastern coast of South America, exhibit a dominant mode three structure. This indicates a lower level of maximum vertical motion.

As the summer monsoon subsides and convective activity decreases over southern Asia, the first internal mode contribution becomes weaker. By pentad 67 (Fig. 4.24) its presence is lacking throughout the tropics except for a small region over southeast Asia. At this time, the ITCZ has weakened over the western Pacific and the SPCZ is intensifying. This is seen in the OLR and divergent wind anomalies in the southwestern Pacific for the higher internal modes three through five. A broad area of convergent winds extends from 30° N– 30° S, stretching longitudinally across the tropics in the eastern Pacific. This decomposition also shows that the intensification and displacement of the seasonal cycle due to the intraseasonal oscillation signature appears dominantly in mode three, as was the case during boreal summer.

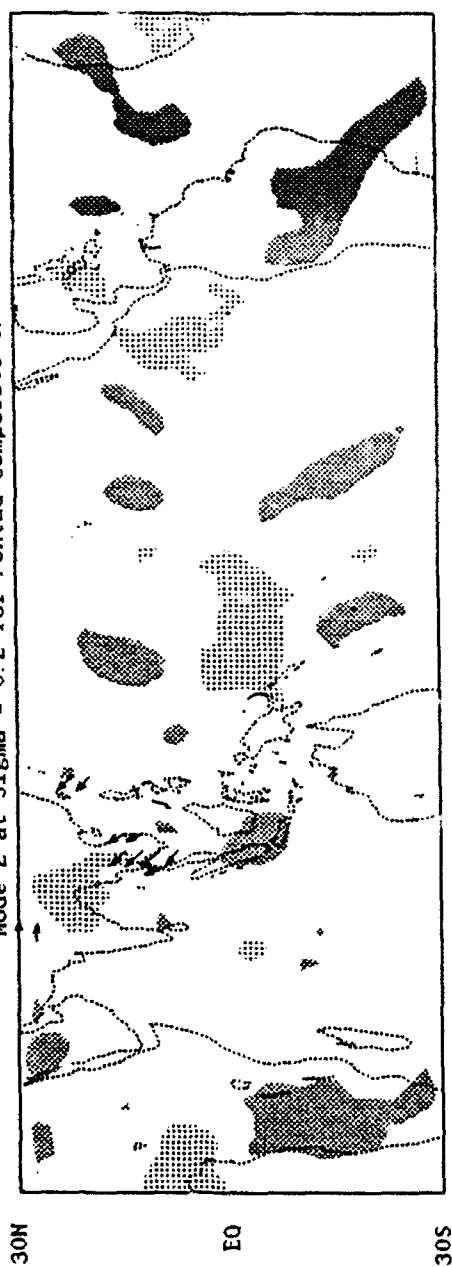
The composite pentads, shown in Figs. 4.22 through 4.24, demonstrate the consistency of the OLR data and the vertical projection. The fact that the annual average was removed to show the intraseasonal variability in the OLR does have meaning because the divergent wind anomalies converge into the areas of relative cooling at this level. This can be seen even with many of the small scale changes, consistent with what would be expected in terms of rising and sinking motions in relation to areas of heating and cooling.

Differences are also found in the vertical structure of the longitudinal and meridional overturnings. This is seen in pentad 22 where the divergent winds in the eastern Pacific show a strong meridional component for mode three, yet they are intensely zonal for mode four. Similarly for pentad 40, the central Pacific displays a strong zonal mode three, and a meridional mode five and even further east, during pentad 67, off the coast of Australia there is again a strong zonal mode three and

Figure 4.24. OLR anomaly and vertical mode contribution to divergent wind anomaly at $\sigma = 0.2$ for composite of pentad 67 for (a) mode 2 (first internal mode), (b) mode 3, (c) mode 4, and (d) mode 5. OLR dark shading for areas $< -20 \text{ W m}^{-2}$, and light shading for areas $> 20 \text{ W m}^{-2}$. Divergent winds only shown when in excess of 0.5 m s^{-1} . Maximum wind values are 0.7 m s^{-1} near 10° S , 104° E in (a), 1.7 m s^{-1} near 28° N , 160° E in (b), 1.2 m s^{-1} near 25° N , 127° E , and 1.2 m s^{-1} near 15° N , 81° E .

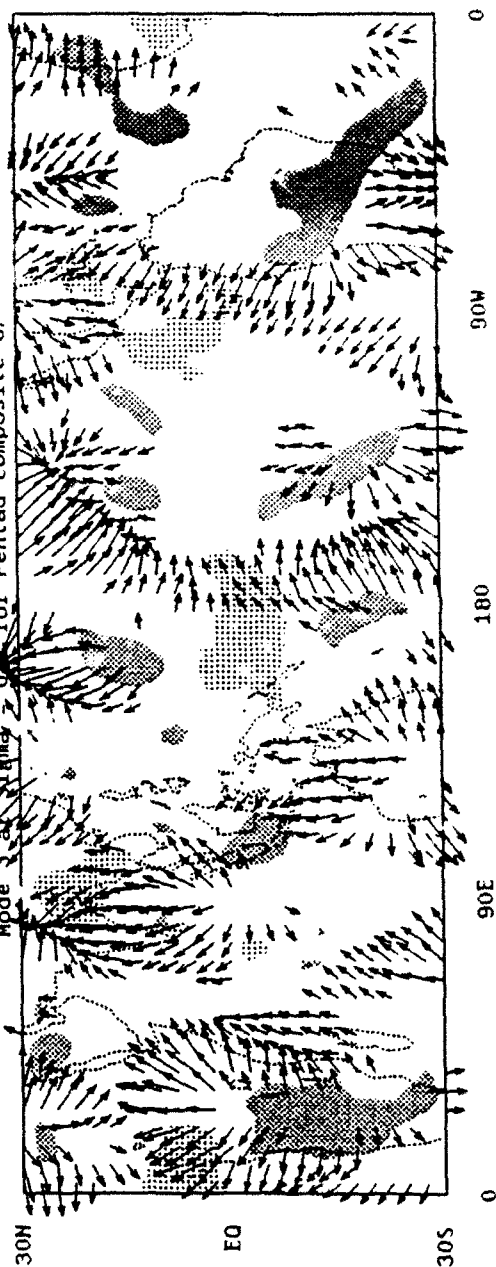
(a)

OLR and Divergent Wind Anomaly

Mode 2 at $\text{Sigma} = 0.2$ for Pentad Composite 67

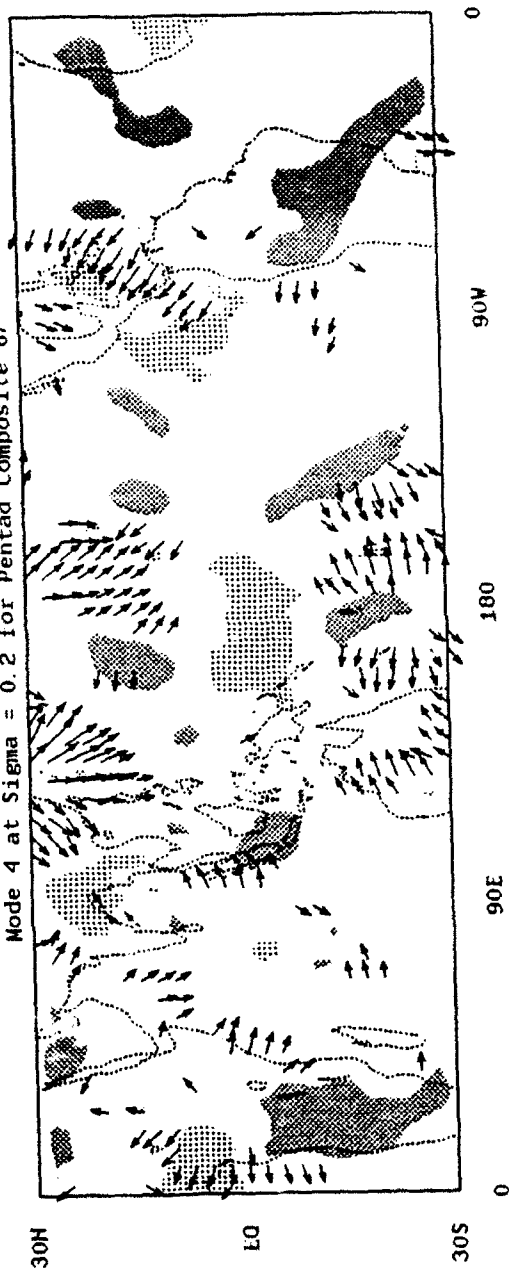
(b)

OLR and Divergent Wind Anomaly

Mode 3 at $\text{Sigma} = 0.2$ for Pentad Composite 67

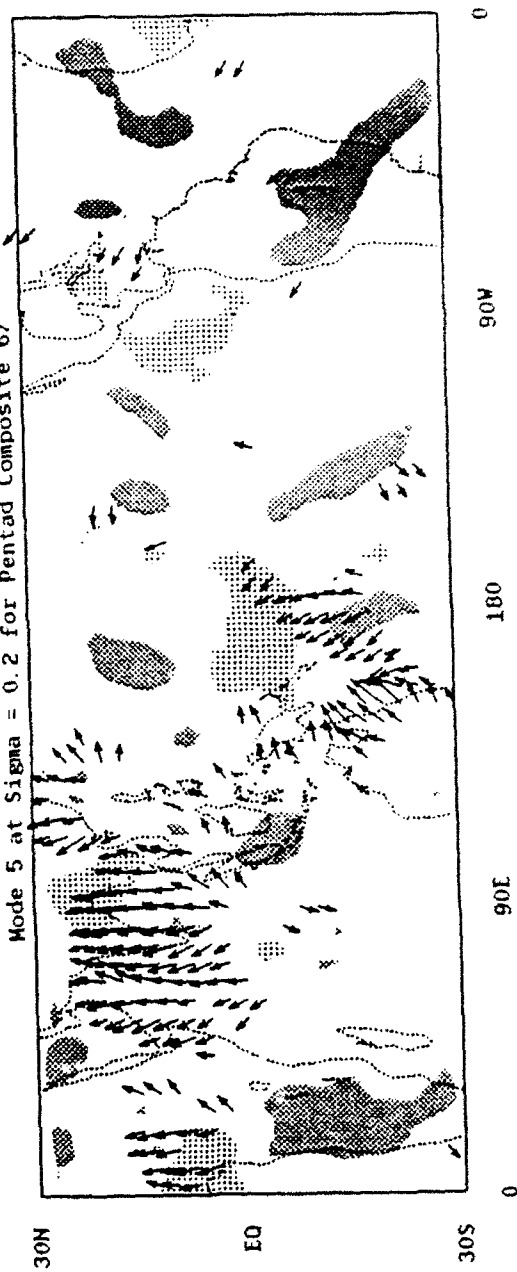
(c)

OLR and Divergent Wind Anomaly
Mode 4 at Sigma = 0.2 for Pentad Composite 67



(d)

OLR and Divergent Wind Anomaly
Mode 5 at Sigma = 0.2 for Pentad Composite 67



a meridional mode five.

In summary, tropical convection shows a preference of low-frequency variability in the seasonal, interannual, and intraseasonal time scales. On the interannual scale, the ENSO episodes display a vertical composition which differs during the warm and cold phases with more contribution by lower modes during the cold phase. Model integrations, completed in the same fashion as described in the previous chapter, are consistent with observations in that wave trains and zonal wind maxima move westward from the warm to the cold phase of the ENSO anomaly. Finally, seasonal composites show a link between the seasonal cycle and the 30-60 day oscillation. In general, when the convective phase of the intraseasonal oscillation is strong compared to the annual average, then the seasonal convective pattern is intensified. A more complete discussion, tying together the findings of this and the previous chapter, follows.

CHAPTER 5

DISCUSSION AND CONCLUSIONS

This research presents findings on the three important low-frequency sub-climatic time scales in the pattern of atmospheric variability in the tropics; the seasonal, interannual, and intraseasonal cycles. This is done for the first time based on a relatively long, coherent data set consisting of 10 years of ECMWF operational analyses. Some of the results confirm those obtained previously by other authors using more limited data sets. This includes the discussion of the zonally-averaged seasonal cycle and its connection with the seasonal migration of tropical heating. Zonal winds are seen to increase during the hemispheric winter, though the SH winds never approach the magnitude of those in the NH. This holds true for the meridional circulation as evident in the strength of the Hadley cell. When OLR values are examined, the regions of low level convergence and upper level divergence, indicated in the meridional wind, coincide with the convective areas.

The background on stationary waves has also been reported by others. The waves reach maximum amplitude near 200 mb with those in the NH exhibiting more pronounced seasonal variability and larger amplitudes. The asymmetric component of the geopotential height also possesses westward tilt with height which at high and mid-latitudes could be caused by topographically forced waves propagating vertically. The horizontal tilt of geopotential height wave is deduced from the momentum transport to be from southwest to northeast at mid-latitudes and from northwest to southeast at high latitudes. Also present is a vertical reversal in

the stationary wave, indicative of mid-atmospheric heating, such as by latent heat release. This vertical profile is found principally in the NH tropics during mid-year (JJA) and to a lesser extent over tropical South America during austral summer (DJF).

New findings on the seasonal cycle come from the decomposition of the wind into rotational and divergent components and then projecting these winds onto a vertical structure function. There is a pronounced change in the vertical structure of the rotational wind planetary waves from vertically reversing winds in the tropics, to equivalent barotropic profiles in the extratropics. The latitudinal shift from one structure to the other taken place abruptly, in most cases within 10° of the convection. The seasonal evolution of the vertical structure of the planetary waves in the divergent and rotational wind components is seen for the first time. Specifically, the results show similar seasonal timing in the onset of the maxima of the zonal equivalent barotropic waves in the extratropics compared to those of the meridional divergent wind waves with deep vertical structures. Though such relationships have been previously found for zonally-averaged circulations, the seasonal linkages between the divergent and rotational wave patterns based on an extensive data set is believed to be new.

Furthermore, it is of interest that the deepest vertical mode for meridional divergent waves is found mostly confined to the summer hemisphere for waves two and three, while the third vertical mode exhibits more of a symmetric structure about the equator, with important contributions into the winter hemispheres. This implies that adequate simulations of meridional cells need to have sufficient vertical resolution to describe convergence at low levels, a rising branch with a high level of nondivergence (~ 300 mb) and a sinking branch with sinking motions maximizing at lower levels (~ 500 mb). Differences are also found between the zonal and meridional divergent wind waves. The largest longitudinal overturnings in the

zonal divergent winds are found at mid-latitudes whereas meridional divergent maxima are also found near the equator. Furthermore, because of the important contribution by the fifth internal mode to the meridional divergent wind, but not to the zonal divergent wind, the first presents more variability at lower levels.

In an effort to quantify how much of the extratropical structure is in response to the seasonal cycle of tropical forcing, linear and PE models are run for comparison. The linear shallow water equation model, using an equivalent depth equal to the third mode, and Paegle's (1989) three-level PE model are forced with January and July heating distributions derived from the averaged OLR field. The PE model is intermediate in generality between a full GCM and the linear model with the advantage of being able to exclude topographical forcing and wave-mean flow interactions. This is accomplished by initializing the PE model with the yearly average of the zonally-averaged zonal wind and nudging the zonally-averaged circulation back to these initial values through the course of the integration. The PE model is integrated for 90 days and the results are averaged for the last 15 days. At this time the PE integrations are similar to those of the linear model in the summer hemisphere, and account for 30 to 50% of the wind response. The PE simulations produce appreciable wave amplitudes in the winter hemisphere, unlike the linear model for which the response is trapped by equatorial easterlies in the summer hemisphere.

The PE model integrations produce wave three patterns for January, in response to the dominant contribution by the heating at this wavelength. This is unlike observations that show a pronounced wave two during NH winter. This is expected since the model does not contain orography, a forcing mechanism essential to explain the observed NH winter waves. The SH winter model response exhibits the observed zonal wind structure which spirals southward around the Antarctic continent. Nevertheless, the PE response is longitudinally shifted by about 100° with respect to

the observations. Close inspection of the simulated divergent outflows reveals that the meridional divergent wind maxima are also further south than the observations and may be the cause for the discrepancies. The observed and simulated patterns, however, are similar enough to warrant the conjecture that, on a seasonal time scale, about 50% of the observed midlatitude SH waves are due to tropical heating. This percentage estimate is only valid to the extent that a more complete version of this PE model adequately simulates atmospheric flows. No statement can be made in this regard, because no control simulations including the earth orography were run.

Variations in the interannual and intraseasonal cycle are also linked to the variations in tropical heating. The vertical structure of the ENSO episodes differs during the cold and warm phase. There are more dominant contributions by the lower vertical modes during the cold phase, when the anomalous convection is displaced towards the western Pacific, than during the warm phase when the tropical convection anomaly is over the central and eastern Pacific. These different structures may be explained by the different air-sea interactive processes acting in the western and eastern Pacific as discussed by Wang (1992). The effect of the tropical convection anomaly in the extratropics was examined with the integrations of the nonlinear PE model as it was done for the seasonal cycle. Motivation for these simulations is provided from recent studies that explain extratropical low-frequency variability by the focussing of energy into preferred locations by the basic flow inhomogeneities (Simmons 1982; Garcia and Salby 1987; Simmons et al. 1983; Branstator 1985; Kasahara and Silva Dias 1986). Branstator (1990) has recently shown that the geographical distribution of low-frequency variance is mostly due to the three-dimensional structure of the basic state, and that it is insensitive to the longitudinal placement of the thermal forcing. His results were obtained by introducing random thermal perturbations in a nine-level linear

PE model and comparing the response to that of a long GCM simulation. The interpretation in this case is that the varying basic state acts to trap disturbances in preferred locations. This conclusion does not consider the role of the external forcing mechanisms responsible for the time-mean three-dimensional basic state.

The PE model is again forced with the heating derived from OLR values, this time, for the warm and cold phase convective anomalies of the 83-85 ENSO episode. As before, these integrations are initialized with the annually-averaged zonal wind, and the model is continually nudged at each time step so that the zonally-averaged wind remains constant through the integration. No other forcing mechanisms are included so that the wave response is due only to the tropical forcing. The PE response is consistent with the observations in that wave trains and zonal wind maxima move westward from the warm to the cold phase of the ENSO anomaly. This result appears to be contrary to the finding of Branstator (1990).

Composites for the departures from annual averages are formed during three different seasons for cases when the convective phase (Gutzler and Madden 1989) of the intraseasonal oscillation was strong. The composites show, in general, an intensification of the seasonal convective patterns. Regions that exhibit convection in the composite, but not in the seasonal average, have dominant contributions from higher vertical modes (mostly mode three) than those associated with seasonal summer convection (mode two for the Indian monsoon). It is also of interest that different vertical structures are found of the longitudinal and meridional overturnings, with the meridional divergent motions displaying contributions by higher vertical modes than their zonal counterparts during the transition, and the opposite, during periods of more active convection.

In conclusion, this research has described the vertical structure of the height and wind fields associated with the seasonal, interannual, and intraseasonal cycles. Although each time scale contains many dissimilarities when compared to one

another, they also each contain many similarities, most notably the tie to tropical convection. The vertical structure of the seasonal cycle and the extent to which observed global patterns may be explained is based on the seasonal march of tropical convection. Additionally, the latitude and longitude where the vertical structure changes from one composed mostly of internal modes into one consisting primarily of the external mode occurs rapidly and within 10° of the convective source regions. Finally, through the use of linear and PE models, the tropical heating is shown to contribute to as much as 50% to SH, and between 30-50% to NH extratropical vertical structure. As mentioned previously, these percentages should be considered as tentative until control runs of this PE model including orography are conducted and shown to adequately simulate the topographically induced midlatitude stationary waves.

REFERENCES

- Barnett, T.P., 1983: Interaction of the monsoon and Pacific trade wind systems at interannual time scales. Part I: The equatorial zone. *Mon. Wea. Rev.*, **111**, 756-773.
- Bjerknes, J., 1966: A possible response of the atmospheric Hadley circulation to equatorial anomalies of ocean temperature. *Tellus*, **18**, 820-829.
- , 1969: Atmospheric teleconnections from the equatorial Pacific. *Mon. Wea. Rev.*, **97**, 163-172.
- Blackmon, M.L., J.M. Wallace, N.-G. Lau and S.L. Mullen, 1977: An observational study of the Northern Hemisphere wintertime circulation. *J. Atmos. Sci.*, **34**, 1040-1053.
- , R.A. Madden, J.M. Wallace and D.S. Gutzler, 1979: Geographical variations in the vertical structure of geopotential height fluctuations. *J. Atmos. Sci.*, **36**, 2450-2466.
- Branstator, G., 1985: Analysis of general circulation model sea surface temperature anomaly models using a linear model. I: Forced solutions. *J. Atmos. Sci.*, **42**, 2225-2241.
- , 1990: Low-frequency patterns induced by stationary waves. *J. Atmos. Sci.*, **47**, 629-648.
- Chao, W.C., 1987: On the origin of the tropical intraseasonal oscillation. *J. Atmos. Sci.*, **44**, 1940-1949.
- Deland, R.J., 1964: Travelling planetary waves. *Tellus*, **16**, 271-273.
- Dickinson, R.E., 1980: Planetary waves: Theory and observation. *Orographic effects in planetary flows*, GARP Publ. Ser. No. 23, Joint Scientific Committee, Geneva, 51-84.
- Eliassen, E. and B. Machenhauer, 1965: A study of the fluctuations of the atmospheric planetary flow patterns represented by spherical harmonics. *Tellus*, **17**, 220-238.
- and ———, 1969: On the observed large-scale atmospheric wave motions. *Tellus*, **21**, 149-165.
- Emanuel, K.A., 1987: An air-sea interaction model of intraseasonal oscillations in the tropics. *J. Atmos. Sci.*, **44**, 2324-2340.
- Errico, R.M., 1987a: *A Description of Software for Determination of Normal Modes of the NCAR Community Climate Model*. NCAR Technical Note NCAR/TN-277+STR, 86pp.

- and B.E. Easton, 1987b: *Nonlinear Normal Mode Initialization of the NCAR CCM*. NCAR Technical Note NCAR/TN-303+IA, 106 pp.
- Fleming, E.L., G.-H. Lim and J.M. Wallace, 1987: Differences between the spring and autumn circulation of the Northern Hemisphere. *J. Atmos. Sci.*, **44**, 1266-1286.
- Garcia, R.R. and M.L. Salby, 1987: Transient response to localized episodic heating in the tropics. Part II: Far-field behavior. *J. Atmos. Sci.*, **44**, 499-530.
- Geisler, J.E. and D.E. Stevens, 1982: On the vertical structure of damped steady circulation in the tropics. *Quart. J. Roy. Meteor. Soc.*, **108**, 87-94.
- Ghil, M. and K. Mo, 1991a: Intraseasonal oscillations in the global atmosphere. Part I: Northern Hemisphere and tropics. *J. Atmos. Sci.*, **48**, 752-779.
- and —, 1991b: Intraseasonal oscillations in the global atmosphere. Part II: Southern Hemisphere. *J. Atmos. Sci.*, **48**, 780-790.
- Gill, A.E., 1980: Some simple solutions for heat-induced tropical circulation. *Quart. J. Roy. Meteor. Soc.*, **106**, 447-462.
- Gutzler, D.S., 1990: Vertical structure and interannual variability of tropical zonal winds. *J. Climate*, **3**, 741-750.
- and R.A. Madden, 1989: Seasonal variations in the spatial structure of intraseasonal tropical wind fluctuations. *J. Atmos. Sci.*, **46**, 641-660.
- and T.M. Wood, 1990: Structure of large-scale convective anomalies over tropical oceans. *J. Climate*, **3**, 483-496.
- Hayashi, Y., 1971: A generalized method of resolving disturbances into progressive and retrogressive waves by space Fourier and time cross-spectral analysis. *J. Meteor. Soc. Japan*, **49**, 125-128.
- Held, I., 1983: Stationary and quasi-stationary eddies in the extratropical atmosphere: Theory. *Large-Scale Dynamical Processes in the Atmosphere*, B.J. Hoskins and R.P. Pearce, Eds., Academic Press, 127-168.
- Hendon, H.H. and B. Liebmann, 1990: The intraseasonal (30-50 day) oscillation of the Australian summer monsoon. *J. Atmos. Sci.*, **47**, 2909-2923.
- Holmström, I., 1963: On a method for parametric representation of the state of the atmosphere. *Tellus*, **15**, 127-149.
- Horel, J.D., 1982: On the annual cycle of the tropical Pacific atmosphere and ocean. *Mon. Wea. Rev.*, **110**, 1863-1878.
- , A.N. Hahmann and J.E. Geisler, 1989: An investigation of the annual cycle of convective activity over the tropical Americas. *J. Climate*, **2**, 1388-1403.
- and J.M. Wallace, 1981: Planetary-scale atmospheric phenomena associated with the Southern Oscillation., **109**, 813-829.
- Horn, L.H. and R.A. Bryson, 1963: An analysis of the geostrophic kinetic energy

- spectrum of large-scale atmospheric turbulence. *J. Geophys. Res.*, **68**, 1059-1064.
- Hsu, C.-P. and J.M. Wallace, 1976a: The global distribution of the annual and semiannual cycles in precipitation. *Mon. Wea. Rev.*, **104**, 1093-1103.
- and —, 1976b: The global distribution of the annual and semiannual cycles in sea-level pressure. *Mon. Wea. Rev.*, **104**, 1597-1601.
- Julian, R.P., 1966: A cross-spectral analysis of zonal index data. *Mon. Wea. Rev.*, **94**, 283-293.
- Kanamitsu, M., K.C. Mo and E. Kalnay, 1990: Annual cycle integration of the NMC medium-range forecasting (MRF) model. *Mon. Wea. Rev.*, **118**, 2543-2567.
- Kao, S.-K. and L.L. Wendell, 1970: The kinetic energy of the large-scale atmospheric motion in wavenumber-frequency space. I. Northern Hemisphere. *J. Atmos. Sci.*, **27**, 359-375.
- Kasahara, A., 1976: Normal modes of ultralong waves in the atmosphere. *Mon. Wea. Rev.*, **104**, 669-690.
- and K. Puri, 1981: Spectral representation of three dimensional global data by expansion in normal mode functions. *Mon. Wea. Rev.*, **109**, 37-51.
- and P.L. da Silva Dias, 1986: Response of planetary waves to stationary tropical heating in a global atmosphere with meridional and vertical shear. *J. Atmos. Sci.*, **43**, 1893-1911.
- Kinter, J.L., J. Shukla, L. Marx and E. Schneider, 1988: A simulation of the winter and summer circulations with the NMC global spectral model. *J. Atmos. Sci.*, **45**, 2486-2522.
- Knuston, T.R. and K.M. Weickman, 1987: 30-60 day atmospheric oscillations: composite life cycles of convection and circulation anomalies. *Mon. Wea. Rev.*, **115**, 1407-1436.
- , — and J.E. Kutzback, 1986: Global-scale intraseasonal oscillations of outgoing longwave radiation and 250 mb zonal wind during Northern Hemisphere summer. *Mon. Wea. Rev.*, **114**, 605-623.
- Krishnamurti, T.N., 1971: Tropical east-west circulations during northern summer. *J. Atmos. Sci.*, **28**, 1342-1347.
- and S. Gadgil, 1985: On the structure of the 30 to 50 day mode over the globe during FGGE. *Tellus*, **37A**, 336-360.
- Lau, K.-M. and P.H. Chan, 1985: Aspects of the 40-50 day oscillation during northern winter from outgoing longwave radiation. *Mon. Wea. Rev.*, **113**, 1889-1909.
- and —, 1986: The 40-50 day oscillation and the El Niño/Southern Oscillation: A new perspective. *Bull. Amer. Meteor. Soc.*, **67**, 533-534.
- and —, 1988: Intraseasonal and interannual variations of tropical convec-

- and —, 1986: The 40–50 day oscillation and the El Niño/Southern Oscillation: A new perspective. *Bull. Amer. Meteor. Soc.*, **67**, 533–534.
- and —, 1988: Intraseasonal and interannual variations of tropical convection: A possible link between the 40–50 day oscillation and ENSO? *J. Atmos. Sci.*, **45**, 506–521,
- and L. Peng, 1987: Origin of low frequency (intraseasonal) oscillations in the tropical atmosphere. Part I: Basic theory. *J. Atmos. Sci.*, **44**, 950–972.
- Lau, N.-C. and J.M. Wallace, 1979: On the distribution of horizontal transports by transient eddies in the Northern Hemisphere wintertime circulation. *J. Atmos. Sci.*, **36**, 1844–1863.
- Liebmann, B. and D.L. Hartmann, 1984: An observational study of tropical – midlatitude interaction on intraseasonal time scales during winter. *J. Atmos. Sci.*, **41**, 3333–3350.
- Lim, H. and C.P. Chang, 1986: Generation of internal and external mode motions from internal heating: Effects of vertical shear and damping. *J. Atmos. Sci.*, **43**, 948–957.
- Lindzen, R.S. and S. Nigam, 1987: On the role of the surface temperature gradients in forcing low level winds and convergence in the tropics. *J. Atmos. Sci.*, **44**, 2440–2458.
- Lorenz, E.N., 1967: *The Nature and Theory of the General Circulation of the Atmosphere*. WMO, 161 pp.
- Madden, R.A. and P.R. Julian, 1971: Detection of a 40–50 day oscillation in the zonal wind in the tropical Pacific. *J. Atmos. Sci.*, **28**, 702–708.
- and —, 1972: Description of global scale circulation cells in the tropics with a 40–50 day period. *J. Atmos. Sci.*, **29**, 1109–1123.
- Mechoso, C.R. and D.L. Hartmann, 1982: An observational study of traveling planetary waves in the Southern Hemisphere, *J. Atmos. Sci.*, **39**, 1921–1935.
- Meehl, G.A., 1987: The annual cycle and its relationship to interannual variability in the tropical Pacific and Indian Ocean region. *Mon. Wea. Rev.*, **115**, 27–50.
- , 1990: Seasonal cycle forcing of El Niño–Southern Oscillation in a global, coupled ocean–atmosphere GCM. *J. Climate*, **3**, 72–98.
- Murakami, T., 1988: Intraseasonal atmospheric teleconnection patterns during the Northern Hemisphere winter. *J. Climate*, **1**, 117–131.
- Neelin, J.D., I.M. Held and K.H. Cook, 1987: Evaporation–wind feedback and low-frequency variability in the tropical atmosphere. *J. Atmos. Sci.*, **44**, 2341–2348.
- Nogués-Paegle, J., Z.-Zhao, G. Sampson and J. Paegle, 1986: Vertical structure of the wind field during the special observing period I of the Global Weather Experiment. *Meteor. Atmos. Phys.*, **35**, 149–165.

- Period of the Global Weather Experiment. *J. Atmos. Sci.*, **44**, 2277-2289.
- , B.-C. Lee and V.E. Kousky, 1989: Observed modal characteristics of the intraseasonal oscillation. *J. Climate*, **2**, 496-507.
- Oort, A.H. and E.M. Rasmusson, 1971: *Atmospheric Circulation Statistics*. NOAA Prof. Paper 5, US Dept. of Commerce, 323 pp.
- Paegle, J., J.N. Paegle, and Y. Hong, 1983: The role of barotropic oscillation within atmospheres of highly variable refractive index. *J. Atmos. Sci.*, **40**, 2251-2265.
- , 1989: A variable resolution global model based upon Fourier and finite element representation. *Mon. Wea. Rev.*, **117**, 583-606.
- and W.E. Baker, 1982: Planetary-scale characteristics of the atmospheric circulation during January and February 1979. *J. Atmos. Sci.*, **39**, 2521-2538.
- and E.M. Tomlinson, 1975: Solution of the balance equation incorporating Fourier transform and Gauss elimination techniques. *Mon. Wea. Rev.*, **103**, 528-535.
- Philander, S.G., 1990: *El Niño, La Niña, and the Southern Oscillation*. Academic Press, 293 pp.
- Randel, W.J., 1987: *Global Atmospheric Circulation Statistics, 1000-1 mb.*, NCAR Technical Note, NCAR/TN-295+STR, 245 pp.
- , D.E. Stevens and J.L. Stanford, 1987: A study of planetary waves in the southern winter troposphere and stratosphere. Part II: Life Cycles. *J. Atmos. Sci.*, **44**, 936-949.
- Rasmusson, E.M. and T.H. Carpenter, 1982: Variations in tropical sea surface temperature and surface wind fields associated with the Southern Oscillation/El Niño. *Mon. Wea. Rev.*, **110**, 354-384.
- Sardeshmukh, P.D. and B.J. Hoskins, 1988: The generation of global rotational flow by steady idealized tropical divergence. *J. Atmos. Sci.*, **45**, 1228-1251.
- Schneider, E.K., 1987: A simplified model of the modified Hadley circulation. *J. Atmos. Sci.*, **44**, 3311-3328.
- Schubert, S., C.-K. Park, W. Higgins, S. Moorthi and M. Suarez, 1990a: *An atlas of ECMWF analyses (1980-1987): Part I - First moment quantities*. NASA Technical Memorandum 100747, January 1990, 253 pages.
- , —, —, — and —, 1990b: *An atlas of ECMWF analyses (1980-1987): Part II - Second moment quantities*. NASA Technical Memorandum 100762, June 1990, 262 pages.
- Shaw, D.B., P. Lonnerberg, A. Hollingsworth and P. Unden, 1987: Data assimilation: The 1984/85 revisions of the ECMWF mass and wind analysis. *Quart. J. Roy. Meteor. Soc.*, **113**, pp. 533-566.
- Silva Dias, P.L., W.H. Schubert and M. DeMaria, 1983: Large scale response of the tropical atmosphere to transient convection. *J. Atmos. Sci.*, **40**, 2689-2707.

- and J.P. Bonatti, 1985: A preliminary study of the observed vertical mode structure of the summer circulation over tropical South America. *Tellus*, **37A**, 185-195.
- Simmons, A.J., 1982: The forcing of stationary wave motion by tropical diabatic heating. *Quart. J. Roy. Meteor. Soc.*, **108**, 503-534.
- , J.M. Wallace and G. Branstator, 1983: Barotropic propagation and instability, and atmospheric teleconnection patterns. *J. Atmos. Sci.*, **40**, 1363-1392.
- Tanaka, H., 1985: Global energetics analysis by expansion into three-dimensional normal mode functions during the FGGE winter. *J. Meteor. Soc. Japan*, **63**, 180-200.
- and E.C. Kung, 1988: Normal mode energetics of the general circulation during the FGGE year. *J. Atmos. Sci.*, **45**, 3723-3736.
- and —, 1989: A study of low-frequency unstable planetary waves in realistic zonal and zonally varying basic states. *Tellus*, **41A**, 179-199.
- Trenberth, K.E. and J.E. Olson, 1988: An evaluation and intercomparison of global analyses from the National Meteorological Center and the European Centre for Medium Range Weather Forecasts. *Bull. Amer. Meteor. Soc.*, **69**, 1047-1057.
- and D.J. Shea, 1987: On the evolution of the Southern Oscillation. *Mon. Wea. Rev.*, **115**, 3078-3096.
- Uppala, S., 1986: *The assimilation of the final level II-b data set at ECMWF, Part I*. Proceedings of the U.S. Natl. Conference on the scientific results of the First GARP Global Experiment FGGE, January 14-17 1986, American Meteorological Society, 24-30.
- van Loon, H. and R.L. Jenne, 1972: The zonal harmonic standing waves in the Southern Hemisphere. *J. Geophys. Res.*, **77**, 992-1003.
- Walker, G.T. and E.W. Bliss, 1932: World Weather V. *Mem. Roy. Meteor. Soc.*, **4**, 53-84.
- and —, 1937: World Weather VI. *Mem. Roy. Meteor. Soc.*, **4**, 119-139.
- Wallace, J.M., 1983: The climatological mean stationary waves: Observational evidence. *Large-Scale Dynamical Processes in the Atmosphere*, B.J. Hoskins and R.P. Pearce, Eds., Academic Press, 27-53.
- Wang, B., 1992: The vertical structure and development of the ENSO anomaly mode during 1979-1989. *J. Atmos. Sci.*, in press.
- Weickmann, K.M., 1983: Intraseasonal circulation and outgoing longwave radiation modes during northern hemisphere winter. *Mon. Wea. Rev.*, **111**, 1838-1858.
- , G.R. Lussky and J.E. Kutzbach, 1985: Intraseasonal (30-60 day) fluctuations of outgoing longwave radiations and 250 mb streamfunction during northern winter. *Mon. Wea. Rev.*, **113**, 941-961.

- White, G.H., 1982: An observational study of the Northern Hemisphere extratropical summertime general circulation. *J. Atmos. Sci.*, **39**, 24-40.
- Wiin-Nielsen, A., 1967: On the annual variation and spectral distribution of atmospheric energy. *Tellus*, **19**, 540-559.
- , 1971a: On the motion of various vertical models of transient, very long waves. Part 1. Beta plane approximation. *Tellus*, **23**, 87-98.
- , 1971b: On the motion of various vertical models of transient, very long waves. Part 2. The spherical case. *Tellus*, **23**, 207-217.
- Yamagata, T. and Y. Hayashi, 1984: A simple model for the 30-50 day oscillation in the tropics. *J. Meteor. Soc. Japan*, **62**, 709-717.
- Ziemke, J.R. and J.L. Stanford, 1990: One-to-two month oscillations in the stratosphere during southern winter. *J. Atmos. Sci.*, **47**, 1778-1793.